Govind R. Kadambi
Preetham B. Kumar
Vasile Palade   *Editors*

Emerging Trends in Photonics, Signal Processing and Communication Engineering

Proceedings of ICPSPCT 2018

Springer

Lecture Notes in Electrical Engineering

Volume 649

The book series *Lecture Notes in Electrical Engineering* (LNEE) publishes the latest developments in Electrical Engineering - quickly, informally and in high quality. While original research reported in proceedings and monographs has traditionally formed the core of LNEE, we also encourage authors to submit books devoted to supporting student education and professional training in the various fields and applications areas of electrical engineering. The series cover classical and emerging topics concerning:

- Communication Engineering, Information Theory and Networks
- Electronics Engineering and Microelectronics
- Signal, Image and Speech Processing
- Wireless and Mobile Communication
- Circuits and Systems
- Energy Systems, Power Electronics and Electrical Machines
- Electro-optical Engineering
- Instrumentation Engineering
- Avionics Engineering
- Control Systems
- Internet-of-Things and Cybersecurity
- Biomedical Devices, MEMS and NEMS

For general information about this book series, comments or suggestions, please contact leontina.dicecco@springer.com.

To submit a proposal or request further information, please contact the Publishing Editor in your country:

China

Jasmine Dou, Associate Editor (jasmine.dou@springer.com)

India, Japan, Rest of Asia

Swati Meherishi, Executive Editor (Swati.Meherishi@springer.com)

Southeast Asia, Australia, New Zealand

Ramesh Nath Premnath, Editor (ramesh.premnath@springernature.com)

USA, Canada:

Michael Luby, Senior Editor (michael.luby@springer.com)

All other Countries:

Leontina Di Cecco, Senior Editor (leontina.dicecco@springer.com)

** Indexing: The books of this series are submitted to ISI Proceedings, EI-Compendex, SCOPUS, MetaPress, Web of Science and Springerlink **

More information about this series at http://www.springer.com/series/7818

Govind R. Kadambi · Preetham B. Kumar ·
Vasile Palade

Editors

Emerging Trends in Photonics, Signal Processing and Communication Engineering

Proceedings of ICPSPCT 2018

Editors
Govind R. Kadambi
Research Division
M. S. Ramaiah University
of Applied Sciences
Bengaluru, Karnataka, India

Preetham B. Kumar
Department of Electrical
and Electronic Engineering
California State University, Sacramento
Sacramento, CA, USA

Vasile Palade 🆔
Faculty of Engineering and Computing
Coventry University
Coventry, UK

Preface

Welcome to Springer Book Volume *Emerging Trends in Photonics, Signal Processing and Communication Engineering* from selected papers from the inaugural International Conference on Photonics, Communication and Signal Processing Technologies (ICPSPCT). ICPSPCT was held from July 18 to 20 2018 in Ramaiah University of Applied Sciences (RUAS), Bengaluru, India. ICPSPCT was jointly organized by Centre for Signal Processing and Communication System Research (CSPCSR) and Photonics Research Centre (PRC) of RUAS, Bengaluru, India. It is imperative that the resulting success of technological advancements in communication technologies which has revolutionized the outlook of the standard of living of modern era is also attributed to interleaved contemporary evolutionary progress in Signal Processing. In the emerging Opto-Electronics Technology, Photonics has established itself as a prominent research domain to reckon with through multiple conceptual breakthroughs. Therefore it is but obvious that ICPSPCT served as a platform for students, research scholars, academicians, industry professionals and researchers to publish their innovative research concepts as well as contributory research findings. This conference encouraged submission of research papers highlighting analytical formulation, solution, simulation, algorithm development, experimental research and experimental investigations in the broad domains of Photonics, Signal Processing and Communication Technologies. This conference envisaged and also encouraged publication of research papers from allied fields of science and engineering depicting multidisciplinary research and industry-academia synergy. The theme of the ICPSPCT included Signal Processing, Image Processing, Communication, Microwave (Antenna/Measurements), Photonics, VLSI Circuits and Systems, Communication Networks, System Design and System Engineering.

The program of this three-day conference included a pre-conference Invited Expert Lecture series followed by the paper presentation. In the forenoon of Invited Expert Lecture Series, Prof. Urbasi Sinha of Raman Research Institute, Bengaluru delivered a lecture on "Quantum Information Processing" followed by a session on "Wireless Communication Technologies: Challenges, Future Trends, and their Relevance to India" by Prof. K. Giridhar, IIT, Madras. Prof. Bharadwaj Amrutur, Department of ECE, RBCCPS, IISc, delivered a talk on "Internet of Things". In the

afternoon session, Dr. Anil Kumar of TCS Innovation Labs, Bengaluru discussed about the "Sparse Sensing" followed by a talk of Prof. R. Hariharan, RUAS, on "Deep Learning Algorithms". In the inaugural address of the conference, Dr. M. Nageswara Rao, Director, Satellite Infrastructure Programme Office, ISRO HQ, Bengaluru, highlighted the role of Photonics in Satellite Technology. Dr. Dipanjan Pan, University of Illinois at Urbana—Champaign, USA, delivered the keynote address dwelling upon the "Molecular Medicine from Advanced Imaging to Therapy". The first invited talk by Dr. M. Girish Chandra covered the "Graph Signal Processing". It was followed by the talk of Dr. Varun Raghunathan, Department ECE, IISc, Bengaluru, on "Photonics". Dr. Jay Gubbi of TCS Innovations Lab, Bangalore, delivered a session on "Robotic Vision". An invited session on "Wireless Systems" by Prof. Jyotsna Bapat, IIIT, Bengaluru, was also a highlight of the conference. The last invited talk was by Dr. M. R. Ananthasayanam, Professor (Retd.), Department of Aerospace Engineering, IISc, Bengaluru, on "Kalman Filters". Out of the 118 papers received, 45 papers were selected for presentation after going through the specified review procedure.

The ICPSPCT 2018 witnessed a presentation of 33 papers by the authors. When the nature of presented papers is viewed with the perspective of a more specific topic, 3 presented papers were under the purview of MIMO covering MIMO-OFDM, IDMA-MIMO-OFDM and antenna design for MIMO. The conference had 5 papers aligned with the broad field of Biomedical Applications and Devices comprising the specific topics of Hand Held Device for Early Detection of Oral Cancer, Bite force Measurement, Time Series Analysis based Body Monitoring and Reporting System and Assessment of re-mineralization potential of Cranberry extract and novel varnish through Optical methods and Laser Fluorescence. Photonics and Optics attracted 7 papers with special emphasis to Photon Counter for Silicon Carbide Ultraviolet Photometer, Detection of CO_2 through Optical Micro-Ring Resonator, Optical Orbital Angular Momentum sorter, P-cycle Based Survivable Multicast RSA in Elastic Optical Networks, Protective Shield in Phototherapy through Photonic based crystal and Refractive Index of Deposited Sebum by using Total Internal Reflection. There was a paper on metamaterial for high performance of microstrip antenna. The broad domain of VLSI attracted 4 papers dealing with 32 nm CMOS SRAM cells, An approach for 3-logical input optical look up table and optical memory, Model for Tunnel Field Effect Transistor involving two dimensional potential and Low Power Robust 9T Static RAM using FINFETs. Four papers under IoT and Network Security dealt with IoT based Walking Stick, IoT based Rodent Monitoring and Avoidance System in Large Scale Grain Storages, Security System and its interconnection with lighting and quality correlation approach for efficient Web Object Caching. Under the purview of the communication engineering, there were 6 papers with a focus on Neural Network for universal digital demodulator, Singer Identification using Time-series Auto-regressive Moving Average, Routing Protocol Performance for V2X Communication, Speech Corpus Development for Voice Controlled MAV, ZADOFF CHU Spreading Sequence for 5G Wireless Communications and Li-Fi Technology for Future of Smart Vehicle Communication. The paper on Half tone

Visual Cryptography for Color Images using Error Diffusion and Direct Binary Search constituted the lone paper under Digital Image Processing. Under Automotive Electronics, the two presented papers had their focus on Automotive Crash Detection using Multi Sensor Data Fusion and Monitoring system for Fuel Efficiency. The editors would like to thank everyone at Springer for their assistance in producing this volume.

Bengaluru, India   Govind R. Kadambi
Sacramento, USA   Preetham B. Kumar
Coventry, UK   Vasile Palade

Contents

About the Editors

Govind R. Kadambi is a Professor and Pro-Vice Chancellor in M.S. Ramaiah University of Applied Sciences. He has over 40 years of experience in both industry and academia, and specializes in numerical analysis and simulation, adaptive techniques in communication and signal processing, and antenna research, including analysis, measurement, design and applications. He has authored 1 book chapter and over 100 research papers, and holds 41 patents in various countries.

Preetham B. Kumar is a Professor in the Department of Electrical and Electronic Engineering, California State University, Sacramento (USA). His research focuses on antennas, RF testing, EMI study, hyperthermia treatment of cancer. He has authored 6 book chapters 14 technical reports and 59 peer-reviewed articles in reputed journals and conferences.

Vasile Palade is a Reader in Pervasive Computing in the Department of Computing, Faculty of Engineering and Computing, Coventry University, UK. His research interests include machine learning/computational intelligence, encompassing hybrid intelligent systems, neural networks, fuzzy and neuro-fuzzy systems, nature inspired algorithms (genetic algorithms, particle swarm optimization), ensembles of classifiers, class imbalance learning. He has authored 4 authored books, 3 edited books and 5 conference proceedings, 7 book chapters and 110+ papers in journals and conference proceedings.

Design and Development of a Bite Force Measuring Device

P. D. Seema, V. Suchitra, Shweta S. Hooli, H. K. Pavithra, Aditi S. Nagulpelli, Adel Khizar Hashmi, L. S. Praveen, and Preetham Shankapal

Abstract Oral condition is a general health concern that has an effect on the quality of life. The common dental issues are bruxism and misalignment of teeth among others. The use of faulty prosthesis and dental implants also creates a problem leading to discomfort and complications. In order to diagnose these, bite force measuring (BFM) device is used to measure the bite force exerted by the teeth/jaws. This information is considered to be a significant parameter as it helps comprehend biomechanics of the prosthetic devices and in classifying the severity of bruxism. But, the existing devices are expensive and not available easily. In order to overcome this, a cost-optimized BFM system has been designed and developed to measure as well as display the bite force measurements graphically and numerically. The BFM device is indigenously designed using sensors placed on an impression tray and is interfaced to the MyRIO microcontroller and programmed in LabVIEW. The graphical coding ensures data acquisition, voltage to force conversion and displays the force results in the front panel. In addition to the software display, the code also controls the ON–OFF of LEDs placed on an external denture model. The LEDs indicate the positions where high bite force is exerted. The limitation of this project is that the sensors yield force values from 0 to 10 N but human bite force is ~700 N. Hence, a sensing system could be designed in order to measure greater force. On the bright side, the fabricated BFM device is compact, economic and can assist dentists in understanding and diagnosing dental problems.

Keywords Bite force measuring device · LabVIEW · MyRIO · Flat force sensors

P. D. Seema (✉) · V. Suchitra · S. S. Hooli · H. K. Pavithra · A. S. Nagulpelli · A. K. Hashmi · L. S. Praveen · P. Shankapal
Faculty of Engineering, Department of Electronics and Communication, M S Ramaiah University of Applied Science, Bengaluru, India
e-mail: seema.biomedical@gmail.com

1 Introduction

Dental health in humans is linked to the quality of life which in turn impacts the day-to-day activities and overall contentment in life. Dental issues often go unnoticed as they do not report the problem to the dentists and in most cases even if they do, poor diagnostic procedures are carried out. The most common dental complications include bruxism which is 8–31% prevalent in the general population [1], misalignment of teeth and inability to bite and move the masticatory muscles. The aforementioned dental problems are accompanied by severe headache and excruciating facial pain. The lack of usage of appropriate diagnostic tools and practices by the dentists for the said problems lead to wrong diagnosis eventually giving rise to furthermore complications. The prevalence of dental issues is significantly high and needs proper diagnosis and the right treatment.

One of the common parameters taken into consideration for the dental diagnostic purpose is the bite force measurements. Bite force is defined as the force exerted by the lower mandible against the upper mandible (or vice versa) during a voluntary dental occlusion in dentulous and edentulous people. The device used to measure this force is known as gnathodynamometer or occlusometer or simply bite force measuring (BFM) device [2]. The unit used for the bite force measurement is Newton (N). The device particularly works well in computing the bite force exerted by the incisor and molar teeth since the maximum bite force is exerted by them. Knowing the magnitude of the bite force is beneficial in comprehending the functional state of the dental system, in diagnosing the problematic tooth/teeth and classifying the stages of bruxism.

The fact that the existing BFM devices are not easily available and are super expensive along with other shortcomings mentioned further has been a motivating factor in order to design and develop a cost-optimized BFM device. One of the BFM devices that are currently being used is the TekScan which costs a whopping amount of 10–15 lakhs INR for the device alone and an additional cost for the tactile sensors which costs roughly around 700–1000 INR while the other BFM devices also cost around the same range [3]. The expenditure incurred in buying such BFM devices is huge; thereby the demand for the same is less. Moreover, the tactile sensors used in this device do not work standalone, they work only when fitted in that particular device. These BFM devices are not readily available in countries like India but are extensively used in foreign countries like USA, UK and so on. Another BFM device—the miniature silicon bite force recorder employs a single sensor intended to record the bite force of a single tooth at a time [4]. This process seems to be very cumbersome and time-consuming and the material of the sensor is damage-prone. Also, in order to counter the problem of faulty diagnosis, there is a need for a better diagnosing tool. The BFM device that is designed and developed serves the right purpose to counter the aforementioned problems.

The developed project of BFM device aids in diagnosing various orofacial and dental issues. It also helps in comprehending the biomechanics of the masticatory muscles involved in dental occlusion. The device is useful in measuring the bite

force of edentulous patients before and after having a denture set and also for estimating post-surgical evolution. The information on bite force measurements aid in understanding the characteristics of occlusal pathologies such as bruxism. Since the device is cost-optimized, there will be no mammoth expenses in buying the same and thereby used by many dentists to diagnose the patients accurately. To top it all off, proper diagnosis of dental problems will be done and also helps in the comparison of alternative treatments to be given, thereby significantly improving the overall oral health of the population.

2 Methodology

In order to design the BFM device, the FSR 400 series flat force sensors are mounted on plastic full arch dental impression tray and neatly soldered, which is connected to the potential divider circuit on PCB board. The sensors are compact in size and the sensing region is around 7.62 mm in diameter. It is therefore apt and viable for usage in the dental application for bite force measurement and 10 units of FSR 400 series flat force sensors were positioned on the tray juxtaposing the teeth positions from the impression taken using dough shown in Fig. 1b and a, respectively. These sensors can measure force range of 0–10 N. Ten units of sensors are incorporated since the MyRIO controller can accommodate only 10 analog I/O channels.

The connections from the PCB board are given to the MyRIO microcontroller interfaced with LabVIEW software. The output is processed and captured in the same. The LabVIEW program receives the data from the MyRIO microcontroller and processes it to project the force values on the user display. The other display is the LED-affixed denture model, which indicates by the glow of LED if the force value is exceeding the given threshold. The other part of the program verifies each sensors value and compares it to the set maximum safe value. The sensors are virtually (in program) given to the digital pins, acting as output from the MyRIO. The digital
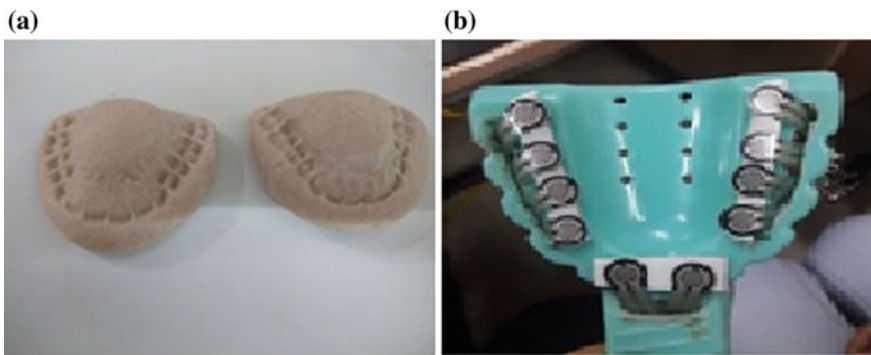
Fig. 1 **a** Teeth impressions. **b** Sensors positioned accordingly
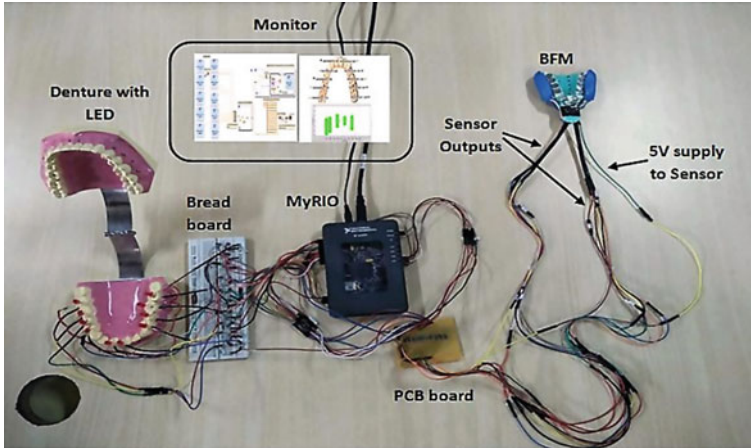
Fig. 2 Hardware system interfacing

pins of MyRIO are connected to the LEDs through resistors. The digital pins of the corresponding sensors go high which is measuring the force above the set value. Fig. 2 shows the complete hardware system interfacing.

The software performs four important functionalities, namely, data acquisition, processing, control and display. The step-by-step algorithm is elucidated as follows:

Step 1: The sensors are connected to the MyRIO microcontroller and interfaced with LabVIEW. Through block diagram coding, these signals are received as analog inputs. These are stored in the form of an array.

Step 2: The analog voltage values stored in the array are retrieved using a loop and converted to the corresponding force value in Newton.

Step 3: Control action is performed by monitoring each of the acquired force values. The array containing force values is accessed one-by-one in a For-loop. Each element is compared with the assumed threshold value of 7 N. If the force sensed by the sensor is greater than 7 N, then the digital output pin to which the LED is connected is made high. If the value is less than 7 N, then digital output remains low. Simultaneously, a software LED indicator is also used to show high and low values.

Step 4: The converted force values can now be displaced as a bar graph. Also, these force values are numerically displayed along with the teeth positions.

3   Results and Discussion

The BFM was tested by housing it in a zip lock pouch and inserting it in the mouth to be bitten. The sensors placed on top of the tray will come in contact with the teeth and measure the force exerted when it is voluntarily bit. The testing of the device was done by connecting it to the MyRIO microcontroller and LabVIEW as elucidated in

Fig. 3 Front panel display of LabVIEW

Sect. 2. As the device is bit, the resistance of the sensors will change. The change in resistance is obtained as a corresponding voltage by using the potential divider circuit. The varying voltage signal is acquired by the MyRIO which acts as the data acquisition unit. The LabVIEW code is executed and the front panel or the control panel begins to display the force exerted at various teeth locations. This is seen as green-colored bar graphs on the panel. The accurate force values are also displayed on the super-imposed teeth image just above the graph, both shown in Fig. 3. The force values are compared to the threshold and if exceeded, the green led indicator turns ON and the LED drilled to the denture set will also turn ON.

It can be seen that the force exerted by the teeth is visualized in the bar graph. This enables the dentists to better correlate the force value with the tooth position. The nomenclature of the tooth position is according to the dental standards and sensor placement and is already discussed in the earlier sections. Thus the tailored display is intended to facilitate quicker diagnosis and comprehension.

In addition, the numeric value of force is also displayed above the graph. The value, in Newton, will vary between 0 and 10 and displayed as numeric displays. Since the bar graph does not give the exact value, the numeric displays are used. It gives a more precise value of the exerted force as a floating point numeric. Wherever the force is greater than 7 N, the LED indicator is turned on. Similarly, the LEDs connected to the denture set will also glow.

By looking at the glowing LEDs and the force values on the display panel, the dentists will be able to understand the jaw activities and the associated occlusal mechanics. Also, the oral camera can be used to monitor the faulty tooth. It provides a vivid picture of the tooth in real time. This analysis and force measurement can be done simultaneously for accurate diagnosis.

Depending on the force of the voluntary human bite, the magnitude and position of the force sensed by the force sensors will vary. This is carefully acquired, processed

and captured in LabVIEW. An additional denture set model with LEDs drilled at the tooth positions will also indicate the spots of high and dangerous force values.

Thus a cost-effective bite force measurement device is designed, fabricated and interfaced with the microcontroller. It is then tested by actually placing it in the mouth and visualizing the obtained force values, using graphical and using numeric displays as well as a denture model with LEDs.

4   Conclusion

The developed BFM device is an effective cost-optimized tool to measure human bite force. However, with a few further improvisations, the device can produce more accurate results. This prototype incorporated only 10 force sensors owing to the availability of analog I/O channels. Although they are strategically placed to measure the major pressure teeth, however by placing more sensors, the force value at every tooth location can be measured. By using more closely packed sensors, the BFM device can be used on all patients with varying teeth alignment and jaw structure. More the number of sensors, greater the number of force values acquired. Currently, 10 force values are seen, but on using more sensors, the force at other teeth like wisdom teeth, incisors and so on can also be determined.

Since this is a prototype, signals were individually communicated using wires. However, in real time, signals can either be transmitted using a single twisted pair cable with appropriate protocols, or they can be transmitted wirelessly using Bluetooth or over Wi-Fi. These methods will still ensure cost optimization but with superior device handling comfort and portability. The limitation of the designed and developed BFM is that the output range varies only from 0 to 10 N. A better sensing method can be developed in order to withstand greater force, and sensors that give output in the range of ~700 N, which is the generic range of human biting force, can be employed.

With the above improvisations, the BFM device can provide ultimate force measurement in a patient-friendly manner. The device can become more accurate and portable and measurements may be taken more comfortably. Thus, this device can certainly aid dentists to reduce the instance of various dental and implant failures. This results in healthier and happier oral conditions across masses.

References

1. Manfredini D, Winocur E, Guarda Nardini L, Paesani D, Lobbezoo F (2013) Epidemiology of bruxism in adults: a systematic review of the literature. J Orofac Pain 27(2):99–110
2. Koc D, Dogan A, Bek B (2010) Bite force and influential factors on bite force measurements: a literature review. Eur J Dent 4(2):223–232
3. Tekscan (n.d) Pressure mapping, Force measurement and tactile sensors. https://www.tekscan.com/
4. Singh S, Utreja AK, Sandhu N, Dhaliwal YS (2011) An Innovative miniature bite force recorder. Int J Clin Pediatr Dent 4(2):113–118. https://doi.org/10.5005/jp-journals-10005-1093

Future of Smart Vehicle Communication by Using Li-Fi Technology

Raunak Agrawal⬤ **and N. Thangadurai**⬤

Abstract Light-emitting diodes (LEDs) can be used much more than lighting. Studies show that LEDs, which have been used just for machine-to-human interface, that is, either showing status of LED in printed circuit boards (PCBs) or illumination purposes, can also be used for communication between one hop and another at significantly low cost. LED has become a familiar technology for a variety of lighting applications, such as automotive, because of their superior efficiency and quality than halogen lamps. The process of transmission of data through light is termed as light fidelity (Li-Fi). Unlike wireless fidelity (Wi-Fi), which uses radio frequency, Li-Fi is a fifth-generation (5G) visible light communication (VLC) system which provides better capacity, efficiency, availability and security than Wi-Fi. By sending the data through light spectrum which comprises arrays of LED as an optical wireless medium act as signal propagation. In fact, the usage of LED eliminates the need of complex wireless networks and protocols. Exploiting minimal effort of lightning components and LEDs, there are a few windows of chances to utilize this medium, from open web source to get access, vehicle correspondence through road lights, which goes about as a free access point to self-sufficient cars that can impart through their headlights. This paper proposes the idea for vehicle-to-vehicle communication using light, which stimulates the way to pass data about driving conditions and driver behavior between automobiles. This enhances safe driving and makes road use more efficient.

Keywords Visible light communication · Light-emitting diodes · Sensors · Vehicle-to-vehicle communication

R. Agrawal · N. Thangadurai (✉)
Department of Electronics and Communication Engineering, School of Engineering and Technology, JAIN (Deemed-to-be University), Bangalore 562112, Karnataka, India
e-mail: mrgoldjain2015@gmail.com

1 Introduction

Wi-Fi is not used in aircrafts, healthcare, and underwater communications due to electromagnetic waves that cause interference between the devices operating at same frequency and disrupt the communication between radio stations. Inter-vehicle communication is used to communicate between two vehicles and to analyze the pattern of signals so that smart and secure transportation system is achieved. The vehicles could form a mobile ad hoc network among several vehicles that have communication devices [1]. Each vehicle is equipped with a communication device within a decentralized network and can act not only as a communication node but also as a wireless router. The ad hoc network is a temporary network that is created by the absence of any centralized or pre-established infrastructure. This transforms each taking an interest vehicle into a remote wireless switch or hub, permitting vehicle, around 100–300 m of each other to associate and, thus, make a bunch of network system with a scenic. When the signals range is far from the network range then current vehicle drops out of the flag range and different vehicles can participate, interfacing vehicles to each other with the goal that a versatile web connection is made. The advantages of using light signals over other approaches are that they don't need the complex management and processing of signals from hundreds or thousands of cars in the area, rather in the vicinity of the front and rear vehicle. This makes the communication suitable for real-time control function of vehicle [2]. This innovation attempts to create electronic security advancements, for example, vehicle-to-vehicle separate control, helped stopping, path changing, side and back cautions, and comfort advances, for example, all-around-perception, head-up show, and driver state checking to maintain a strategic distance from impacts. Photovoltaic cells be a replacement for windows of the cars, the system can be made to run independent with the power being supplied with the available solar energy. Based on the LEDs ON and OFF be responsible for the distinctive series of 0s and it is conceivable to encode information in the light by changing the rate at which the LEDs glimmer. At the point when LED is on, it transmits 1s and generally 0s. The LED power is regulated so quickly that human eyes can't see, so the yield seems steady and subsequently offering lasting network. These quick exchanging can be accomplished by PWM method to transmit computerized information stream containing strings. To get this, we are customizing the microcontroller to shift the obligation cycle of the pulse width modulation (PWM) technique which has the assignment of directing the current in the LED. The one-sided ebb and flow is nourished to LED driver unit. The energy of LED is changed by the waveform of information flag. At the collector side photodiode sensor creates a present relative to the momentary power already obtained. From this, data can be filtered that can be used to control application systems like motor, lamp and relay, provide internet connectivity and so on [3]. The system can be employed using existing vehicle electronic device management such as controller area network (CAN) bus control signals because of phase-shifting nature of LED. It is important to manufacture the LED with proper analysis of power, control, data transmission and detection signals for efficient performance of devices. Coordinate observable

pathway is not essential for Li-Fi to transmit a flag signal, since light reflected off the dividers can likewise accomplish an estimated speed of 70 Mbps.

2 Literature Review

The term Li-Fi was coined by professor Dr. Harald Hass at TED global talk in 2011, where he surprised audience by streaming high-quality video from a standard LED lamp. His observation alluded to this light signal as D-light that can be utilized to create information on data rates higher than 10 Mbps, which is significantly faster than our normal averaged broadband connections. Muntazir Mohd Tali et al. in their paper elaborate about the light communication, image processing, symbol recognition and wireless communication using Zigbee [4]. Saito et al. describe the road-to-vehicle communication and implemented using LED transmitter and camera receiver, which employs a special complementary metal-oxide semiconductor (CMOS) image sensor [5]. Vaishali et al. propose to use space–time division multiple access (STDMA) for real-time data traffic between vehicles, which was investigated using highway road simulation scenario with promising results [6]. Thangadurai et al. discuss about the general working and construction of Li-Fi along with the comparisons of Wi-Fi and Li-Fi and applications of Li-Fi [7, 8]. Jia-yuan et al. in their paper make use of certain algorithm and show two scenarios using NPN switching circuit and ASCII conversion [9, 10]. Several research works have been carried out on working mechanism of Li-Fi on how it provides better bandwidth, efficiency and better availability and security and on how it has immense possibilities comparing with other wireless communication mediums; but only a few researches have been carried out on practical implementation of Li-Fi. Research has been done on how Li-Fi can be used in illumination and data transmission between devices and also for transportation. The reviewed papers depict about the existing trends and how light fidelity can significantly make a global impact toward better innovation. There are many existing applications where it can be used, such as home internet, aviation, underwater communication, medical centers, but the research is still going on about the technology. Similarly, some papers highlight the use of LED in traffic lights. The fundamental idea about Li-Fi comprises an overhead light fitted with an LED and flag handling innovation which streams information implanted in its beam at very high to the photograph indicator. A collector dongle at that point changes over from amplitude to electrical signals with little changes, which is then changed over once more into an information stream and transmitted to a PC or a cell phone.

3 Working Principle

An LED light fitted with signal processing technology is used to stream data at ultra-high speeds to the photo detector. In every vehicle the LED lights act as transmitter and beneficiary in both rear and front sides of the vehicle. The LEDs are situated in

Following vehicle with camera (reciever)   Vehicle with LED rear lights (sender)

Front camera field of view   PWM-modulated data signal
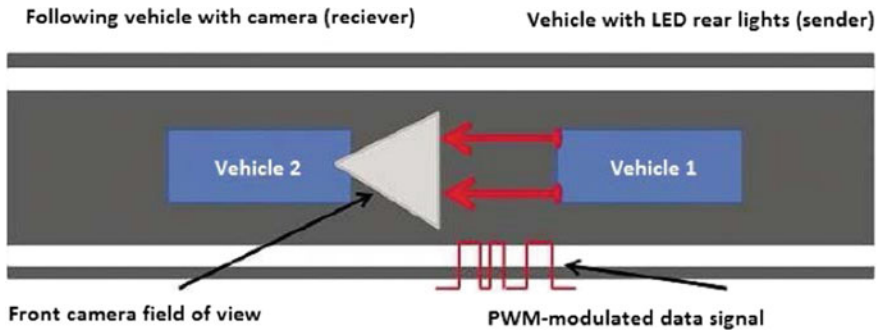
Fig. 1 General working principle

both the side front and back-lights of the car which also contain the photo detector to locate and get the light signal.

The transmitter and receiver, as shown in Fig. 1, are the two major parts in the Li-Fi system. By using the LED array signals output in the form of 0 and 1s, when the bulb flashes the transmitter part modulates the input signal with the required time period. The output will be presented when the beneficiary part finds these flashes using a photodiode and increases the flag. Consequently, all that required is a few LEDs and a controller that is used to code information into those LEDs. Each of the one needs to do is to fluctuate the defer rate at which the LEDs glimmer contingent on the information need to encode. Assist improvements can be made in this technique for parallel information transmission, or using blends of red, green and blue LEDs to modify the light's recurrence with every recurrence encoding an alternate information channel.

4 Proposed System

The existing system makes use of light detection and ranging (Lidar) and computer vision technique to detect the information about millions of small points surrounding the vehicle every second. Li-Fi is used because it is a fast and secured version of Wi-Fi and it is more cost-effective and sustains life-term goal. It uses VLC channel that has spectrum 10,000 times the entire RF spectrum. The major advantages of Li-Fi over the existing system are better bandwidth, working in areas that are susceptible to electromagnetic interference and offering higher transmission speeds. The vehicles used are self-driven and the headlights which already exist can be modified a little and can be used for communication. These schemes use less power and operate in low cost. The system implementation consists of two vehicles in line of sight. The implementation, as shown in Figs. 2 and 3, provides a scenario where car1 is functioned as transmitter and car2 as receiver.
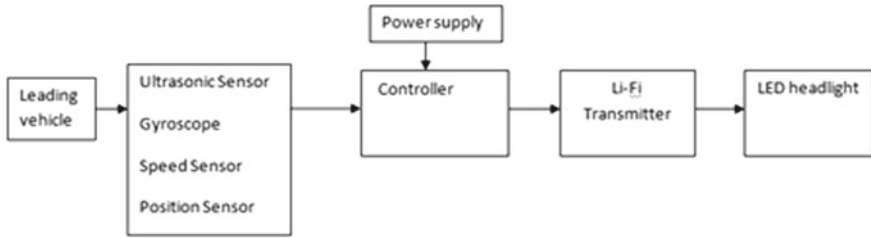
Fig. 2 Transmitting circuit in vehicle
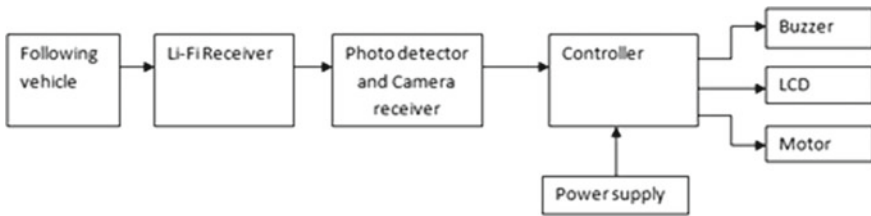
Fig. 3 Receiving unit in vehicle

The speed sensor senses the data to the controller, which will compare between current and previous speed of transmitting car and if it is decreased, it has a keen senses that when brake applied in car the data will be transmitted to LED driver, which also produces constant current to protect LED. The data along with unique vehicle id will be transmitted wirelessly to photodiode through light in the form of current so that another vehicle can identify the source. From another vehicle, the speed information can be received by photodiode to perform necessary action accordingly, like decrease its speed to avoid collision. So also, trigger circuit will detect the adjustment in path of vehicle and illuminate the transmitting circuit, regardless of whether the car is turning left or right. The distance between two vehicles can be calculated from ultrasonic sensor, which is used to sense the time interval to send the signal and receive the echo for the signal. The distance between the vehicles can be apparently calculated as:

Distance = Speed of sound × time taken/2; Speed of sound in air is 344 m/s.

The modulation technique used is on–off keying (OOK). The voltage is varying from 0 to 5 V which represents the information from the data source. Other sensors like infrared (IR), pressure, temperature, gyroscope, altimeter can also be integrated accordingly. A camera can also be integrated in front vehicle as shown in Fig. 4, which can capture traffic signals and symbols so that the required information can be transferred to other following vehicles using Li-Fi. Autonomous vehicles can also make use of GPS, radar and sensors to accurately measure vehicle's orientation and rotation of its wheels to recognize the exact location.

Because of line of sight (LOS) feature of Li-Fi, transmission of data from one vehicle to another takes place easily. A huge communication network has been formed
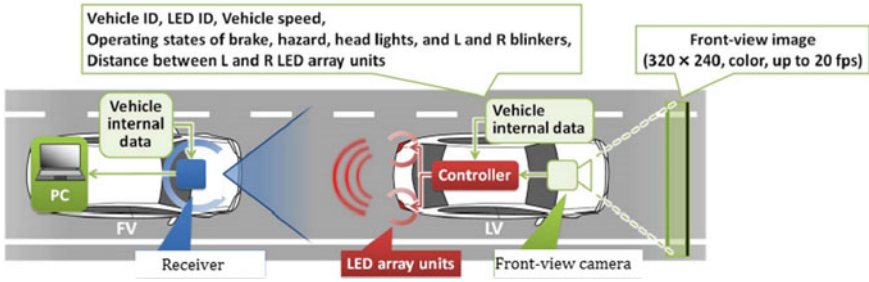
Fig. 4 Real-time scenario of Li-Fi between two vehicles

when each and every single vehicle will transmit information from one to another through LOS. When former vehicle wants to make a turn, it will glow its indicator and the car behind it will capture image with camera using image processing techniques. When any symbol is recognized, the vehicle doing so will send the message to the other vehicles alerting them. This will assure help in maintaining road ethics and will provide safety of the drivers giving warning to them. Similarly, other sensors such as alcohol, eye-blink sensors can be added for piloted vehicles to sense the particular entity and take suitable action. At the same time, if accident happens, relay is turned off, so that ignition of the vehicle is deactivated.

Transmitter:

$$X(t) = P_t\{1 + m_0 d(t)\} \tag{1}$$

$$X(t) = P_t\{1 + m_0 \Sigma[a_k p(t - kT)]\} \tag{2}$$

where LED power transmitted averages is represented as Pt, m_0 = optical modulation index (OMI) of LED, X(t) = OOK signal.

Receiver:

Background noise is one of the major noise which is received along with the signal that affects it in the channel. Received light signal is given as:

$$P_r(t) = hX(t) + n(t) \tag{3}$$

where OOK signal = X(t); DC gain of channel is represented by h; and additive white Gaussian noise (AWGN) = n(t).

The converted electrical form signal from optical signal is

$$I(t) = R\{hX(t) + n(t)\} \tag{4}$$

The ratio of the desired output signal power to the supplied input noise power is known as signal-to-noise ratio (SNR) and is represented as

$$SNR = S \div N \tag{5}$$

where desired signal power $= S$; total AWGN $= N$.

$$S = R^2 P_r^2 \tag{6}$$

where light signal received power is Pr and photo detector responsively is R

Equation (7) gives the calculated total noise as

$$\sigma_{total}^2 = \sigma_{shot}^2 + \sigma_{thermal}^2 \tag{7}$$

$$\sigma_{shot}^2 = 2q\gamma\,P_r B + 2q\,I_{bg} I_2 B \tag{8}$$

$$\sigma_{thermal}^2 = (8\pi kT_k \div G)\,\eta A_r I_2 B^2 + \left(16\pi^2 kT_k \Gamma \div g_m\right)\eta^2 A_r^2 l_3 B_3 \tag{9}$$

where 1.602×10^{-19} C is constant electronics charge q; bandwidth of the system B, Boltzmann's constant k, absolute temperature T_k, voltage gain G, $\eta =$ fixed capacitance of PD per unit area, $\Gamma =$ field effect transistor (FET) channel noise factor, $g_m =$ FET trans-conductance, area of the PD is A_r, noise bandwidth factor I_2 for background noise and $I_3 = 0.0868$.

5 Limitation and Future Scope

The signal can be blocked because of fog or there may be too much light 'noise' in summer, making camera difficult to pick up the signals. One of the issues the researchers are facing is to make system perform effectively in all lighting and weather conditions. As the LED is an opto-electronic device, other instruments also need to be deployed to measure and manage these effects. Some exceptions could be managed in software used for the control functions being fed by the signals. The system could be further enhanced for autonomous vehicles. VLC seems like a pragmatic and relatively straightforward technology to adopt across the automotive market, allowing some of the benefits to be introduced at an early stage as it is in fact complimentary to these approaches. It seems there is a great opportunity to improve road safety, vehicle efficiency and traffic management by simply extending the capabilities and features that already exist on many current vehicle designs, while other vehicle-to-vehicle (V2V)-enabled driver aids will come later as more complicated systems are developed. More refined procedures could significantly build VLC information rates. Concentrating on parallel information transmission utilizing varieties of LEDs like arrays or blend of LEDs to change light's frequency, Li-Fi will make our lives innovative urge in the near future. Li-Fi technology is more costly at initial stages that can be minimized to some extent, and then this concept can be widely used for auto-piloted vehicles.

6 Conclusion

We have presented characteristics and capacities of V2V applications which mainly focused on Li-Fi transmitter and recipient. In rush hour gridlock signals, Li-Fi can be utilized to communicate with the LED lights of the cars, and mischance accidents can be diminished. Li-Fi is perfect for high thickness scope in a restricted area. It is trusted that the innovation can yield a speed which exceeds 10 Gigabits for each second (Gbps). It is the quickest and least expensive remote correspondence which is reasonable for long separation correspondence. Li-Fi will make all lives more innovation-driven sooner rather than the later. Eco-friendly transmission is feasible through light fidelity.

References

1. Charahte DV, Wagh PR, Avhad PV, Mankar SV, Mankar NS (2016) Design of vehicle to vehicle data transmission application using Li-Fi technology. IOSR J Comput Eng 26–29
2. Mali SU, Shinde SS (2017) Vehicle to Vehicle Communication. Int J Sci Res 6(3)
3. Ng SC, Zhang W, Zhang Y, Yang Y (2011) Analysis of access and connectivity probablities in vehicular relay network. IEEE J Sel Areas Commun 29(3):140–150
4. Tali MM, Patil A, Chavan S, Jadhav S (2017) Inter-vehicle communication using Li-Fi technology. Int J Adv Res Comput Commun Eng 6(3)
5. Saito T, Haruyama S, Nakagawa M (2014) A new tracking method using image sensor and photo diode for visible light road-to-vehicle communication. In: Proceedings of the 10th international conference on advanced communication technology 1, pp 673–678
6. Khairnar VD, Kotecha K (2013) Performance of vehicle-to-vehicle communication using IEEE 802.11p in vehicular Ad-Hoc network environment. Int J Netw Secur Its Appl 5(2)
7. Sharma RR, Sanganal A (2014) LI-FI technology transmission of data through light. Int J Comput Technol Appl 5(1):150–154
8. Thangadurai N, Dhanasekaran R, Karthika RD (2013) Dynamic traffic energy efficient topology based routing protocol for wireless ad hoc sensor networks. Int Rev Comput Softw 8(5):1141–1148
9. Jia-yuan W, Nian-yu Z, Dong W, Kentaro I, Zensei I, Yoshinori N (2012) Experimental study on visible light communication based on led. J China Univ Posts Telecommun 19(2):197–200
10. Kumar N, Terra D, Lourenco N, Alves LN, Aguiar RL (2011) Visible light communication for intelligent transportation in road safety applications. In: Proceedings of the 7th international wireless communication mobile computing conference, pp 1513–1518

Detection of Fingerprint Pattern and Refractive Index of Deposited Sebum by Using Total Internal Reflection

Tania Das

Abstract The conventional and well-established technique of fingerprint recording is to record the intensity distribution of the fingerprint through total internal reflection (TIR). The present work proposes a polarization-based non-interferometric technique based on total internal reflection for a quantitative assessment of the refractive index of the sebum associated with the fingerprint as well as its unique pattern. Although the conventional technique of TIR is employed, two polarization-shifted intensity data frames are recorded and combined to arrive at the desired result. It is expected that this additional information may yield a new dimension to forensic science.

Keywords Total internal reflection · Phase difference · Fingerprint · Refractive index

1 Introduction

Analysis of fingerprints has been extensively used for the past few decades in different fields, especially in crime investigation. Fingerprints are also used in biometrics for identity verification [1, 2]. Although different types of patterns and ridges are seen on a fingerprint, it is the presence of minutiae, which are abrupt changes in the ridges that are vitally important to fingerprint detection [3, 4]. Minutiae detection is solely based on the quality of the fingerprint image [5]. Analysis of fingerprints is essentially a pattern recognition system based on acquiring data from an individual. A set of features are extracted from the acquired data [6, 7]. This paper proposes a simple polarization-based setup for high-resolution detection of not only the fingerprint patterns and its analysis but also a quantitative evaluation of the refractive index associated with the sebum, through a simple two-frame algorithm. The sebum that oozes out from the pores is a mixture of water, potassium, urea, lactate, amino acids and bicarbonate, and an over-abundance of one of these constituents is reflected in

T. Das (✉)

Department of Electronics and Communication Engineering, Heritage Institute of Technology, Chowbaga, Kolkata 700107, India

e-mail: taniadas.physics@gmail.com

the evaluated refractive index of the sebum islands, which in some cases may be indicative of the pathological condition of the individual as well. In this paper four different sets of fingerprint are taken from two different people and hence refractive index of sebum is evaluated. Accordingly, different sets of fingerprints are recoded, analyzed and reported in this work.

2 Theoretical Background

If a light beam is totally internally reflected at the interface of two different dielectric medium of refractive indices n_1 and n_2, $(n_1 > n_2)$, as shown in Fig. 1, then phase φ_s and φ_p for transverse electric (s-polarized) and transverse magnetic (p-polarized) polarized light can be expressed as [8]:

$$\phi_p = -2\tan^{-1}\frac{n_1\sqrt{n_1^2\sin^2\theta_1 - n_2^2}}{n_2^2\cos\theta_1}$$

$$\phi_s = -2\tan^{-1}\frac{\sqrt{n_1^2\sin^2\theta_1 - n_2^2}}{n_1\cos\theta_1} \tag{1}$$

The phase difference φ_{diff} between p and s components may be expressed as:

$$\varphi_{\text{diff}} = \varphi_p - \varphi_s = 2\tan^{-1}\left(-\frac{\cos\theta_1\sqrt{n_1^2\sin^2\theta_1 - n_2^2}}{n_1\sin^2\theta_1}\right) \tag{2}$$

The variation in this evaluated phase difference with refractive index n_2 is shown in Fig. 2. This serves as the calibration curve for evaluating n_2 from φ_{diff}.
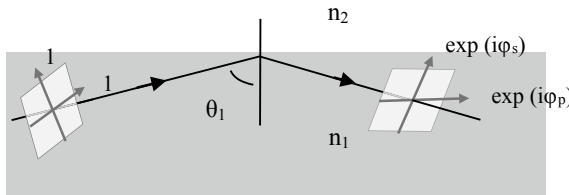
Fig. 1 For a ray of light with normalized s and p amplitude components incident on interface of denser and rarer medium at an angle θ_1 greater than the critical angle, the phases introduced in these components after total internal reflection ray are φ_s and φ_p, respectively

Fig. 2 Calibration curve:
Variation in phase difference
with respect to change of
refractive index of rarer
medium for $\theta_1 = 64.8°$ and
$n_1 = 1.518$
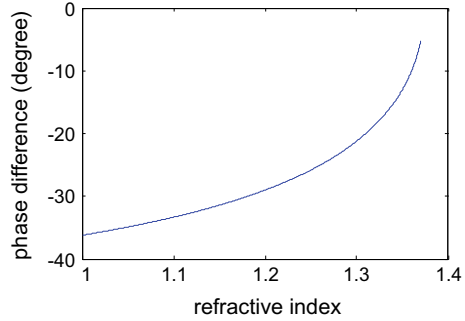
3 Experimental Setup

Figure 3 presents the proposed experimental setup. An isosceles prism with apex
angle 120° is chosen to ensure that light is total internally reflected from the detection
surface. The fingerprint is taken on the prism surface. Circular polarizer (CP) and
linear polarizer (LP1) combination is so oriented that the light from the LED source
(S) entering the prism is linearly polarized at 45°. This ensures that both the s and
p polarized states are present in equal magnitude in the input beam. Two intensity
data frames are recorded on a CCD with the transmission axis of the output polarizer
(LP2) oriented along 45° and 135° so that the s and the p components are added
in-phase and out-of-phase, respectively. The phase of the fingerprint may hence be
evaluated as [9]:

$$\phi_{\text{diff}} = \cos^{-1}\left(\frac{I_{45°} - I_{135°}}{I_{45°} + I_{135°}}\right) \qquad (3)$$

where

$$I_{45°} = 0.5r^2\left|e^{i\phi_s} + e^{i\phi_p}\right|^2 = r^2(1 + \cos\phi_{\text{diff}})$$
$$I_{135°} = 0.5r^2\left|e^{i\phi_s} - e^{i\phi_p}\right|^2 = r^2(1 - \cos\phi_{\text{diff}}) \qquad (4)$$
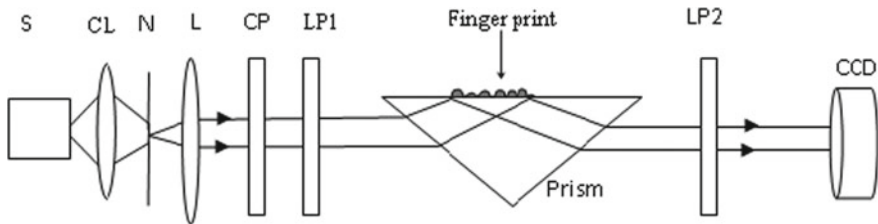
Fig. 3 Schematic diagram of the experimental in-line setup Source = LED, CL = Condenser lens,
N = pin hole, L = Lens, CP = Circular polarizer, LP1 = linear polarizer with 45° angle, LP2 =
Linear polarizer, CCD = Charge coupled device

4 Results and Discussion

Figure 4 shows the evaluated results of a sample fingerprint. The recorded frames I_{45} and I_{135} are shown in Fig. 4a and b, respectively. Figure 4c presents the 3D phase difference ϕ_{diff} profile, and Fig. 4(d) presents the variation in 2D phase difference along a particular cross-section. This is repeated for three more samples as shown in Figs. 5, 6 and 7. A summary of the fingerprint pattern in the different samples taken from two different persons, as well as the average refractive index of the sebum islands, is presented in Table 1.
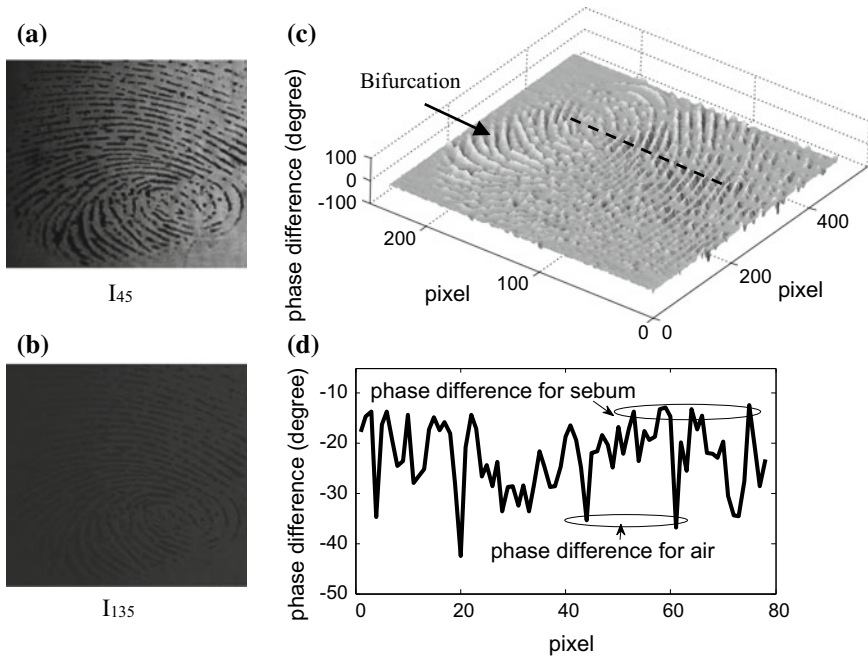
Fig. 4 **a** and **b** Represent intensity data frames for $I_{45}°$ and $I_{135}°$. **c** and **d** Represent 3D and 2D phase profile for fingerprint

(a)

(c)

(b)

(d)
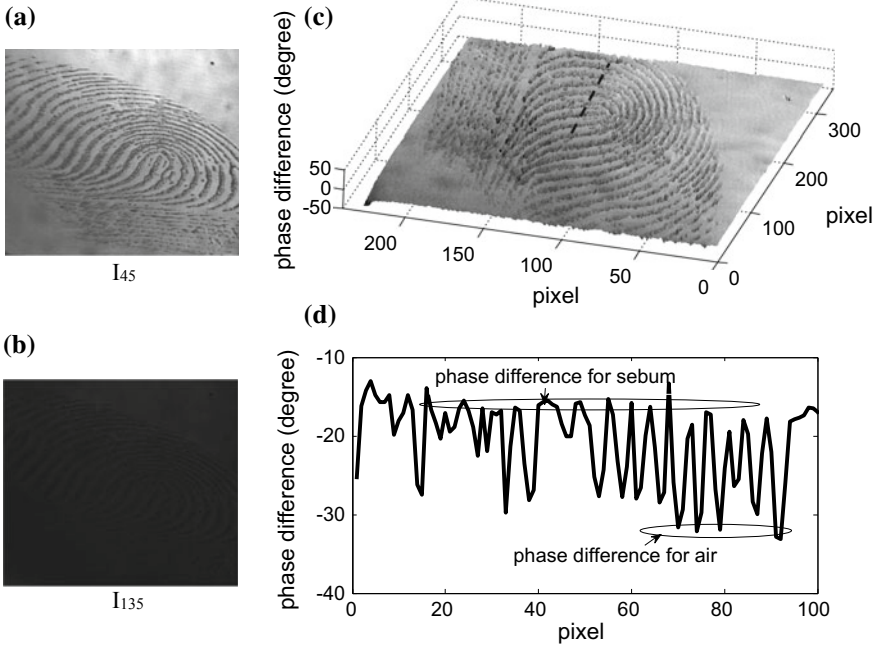
Fig. 5 **a** and **b** Represent intensity data frames for $I_{45}°$ and $I_{135}°$. **c** and **d** Represent 3D and 2D phase profile for fingerprint

5 Conclusion

It has been shown that from the optical phase of the sebum islands left by the fingerprint impression, the refractive index of the sebum can be evaluated. This is expected to add a new dimension to forensic science since the pathological condition of the person may as well have a bearing on the evaluated refractive index.

(a)

I_{45}

(b)

I_{135}

(c)

(d)
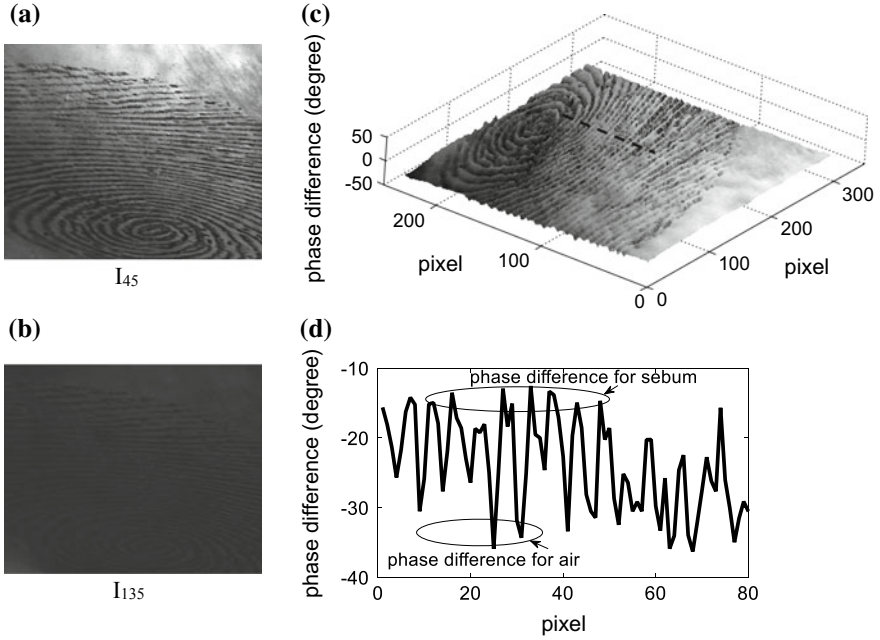
Fig. 6 **a** and **b** Represent intensity data frames for I_{45° and I_{135°. **c** and **d** Represent 3D and 2D phase profile for fingerprint

(a)

I_{45}

(b)

I_{135}

(c)

(d)
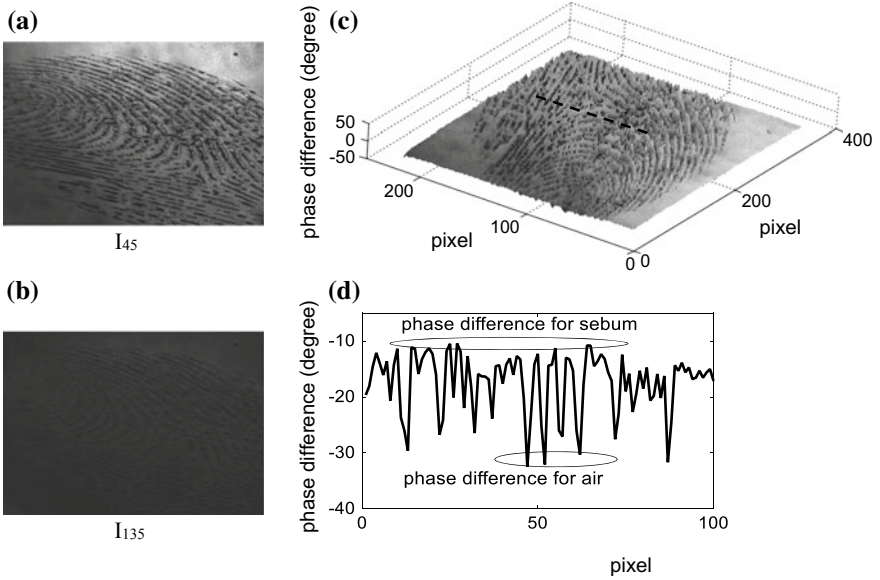
Fig. 7 **a** and **b** Represent intensity data frames for I_{45° and I_{135°. **c** and **d** Represent 3D and 2D phase profile for fingerprint

Table 1 Comparison of refractive indices of deposited sebum and fingerprint patterns between two different persons taking as a sample

	Set number	Fingerprint types	Phase associated with fingerprint (degree)	Refractive index
Person-1	Figure 4	Whorl pattern	−14.57°	1.344
	Figure 5	Loop pattern	−14.78°	1.342
Person-2	Figure 6	Whorl pattern	−12.86°	1.350
	Figure 7	Arch pattern	−12.36°	1.352

References

1. Kaushal N, Kaushal P (2011) Human Identification and fingerprints: a review. J Biom Biostat 2(4)
2. Bana S, Kaur D (2011) Fingerprint recognition using image segmentation. IJAEST 5(1)
3. Yi Y, Cao L, Guo W, Luo Y, Feng J, He Q, Jin G (2013) Optical fingerprint recognition based on local minutiae structure coding. Opt Express 21(14)
4. Jiang X, Yau WY, Ser W (2012) Fingerprint image processing for automatic verification. In: IEEE 2nd international conference on information, communication & signal processing
5. Pavithra MR, Muneeswaran MV (2016) An innovative detection system for fingerprint. IJCSMC 5(2)
6. Jain AK, Ross A, Prabhakar S (2004) An introduction to biometric recognition. IEEE Trans Circuits Syst Video Technol 14(1)
7. Dhanotia J, Prakash S, Bhatia V, Prakash S (2016) Fingerprint detection and mapping using a phase shifted coherent gradient sensing technique. Appl Opt 55(20)
8. Ash III WM, Kim MK (2008) Digital holography of total internal reflection. J Opt Express 16(13)
9. Das T, Bhattacharya K (2017) Refractive index profilometry using total internally reflected light field. J App Opt 56(33)

Zadoff Chu Spreading Sequence for 5G Wireless Communications

Vanita B. Kaba and Rajendra R. Patil

Abstract In recent years, fifth-generation (5G) is receiving attention in wide research and progress efforts from the wireless communication society. 5G provides a new frequency bands alongside amid the wider spectral bandwidth per frequency channel. To solve the new challenges in 5G, different kind of new modulation techniques and multiple access (MA) schemes have to be adopted. To increase spectral efficiency new techniques called orthogonal multiple access (OMA) and nonorthogonal multiple access (NOMA) techniques are used in 5G wireless system. Here, we propose a class of polyphase sequences called Zadoff Chu sequences which have uniform amplitude, and these sequences bear good correlation properties. Since these sequences are also identified as constant amplitude zero autocorrelation (CAZAC) sequences, Zadoff Chu sequences are used to spread data in OMA and NOMA schemes for 5G networks. The simulation result shows that Zadoff Chu sequence has good correlation properties, and ZCT precoded-based OFDM system is capable of reducing the PAPR significantly.

Keywords NOMA · OMA · Precoding · Zadoff Chu sequence · ZCT

1 Introduction

The demand for wireless communication is growing steadily in the last few years. The increased popularity and usage of wireless multimedia applications have led to the evolution of cellular systems, which include 1G, 2G, 3G, 4G and the next-generation 5G till date [1]. For a wireless communication scheme, a primary issue exists of how to provide user data demands for mobile communication by means of

V. B. Kaba (✉)
Department of Electronics and Communication, Godutai Engineering College for Women, Kalaburagi, India
e-mail: vbkaba@gmail.com

R. R. Patil
Department of Electronics and Communication Mysore, GSSS Institute of Engineering and Technology for Women, Mysore, India

limited network resources. These circumstances necessitate enormous connectivity amid high-scheme throughput and enhanced spectral effectiveness and oblige major challenges to the design of common 5G networks. A 4G system is predictable to offer a widespread and secure-based result to laptop and mobile devices [2]. The knowledge similar to orthogonal frequency division multiplexing (OFDM), multiple-input multiple-output (MIMO) and link adaptation are used in fourth-generation wireless scheme [3]. In order to bear superior throughput and massive heterogeneous connectivity for 5G networks, a novel modulation method with much lesser out-of-band (OOB) leakage is required. OFDM provides high spectral efficiency, small realization complexity, less weakness to echoes and nonlinear distortion. One of the most important disadvantages of OFDM is lofty out-of-band leakage (OOB) which increases the complexity and reduces the efficiency of OFDM system.

Initiating precoding to transmit data earlier than OFDM modulation is also a successful approach to diminish leakage. Precoding-based OOB leakage reduction technique is a simple linear technique. Precoding is applied to the OFDM transmitting symbols earlier than inverse fast Fourier transform (IFFT) process to improve the OOB leakage. Precoding is performed by applying Zadoff Chu matrix transformation (ZCT) to constellation symbols before IFFT. Zadoff Chu matrix transformation (ZCT) precoder matrix is formed by reshaping the Zadoff Chu sequence [7].

Nonorthogonal multiple access (NOMA) uses power and/or code fields in multiplexing to bear added users in the similar resource block [4] in order to support enormous connectivity for 5G networks NOMA schemes multiplexing in multiple domains, that is, spatial domain [6]. Zadoff Chu sequences are used to spread and generate code domain nonorthogonal multiple access for 5G networks [8]. The rest of the manuscript is prepared as follows: Sect. 2 anticipated model, Sect. 3 presents properties of Zadoff Chu series, Sect. 4 presents simulation outcome, and Sect. 5 conclusion.

2 Proposed Scheme

2.1 Zadoff Chu Sequence

Zadoff Chu sequences are a set of complex exponential polyphase progressions with stable amplitude. The autocorrelation of a major span Zadoff Chu series has a nil autocorrelation, that is, it is non-zero only at one instant corresponding toward the cyclic change. Therefore, this series is also known as zero autocorrelation series [8].

$$Z_r(n) = e^{-j\frac{2\pi}{N}*\frac{rn(n+2q)}{2}} \text{ for N even}$$
$$e^{-j*\frac{2\pi}{N}*\frac{rn(n+1+2q)}{2}} \text{ for N odd} \tag{1}$$

where $N =$ Length of sequence $r =$ root index of sequence relatively prime to N and $q =$ arbitrary integer, $n = 0, 1 \ldots N - 1, = \sqrt{-1}$. Zadoff Chu sequence has good periodic correlation properties. Zadoff Chu matrix transformation (ZCT) precoder is used to reduce OOB leakage of OFDM system. The precoding matrix Z of size N $\times$ N is applied to QAM constellation points of complex vector $X = [X_0, X_1, X_2 \ldots X_{N-1}]^T$, which transforms X into new vector $Y = ZX = [Y_0, Y_1, Y_2 \ldots Y_{N-1}]^T$ [1]. By reordering $n = mN + l$ matrix Z with row-wise reshaping is given by

$$Z = \begin{bmatrix} z_{00}z_{01} & \cdots & z_{0(N-1)} \\ z_{10}z_{11} & \cdots & z_{1(N-1)} \\ z_{(N-1)0} \; z_{(N-1)1} & \cdots & z_{(N-1)(N-1)} \end{bmatrix} \tag{2}$$

where $m = 0, 1, 2 \ldots N - 1$, $Z_{m,l}$ mean mth row lth column of precoder matrix y_m represents the ZCT precoded constellation symbols.

3   Properties of Zadoff Chu Sequence

3.1   Periodicity Property

They are periodic with period N, where N is the length of the sequence, r is the root index and n varies from 0 to N–1

$$Z_r (n + N) = Z(n) \tag{3}$$

3.2   Correlation Property

The autocorrelation of a prime length Zadoff Chu series with a periodically shifted form of its own has zero autocorrelation, meaning that it is nonzero only at one moment which corresponds to the cyclic shift [9]. Here autocorrelation is defined as

$$R_{x,x}[n] = \sum_{k=-\infty}^{\infty} x[k]x[n - k] \tag{4}$$

Cross-correlation describes the relationship between two sequences. The cross-correlation stuck amid two prime lengths Zadoff Chu series is a correlation between sequences of same length but with different root value r. The cross-correlation function of any two sequences is given by

$$R_{x,y}[n] = \sum_{k=-\infty}^{\infty} x[k]y[n-k] \qquad (5)$$

3.3 Fourier Duality Property

Zadoff Chu sequences can be generated directly in frequency domain exclusive of any DFT operation. Here $Z_r[n]$ represents N-point DFT of a time-domain Zadoff Chu series $z_r[n]$

$$Z_r[n] = Z_0 \times z_r^*[r'n] \text{ where } n = 0, 1 \ldots N-1 \qquad (6)$$

For odd length sequence expression for Zadoff Chu using Eq. (1), specifying $q = 0$ is given by

$$Z_r(n) = e^{-j\frac{2\pi}{N}*\frac{rn(n+1)}{2}} \qquad (7)$$

For $Z_r(n)$ in time-domain representation, the case is $\theta n = 2\pi N*rn(n+1)/2$ and for $z_r^*[r'n]$ in frequency-domain representation, the case is represented as $\theta[n] = \frac{2\pi}{N} * \frac{r'n(r'n+1)}{2}$

4 Simulation Results

4.1 Zadoff Chu Sequence Generation

Figure 1 shows the MATLAB simulation for Zadoff Chu sequence that is generated with length $N = 257$ and root index $r = 1$

Autocorrelation property

Figure 2 shows autocorrelation of Zadoff Chu sequence, Gold sequence and M length sequence of length $N = 256$ and root index $r = 1$. We can see that for Zadoff Chu sequence there is maximum peak value that occurs at zero and all other samples are zero values.

4.2 Cross-correlation

Figure 3 shows the MATLAB simulation for cross-correlation of two Zadoff Chu
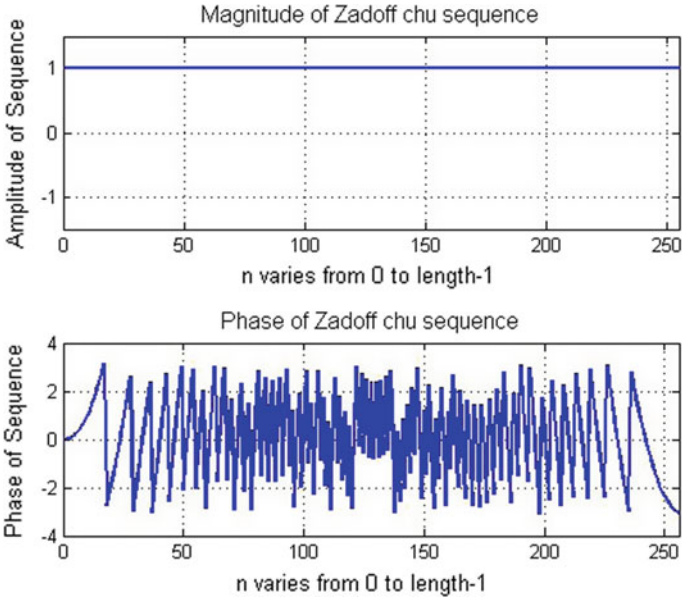
Fig. 1 Zadoff Chu sequence

Fig. 2 Autocorrelation property
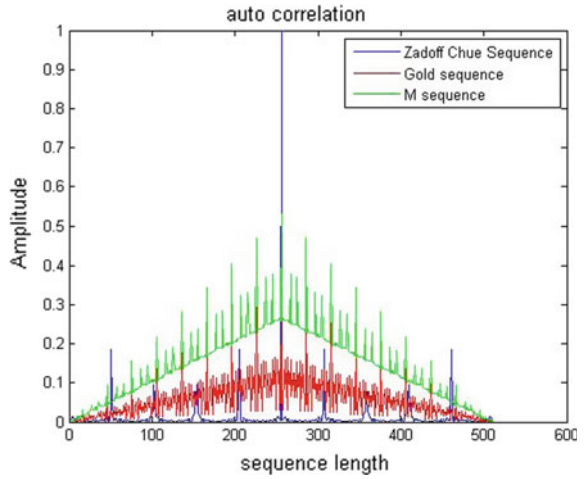
Gold sequence and M length sequence of length $N = 256$. As cross-correlation value is less, there is more similarity between the sequences.
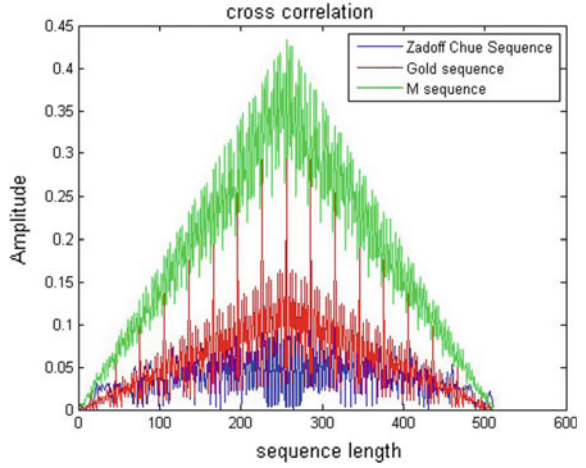
4.3   ZCT Precoded-Based OFDM

Figure 4 shows CCDF comparison of PAPR of higher transmitting bits of OFDM
system and Zadoff Chu matrix transformation precoding-based OFDM. The PAPR
of OFDM system is high compared to precoded OFDM system.

Fig. 4 ZCT precoded-based
OFDM system
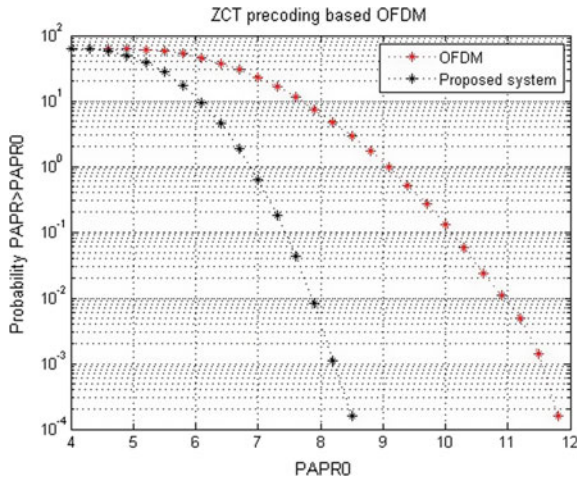
5   Conclusion

In this paper a spreading sequence for OMA and NOMA for 5G wireless scheme is projected. Zadoff Chu series is the subcategory of polyphase series. Zadoff Chu sequences are complex-valued sequences which have constant amplitude and zero autocorrelation; that is maximum peak value occurs at zero time lag. Using ideal autocorrelation properties, reshaping of the Zadoff Chu matrix transform is carried out for precoding. Hence by observing Matlab simulation results, we can conclude that PAPR of conventional OFDM is high compared to ZCT precoding-based OFDM system. OFDM systems with 16-QAM modulation have clip rate of 10^{-2}, the PAPR is 11.0 dB and ZCT precoding-based OFDM system is 8.9 dB.

References

1. Wei L, Hu RQ, Qian Y, Wu G (2014) Key elements to enable millimeter wave communications for 5G wireless systems. IEEE Wirel Commun
2. Zappone A, Sanguinetti L, Bacci G, Jorswieck E (2014) Energy-efficient power control: a look at 5G wireless technologies. In: IEEE international conference on communications (ICC15). London, UK
3. Akbil B, Aboutajdine D (2015) Improved IDMA for multiple access of 5G. Int J Commun Netw Inf Secur (IJCNIS) 7(3)
4. Timotheou S, Krikidis I (2015) IEEE: fairness for non-orthogonal multiple access in 5G systems. IEEE
5. Ding Z, Liu Y, Choi J, Sun Q, Elkashlan M, Chih-Lin I, Poor HV (2015) Application of non-orthogonal multiple access in LTE and 5G networks. IEEE Commun Mag
6. Bana SV, Varaiya P (2003) Space division multiple access (SDMA) for robust ad hoc vehicle communication networks. In: The IEEE fourth international conference on intelligent transportation systems
7. Zhao Z, Miao D (2016) Uplink contention based transmission with non-orthogonal spreading. IEEE
8. Baig I, Varun (2010) Electronic engineering department, Universiti teknology Malaysia: A new ZCT precoded OFDM system with improved PAPR. In: Asia Pacific conference on circuits and system
9. Chu DC (1972) Polyphase codes with good periodic correlation properties. IEEE Trans Inf Theory IT-18, 531–532
10. Budisin S (2010) Decimation generator of zadoff CHU sequences. In: Sequences and their application–SETA
11. Baig I, Varun (2010) Electronic engineering department, Universiti teknology Malaysia: PAPR reduction in OFDM systems: Zadoff Chu matrix transform based pre/post-coding techniques. In: Second international conference on computational intelligence, communication systems and networks
12. Mohammad M (2009) Mansour: optimized architecture for computing Zadoff Chu sequences with application to LTE. Department of Electrical and Computer Engineering, American University of Beirut Beirut, Lebanon

An MIMO–OFDM System Implementation Using Visible Light Communication

R. Sindhuja, Arathi R. Shankar, and Subhashini Gopinath

Abstract In recent years, the demand for data has exponentially increased by a considerable rate which increases the dependency of bandwidth in the RF spectrum. So there is a need to look for an alternate spectrum which can serve the purpose and facilitate the customer with better quality of service. In order to achieve this performance, visible light spectrum is considered for communication purposes. An attempt has been made by the authors to simulate visible light communication based on MIMO–OFDM system. OFDM provides better spectral efficiency as compared to any other single-carrier modulation techniques.

Keywords Multiple input multiple output (MIMO) · Orthogonal frequency division multiplexing (OFDM) · Visible light communication (VLC)

1 Introduction

The motivation for usage of VLC was provided by the evolution in the solid-state lighting. This leads to the replacement of florescent lamps by LEDs. It is challenging to achieve high data rate transmission, though the visible light spectrum has a wide range of frequency of about THz due to the limited bandwidth of the off-the-shelf LED [1]. To overcome this drawback in a single room multiple LEDs are installed. Therefore to boost the data rate the MIMO techniques are employed in indoor atmosphere and investigation of various MIMO techniques is undertaken. In this paper, the primary concern is to achieve better performance in indoor environment using VLC. It has been shown in the paper that combining OFDM and MIMO fading can be largely reduced and yields frequency-flat MIMO channel by spatial diversity [2]. The effect of increasing the number of LEDs on the fixed-sized environment is also analysed.

R. Sindhuja · A. R. Shankar (✉)
BMS College of Engineering, Bengaluru, India
e-mail: arathi.ece@bmsce.ac.in

S. Gopinath
RBEI, Bengaluru, India

2 Methodology

2.1 MIMO–OFDM Transreceiver System Using VLC

Figure 1 presents the block diagram of the proposed transmitter. The proposed transmitter is a combination of three technologies, namely MIMO, OFDM and VLC.

The data to be transmitted over the visible light is in binary format. Binary data is represented by series of 0s and 1s. The output binary data is the input to the serial/parallel (S/P) block. S/P block converts the data in serial format into parallel format. The resulting signal is given as input to the OFDM modulator. Within the OFDM modulator the data is mapped using different mapping techniques such as BPSK, QPSK or QAM. According to the analysis, 16-QAM gives a better performance for OFDM. So QAM is selected as the mapping technique. Further cyclic prefix (CP) is added to the signal. Now to make the signal compatible for VLC the negative parts of the signals have to be removed. So the signal is DC-biased. Only the positive and real part is retained for further communication. DC-biased optical OFDM (DCO-OFDM) is the modulation technique used. The electrical signal is converted into optical signal using LEDs. LEDs are the transmitters in case of VLC. The data is transmitted in the form of light [3].

In VLC the medium of propagation is light. MIMO configuration is incorporated based on the number of LEDs used. Multiple LEDs are used to improve the performance of the system. The MIMO configuration at the front end of the receiver is maintained by incorporating multiple LEDs.

Figure 2 presents the block diagram of the proposed receiver. Photo detector (PD) is used for the reception of light. It converts the optical signal into electrical signal. In VLC system PD is the receiver. Number of PDs at the receiver depends on the number of LEDs. The output of the analogue to digital converter (ADC) is fed as
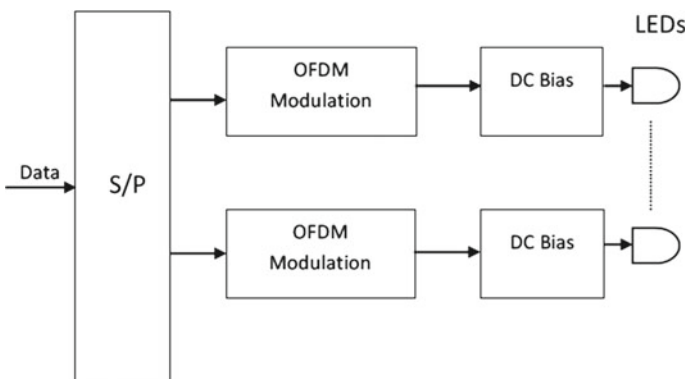
Fig. 1 MIMO–OFDM VLC transmitter
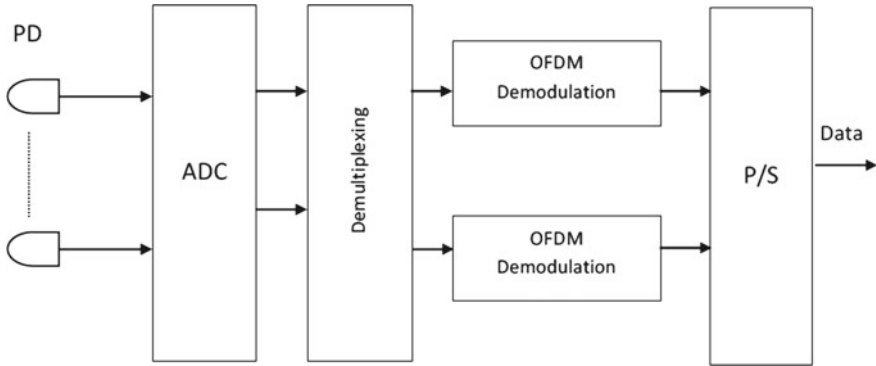
Fig. 2 MIMO–OFDM VLC receiver

input to the demultiplexer. The further processing of the signal is performed by giving the output of the demultiplexer as input to the OFDM demodulator.

Figure 3 explains the block diagram of OFDM. The incoming serial data is converted to a block of specific size to process it block by block. Serial to parallel converter is used, which will be mapped using signal mapper corresponding to the chosen modulation technique. IFFT is carried out on the output of signal mapper and ISI cyclic prefix is added to the IFFT output. After adding cyclic prefix the output data is serialized using parallel to serial converter, which can be up-converted and transmitted to the wireless channel. Information signal will be affected depending on channel noise. At the receiver the incoming serial data is converted to a block of specific size that was followed during modulation. The cyclic prefix which was
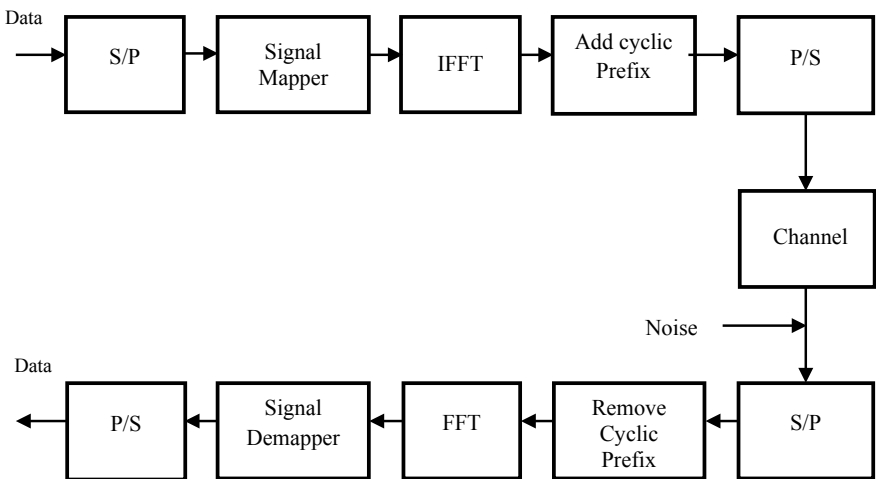
Fig. 3 OFDM block diagram

added during modulation is removed for further processing. The FFT is carried out on the data block and applied to signal de-mapper. The de-mapped data symbols are converted from parallel data to serial data using serial to parallel converter.

A multicarrier system, such as FDM, is used to transmit multiple carriers in parallel to the total available bandwidth in the spectrum into sub-bands. By placing carriers closely in the spectrum high data rate can be achieved. However, due to lack of spacing separating the carriers leads to inter-carrier interference (ICI). Guard bands need to be placed in between any adjacent carriers in order to reduce ICI, which results in lowered data rate.

2.2 Software Specifications

An indoor room environment is simulated using MATLAB and the room dimensions and other specifications are listed in Table 1.

The user can decide the number of LEDs to be placed in the specified dimension. DCO-OFDM is simulated for 16-QAM and the output of this is given as the input to VLC. Here LEDs are the transmitters and PDs are the receivers. From the received input, the received power, intensity of LEDs and effect of reflectivity are calculated. These parameters are further used to calculate the performance parameters like SNR in dB, capacity of the channel and received power. Here, the information carrier is a light wave whose dimensions are in the order of thousands of wavelengths, leading to spatial diversity, which prevents multipath fading. For these reasons multipath fading can be ignored and only AWGN channel is considered. Based on the SNR values 3D plots are generated and the results are analysed.

Table 1 System model specifications

Specifications	Value
Room size (meters)	$5 \times 5 \times 3$
Distance between Tx and Rx (meters)	1.5
R (photodiode responsivity)	0.4 (A/W)
Single LED power	50 mW
Ba (amplifier bandwidth)	4.566 (Hz)
Reflectivity due to ceiling	0.8
Reflectivity due to floor	0.15
Reflectivity due to wall	0.9

Table 2 SNR values for different number of LEDs

No. of LEDs	SNR value (dB)
4	9.202
32	45.33
128	69.41

Table 3 AWGN channel value for different number of LEDs

No. of LEDs	AWGN channel capacity (bits/s/Hz)
4	0.9694
32	4.533
128	6.941

3   Results and Discussions

3.1   Analysis of SNR Value

The spectrum infers that at 0.5 m^2 the value of SNR is high around 69.41 dB for 128 LEDs. At the corners of the room the value of SNR decreases and this mainly depends on the distribution of LEDs.

From Table 4 it is shown that by analysing different SNR spectra for different number of LEDs in an indoor environment, it can be observed that as the number of LEDs increases the SNR value increases.

3.2   Analysis of Capacity of AWGN Channel

From Table 3, by analysing different channel capacity spectrum for different number of LEDs in an indoor environment, it can be observed that as the number of LEDs increases the value of channel capacity also increases.

3.3   Analysis of Received Power

From Table 4, it can be analysed that as the number of LEDs increases the value of

Table 4 Receiver power for different number of LEDs

No. of LEDs (in Tx and Rx)	Receiver power in dB
4	−31.81
32	−11.02
128	−2.846

received power increases and for lesser number of LEDs the difference between the received and transmitted power is high.

4 Conclusion and Future Scope

VLC is considered advantageous than the existing RF communication because of the abundant range of spectrum available. As per the result obtained in this paper, multicarrier modulation technique like OFDM shows better performance than single-carrier modulation. To attain high spectral efficiency 16-QAM is used as the mapping technique over QPSK. To check the performance of VLC for indoor environment different parameters like SNR, channel capacity and received power is analysed. As per the results obtained, as the number of LEDs increases in a closed room, SNR, channel capacity and received power show better performance. In this paper binary data is considered for communication and it can be further analysed for QoS of audio and voice data. This paper explores only spatial diversity of MIMO. Spatial multiplexing of MIMO is yet to be explored. Performance analysis in outdoor environment is to be simulated.

References

1. Panwara N, Sharma S, Singh AK (2016) A survey on 5G: the next generation of mobile communication. Phys Commun 18:64–84
2. Tayade PP, Rohokale VM (2015) Enhancement of spectral efficiency, coverage and channel capacity for wireless communication towards 5G. In: IEEE international conference on pervasive computing (ICPC), ISBN: 978-1-4799-6272-3
3. Feng L, Hu RQ, Wang J, Xu P, Qian Y (2016) Applying VLC in 5G networks: architectures and key technologies. IEEE Netw, ISBN: 0890-8044

Photonic Crystal Based Protective Shield for Medical Treatment with Phototherapy

S. Amuthavalli ⃝**, Manisha Chakraborti (Manisha Chattopadhyay)** ⃝ **and Tapanendu Kundu** ⃝

Abstract Photonic crystals are optical materials with repeating structures that have specific filtering characteristics, among other properties. The impact of materials, periodicity, and thickness of one-dimensional photonic crystal layer on modeling of light is analyzed using Comsol simulations which are based on Finite Element Method (FEM). The influence on the behavior of light transmission characteristics by breaking the periodicity is also observed. In this paper, narrow transmission of photons selectively in the range 311–313 nm is obtained by appropriate inclusion of defect. And also blockage of remaining Ultra Violet (UV) radiation is attained. Phototherapy requires this radiative property for the treatment of Psoriasis. Photonic crystal as a protective shield for psoriasis phototherapy to make it safe and effective is proposed in this paper.

Keywords Periodicity · Radiative · Phototherapy

1 Introduction

Psoriasis is a prolonged inflammatory skin condition instigated by an overactive immune system. Most dermatologists prescribe phototherapy for psoriasis since it is a safe and effective therapy for psoriasis that can be favored for more extreme cases. Phototherapy remains a mainstay treatment in which it operates on the basis of exposure of skin to light.

There are three types of phototherapy applied for the treatment of psoriasis: Broadband Ultraviolet B (BB-UVB), Narrowband Ultraviolet B (NB-UVB), and Psoralen in addition to Ultraviolet A (PUVA). BB-UVB radiates wavelengths of light between 290 and 313 nm whereas NB-UVB uses between 311 and 313 nm. UVA, with wave-

S. Amuthavalli (✉) · M. Chakraborti (Manisha Chattopadhyay)
Department of Electronics and Communication, VESIT, Mumbai, India
e-mail: amuthakrishnan20@gmail.com

T. Kundu
IITB, Maharashtra, India

lengths of 320 to 400 nm, is utilized as a part of psoralen, which is taken orally prior to UVA exposure in systemic PUVA. In spite of the fact that PUVA is extremely effective, it is utilized less regularly because of its intense side effects, such as nausea from psoralen ingestion and cutaneous malignancies. Also, studies demonstrated that wavelengths around 311 nm have more impact than broad-spectrum UVB in clearing psoriasis. Hence NB-UVB is the most commonly preferred phototherapy modality today as it has more extensive application across various dermatologic conditions. And also, in comparison with BB-UVB or PUVA, NB-UVB has lesser side effects [1].

Designing of NB-UVB lamps with narrow band is troublesome. In the meantime, UV lamps or tubes emit UVA radiation along with the required NB-UVB. Since such radiation can cause unfavorable impacts in the skin. Hence only required wavelength should be permitted by blocking the hazardous wavelength to pass through the skin. Solid state approaches also find applications to UV shield in the field of skin protection. The radiation blockage can be achieved as a result of strong reflectance by the optical interference effects.

For this reason, Photonic Crystal (PC) is proposed due to its flexibility in designing for an appropriate wavelength. Photonic crystals are a periodic arrangement of materials with alternate refractive indices. This difference in refractive index denotes the periodic potential that a photon experiences when propagating through this periodic structure. If the difference in refractive index between the two layers is large, then more photons will be confined within the optical material. This confinement brings about the formation of photonic bandgap. The patterned material will block light with wavelengths in the photonic bandgap, while enabling other wavelengths to pass through. And if the periodicity of PC is destroyed by introducing a defect factitiously, a defect mode with a very narrow bandwidth will appear in the photonic bandgap. The photons whose wavelength coincides with the defect mode will be transmitted inside the bandgap. The remaining will be attenuated immediately as long as the wavelength departs from this location. On choosing different materials and by adjusting geometrical parameters and structures, the propagation of light in the PC can be controlled.

The observation of one-dimensional (1D) PC was reported in [2] that the width and position of the band gap depend on the index difference, number of layers, layer thickness. The impact of defect layers in one-dimensional (1D) photonic crystal and accordingly, the spectral characteristics changes of photonic crystal due to the defect was also presented in [3, 4]. 1D photonic crystals can be used as frequency selective filters in thermophotovoltaic system which was proposed in [5].

In this paper, we proposed that the photonic crystal can be used as a protective shield from hazardous wavelength and passing a certain wavelength for Psoriasis treatment. Instead of fabricating UVB lamps, any UV lamps such as Mercury and Xenon lamps with photonic crystal shield can be preferred.

2   Designing Methodology

The behavior of light in PC are investigated by means of FEM which is utilized to obtain the approximate solution for any given physical phenomenon. It is compared with other methods (Bloch Wave Method) in order to validate the modeling process. To simulate the wave propagation, it is required to solve these equations with appropriate boundary conditions [6].

$$\nabla \times (\nabla \times E) - k_0^2 \epsilon_r E = 0 \tag{1}$$

$$E(x, y, z) = E(x, y)e^{-ik_z z} \tag{2}$$

3   Experimental Results and Discussion

3.1   Description of the Structure

The structure is composed of two layers: A and B with refractive indices $n_1 = 1.36$ and $n_2 = 2.4$ with repeating structures of N = 10 periods MgF$_2$ (Magnesium Fluoride) and TiO$_2$ (Titanium di oxide). The central wavelength λ is located in 350 nm. The thickness of the first layer and the second layer is a = $\frac{\lambda}{4*n_1}$ and b = $\frac{\lambda}{4*n_2}$ in Fig. 1. Figure 2 depicts the defect (D) by replacing material in the periodic structure which is examined in Sect. 3.2 with the light transmission characteristics.

Fig. 1 Structure of 1D PC
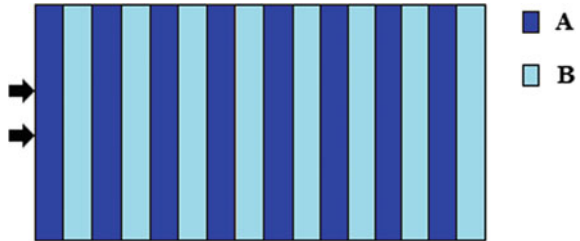
Fig. 2 Structure of 1D PC with defect
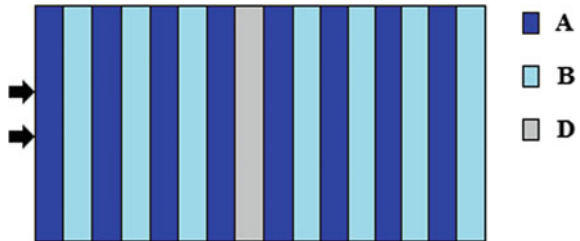
3.2   Behavior of Light Characteristics of 1 D PC Without Defects

Influence of Refractive Index Contrast: By changing n_1 = 1.36, 1.46, 1.76, 2.2, it is observed in Figs. 3 and 4 that both the reflection coefficient and bandwidth increase with the increase in refractive index contrast.

Influence of No of Periods: Due to the increase in layer, the structure experiences increase in multiple reflections and transmissions caused by the variation of refractive index. Hence it leads to increase in the reflection coefficient. In Fig. 5, it is clearly shown that the reflection reaches to unity as the no of period increases but bandwidth reduces. In Fig. 6, the transmission rapidly falls on the bandwidth when period increases. Hence the number of periods should be optimum for the structure.

Fig. 3 Comparison of reflection characteristics for different materials
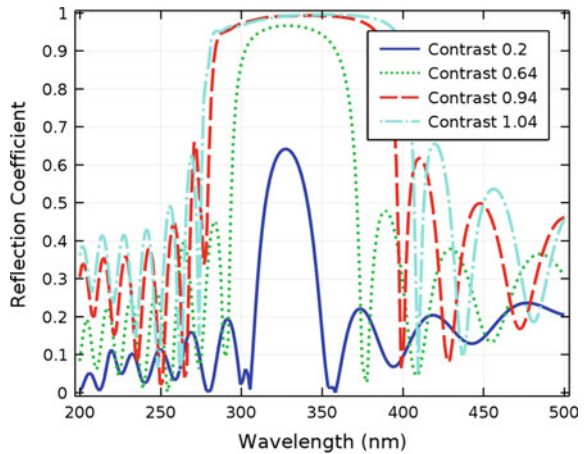
Fig. 4 Comparison of transmission characteristics for different materials
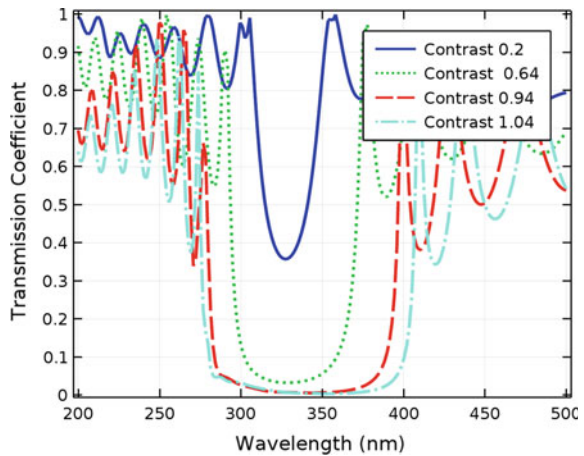
Fig. 5 Comparison of reflection characteristics for different periods
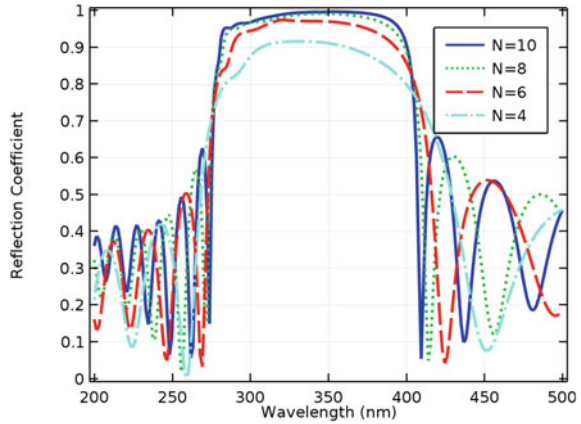
Fig. 6 Comparison of transmission characteristics for different periods
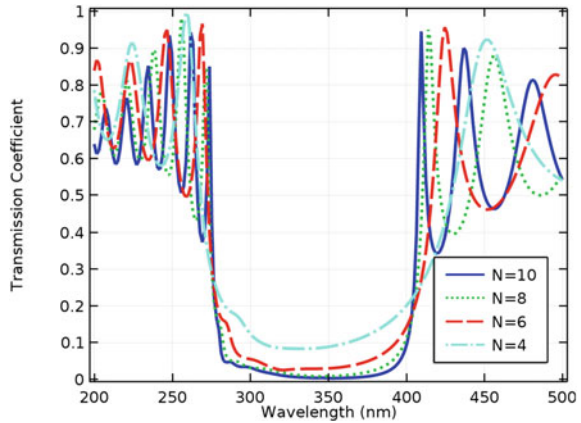
Influence of Thickness of the layer: Figures 7 and 8 show the shift in the reflection and transmission characteristics of 1D PC that occurs by varying the thickness of the layer.

3.3 Behavior of Light Characteristics of 1 D PC with Defects

Influence of Defect Position and Material: Analysis is done by inserting defect material (ZnO) in different positions. From the Fig. 9, it is evident that the resonant transmission that occurs in the photonic bandgap is maximum when the defect is placed in the middle of the structure. It is observed that the position of the defect is responsible only for the depth of the resonant transmission and not for the position of the resonant transmission. The response is observed for various materials as a defect in the middle of structure by replacing the material in the periodic structure

Fig. 7 Comparison of
reflection characteristics for
different thicknesses
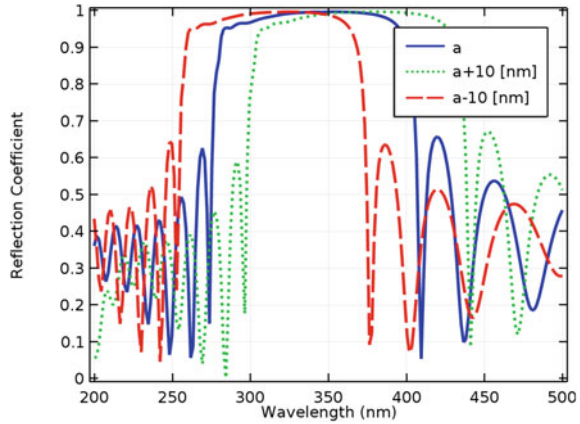
Fig. 8 Comparison of
transmission characteristics
for different thicknesses
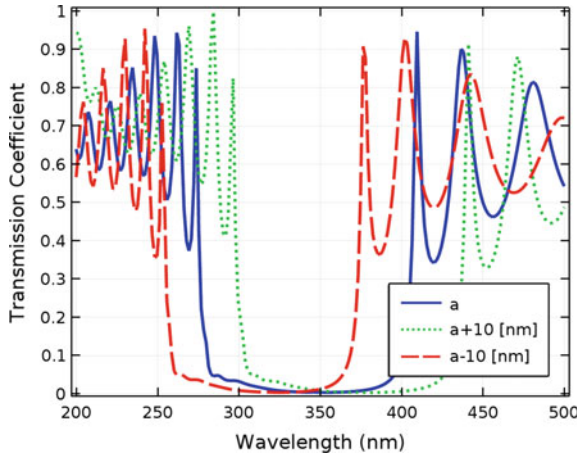
in Fig. 10. The resonant transmission occurs in different positions as the material of
the defect changes. This helps in fixing the position of the resonant transmission.
Similarly by changing the thickness of the defect, the depth of resonant transmission
can be achieved more.

Similarly the analysis is done by placing the defect in two positions in the
periodic structure with respect to the center. The wavelength range is observed
in the entire UV range between 280 and 400 nm. Based on the range of wave-
length to be blocked, the material A and B should be selected. The structure
Air/$AB_m DB_x AB_n DB_x AB_m$/Substrate with different cycles (i.e. m, n, x = 1, 2, 3)
is analyzed. It is concluded that by choosing appropriate material combination with
suitable defect and placing in an appropriate position, 100% transmission in the range
311–313 nm can be achieved which is shown in Fig. 11a. The glass substrate coated
with this PC acts as a shield for any UV lamp to transmit the specified wavelength.

Fig. 9 Comparison of transmission characteristics for different positions of the defect
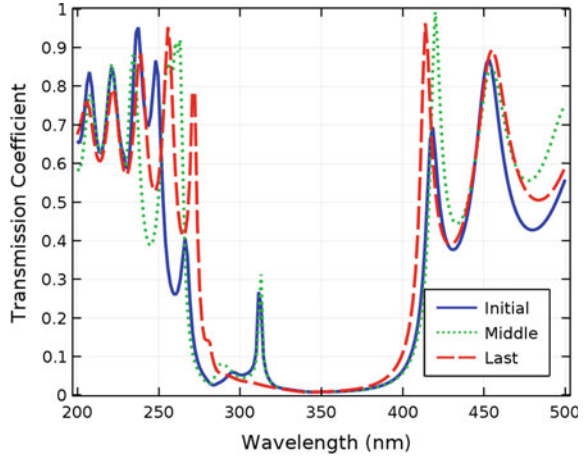
Fig. 10 Comparison of transmission characteristics for different material defects
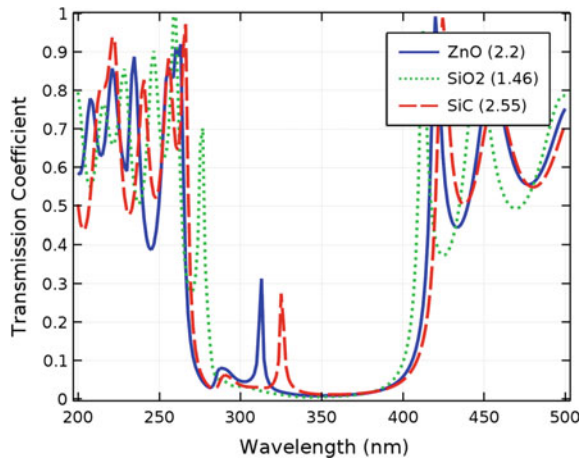
Similarly, by changing the center wavelength with the same structure and material, it is possible to shift the radiation to any wavelength range is shown in Fig. 11b.

4 Conclusion

The behavior of light reflection characteristics in UV range is evaluated with the variation of structural parameters. The analysis on the insertion of defect provides information about the resonant transmission in the photonic band gap. It is concluded that narrow transmission gap can be achieved by placing two defects in an appropriate position. This is done in accordance with the results obtained by Vladimir et al. [3]. Also, 100% transmission is obtained with the narrow bandgap in the range 311–
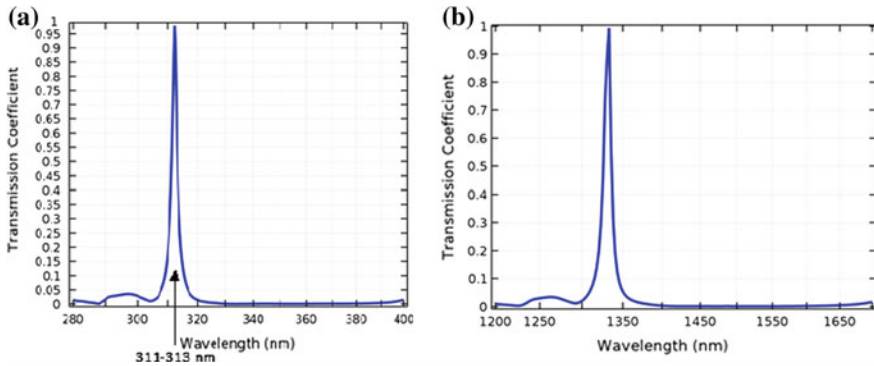
Fig. 11 **a** Result of photonic crystal as protective shield for psoriasis treatment $\lambda = 350$ nm, **b** impact of center wavelength $\lambda = 1500$ nm

313 nm. The glass substrate coated with this PC can be used as a protective shield in phototherapy treatment. This protective shield blocks all UV radiations completely in the range 280–400 nm and it transmits only the required wavelength in the range 311–313 nm which is the requirement for NB-UVB Phototherapy. It is clear that instead of fabricating NB-UVB lamps for the treatment of Psoriasis which makes it expensive, any UV lamp can be preferred. By providing a shield over the UV lamp, it allows only a required wavelength and reflects the unwanted harmful UV rays which makes the Phototherapy treatment as more feasible and effective.

References

1. Nakamura M, Farahnik B, Bhutani T (2016) Recent advances in phototherapy for psoriasis
2. Ouahab I, Dekkiche L, Naoum R (2013) Impact of the opto-geometric parameters on the band diagram and transmission and reflection spectrum of the Bragg structure. Opt Photon 184–189
3. Moskaliuk V, Tsyba Y (2017) Simulation of defects in one-dimensional photonic crystal. In: International conference on electronics and nanotechnology
4. Petcu A, Preda L (2009) The optical transmission of one-dimensional photonic crystal. Rom J Phys 539–546
5. Kwefeu Mbakop F, Djongyang N, Raidandiz D (2016) One dimensional TiO2/SiO2 photonic crystal filter for thermophotovoltaic applications. J Eur Opt Soc Rapid Pub
6. Amuthavalli S, Chattopadhyay M (2018) Optimization of one dimensional photonic crystal structure with light reflection characteristics. In: 2018 2nd international conference on trends in electronics and informatics (ICOEI),Tirunelveli, 2018, pp 642–646

Simulation Study and Performance Comparison of Various SRAM Cells in 32 nm CMOS Technology

R. Krishna and **Punithavathi Duraiswamy**

Abstract Cell stability and leakage power consumption are major concerns in SRAM cell design in deep submicron technology due to a decrease in DC supply voltage and variability in technology. This paper presents a simulation study and performance comparison of four SRAM cells, which include the traditional 6T, 7T, 8T and 9T cell implementations. In particular, the Static Noise Margin (SNM) and leakage power of each cell are analyzed in 32 nm technology. The 9T SRAM cell provides 1.05 times stronger write ability and 1.65 times stronger read stability compared to traditional 6T SRAM cell. The leakage power of 7T SRAM cell and 9T SRAM cell is 2.3% and 1.11% less compared to standard 6T SRAM cell. The effect of DC supply and temperature on SNM is also analyzed and simulation results are presented.

Keywords CMOS · Stability · Noise margin · Leakage power · SRAM

1 Introduction

The continuously growing demand for low power, high speed embedded memory has been a driving force in the development of new Static Random Access (SRAM) designs techniques [1]. In deep submicron regime, design of stable, robust and low leakage SRAM cell becomes a challenging task. In memory circuits, a significant portion of the total power consumption is mainly due to leakage or static power. Because of low threshold voltage and ultra-thin gate oxide, the leakage current in the

R. Krishna (✉)
Department of Electronics and Communication Engineering,
Bangalore Institute of Technology, Bengaluru, India
e-mail: krishnar129@yahoo.com

P. Duraiswamy
Department of Electronic and Communication Engineering,
M. S. Ramaiah University of Applied Sciences, Bengaluru, India
e-mail: punithavathi.ec.et@msruas.ac.in

transistor is increased as it cannot be turned off completely. Also, the read and write margins of the SRAM is affected by the supply voltage and temperature variations and threshold voltage. In higher threshold voltage SRAM circuits, SNM strongly depends on supply voltage and temperature [2].

In this paper, we compare four different SRAM cells (6T, 7T, 8T, 9T) on the basis of performance metrics like read stability, write ability and leakage power consumption. The effect of temperature and power supply variations on the noise margins is also studied. The simulations are performed in 32 nm CMOS technology using HSPICE tool and the results are presented.

2   Static Noise Margin

There are three states in SRAM cell; read, write and hold state. Static Noise Margin (SNM) is an important parameter in SRAM design as it is used to measure the cell stability. It is the maximum value of a dc disturbance that the cell can withstand before changing state. Graphically, the SNM is represented by the largest square box that can be fitted in the butterfly characteristic curves of the SRAM cell. SNM of SRAM depends on cell ratio, pull-up ratio, supply voltage and temperature [3]. Read Static Margin (RSNM) is the maximum DC noise voltage that the cell can withstand without losing data during the read operation. Similarly, write ability is measured in terms of Write Static Noise Margin (WSNM) and it is the maximum noise voltage present at the bit lines during a successful write operation [4, 5]. Lower values of RSNM and WSNM indicates poor ready stability and write ability. Both read and write margin of SRAM can be improved by read and write assist techniques [6, 7].

3   Leakage Power

Leakage power also called static power is the power consumed when a circuit is in sleep mode or standby mode. Leakage power reduction has become very important in high-performance, portable and embedded applications [2, 8]. In MOSFET, the leakage current is due to various components, such as sub-threshold leakage, gate leakage and junction tunneling effect. Among these, sub-threshold leakage is the most dominant [9] and for a MOS device with a channel width of W and length of L, it can be expressed as follows:

$$I_{leakage} = I_o e^{\frac{V_{gs} - V_T}{n V_{th}}} (1 - e^{-\frac{V_{ds}}{V_{th}}}) \tag{1}$$

$$I_o = \mu_o C_{ox} \frac{W}{L} V_{th}^2 \tag{2}$$

where μo is the electron mobility, C_{ox} is the gate capacitance per unit area, V_{th} is the threshold voltage, n is the sub-threshold swing co-efficient, V_T is the thermal voltage,

(a) 6T SRAM cell   (b) 7T SRAM cell

(c) 8T SRAM cell   (d) 9T SRAM cell
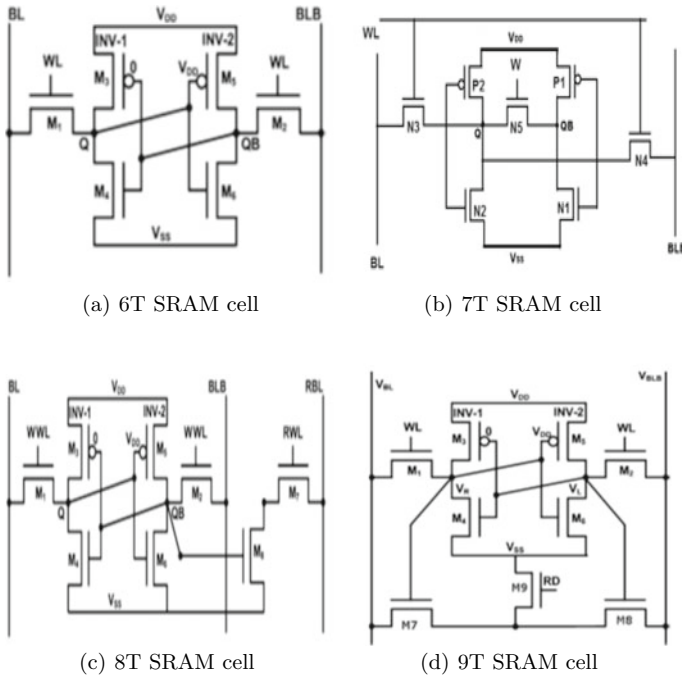
Fig. 1 SRAM cell implementations

V_{gs} is the gate to source voltage of MOS and V_{ds} is the drain to source voltage of MOS [10]. In SRAM, leakage power originates from various sources. They are bit line leakage, word line and cell array leakage. The leakages arising from the the bit line (BL) and word line (WL) are less compared to SRAM cell leakage. However, it affects the reliability of the SRAM. Here, we focus on sub-threshold leakage power calculation of the SRAM cell. The next section presents the simulation results and comparison of 6T, 7T, 8T and 9T SRAM cells in Fig. 1.

4 Simulation Results

The simulations were carried out using HSPICE tool in 32 nm CMOS technology. The simulation parameters used for noise margin analysis are cell ratio used is two and pull-up ratio used is one. The temperature and the supply voltage used are 100 °C and 1 V, respectively. The butterfly curves for RSNM and voltage transfer characteristics for WSNM are shown in Fig. 2 and Fig. 3, respectively, for the four SRAM cells. From Table 1, it is seen that the increase in RSNM is higher compared to WSNM with increase in the number of transistors. Simulation results also reveal that the RSNM of 9T cell is 1.65 times better than the conventional 6T SRAM

(a) 6T   (b) 7T

(c) 8T   (d) 9T
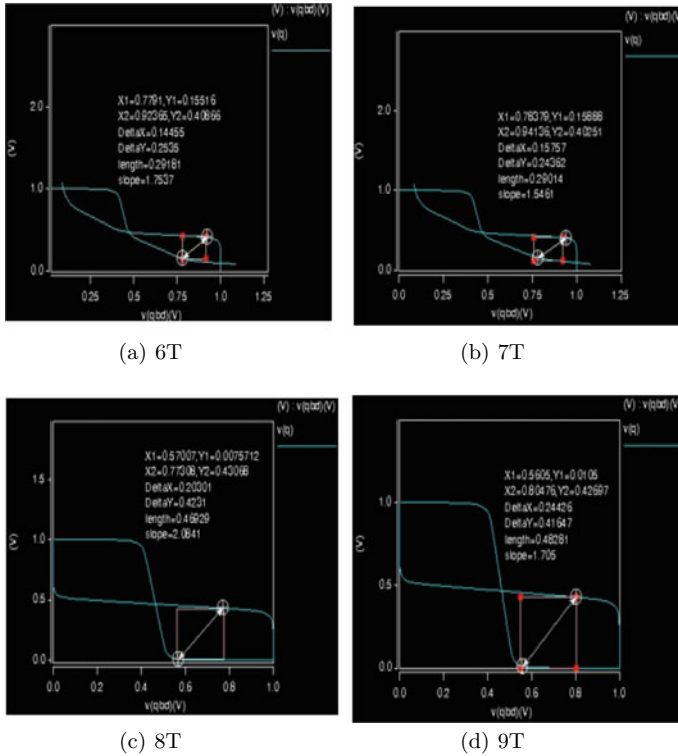
Fig. 2 Butterfly curves for measuring RSNM

cell. Even though the stability of 9T SRAM cell is better than the other cells, it leads to extra area overhead and a complex layout. Supply voltage dependence of RSNM and WSNM was investigated by varying supply from 0.6 to 1.3 V at constant temperature of 100 °C. Figure 4 shows the impact of supply voltage over RSNM and WSNM values. Simulation results shown in reveals that, with the increase in supply voltage, Read/Write SNM increases. The increase in RSNM and WSNM is higher in 7T and 8T cell, respectively, as compared to other cells. Similarly, the temperature dependence of RSNM and WSNM was investigated by varying temperature from 40 to 100 °C at constant supply voltage of 1 V. From the results shown in Fig. 4, it is clear that RSNM and WSNM decrease as temperature increases. The decrease in RSNM and WSNM is higher in 7T and 8T cell, respectively, as compared to other cells. Sub-threshold Leakage power consumption for all the four types of SRAM cells were measured by making the word line (WL) zero and disconnecting the bit line (BL) and bitline bar $\bar{BL}$ from the inverter circuit. The leakage power of 7T SRAM cell and 9T SRAM cell is 2.3 and 1.11% less compared to standard 6T SRAM cell. Table 1 gives the sub-threshold leakage power measured from HSPICE simulation.

(a) 6T

(b) 7T

(c) 8T

(d) 9T
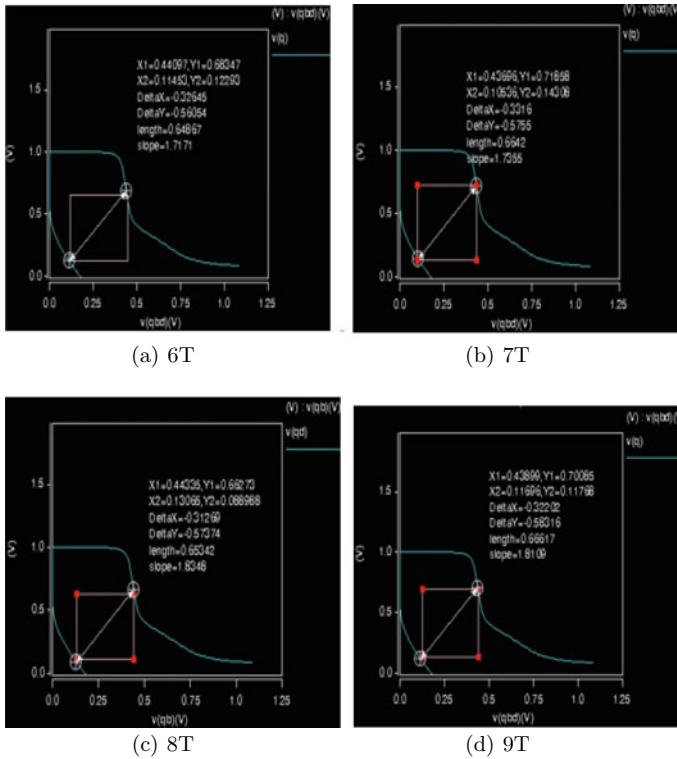
Fig. 3 Voltage transfer characteristics curve for measuring WSNM

Table 1 Comparison of SNM and leakage power for various SRAM Cells

SRAM cell	RSNM (mV)	WSNM (mV)	Leakage power (nW)
6T	208	447	181
7T	219	459	177
8T	327	463	180
9T	342	470	179

5   Conclusion

An analysis on the stability performances of four SRAM cell (6T, 7T, 8T, 9T) has been presented in 32 nm technology. With the advancement in process technologies, the speed of SRAMs will increase, However, it will be more susceptible to mismatches affecting the stability of the SRAM. The 7T, 8T and 9T SRAM cells offer greater data stability compared to the conventional 6T SRAM cell as it employs separate read and write ports. The 9T SRAM cell provides 1.05 times stronger write ability and 1.65 times stronger read ability compared to traditional 6T SRAM cell. The

Fig. 4 Effect of supply voltage and temperature on SNM
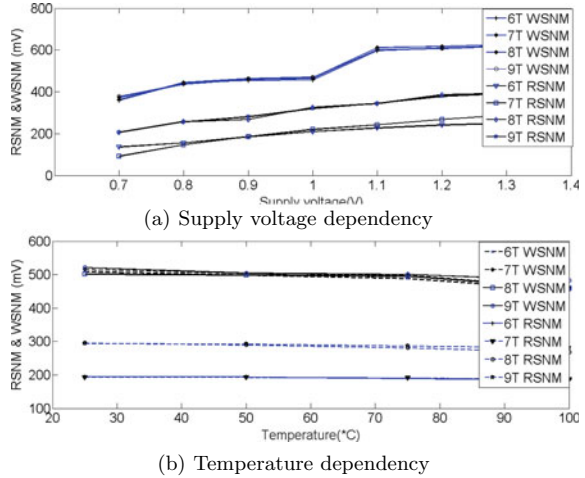
(a) Supply voltage dependency

(b) Temperature dependency

leakage power of 7T SRAM cell and 9T SRAM cell is 2.3 and 1.11% less compared to standard 6T SRAM cell. From the simulation study, it can be concluded that 9T SRAM cell is more desirable for low power applications where data stability and leakage power are critical.

References

1. Kavitha, Govindaraj T (2016) Low-power multimodal switch for leakage reduction and stability improvement in SRAM cell. Springer Res Article 2945–2955
2. Calimera A, Alberto, Enrico, Massimo (2012) Design techniques and architectures for low leakage SRAMs. IEEE Trans Circuits Syst 59:1992–2006
3. Evelyn, Karen (2006) Read stability and write ability analysis of SRAM cells for nanometer technologies. IEEE J Solid State Circuits 41:2577–2587
4. Andrei, Manoj (2008) CMOS SRAM circuit design & parametric test in nano scaled technologies. Springer series
5. Hong, Volkan (2014) A comprehensive comparison of data stability enhancement techniques with novel nanoscale SRAM cells under parameter fluctuations. 611473–611484
6. Sanjay S (2012) Leakage current reduction techniques for 7T SRAM cell in 45 nm technology. Springer Wirel Pers Commun 123–136
7. Vijay, Sumit, Manisha (2014) High performance process variations aware technique for sub-threshold 8T SRAM cell 57–68
8. Majid, Somayeh, Mohammed (2015) An ultra-low-power 9T SRAM cell based on threshold voltage techniques. Springer Circuits Syst Sig Process 1437–1456
9. Adam, Anatoli, Janna, Alexander (2012) A 40-nm sub-threshold 5T SRAM bit cell with improved read and write stability. IEEE Trans Circuits Syst 59(12):873–877
10. Kaushik, Saibal (2003) Leakage current mechanisms and leakage reduction techniques in deep-submicrometer CMOS circuits. Proc IEEE 91305–91327

Planar Waveguide Bragg Grating Pressure Sensor—Design and Applications

Madhuri R. Kulkarni, B. R. Manoj Kumar, Mayur Mohan Malghan, G. Mohamedarif, and Rajini V. Honnungar

Abstract We design and simulate the waveguide Bragg grating pressure sensor on Boro float glass substrate. Rib waveguide structure is used for the design of pressure sensor, centered at 632.8 nm. The pressure sensor is simulated for a range from 5 to 80 MPa. Poly(methyl methacrylate) is used as the waveguiding material and air as the cladding surface. The rib waveguide is designed in RSoft tool using beam propagation method, and GratingMOD is used to create periodic perturbations on it. The pressure sensitivity as observed after simulation is 0.074 nm/MPa.

Keywords Waveguide Bragg grating · Pressure sensor · Rib waveguide · Poly(methyl methacrylate)

1 Introduction

An optical waveguide is being designed for many applications such as medical assistance, communication and hydraulics. The sensor is designed for the unique needs of extreme endurance, high-power hydraulic cylinders and accumulators, such as those used in offshore oilfield mining and drilling operations or heavy-duty construction, pipeline pressure measurement, oil reservoir monitoring, radar applications, downhole pressure monitoring and military vehicles. An optical integrated circuit is a thin film type optical circuit designed to perform a specific function by integrating optical waveguides and other functional components all on a single substrate. The basic structures of optical waveguide consist of core and clad. In a nonplanar waveguide, the core is surrounded by the cladding in all transverse directions. For device applications, extensively used waveguide is the nonplanar waveguides [1]. We use rib waveguide for this design and its structure is shown in Fig. 1.

M. R. Kulkarni · B. R. Manoj Kumar · M. M. Malghan · G. Mohamedarif · R. V. Honnungar (✉)
Department of ECE, RNSIT, Bengaluru, Karnataka, India
e-mail: rajinivh@gmail.com

Fig. 1 Rib waveguide
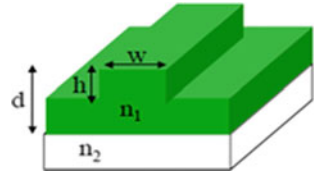
2 Theory

2.1 Fiber Bragg Grating Principle

In principle, the FBG reflects particular wavelengths of light near Bragg resonance and the rest of the spectrum is being transmitted.

Figure 2 shows the core of a single-mode fiber exposed to periodic pattern of intense ultraviolet light. A permanent increase in refractive index of the core is produced by the exposure, creating a fixed periodic grating. A small amount of light is reflected at each periodic refraction change.

When the grating period is approximately half the input light's wavelength, all the reflected light signals combine coherently to one large reflection at a particular wavelength. This is known as the Bragg condition, and the wavelength at which this reflection occurs is called the Bragg wavelength. Wavelengths that satisfy the Bragg condition are affected and strongly back-reflected. The reflected component's central wavelength satisfies the Bragg relation:

$$\lambda_{ref1} = 2 \times n \times \Lambda \tag{1}$$

where n is the refractive index of the core, and Λ is the grating period.

Since n and Λ are temperature and strain dependent, as temperature and strain vary, the wavelength of the reflected component will shift by a particular value proportional to the temperature/strain.

Fig. 2 Fiber Bragg grating principle
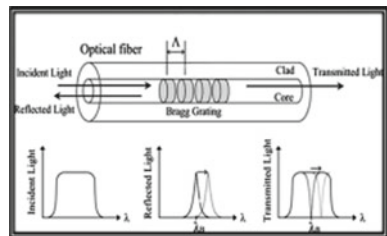
2.2 Waveguide Bragg Grating Principle

The optical waveguide consists of core, clad and substrate. The materials used in our work are PMMA, air and Boro float glass, respectively.

Bragg grating is an optical waveguide formed by creating periodic perturbations or refractive index modulation. Light is made to propagate through the core. A particular wavelength, that is, the centre wavelength will be reflected due to the presence of grating [2].

When there is an application of pressure there is a shift in the wavelength of light. This shift in wavelength is calculated using the Bragg's law,

$$\lambda_{new} = 2 \times n \times \Lambda \tag{2}$$

2.3 Materials Used for the Design

PMMA. Poly(methyl methacrylate) or poly(methyl 2-methylpropenoate) is the polymer of methyl methacrylate, with chemical formula $(C_5H_8O_2)_n$. It is also known as acrylic glass or simply acrylic.

Properties of PMMA materials. PMMA is a linear thermoplastic polymer. PMMA has high Young's modulus, high mechanical strength and low elongation at break. It does not shatter on rupture. It is one of the hardest thermoplastics and is also highly scratch-resistant. It exhibits good water-absorbing capacity and low moisture, due to which products produced have good dimensional stability. As the temperature rises, both of these characteristics increase.

Why PMMA material. Due to low cost, ease of fabrication and assembly, and compatibility with other materials, polymer materials provide a potent alternative to conventional optical materials. One of the important characteristic of polymeric optical materials is their relatively high light absorption rates, at approximately 0.2 dB/cm, as compared to 0.2 dB/km for glass fibers at wavelengths of 1550 nm.

3 Design of Waveguide

3.1 Rib Structure

In multimode waveguides that support more than two guided modes, power gets distributed to the clad and substrate regions causing losses. To avoid this, most waveguide devices consist of single-mode 3D waveguides [3].

Rib waveguide is a waveguide in which the guiding layer basically consists of the slab with a strip superimposed onto it. Rib waveguides provide confinement of the wave in two dimensions. The optical losses are lower for rib waveguides than for strip ones. For the simulation of the rib waveguide, the following parameters were considered:

a. Waveguide model dimension: 3D
b. Simulation tool: BeamPROP
c. 3D structure type: Rib
d. Free space wavelength: 632.8 nm
e. Background index: 1.4699
f. Index difference: 0.0207
g. Waveguide width: 5 μm
h. Waveguide height: 5 μm
i. Profile type: Step-index

The background index is the refractive index of the substrate and the index difference is the difference between the refractive index of the core and the substrate.

3.2 RI Profile

A refractive index profile is the distribution of **refractive indices** of materials within an **optical waveguide** [4]. It signifies the light distribution in the optical fiber. Figure 3 shows the RI profile in which the low index value indicates the refractive index of the substrate and the high index value indicates the refractive index of the core.

Fig. 3 RI profile of the rib waveguide
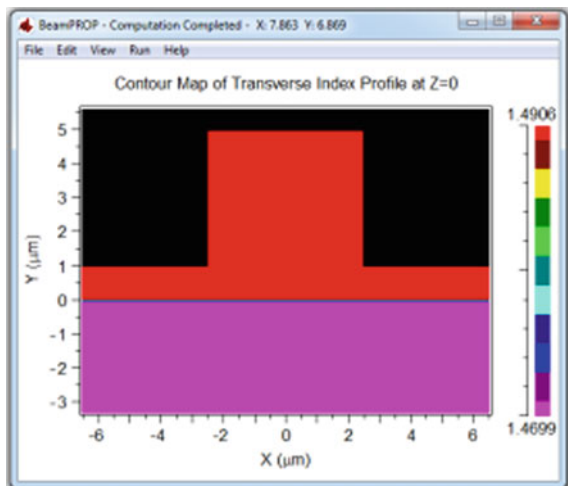
Fig. 4 Mode profile in the rib waveguide
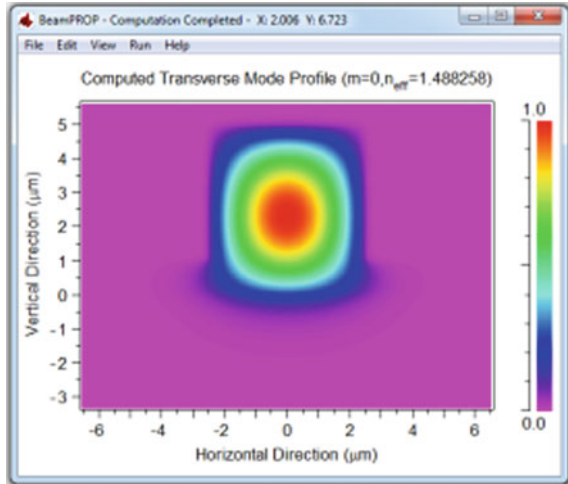
3.3 Mode Profile

The mode profile represents the light confinement in different regions of the waveguide. Figure 4 shows the mode profile in the rib waveguide.

3.4 Principle of Pressure Sensing

The effective index of refraction and the periodicity of the grating determine its center wavelength. When the pressure is applied, the grating period changes and hence wavelength shifts according to the Bragg's condition given by Eq. (2) (Tables 1 and 2).

Table 1 Comparison of analytical and practical values of wavelengths

Pressure (in MPa)	Pressure sensing $E_{ps} = \frac{p \times [1-[2 \times \nu]]}{E}$	$\lambda_{new} = \Delta\lambda + \lambda_c$ in μm	λ RSoft in μm
5	0.653061×10^{-3}	0.6331701	0.635
7	0.9142857×10^{-3}	0.63331825	0.6351
10	1.3061224×10^{-3}	0.63354036	0.6353
15	$1.959183673 \times 10^{-3}$	0.63391055	0.6357
20	$2.6122448898 \times 10^{-3}$	0.6342807	0.6361
40	5.2244897×10^{-3}	0.6357614	0.6376
60	7.836734×10^{-3}	0.6372421	0.639
80	10.44897×10^{-3}	0.6387229	0.6405

Table 2 Comparison of effective refractive index values by analytical method and RSoft tool

Waveguide width (μm)	n_{eff} Analytical method	n_{eff} RSoft
2	1.47200	1.482553
4	1.48900	1.487608
6	1.49013	1.488621
8	1.49038	1.488992
10	1.49048	1.489167

$$\lambda_{new} = 2 \times n \times \Lambda \tag{3}$$

Pressure sensing equation by analytical method:
Poisson ratio, $\nu = 0.34$
Strain optic coefficients: $P_{11} = 0.3$; $P_{12} = 0.297$
Effective index of refraction, $n_{eff} = 1.489$
Young's modulus, $E = 2.45$ GPa
Pressure sensing equation,

$$E_{ps} = pressure \times \left[\frac{(1 - 2 \times v)}{E} \right] \tag{4}$$

Strain optic constant,

$$P_E = \frac{n_{eff}^2}{2} \times [P_{12} - (v \times \{P_{11} + P_{12}\})] \tag{5}$$

Shift in wavelength:

$$\Delta\lambda_B = \lambda \times (1 - P_E) \times E_{ps} \tag{6}$$

$$\lambda_{new} = centerwavelength + \Delta\lambda_B \tag{7}$$

4   Result and Discussions

Table 3 shows the sensitivity of different FBG pressure sensors with different center wavelengths.

On collation of Figs. 5, 6 and 7, the shift in wavelength spotted identical.

Figures 8 and 9 illustrate that pitch period and shift in wavelength vary linearly with pressure applied.

Figure 10 outlines the rise in waveguide width and the rise in effective RI. From

Table 3 Summary of FBG pressure sensors in order of sensitivity [5]

Sensitivity	Range	Wavelength	FBG type novelty
3 pm/MPa	70 MPa	–	Standard/bare
7 nm/MPa	–	–	Standard/diaphragm
1.57 pm/kPa	0–1 MPa	–	Standard/diaphragm
51 pm/MPa	–	–	Long period grating
265 pm/kPa	–	–	Photonic crystal fiber
28 nm/MPa	–	–	Standard/temperature insensitive
0.116 nm/kPa	15 kPa	1550 nm	Standard/rubber diaphragm
1.32 pm/kPa	–	–	Polymer fiber/vinal diaphragm

Fig. 5 Plot of maximum reflectivity as function of wavelength (MATLAB)
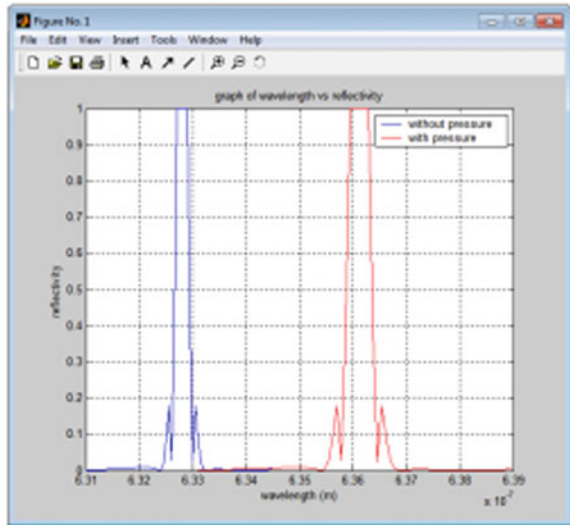
6 µm RI becomes constant. Thus optimization of waveguide width dimensions is achieved.

Fig. 6 Grating spectral
response with apodization
(RSoft)
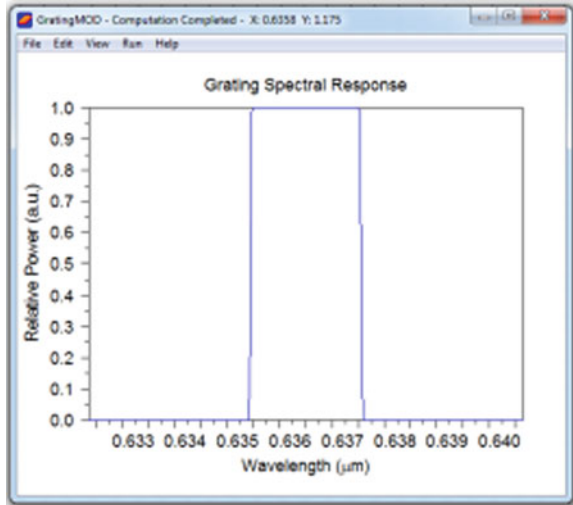
Fig. 7 Grating spectral
response without apodization
(RSoft)
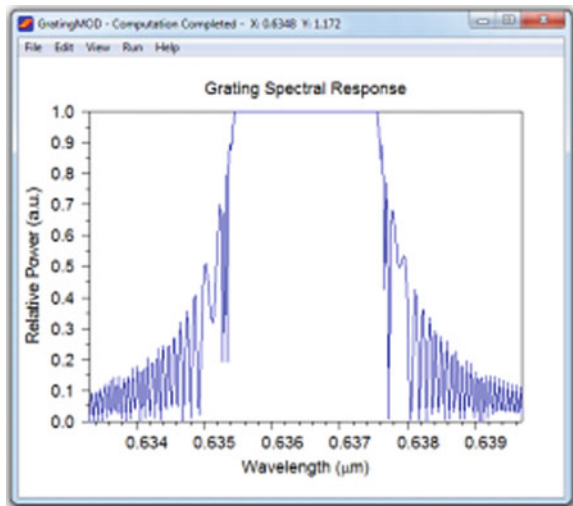
Fig. 8 Plot of pitch period and wavelength as function of pressure
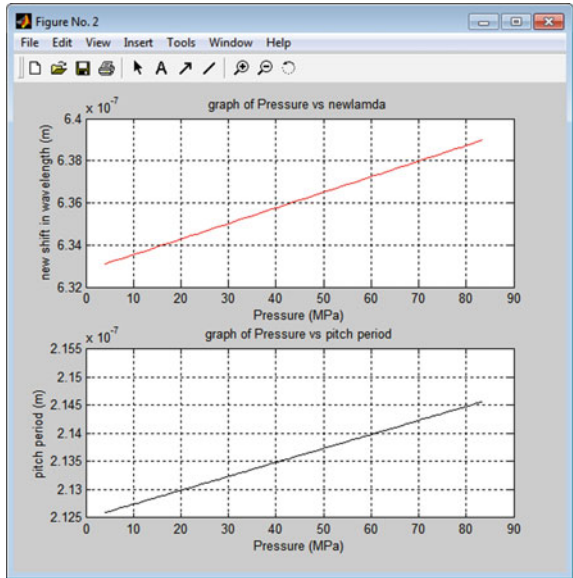
Fig. 9 Plot of pitch period as function of new shift in wavelength
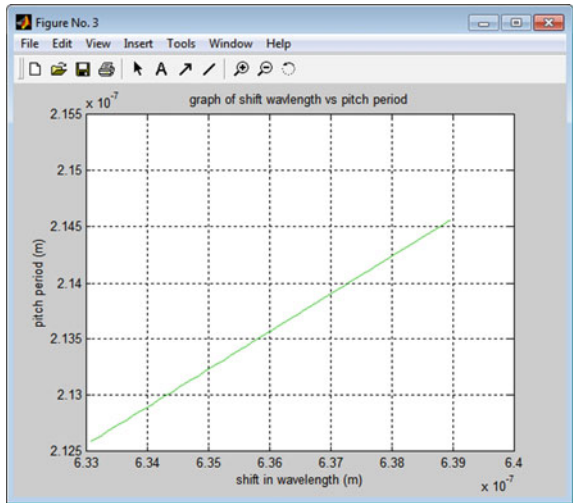
Fig. 10 Plot of effective refractive index as function of waveguide width
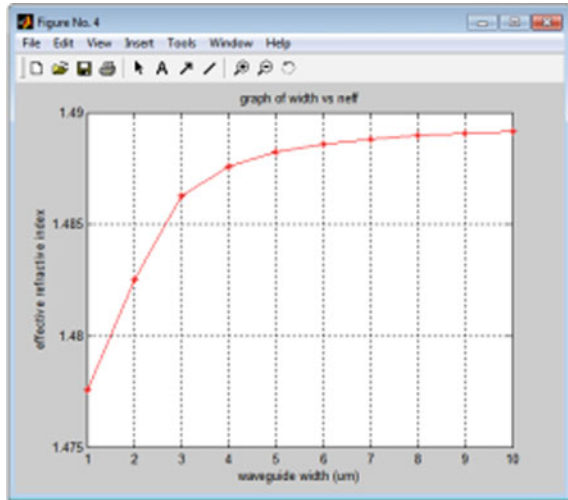
5 Conclusion

The waveguide Bragg grating sensor has been designed and simulated in this work. The sensor is observed to have the sensitivity of 0.074 nm/MPa. This sensor can be used for hydraulic applications. The sensor can be further used for similar kind of pressure-sensing applications in industries.

References

1. Ambrosio R, Lara G, Jimenez A, Mireles J, Ibrarra J, Heredia A (2012) Design and simulation of a pressure sensor based on optical waveguides for applications in hydraulic fracturing. In: SISPAD, Denver, CO, USA, pp 5–7 Sept 2012
2. Mondal B, Sharan P, Hussain Z (2014) Modelling and simulation of pressure sensitivity of bragg grating sensor for structural health monitoring application. Int J Comput Technol 1(2)
3. Prajzler V, Klapuch J, Lyutakov O, Huttel I, Spirkova J, Nekvindova P, Jerabek V (2011) Design, fabrication and properties of Rib Poly (methylmethaacrylimide) optical waveguides. Radio Eng 20(2)
4. Nishihara H, Haruna M, Suhara T. Chapter 26: optical integrated circuits
5. Allwood G, Wild G, Hinckley S. Fiber bragg grating sensors for mainstream industrial processes

Two-Dimensional Potential-Based Model for Tunnel Field-Effect Transistor (TFET)

Netravathi Kulkarni and P. Vimala

Abstract In this paper, we propose a two-dimensional analytical model of silicon-on-insulator tunneling field-effect transistors (SOI TFETs) by applying the superposition principle. By solving 2D Poisson's equation with the help of boundary conditions of channel region and gate oxide region, we calculated the surface potential and electric field for both lateral and vertical directions. Here, we have demonstrated the results obtained from an analytical expression which has been compared with TCAD 2D simulator for some parameters, like gate oxide thickness, by varying the channel length with different V_{gs} and V_{ds} values.

Keywords TFET · Analytical modeling · Poisson's equation · Surface potential · Electric field

1 Introduction

The nanoscale CMOS performance has degraded due to their aggressive scaling. Due to this, the metal-oxide semiconductor (MOS) device was strictly affected by short-channel effects (SCEs) such as drain-induced barrier lowering, hot carrier effects, reduced I_{ON}/I_{OFF} ratio and wide increase in leakage current. A reduced gate length leads to a reduced gate capacitance; therefore, the switching speed of the circuit increases [1]. Thus, the voltage scaling is an essential part of device miniaturization that also helps in the reduction of power consumption of the device. Moreover, the sub-threshold swing of the MOS is limited to 60 mV/decade at room temperature. So it is difficult to scale down the supply voltage in order to realize a large I_{ON}/I_{OFF} ratio [2–5]. To overcome these problems, some novel engineering solutions have been proposed to achieve a sub-60 mV/dec sub-threshold swing (SS) such as impact-ionization MOS devices [6], nano-electromechanical FETs [7], suspended

N. Kulkarni (✉) · P. Vimala
Department of Electronics and Communication Engineering, Dayananda Sagar College of Engineering, Bangalore, India
e-mail: netranetu00@gmail.com

gate MOSFETs [8] and tunneling FETs (TFETs) [9–12]. Among these, we considered the TFETs in this paper, because of the following advantages: (1) lower leakage current and (2) provide a steep sub-threshold swing (SS). The analytical model for the SOI TFET has been already developed by using parabolic-approximation technique. Here we applied the superposition principle, to get accurate results compared to parabolic-approximation method.

In this paper, a 2D analytical solution of silicon-on-insulator (SOI) TFETs has been presented. In order to derive the analytical expressions for surface potential and electrical field, a two-dimensional Poisson's equation has been solved. This paper is described as follows: The device structure of TFET and its working function is explained in Sect. 2. By using 2D Poisson's equation, analytical solutions for surface potential and electric field in the channel are derived in Sect. 3. In Sect. 4 the model is validated by comparing it with TCAD 2D simulation results for different parameters, like channel length, gate oxide thickness (t_{ox}) and thickness of silicon (t_{si}) with different voltages.

2 Device Structure

The schematic of SOI TFET is shown in Fig. 1a. In this figure, t_{ox} is the thickness of gate oxide, t_{si} is the silicon thickness, L_{CH} is the length of the channel. If the bottom of the buried oxide (BOX) layer is grounded, the BOX layer thickness (t_{BOX}) becomes small. Hence the voltage drop across BOX region will be negligible.

Here the TFET is operated in sub-threshold region, where it reduces the minority, carries and abrupts the source channel and drain channel regions. By assuming that, in the source and drain region there is no depletion. The band diagram of the ON and OFF state of n-channel TFET is shown in Fig. 1b. Since the potential barrier between channel and source region is too wide, tunneling does not occur in the OFF state. Therefore, there exists too small leakage current. When the gate voltage is more than
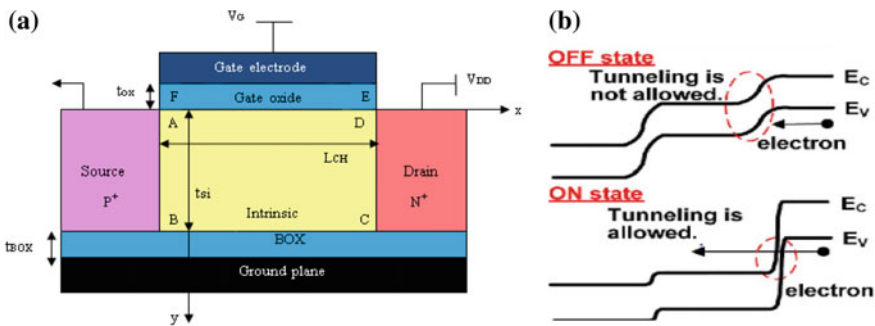
Fig. 1 a Schematic of SOI TFET b band diagram of n-channel TFET

the threshold voltage, the potential barrier between the source and the channel region becomes narrow, so that it allows a substantial tunneling current in the ON state.

3 Analytical Model Derivation

The surface potential in the channel and gate oxide region of TFET is given by the two-dimensional Poisson's equation:

$$\frac{\partial^2 \varphi}{\partial x^2} + \frac{\partial^2 \varphi}{\partial y^2} = 0 \tag{1}$$

By solving (1), the silicon material is used instead of gate oxide region where permittivity difference is considered. Hence, the thickness of oxide (t_{ox}) is converted by t_{1ox} which is given as:

$$t_{1ox} = \frac{\varepsilon_{si}}{\varepsilon_{ox}} t_{ox} \tag{2}$$

where ε_{si} is the relative permittivity of silicon and ε_{ox} is the relative permittivity of silicon dioxide. The boundary conditions for channel region are:

$$\varphi(0, y) = -\varphi_{bi} = -\frac{E_g}{2q} = \varphi_{AB} \tag{3}$$

$$\varphi(L_{ch}, y) = \varphi_{bi} + V_{ds} = \varphi_{CD} \tag{4}$$

$$\varphi(x, t_{si}) = 0 = \varphi_{BC} \tag{5}$$

The boundary conditions for gate oxide region are:

$$\varphi(x, -t_{1ox}) = V_{gs} - V_{fb} = \varphi_{FE} \tag{6}$$

$$\varphi(0, y) = \frac{\varphi_{AB} - \varphi_{FE}}{t_{1ox}} y + \varphi_{AB} = \varphi_{FA} \tag{7}$$

where V_{gs} is the gate voltage, V_{fb} is the flat band voltage, φ_{bi} is built in potential, q is the elementary charge and E_g is the band gap energy. The general solution of (1) is written as:

$$\varphi(x, y) = V(y) + u_L(x, y) + u_R(x, y) \tag{8}$$

where $u_L(x, y)$ and $u_R(x, y)$ are the solutions of (1).

$V(y)$ is the solution of one-dimensional Poisson's equation in y-direction as follows:

$$V(y) = -\frac{\varphi_s}{t_{si}}(y - t_{si}) \text{ in the channel region} \tag{9}$$

$$V(y) = \frac{\varphi_s - \varphi_{FE}}{t_{1ox}} y + \varphi_s \text{ in the gate oxide region} \tag{10}$$

where φ_s is the surface potential, which is given as:

$$\varphi_s = \frac{V_{gs} - V_{fb}}{1 + t_{1ox}/t_{si}} \tag{11}$$

By separation of variables, $u_L(x, y)$ and $u_R(x, y)$ can be rewritten as follows:

$$u_L(x, y) = \sum_{n=1}^{\infty} b_n^* \frac{\sinh\left(\frac{n\pi(L_{CH}-x)}{\beta}\right)}{\sinh\left(\frac{n\pi L_{CH}}{\beta}\right)} \sin\left(\frac{n\pi(y + t_{1ox})}{\beta}\right) \tag{12}$$

$$u_R(x, y) = \sum_{n=1}^{\infty} c_n^* \frac{\sinh\left(\frac{n\pi x}{\beta}\right)}{\sinh\left(\frac{n\pi L_{CH}}{\beta}\right)} \sin\left(\frac{n\pi(y + t_{1ox})}{\beta}\right) \tag{13}$$

where $\beta = t_{si} + t_{1ox}$.

The coefficient b_n^* and c_n^* values has been taken from [12]. Hence (8) can be rewritten as:

$$\varphi(x, y) = \left\{ -\frac{\varphi_s}{t_{si}}(y - t_{si}) + \sum_{n=1}^{\infty} b_n^* \frac{\sinh\left(\frac{n\pi(L_{CH}-x)}{\beta}\right)}{\sinh\left(\frac{n\pi L_{CH}}{\beta}\right)} \sin\left(\frac{n\pi(y + t_{1ox})}{\beta}\right) \right.$$

$$\left. + \sum_{n=1}^{\infty} c_n^* \frac{\sinh\left(\frac{n\pi x}{\beta}\right)}{\sinh\left(\frac{n\pi L_{CH}}{\beta}\right)} \sin\left(\frac{n\pi(y + t_{1ox})}{\beta}\right) \right\} \tag{14}$$

The total electric field (E) is given as:

$$E = \sqrt{E_x^2 + E_y^2} \tag{15}$$

where $E_x(x, y)$ is the lateral electric field calculated by $E_x(x, y) = -\partial\varphi(x, y)/\partial x$ and $E_y(x, y)$ is the vertical electric field calculated by $E_y(x, y) = -\partial\varphi(x, y)/\partial y$

4 Results and Discussion

The surface potential and electric field are calculated from 2D Poisson's analytical expression. The performance of derived analytical model has been verified and analyzed by TCAD 2D simulator. By changing the value of channel length (L_{CH}) and voltages (V_{gs} and V_{ds}), the surface potential and electric field graphs are plotted.

Figure 2a, b shows the plot of surface potential versus channel location with a channel length kept as 50 nm and 30 nm, respectively. The surface potential varies with different gate voltage V_{gs} (0–0.5 V) by keeping the drain voltage V_{ds} as a constant (0.1 V). When the channel length is 50 nm, the gate voltage is applied from initial 0 V, and the surface potential rises. By keep on increasing the gate voltage, the surface potential also increases, which is shown in Fig. 2a. By changing the channel length L_{CH} value as 30 nm, the surface potential linearly increased as compared to $L_{CH} = 50$ nm, which is shown in Fig. 2b. Thus the drain potential affects the entire channel region less in the long-channel TFETs than the short-channel TFETs.

Figure 3a, b shows the graph plotted as total electric field E and the channel
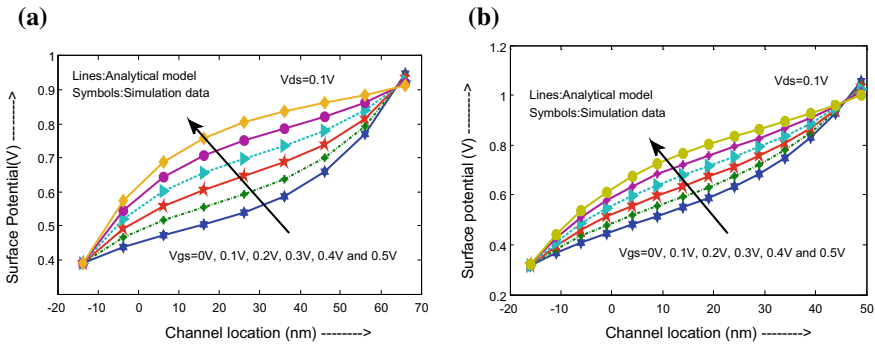
Fig. 2 Surface potential versus channel location for different V_{gs}. **a** $L_{CH} = 50$ nm **b** $L_{CH} = 30$ nm
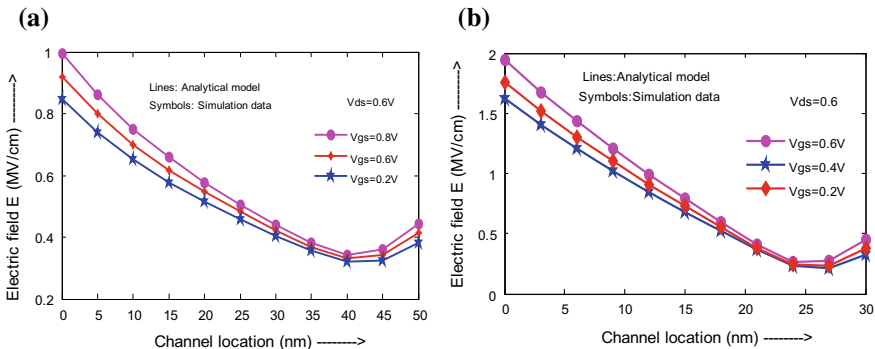
Fig. 3 Electric field versus channel location for different V_{gs}. **a** $L_{CH} = 50$ nm **b** $L_{CH} = 30$ nm

(a)

(b)
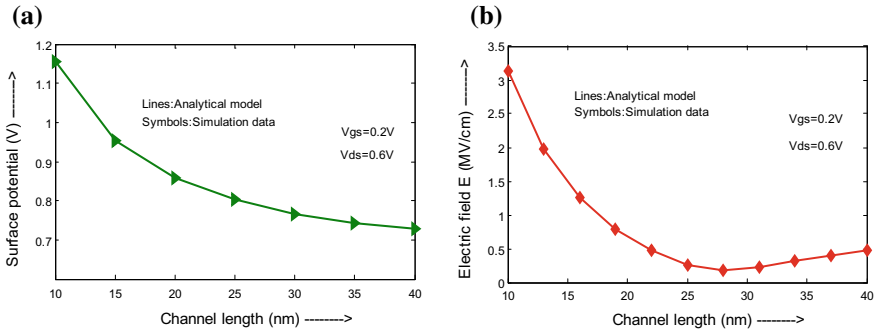
Fig. 4 **a** Surface potential versus channel length and **b** electric field versus channel length

location with channel length kept as 50 nm and 30 nm, respectively. Based on increment in the channel location, electric field E linearly decreases. After a particular point, the drain region along the electric field E values linearly increases for different L_{CH} values. This Fig. 3 also shows the variation in the V_{gs} along with total electric field E, and on increment of V_{gs} values (say 0.2, 0.4 and 0.6 V) the electric field E also increases. Thus the electric field in the whole-channel region of short-channel TFETs becomes higher than those of long-channel TFETs. Since the channel length is smaller, it causes the unwanted band to band tunneling through whole-channel region and off current will raise.

Figure 4a, b shows the plot of surface potential and total electric field versus channel length, respectively. Here t_{ox}, V_{gs}, V_{ds} are kept as constant value. When channel length is small, we have higher surface potential and higher electric field. Hence the surface potential and electric field both were linearly increased in the short-channel TFETs as compared to long-channel TFETs.

5 Conclusion

This paper presents an analytical model for the surface potential and electric field of SOI TFETs. The derivation is done by using 2D Poisson's expression along with suitable boundary conditions by applied superposition technique. The surface potential and electric field (E) varies with different parameters such as gate oxide thickness, by varying the channel length with different voltages (V_{gs}, V_{ds}) which are validated in TCAD 2D simulator. This potential-based analytical model can further develop for the parameters like the drain current, sub-threshold swing (SS) and threshold voltage of SOI TFET.

References

1. Nagavarapu V, Jhaveri R, Woo JCS (2008) The tunnel source (PNPN) n-MOSFET: a novel high performance transistor. IEEE Trans Electron Device 55(4):1013–1019
2. Choi WY, Park BG, Lee JD, Liu TJK (2007) Tunneling field-effect transistors (TFETs) with sub threshold swing (SS) less than 60 mV/dec. IEEE Electron Device Lett 28(8):743–745
3. Zhang Q, Zhao W, Seabaugh A (2006) Low subthreshold-swing tunnel transistors. IEEE Electron Device Lett 27(4):297–300
4. Vimala P, Balamurugan NB (2013) Modelling the centroid and charge density in double-gate MOSFETs including quantum effects. Int J Electron 100(9):1283–1295
5. Vimala P, Balamurugan NB (2014) A new analytical model for nanoscale trigate SOI MOSFETs including quantum effects. IEEE J Electron Devices Soc 2(1):1–7
6. Choi WY, Song JY, Lee JD, Park YJ, Park BG (2005) 100 nm n-/p-channel I-MOS using a novel self-aligned structure. IEEE Electron Device Lett 26(4):261–263
7. Kam H, Lee DT, Howe RT, King TJ (2005) A new nano-electromechanical field effect transistor (NEMFET) design for low-power electronics. In: IEEE international electron device meeting 2005 IEDM Technical Digest, pp 463–466
8. Abele N, Fritschi N, Boucart K, Casset F, Ancey P, Ionescu AM (2005) Suspended-gate MOS-FET: bringing new MEMS functionality into solid-state MOS transistor. In: IEEE international electron device meeting 2005 IEDM Technical Digest, pp 1075–1077
9. Kumar S, Goel E, Singh K, Singh B, Singh PK, Baral K, Jit S (2017) 2-D Analytical modeling of the electrical characteristics of dual-material double-Gate TFETs With a SiO2/HfO2 stacked gate-oxide structure. IEEE Trans Electron Device Publ 64
10. Wang P-F, Hilsenbeck K, Nirschl T, Oswald M, Stepper C, Weiss M, Schmitt-Landsiedel D, Hansch W (2004) Complementary tunneling transistor for low power applications. Solid State Electron 48(12):2281–2286
11. Choi WY, Song JY, Lee JD, Park YJ, Park BG (2005) 70-nm impact-ionization metal–oxide–semiconductor (I-MOS) devices integrated with tunneling field-effect transistors (TFETs) In: IEEE international electron device meeting 2005 IEDM Technical Digest, pp 975–978
12. Lee MJ, Choi WY (2011) Analytical model of single-gate silicon on insulator (SOI) tunneling field effect transistors (TFETs). Solid State Electron 63(1):110–114

Efficient Web Object Caching Through Query Correlation Approach

T. S. Bhagavath Singh and S. Chitra

Abstract Web object search engines are a new breed of Web Information Retrieval systems, wherein, the focus is to provide relevant results, such that, the result set has a limited influx of unnecessary information. To achieve this said goal, the document information is extracted and reorganized in the Web object repository, wherein, Web objects are logical entities such as cities, authors and stadiums. Caching has become an integral part of modern Web search engines. Many efficient caching schemes have been proposed for this domain. However, the same attention is lacking for Web object search engines. The contemporary solution in the literature is quite primitive and lacks the required effectiveness. In this work, a new caching mechanism based on query clustering is presented. The proposed caching mechanism is evaluated empirically along with the contemporary technique. Empirical results exhibit superior performance of the proposed scheme in terms of cache hit ratio and query execution time.

Keywords Web object search · Caching · Query clustering

1 Introduction

Overview

Modern Web search engines focus on retrieving the relevant Web documents for the user query. However, the Web documents might contain numerous Web object information, and the user might require information for only a single or few Web objects. In such situation, the user has to browse manually to search for the specific object information in the retrieved Web documents, which can decrease the overall

T. S. Bhagavath Singh
Department of CSE, Anna University, Chennai, India
e-mail: rnsit.tpo@gmail.com

S. Chitra (✉)
Er. Perumal Manimekalai College of Engineering, Hosur, India
e-mail: schitra3@gmail.com

effectiveness of the Web search engine. To circumvent this issue, a new breed of IR systems called Web object search engines has been proposed. Here, the required objects are first identified, the relevant information for the corresponding objects are extracted from different Web documents and stored in object repository. The object information is structured in terms of tuples and attributes.

Overview on IR Caching

Generally, Caching refers to storage of query accessed objects—which have high potential to be retrieved large number of times by the future queries—inside fast access storage system. This strategy aids in quicker response time for query execution. If the desired result for a query is not found in the cache, the corresponding data repository is accessed, and this situation is denoted as Cache Miss. The ideal caching strategy must minimize cache miss ratio.

Reserving component have become a significant part of numerous contemporary IR framework [1–4], in order to improve their reaction time. Most of these caching mechanisms store queries which are submitted with high frequency and their corresponding result set.

Contributions

In this work, the following contributions are made:

1. A new distributed Web object caching mechanism is proposed; wherein, queries which have high potential to be submitted in future and their corresponding result set are stored in query cache. The cache queries are selected through the aid of a scoring function. These selected queries are grouped based on their similarity w.r.t result sets. The queries in each group are likely to have good number of overlapping results. This grouping is achieved through correlation coefficient function. Each group is again scored w.r.t the number of high potential queries present in it. The highest ranked groups are selected to be placed in the cache storage.
2. The proposed caching mechanism is implemented in a custom-built Web object search engine. The object repository is created by using real-world Wikipedia data set. The empirical results demonstrate orders of magnitude improvement in query response time and superior cache hit ratio when compared with the contemporary caching technique [5].

2 Query Correlation Oriented Web Object Caching Technique

Architecture

The architecture of the proposed Web object search engine is illustrated in Fig. 1.

The query processing component is responsible for performing pre-processing on the user query and to identify the different object data sources, which can provide
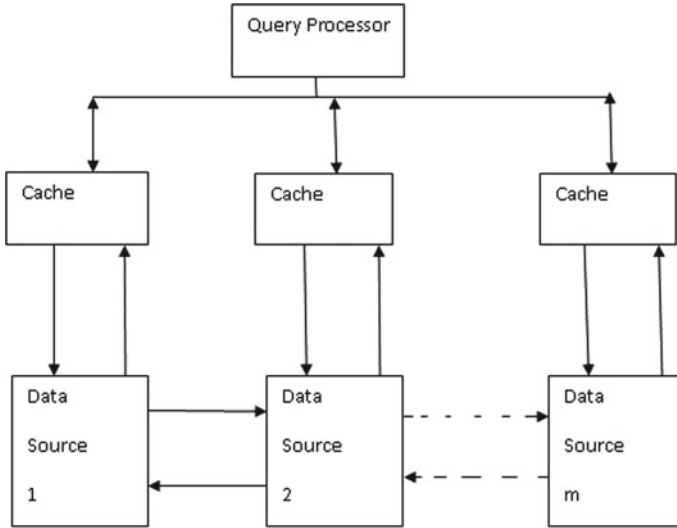
Fig. 1 Web object search engine architecture

the required results. Distributed architecture is utilized for achieving the required scalability in Big Data environments. Each object data source also contains a cache storage system.

Since the result set of many queries might contain Web objects which belong to different object data sources, and due to the availability of excellent bandwidth facility in today's systems, it is assumed that the cache corresponding to a specific object data source can store Web objects which might belong to other object data sources.

The Web object search engine is composed of m object data sources indicated by $D_1, D_2, \ldots, D_m$. The cache system for the $D_i (1 \leq i \leq m)$ object data source is indicated by C_i. The storage capacity of C_i is indicated by $size(C_i)$. The cache capacity of the entire Web object search engine is indicated by $size(C)$, where C indicates the cache for the entire Web object search engine which includes all the individual caches of different Web object data sources, and $size(C)$ is represented in Eq. (1).

$$size(C) = \sum_{t=1}^{m} size(C_i) \tag{1}$$

Query Score Function

In this section, scoring function to decide the potential of a query to be submitted in future is presented. Let, there be k queries present in the query log, and these queries are indicated by $Q_1, Q_2, \ldots, Q_k$. The queries which are present in the query log for a defined time interval T are selected, in order to obtain the recent submitted query statistics. The score for the query $Q_j (1 \leq j \leq k)$ is represented in Eq. (2). Here,

$score(Q_j)$ indicates the score of Q_j, larger score indicates higher potential of Q_j being submitted in the future, $freq(Q_j)$ indicates the frequency Q_j in the extracted section of the query log and hot $time(Q_j)$ indicates the difference between T and the last time Q_j has appeared in the query log.

$$score(Q_j) = \frac{freq(Q_j)}{hot\_time(Q_j)} \tag{2}$$

Consider a query group G_b which contains $Q_{|G_b|}$ number of queries indicated by $Q_1, Q_2, \ldots Q_{|G_b|}$. The score for this group is represented in Eq. (3). Here, group $score(G_b)$ indicates the group score of G_b, and higher group score indicates that this group contains queries which have high potential to be submitted in future.

$$group\_score(G_b) = \sum_{j=1}^{|G_b|} score(Q_j \in G_b) \tag{3}$$

Query Feature Vector

In this section, the feature vector required for detecting query correlation is presented. Let, n Web objects be present in the object repository, which includes all the individual object data sources. These Web objects are identified as $O_1, O_2, \ldots, O_n$. The query feature vector for Q_j is represented in Eq. (4). Here, V_j indicates the query feature vector for Q_j and $v(O_i)(1 \leq i \leq n)$ is represented in Eq. (5).

$$V_j = \begin{bmatrix} v(O_1) \\ v(O_1) \\ \vdots \\ v(O_n) \end{bmatrix} \tag{4}$$

$$V(O_i) == \begin{cases} 1, & \text{if } O_i \text{belongs to the result set of } Q_j \\ 0, & \text{Otherwise} \end{cases} \tag{5}$$

The group feature vector represents a query group. The group feature vector of G_b is represented in Eq. (6). Here, it represents the logical or operator, wherein the components in a specific position for two vectors are subjected to the logical or operation, $group\_vector(G_b)$ indicates the group feature vector of G_b and $V_1, V_2, \ldots, V_{|G_b|}$ indicate the query feature vectors of all the queries $Q_1, Q_2, \ldots, Q_{|Gb|}$, which $\in G_b$.

$$group\_vector(G_b) = V_1||V_2||\ldots||V_{||G_b||} = \begin{bmatrix} V_G(O_1) \\ V_G(O_2) \\ \vdots \\ V_G(O_n) \end{bmatrix} \tag{6}$$

The size of $size(G_b)$ is represented in Eq. (7). Here, $size(O_i)(1 \leq i \leq n)$ indicates the size of Web object O_i and $size(G_b)$ indicates the size of G_b. The Eq. (7) indicates that if any Web object O_i is part of the result set of many queries that $\in G_b$, then only a single copy of O_i will be considered inside the group G_b.

$$size(G_b) = \sum_{t=1}^{n} v_G(O_i) \times size(O_i) \tag{7}$$

Query Correlation Function

In this section, the correlation function to detect similarity or distance between queries is presented. The correlation function for the queries Q_i and Q_j, where, $i \neq j$ is represented in Eq. (8). Here, $corr(V_i, V_j)$ indicates the function value, $var(V_i)$ and $var(V_j)$ indicate the variance of the values present in V_i and V_j, respectively, and they are represented in Eqs. (9) and (10), respectively. Here, V_i and V_j indicate the sample mean of V_i and V_j, respectively, and which are represented in Eqs. 11 and 12, respectively. The function $covar(V_i, V_j)$ indicates the covariance of the values present in V_i and V_j, and it is represented in Eq. (13).

$$corr(V_j, V_j) = \frac{covar(V_i, V_j)}{\sqrt{var(V_i)var(V_j)}} \tag{8}$$

$$var(V_i) = \frac{1}{n-1} \sum_{r=1}^{n} (v(O_r) - \overline{v_i})^2 \tag{9}$$

$$var(V_j) = \frac{1}{n-1} \sum_{r=1}^{n} \left(v(O_r) - \overline{v_j}\right)^2 \tag{10}$$

$$\overline{V_i} = \frac{\sum_{r=1}^{n} v(O_r)}{n} \tag{11}$$

$$\overline{V_j} = \frac{\sum_{r=1}^{n} v(O_r)}{n} \tag{12}$$

$$covar(V_i, V_j) = \frac{1}{n-1} \sum_{r=1}^{n} (v(O_r) - \overline{v_i}) \left(v(O_r) - \overline{v_j}\right) \tag{13}$$

The distance between 2 queries Q_i and Q_j is calculated through the distance metric represented in Eq. 14. If the value of $corr(V_i, V_j)$ is high, it indicates that there is significant overlapping in the corresponding result sets of Q_i and Q_j. Equation 14 ensures that the query pairs which have significant overlapping in their result sets are considered closer to each other in distance.

$$distance(V_i, V_j) = \frac{1}{corr(v_i, v_j)} \qquad (14)$$

Algorithm

The proposed Web object caching technique is outlined in Algorithm 1. The technique involves two stages. In the first stage, cohesive query clusters are created so that intra cluster queries have significant result set overlapping in order to maximize space efficiency inside cache; p clusters are created for the k query feature vectors by using $Cluster\_Create(V_1, V_2, \ldots, V_k)$. The functioning mechanism of refine $cluster(cluster_p)$ is as follows: initially, p clusters are created randomly, and each cluster is associated with a centroid, which is calculated by using the corresponding query feature vectors. For each query, the distance between the query and other cluster centroids is calculated by using the distance metric represented in Eq. 14. If the centroids of other clusters are nearer to the query compared to the existing centroid, then the query is migrated to the nearest centroid represented cluster. The new cluster centroids for all p clusters are recalculated. The query cluster reorganization process is again repeated multiple times until cohesive clusters are formed.

The second stage is responsible for storing the selected queries and their corresponding result set inside the cache. The queries that are stored in the cache will only store a single copy of the non-unique result set Web objects in order to maximize space efficiency.

3   Results and Discussions

Experimental Setup

To perform empirical analysis on the proposed caching system, custom-built Web object search engine is utilized, because the available Web object search engines cannot be accessed in open source format. The Wikipedia data set is utilized for building the object repository. The size of the data set is around 50 GB. The number of test samples performed on the cache queries were around 100.

Web objects were created using the Wikipedia data set. The cache size was varied between 1 and 5 GB. The queries used for executing caching mechanism are termed as cache queries. The subset of cache queries is stored in the cache. The queries which are used for analyzing the performance of caching mechanism are termed as test queries.

Totally, 10 users were asked to submit their queries on the custom-built Web object search engine. The queries submitted by the users over a period of 3–5 days were collected and used as cache queries. After executing the caching mechanism, the users were asked to again submit queries, which were used as test queries.

The number of cache queries varied between 500 and 1000. The number of test queries was around 100. The metric cache hit ratio is the portion of test queries which are located in the cache. The metric average execution time refers to the average time
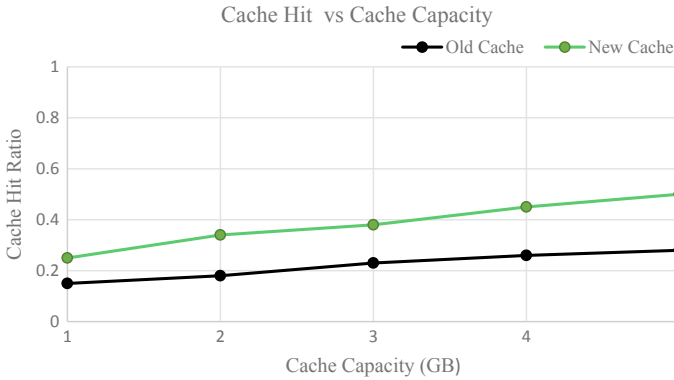
Fig. 2 Cache hit versus cache capacity

taken to execute all the test queries. The number of query groups used to perform caching is varied from $p = 5$ to $p = 15$.

The proposed caching mechanism is termed as new-cache for the ease of reference. This proposed caching mechanism is compared with contemporary technique [5], which is termed as old-cache. The old-cache does not perform query caching, but it performs Web object caching. So, a test query is considered to be located in the cache, only if the entire result set of the query is found in the cache.

Empirical Result Discussions

The first experiment analyzes the performance of old-cache and new-cache when the cache capacity is varied. The result w.r.t cache hit ratio is illustrated in Fig. 2. The increase in cache capacity provides an opportunity to store more queries and their corresponding result set in the cache, which results in better cache hit ratio. Since old-cache only stores the Web objects, and due to its primitive design, new-cache outperforms old-cache. The result w.r.t average execution time is illustrated in Fig. 3. Due to superior cache hit ratio of new-cache, the average execution time also improves.

The second experiment analyzes the performance of old-cache and new-cache when the number of cache queries is varied. The result with respect to cache hit ratio is illustrated in Fig. 4. As the number of cache queries increases, the query distribution information becomes more precise, which in turn helps in identifying queries which have high potential to be submitted in future. Hence, cache hit ratio improves with the increase in number of cache queries. The result with respect to average execution time is illustrated in Fig. 5. The new-cache outperforms old-cache for the same reasons explained before.

The third experiment analyzes the performance of new-cache when the parameter p is varied. The old-cache is ignored in this experiment, because the parameter p has no influence on it. The result with respect to cache hit ratio is illustrated in Fig. 6. Large values of parameter p indicates that more number of query groups, which
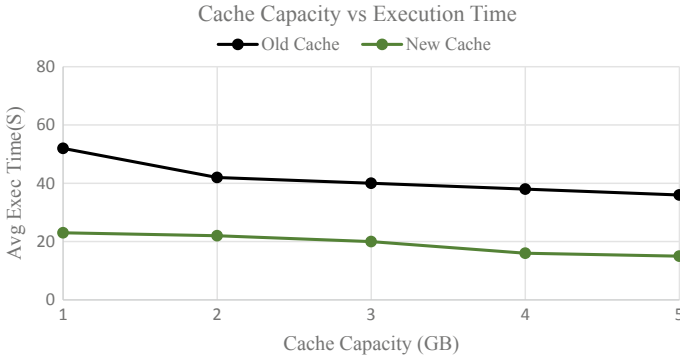
Fig. 3 Cache capacity versus exe time
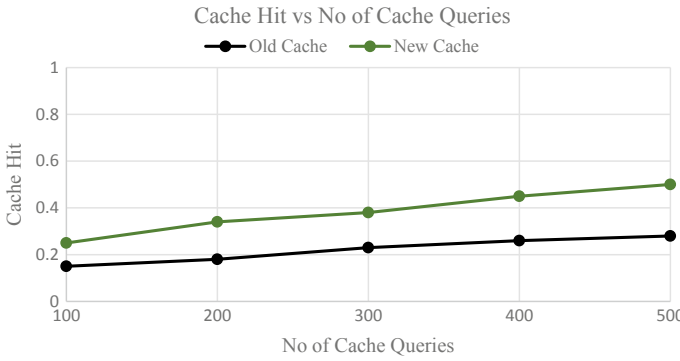
Fig. 4 Cache hit versus no of cache queries

Fig. 5 No of cache queries
versus exe time
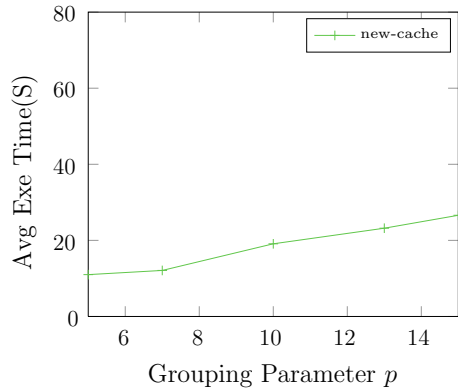
Fig. 6 Cache hit versus *p*
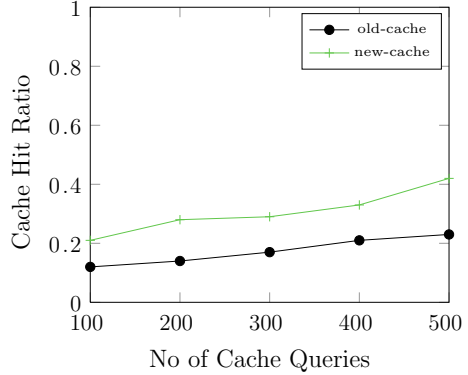
Fig. 7 *p* versus exe time
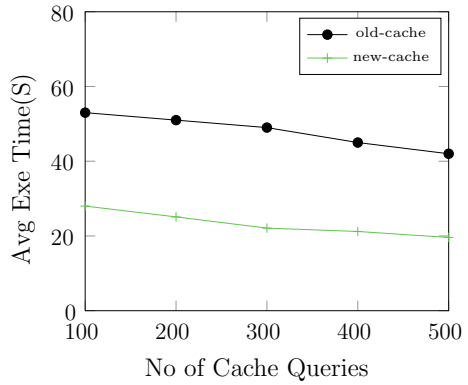
exhibit high intra query and low inter query cohesiveness, are created. Lower values of p indicate that small number of groups, which have good intra query cohesiveness, are created. For higher values of p, more number of query groups get opportunity to be considered for being stored in the cache. Since inter group cohesiveness is limited, only few queries get an opportunity to be stored in the cache because of minimal overlapping between the result sets of inter group queries. Hence, the cache hit ratio reduces. The result with respect to average execution time is presented in Fig. 7.

4   Conclusion

In this work, the importance of caching in Web object search engines was described. The limitations of the contemporary caching technique [5] were highlighted. A new caching mechanism based on query correlation approach was presented. This proposed caching technique achieves dual goal of storing queries which have high potential in being submitted in future, and more number of queries which have significant

Algorithm 1 Web Object Caching Technique

[Stage 1: Query Clustering]
$cluster_p = Cluster\_Create(V_1, V_2, \ldots, V_k)$
$refine\_cluster(cluster_p)$
[Stage 2: Cache storage]
$[G_1^s, G_2^s, \ldots G_p^s] = sort\_group\_clec\_score(G_1, G_2, \ldots, G_p)$
$calculate\_group\_size(G_1^s, G_2^s, \ldots G_p^s)$
[Case 1]
if $size(G_1^s) > size(C)$ **then**
  $pivot(G_1^s) = sort\_query\_inc\_score(G_1^s)$
  while $size(G_1^s) > size(C)$ **do**
    $extract\_query(pivot((G_1^s)))$
    $pivot\_increment(pivot(G_1^s))$
  end while
  $store\_cache(G_1^s)$
end if
[Case 2]
if $size(G_1^s) < size(C)$ **then**
  $L_G = create\_empty\_list()$
  $group\_pivot = create\_group\_pivot([G_1^s, G_2^s, \ldots G_p^s])$
  while $size(L_G) < size(C)$ **do**
    $add\_list(L_G, group\_pivot)$
    $pivot\_incrernent(group\_pivot)$
  end while
  $G_t = select\_group(L_G, last)$
  $pivot(G_t) = sort\_queries\_inc\_score(G_t)$
  while $size(L_G) > size(C)$ **do**
    $extract\_query(pivot(G_t))$
    $pivot\_incrernent(G_t)$
  end while
  $store\_cache(L_G)$
end if
[Case 3]
if $size(G_1^s) = size(C)$ **then**
  $store\_cache(G_1^s)$
end if

overlapped result set are selected for storing in cache. The empirical results demonstrate the improved effectiveness of the proposed technique over the contemporary technique [5] w.r.t cache hit ratio and execution time.

In future, dimensionality reduction techniques need to be explored for their effectiveness in designing Web object caching mechanism. The contemporary technique [5] has a different caching approach than the proposed caching mechanism, wherein, instead of queries and their result set, the Web objects are stored in the cache. New mechanisms which can improve the results for this caching approach also need to be explored.

References

1. Lu Z, McKinley KS (2000) Partial collection replication versus caching for information retrieval system. In: Proceedings of 23rd annual international ACM SIGIR conference on research and development in information retrieval
2. Zhang W, He H, Ye J (2013) A two-level cache for distributed information retrieval in search engines. Sci World J
3. Anand A, Peng XH, Haywood R (2009) Efficient information retrieval via proxy caching mechanisms within a lossy environment. In: International conference for internet technology and secured transactions
4. Lee R, Goshima K, Kambayashi Y, Takakura H (2017) Caching scheme for mobile web information retrieval. Technical report
5. http://techniet.microsoft.com/en-us/library/cc995252.aspx

Speech Corpus Development for Voice-Controlled MAV

D. K. Rahul, S. Veena, H. Lokesha, and P. Lakshmi

Abstract The main idea of this paper is to bring out the uniqueness of the speech corpus required for development of command and control applications such as voice-controlled MAV. Since MAV finds application in adverse environments, the effect of noise degrades ASR performance. Since English words uttered are greatly influenced by user's mother tongue, there is a necessity to create a customized speech corpus. The corpus creation is accomplished by a NALVoiceCorpus tool, which is designed to capture the specific requirements of the corpus. The tool is quite generic in nature and it can find application in development of any ASR system.

Keywords Acoustic model · Language model · Speech corpus for MAV · HMM training · Voice-controlled mission planner GCS

1   Introduction

The micro air vehicles (MAVs) can be deployed for numerous applications, spanning both civilian and military roles. MAVs are remote controlled using a portable ground control station (GCS) or radio controlled (RC). To fly MAV using RC requires skill in handling the controls on RC to realize a perfect flight. Even though GCS offers auto mode, configuring this mode requires knowledge about flight operations. GCS features multiple menu pages accessed by keyboard and/or mouse button presses, which are very tedious and time-consuming [1]. But to realize successful MAV applications, untrained personnel should also be able to fly and control the MAV operations. Voice commanding can be a convenient mechanism in such a scenario [2].

The heart of any voice-commanding system is an automatic speech recognition (ASR) block which recognizes the commands textually. ASR is basically a pattern recognition problem which requires large amount of voice/speech data for training. The database used for training is referred to as corpus and contains speech audio

---

D. K. Rahul · S. Veena (✉) · H. Lokesha · P. Lakshmi
CSIR National Aerospace Laboratories, 560017 Bengaluru, India
e-mail: veenas@nal.res.in

files and its text transcriptions. Even though there are plenty of corpora available for general-purpose speech applications, in the case of MAV there is unavailability of any such standard corpus and it is very much essential to build a good corpus to achieve accurate speech recognition. Further, the existing speech corpora are unable to cater for Indian accents [3].

This paper proposes a scheme to effectively capture the relevant speech data in a corpus through a developed tool named NALVoiceCorpus tool.

2 Speech Corpus for ASR Application

In an ASR, the feature extraction is done for the command uttered and these features are used to arrive at the best matching speech text corresponding to the uttered speech based on the three models, namely the acoustic model, language model and the lexicon/pronunciation model (see Fig. 1).

An acoustic model is used in ASR to represent the relationship between an audio signal and the phonemes or other linguistic units that make up speech. The model is learned from a set of audio recordings and their corresponding transcripts. Pronunciation model defines the probability of the phone states given the words. A statistical language model describes the probability distribution over sequences of words. All these models are developed based on the speech corpus.

In general the speech corpora can be broadly classified as the read speech, which includes book excerpts, broadcast news, lists of words and sequences of numbers, and the spontaneous speech, which includes dialogs, narratives, map tasks and appointment tasks. Further, they are classified as native (English) and non-native speech

Fig. 1 Block diagram of ASR
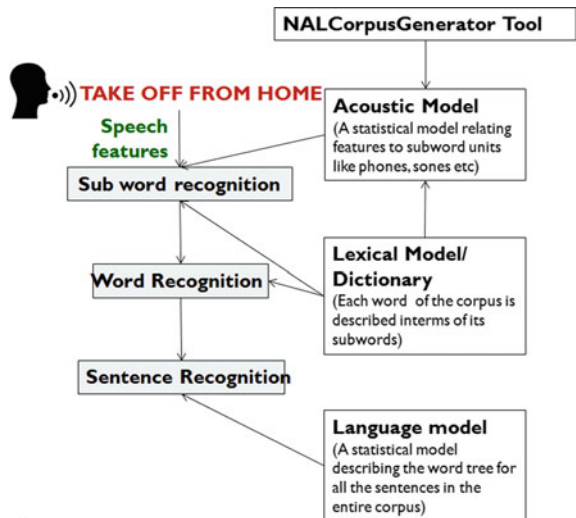
databases that contain speech with foreign accent. The Google [4] and Apple [5] clouds have very rich corpus, however, they are of not much use to the application under consideration as they heavily depend on the availability of data network. Since MAVs operate in remote areas the availability of network cannot be ensured.

There are special speech corpora for command and control applications which fall under the category [6] of key word spotting (KWS) that is capable of identifying specific words or phrases from a list of items in the language being spoken. Reference [6] also emphasizes the need to create an ASR technology capable of accurately determining speech activity regions, detecting key words, identifying language and speaker in highly degraded, weak and/or noisy communication channels. To meet such requirements there is a necessity to have an application-specific speech corpus. Under this category, the ATCOSIM, air traffic control simulation speech corpus is a speech database of air traffic control (ATC) operator speech. It consists of speech data, which were recorded during ATC real-time simulations and the utterances are in English language and pronounced by ten non-native speakers [7]. Some works in the field of voice-controlled UAVs are available [8], but information about the speech corpus used is not available. Hence, there is a necessity to develop a MAV-specific speech corpus.

Even though speech corpus collection is only a procedure, it decides the quality and efficiency of the ASR system. Therefore, the production procedure of speech corpus should be standardized [9].

3   Corpus Design for Voice-Controlled MAV

The MAV speech corpus development is done around mission planner [10], which is an open source ground control station for MAVs. However, the corpus generated can be used for any MAV GCS.

A brief explanation regarding the functionality of GCS leading to command identification is given in this section. In an MAV operation, the first step is the establishment of connection between the MAV and GCS. Once the connection is established, the next task is to plan the course of MAV flight. This is done using the FLIGHT PLAN window. Another important window is FLIGHT DATA, which gives all the information related to the current flight/mission (see Fig. 2). These screens are accessed continuously during MAV flight and hence are considered for voice activation. Further, the MAV mission from takeoff to landing can be activated through speech. Table 1 lists command candidates to be replaced by speech commands. This list is not exhaustive and commands can be added based on the user requirement.

Fig. 2 GUI of flight data in mission planner

4 NALVoiceCorpus Tool

The "NALVoiceCorpus" tool is developed in C# to generate the MAV-specific corpus in a systematic way such that it can be accessed directly by acoustic and language modeling tools such as HTK toolkit and CMUSphinx. The front end of the application (see Fig. 3) collects the speaker information and creates the file path as per the predefined directory structure. The tool records speech at 16 bit, 16000 Hz. The commands in Table 1 is saved to a text file and loaded into the workspace. These command sentences appear one by one in the box and the user has to utter the same. To precisely capture only the speech part, the tool incorporates a voice activity detector (VAD). Once the VAD is done, a green tick mark appears and the next sentence to be uttered is displayed. The captured speech waveform is stored as a wave file (wav).

In an ASR, the accuracy of the models can be improved by training the models with data collected from realistic environments [11]; however, collection of corpus in realistic environments may not be feasible. To address this, the tool simulates realistic environments, such as traffic, wind, forest and battle field, while recording the corpus speech. This feature is activated by selecting field option (see Fig. 3).

Further, ASR performance gets affected by user mood such as anxiety, haste and fatigue [12]. While flying an MAV, the user is bound to get anxious and may issue some commands in haste to take control of the situation. The tool has a facility to simulate a MAV flight-like scenario while uttering voice commands. This is accomplished by integrating mission planner [10] to flight gear [13] simulator. This option can be invoked by clicking mission option of the tool.

Table 1 List of voice commands

Operation	Voice command	Action
Initiation	Get ready	MAV connects to GCS HUD displays MAV status
Mission commands	Take off	Arms and takes off
	Move up/Go up/come down by $number meter/feet/foot	Change in the altitude
	Slow down/Go faster	Change in speed
	Go forward/backward	Moves forward/backward
	Go/turn left/right	Turns left/right
	Loiter	Circles around current location
	Stop/I say stop/Stop there	MAV stationary/hovers
	Come down/come down by $number meters	Slowly comes down
	Land	Landing
Display	Show map	Displays map
	Zoom in/zoom out	Enlarges/condenses the map
	Unable to find you	Sets panning area
Requests	Battery level	Displays battery status
	Altitude	Displays altitude information
	Where you are	Displays location information
Menu commands	Flight data	Displays "FLIGHT DATA"
	Flight plan	Displays "FLIGHT PLAN"
	Actions	Displays issued mission commands

Fig. 3 Front end of GUI of the NALVoiceCorpus tool
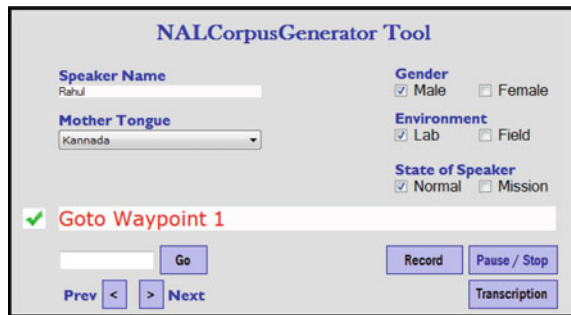
Table 2 ASR performance comparison

Commands uttered	Recognition accuracy	
	CMU Sphinx model	NALVoiceCorpus model (%)
Actions	95%	92
Flight data	90%	93
Flight plan	80%	95
Takeoff	0	100
Goto Waypoint One	0	90

5 NALVoiceCorpus Evaluation

The NALVoiceCorpus was evaluated by collecting speech from 25 users with varying accents for commands given in Table 1. The acoustic model and language model were created using CMUSphinx tool box.

The ASR capability of these models was compared with Indian English model available in CMUSphinx for some of the commands. The models developed with NALVoiceCorpus give superior performance compared to existing model (Table 2) as the training data is MAV-specific. From the table it is observed that "Takeoff" and "Goto Waypoint One" are not recognized as language model based on standard English treats takeoff as two separate words and the word waypoint are not present in standard dictionary.

6 Conclusion

This paper proposed the development of dedicated speech corpus for voice control of MAV. The specific command list was formulated based on the functionality of MAV ground control station. Further, a tool named NALVoiceCorpus, specifically developed for corpus collection, was used for corpus generation and models were created using this corpus. The ASR performance was found to be superior compared to usage of general-purpose models. Even though the tool was developed for this application, it can be easily extended for any other application.

References

1. Kang Y, Yuan M (2009) Software design for mini-type ground control station of UAVICEMI'09. In: 9th International conference on electronic measurement and instruments IEEE
2. Draper M et al (2003) Manual versus speech input for unmanned aerial vehicle control station operations. In: Proceedings of the human factors and ergonomics society annual meeting, vol 47(1). CA: SAGE Publications, Sage CA: Los Angeles
3. Shrishrimal PP, Deshmukh RR, Waghmare VB (2012) Indian language speech database: a review. Int J Comput Appl 47(5):17–21
4. Google cloud speech-to-text documentation page. https://cloud.google.com/speech/docs/
5. Speech recognition in IOS. https://developer.apple.com/documentation/speech
6. Robust Automatic Transcription of Speech (RATS), for Information Processing Techniques Office (IPTO), Defense Advanced Research Projects Agency (DARPA), DARPA-BAA-10-34, (2012)
7. Hofbauer K, Petrik S, Hering H (2008) The ATCOSIM corpus of non-prompted clean air traffic control speech. In: LREC
8. Ayres Tony, Nolan Brian (2006) Voice activated command and control with speech recognition over WiFi. Sci Comput Program 59(1-2):109–126
9. Li A-J, Yin Z-G (2007) Standardization of speech corpus. Data Sci J 6:806–812
10. Mission planner overview, ardupilot.org/planner/docs/mission-planner-overview.html
11. Paliwal KK, Yao K (2010) Robust speech recognition under noisy ambient conditions. In: Human-centric interfaces for ambient intelligence, 135–162
12. Benzeghiba M et al (2007) Automatic speech recognition and speech variability: a review. Speech Commun 49(10–11):763–786
13. Flight gear simulator homepage, home.flightgear.org/

Single-Ended Low Power Robust 9T Static Random Access Memory Using FinFETs

Pavankumar R. Vijapur and B. V. Uma

Abstract Advancement in CMOS technology has made the Static Random Access Memory (SRAM) design to be very demanding. The designers face several challenges in improving the performance by improving read stability, write ability and leakage power. The design in the proposed design uses power gating strategy to lower leakage power. It is known that for 2 bit-line scheme of SRAM, some amount of power is wasted in the form of charging or discharging the bit-lines. The design in the proposed cell dissipates 67.7% less leakage power, 58.18% less writing power and 70.78% less reading power when compared to the double bit-line SRAM at 1 V of supply voltage. In addition to it, the design has good read stability, write ability and better read/write performance.

Keywords N-curve · Low leakage current · FinFETs · SRAM

1 Introduction

The performance of any system greatly depends on SRAM as it is the key contributor to the area in any system. In addition to it, the demand for mobile gadgets and also various applications such as wireless body sensing networks that is due to the tremendous growth in technology has led to the need for low power SRAM designs. Hence, the research in the area of SRAM towards developing the designs that are of high speed and low power has gained importance in recent years [1–3]. The designer will face many challenges while designing the low power SRAM as it is known that at deep sub-micrometer technology, the design margin and process variation makes it very difficult for subthreshold operation. The amount of leakage power in total

P. R. Vijapur (✉)
M. Tech VLSI Design and Embedded Systems, R.V. College of Engineering, 560059 Bengaluru, India
e-mail: pavan.vijapur2@gmail.com

B. V. Uma
Department of Electronics and Communication Engineering, R.V. College of Engineering, 560059 Bengaluru, India

power dissipation is also increasing with technology node [4], [5] and this leads to an enormous expansion in Read Static Noise Margin (RSNM) that might lead to increase in the read failure rate [4]. Fin Field Effect Transistors(FinFET) are the promising technology that can replace the conventional Metal-Oxide-Semiconductor Field Effect Transistors (MOSFET).

The read stability and write ability of 6T SRAM cell degrades with V_{dd} scaling and these degrade to undesired levels with very low supply voltage which has become quite common due to advancement in CMOS processes. Several designs have been already proposed to overcome the problems explained before. Some of them are 7T [6], 8T [7], 9T [8], 10T [9]. In all these proposed designs, the core of the cell is isolated from the read path so that the read-write disturbance that was faced by 6T SRAM cell can be eliminated. There are separate bit-lines for reading and writing and read path consist of two extra transistors and this makes 8T SRAM [7] structure which increases the (Static Noise Margin) SNM but will also increase leakage power due to the use of two transistors in read path and moreover this increase with V_{dd} scaling. A differential scheme that uses differential read and write was proposed in [8] wherein more number of transistors are attached to the bit-lines. Due to the increase in the number of connections to the bit-line, the parallel use of the SRAM bit-line is limited and this affects the array that is to be implemented using this structure. In [9], a new structure that uses 10T which is very suitable for bit interleaved architecture was designed. The buffers were used to decrease the leakage power but due to the use of two transistors in the write path, the write margin was decreased which reflected the difficulty in write operation.

Looking into above-specified constraints and solutions, we have proposed a new SRAM structure that consists of 9T and this will consume less power and also dissipate low leakage power. The proposed design is robust as it takes less time for both read and write operations when compared to other existing designs.

2   Proposed 9T SRAM Cell Design

The design of the proposed 9T SRAM design is shown in Fig. 1. There are two isolated bit-lines for read and write operations and these are termed as Read-bit-line (RBL) and Write-bit-line(WBL). The other control signals are write word-line (WWL), read word line (RWL) and SLEEP control signal. The SLEEP control signal is provided as a part of power gating strategy. Except for hold operation, for all the other operations, the circuit will be connected to full power supply and for the hold operation, it will be connected to half of the power supply. This will help to decrease the leakage power during the standby mode of operation.

Since the proposed design has single-end write, to facilitate the write operation, Virtual Ground (VGND) pin is provided. The condition of different control signals is shown in Table 1.
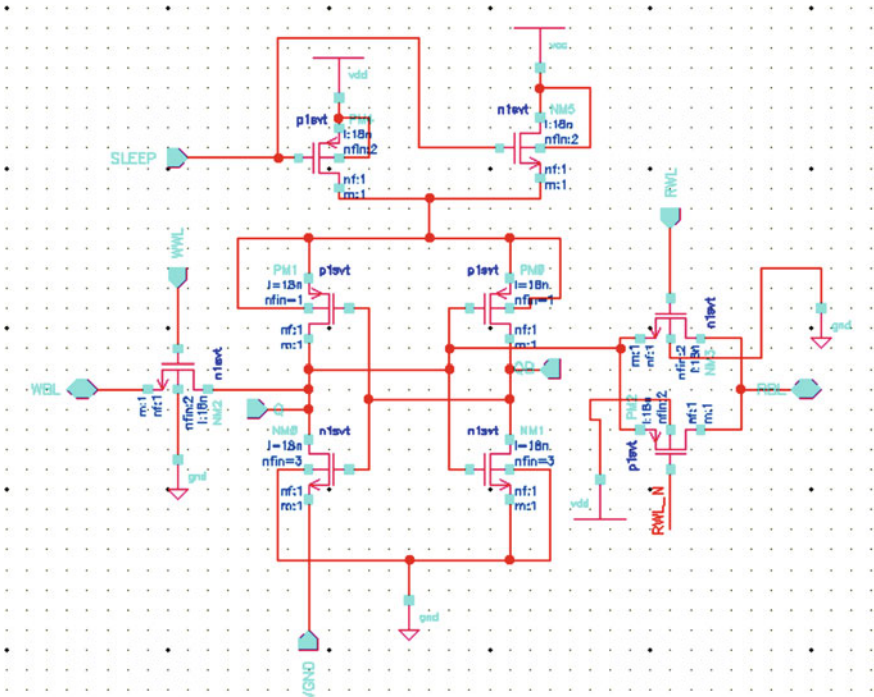
Fig. 1 Schematic of the proposed design

Table 1 Operation table of the proposed 9T SRAM cell

Signal	Hold	Read	Write
WBL	–	–	VDD/GND
WWL	GND	GND	VDD
RWL	GND	VDD	GND
VGND	GND	GND	FLOAT
SLEEP	VDD	GND	GND

3 Simulation Setup

The proposed cell is simulated for its functionality and different performance measures are calculated using Cadence Virtuoso tool. The technology used is FinFET based and is of 18 nm. The different parameters considered for comparison are read stability, write ability, read and write access time, read and write power and leakage power.

The stability of any SRAM design is decided by the Static Noise Margin (SNM). The noise margins must be measured to confirm that there is no destruction of data stored in the cell takes place. Static noise margin is usually measured with the help

of butterfly curve [10]. It is already shown that N-curve gives better information regarding stability [11].

- Read Stability and Write Ability: As explained earlier, the static power noise margin gives information regarding the read stability. More the SPNM more is the read stability. Write Trip Power (WTP) acts as a parameter to compare the write ability of different cells.
- Read and Write Access time: It is the time taken for the activation of the word-line responsible for the read operation to the change in the bit-line value to reach the stored bit value. The thresholds considered for this operation were 10% of the low voltage value to 90% of the high voltage value. Write access time '1' is described as the time required for writing, logical '1' is the time duration between the activation of the word-line responsible for the write operation to that of the time taken to change the output node 'Q' to '1'. Similarly, write access time '0' is described as the time required for writing, logical '0' is the time duration between the activation of the word-line that is responsible for the write operation to that of the time taken to change the output node 'Q' to '0'.
- Read/Write Power: The amount of power dissipated for successful write operation is known as write power and the amount of power dissipated doing a successful read operation is known as read power.
- Leakage power: The subthreshold leakage at deep sub-micrometer technology nodes in embedded cache is a very serious issue [12]. The major source for the leakage power is the cross coupled inverter which is the core of any SRAM cell that helps in storing the data of interest indefinitely given that the power supply is present. For the proposed design, the transistors are maintained to be of minimum size. Since the proposed design uses power gating strategy, the leakage power dissipation should be minimum.

4 Results

The simulation is done to validate the functionality of the proposed cell. The graphs of various simulation results are shown in the following figures. Figure 2 shows the simulation of write, hold and read operation in the proposed design. As shown in Fig. 2, all the operations can be performed successfully in the proposed design. Table 2 shows the comparison of physical features that are considered for comparison.

Table 3 shows the comparison of performance parameters between SRAM cells. If SVNM and SINM are considered that tells about the read stability, it can be observed that for SVNM the proposed design has the least value but for SINM it has the highest value. Thus, to overcome this confusion, SPNM can be considered and it can be observed that the proposed cell has the best read stability. For write ability, the WTV and WTI must be minimum and it can be observed that for WTV, the proposed cell has very high value and WTI is very less thus to actually determine the write ability, we need to consider the WTP and it can be seen that the proposed cell has
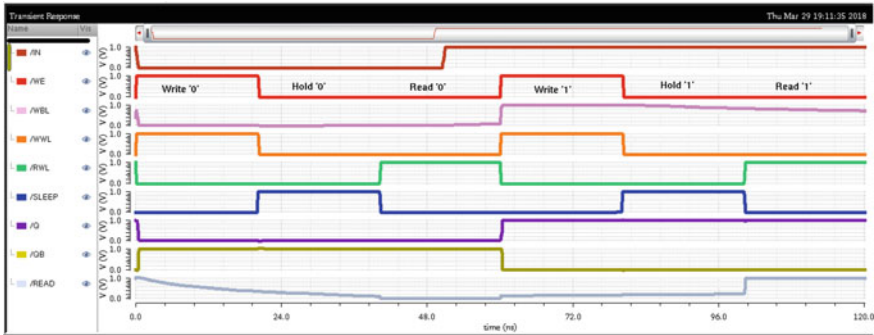
Fig. 2 Write, hold and read operation

the lowest value thus showing that the proposed cell has the best write ability. The read and write access time are comparable with the existing designs. For the read and write power although the proposed design doesn't consume the least power but will consume very less power compared to [9]. The leakage power is reduced to greater extent due to the use of the power gating strategy.

5 Conclusion

A robust single-ended low power 9T SRAM cell is designed and is tested for its operations. Further, the designed SRAM cell is correlated with the existing designs and it is observed that the proposed cell has good read stability and write ability. Due to the use of transmission gate in the read path, the read access time is reduced to a greater extent. Due to the use of power gating strategy, the leakage power is also reduced to a greater extent. If the proposed is compared with the dual bit-line scheme of SRAM that has same number of transistors, i.e. [9] then it can be said that the proposed cell dissipates 67.67% of less leakage power and consumes approximately 26%, 43.42% less power for reading and writing data '0'and 70.8%, 58.18% less power for reading and writing data '1'. The access time to read '0' is little high due to the use of single-ended scheme but it is compensated in the form of less power consumption for read and write operations.

Thus it can be said that the designed 9T single bit-line cell while maintaining the performance measures shows very low power consumption with less leakage power dissipation.

Table 2 Comparison of physical features of SRAM cell comparison

Cell feature	Conv. 6T	Ramy. 7T [6]	Fried. 8T [7]	Liu. 9T [8]	Wen. 8T [13]	Chang. 10T [9]	ST1 [14]	ST2 [15]	Prop novel 9T SRAM
Reading/ Write	Diff/Diff	SE/SE	SE/Diff	Diff./Diff	SE/SE	Diff/Diff	Diff/Diff	Diff/Diff	SE/SE
Bit-lines	2-BL	1-WBL 1-RBL	1-RBL 2- WBL	2-BL	1-WBL 1-RBL	2-BL	2-BL	2-BL	1-WBL 1-RBL
Control signals	1-WL	1-WL 1-W 1-R	1-WWL 1-RWL	1-WR 2-RD	1-WWL 1-WL 1-RWL	1-WWL 1-WL 1-VGND	1-WL	1-WL 1-WWL	1-WWL 1-RWL 1-VGND 1-SLEEP
No. of tran in read path	2	2	2	2	2	2	2	2	2

Diff—Differential, BL—Bit-line, SE—Single-Ended, WBL—Write BL, RBL—Read BL, WWL—Write BL, RBL—Read BL, VGND—Virtual Ground

Table 3 Performance parameter comparison of SRAM cells

Performance parameter	Conv. 6T	Ramy. 7T [6]	Fried. 8T [7]	Liu. 9T [8]	Wen. 8T [13]	Chang. 10T [9]	ST1 [14]	ST2 [15]	Prop novel 9T SRAM
SVNM	0.416 V	0.416 V	0.452 V	0.472 V	0.472 V	0.472 V	0.592 V	0.467 V	0.363 V
SINM	50.59 µA	42.5 µA	24.85 µA	26.85 µA	30.5 µA	26.84 µA	36.85 µA	31.35 µA	32.5 µA
SPNM	14.09 µW	11.924 µW	18.63 µW	18.6361 µW	20.76 µW	18.632 µW	25.55 µW	20.39 µW	27.26 µW
WTV	0.582 V	0.582 V	0.527 V	0.527 V	0.3042 V	0.5273 V	0.406 V	0.535 V	0.635 V
WTI	−19.1 µA	−19.08 µA	−18.24 µA	−18.242 µA	−30.06 µA	−18.24 µA	−18.2 µA	−18.2 µA	−15.46 µA
WTP	−8.342 µW	−8.34 µW	−13.2 µW	−13.43 µW	−22.47 µW	−13.43 µW	−12.75 µW	−13.52 µW	−7.31 µW
Read access time '0'	64.36 ps	6.37 ps	24.79 ps	9.85 ps	33.32 ps	12.72 ps	12.45 ps	6.9 ps	20.44 ps
Read access time '1'	71.88 ps	21.88 ps	30.23 ps	16.04 ps	26.3 ps	14.64 ps	14.64 ps	25.74 ps	15.35 ps
Write access time '0'	92.97 ps	100.3 ps	103 ps	138.7 ps	95.32 ps	113.3 ps	98.82 ps	111.3 ps	82.52 ps
Write access time '1'	92.47 ps	67.75 ps	94.26 ps	160.1 ps	112.3 ps	152.5 ps	116.4 ps	104 ps	119.5 ps
Read power '0'	72.54 nW	398 nW	131.1 nW	219.4 nW	142.4 nW	2930 nW	3869 nW	2464 nW	162.3 nW
Read power '1'	74.31 nW	244.1 nW	74.22 nW	218.8 nW	3025 nW	2930 nW	3369 nW	44.92 nW	63.84 nW
Write power '0'	107.3 nW	124.3 nW	125.4 nW	200.3 nW	194.8 nW	168.2 nW	158.6 nW	110.8 nW	110.2 nW
Write power '1'	2931 nW	160.4 nW	87.61 nW	214.2 nW	194 nW	151.9 nW	167.2 nW	85.69 nW	89.57 nW
Leakage power	13.37 µW	15.48 µW	14 µW	9.9 µW	50 µW	15.48 µW	18.22 µW	10.25 µW	3.26 µW

References

1. Yang S, Wang W, Vijaykrishnan N, Xie Y (2005) Low leakage robust SRAM cell design for sub-100 nm technologies. In: Proceedings of ASP-DAC, pp 539–544
2. Samandari-Rad J, Guthaus M, Hughey R (2014) Confronting the variability issues affecting the performance of next-generation SRAM design to optimize and predict the speed and yield. IEEE Acess 2:577–601
3. Tu MH, Lin JY, Tsai MC, Jou SJ, Chuang CT (2010) Single-ended subthreshold SRAM with asymmetrical write/read-assist. IEEE Trans Circuits Syst I Reg Papers 57(12):303–3047
4. Chiu YW et al. (2014) 40 nm bit-interleaving 12T subthreshold SRAM with data-aware write-assist. IEEE Trans Circuits Syst I Reg Papers 61(9):2578–2585
5. Islam A, Hasan M (2012) Leakage characterization of 10T SRAM cell. IEEE Trans Electron Devices 59(3):631–638
6. Aly RE, Bayoumi MA (2007) Low-power cache design using 7T SRAM cell. IEEE Trans Circuits Syst II Exp Breifs 54(4):318–322
7. Chang L et al (2005) Stable SRAM cell design for the 32 nm node and beyond. In: Proceedings of the symposium on VLSI technology, pp 128–129
8. Liu Z Kursun V (2008) Characterization of a novel nine-transistor SRAM cell. IEEE Trans Very Large Scale Integr (VLSI) Syst 16(4):488–492
9. Chang IJ, Kim JJ, Park SP, Roy K (2008) A 32 kb 10T subthreshold SRAM array with bit-interleaving and differential read scheme in 90 nm CMOS. In: Proceedings of IEEE International Solid State and Circuits Conference, Feb, pp 388–622
10. Seevinck Evert, List Frans J, Lohstroh Jan (1987) Static noise margin analysis of MOS SRAM cells. IEEE J Solid-State Circuits 22(5):748–754
11. Grossar Evelyn, Stucchi Michele, Maex Karen, Dehane Wim (2006) Read stability and write ability analysis of SRAM cells for nanometer technologies. IEEE J Solid State Circuits 41(11):2577–2588
12. Lindert N, Chang L, Choi YK, Anderson EH, Lee WC, King TJ, Bokor J, HuC (2001) Sub-60 nm quasi-planar FinFETs fabricated using a simplified process. IEEE Electron Device Lett 22(10):487–489
13. Wen L, Li Z, Li Y (2013) Single-ended, robust 8T SRAM cell for low-voltage operation. Microelectron J 44(8):718–728
14. Kulkarni JP, Kim K, Roy K (2007) A 160 m V Robust Schmitt trigger based sub threshold SRAM. IEEE J Solid-State Circuits 42(10)
15. Kulkarni JP, Roy K (2012) Ultralow-voltage process-variation-tolerant Schmitt-trigger-based SRAM design. IEEE Trans Very Large Scale Integr (VLSI) Syst 20(2):319–332

Halftone Visual Cryptography for Color Images Using Error Diffusion and Direct Binary Search

Sandhya Anne Thomas and Saylee Gharge

Abstract Visual cryptography is a cryptographic technique which enhances the security of the image and uses the characteristics of human vision to decrypt encrypted images. Halftone Visual Cryptography uses halftoning techniques for converting the color image into binary images. The problem of encoding color image into n shares of meaningful halftone images is considered in this paper. The halftone techniques used are Error Diffusion and Direct Binary Search. Using these techniques, a secret pixel of a color image can be encoded into shares. These two techniques are compared on the basis of Peak to Signal Noise ratio (PSNR), Correlation, Universal Quality Index (UQI) and Structural Similarity (SSIM).

Keywords Visual cryptography · Halftone · Error diffusion · Direct binary search · Extended visual cryptography

1 Introduction

With the rapid development and increased need of computer and communication technology, more secret information are transmitted through the Internet. Therefore, protecting the secret information from being suspected and decrypted has become critical task. In 1994, a new information security technique called Visual Cryptography (VC) [1] was invented. VC is a cryptographic scheme in which decrypting of hidden images is done using human eyes. No previous knowledge of cryptography or computation is required for decoding which is the advantage of using in this technique along with high security offered using this technique. Visual cryptography scheme (VCS) [2] is a scheme which allows the encryption of a secret image into

S. A. Thomas (✉) · S. Gharge
Department of Electronics and Communication Engineering, VESIT,
Chembur, Mumbai, MH, India
e-mail: sandhya.thomas@ves.ac.in

S. Gharge
e-mail: saylee.gharge@ves.ac.in

n shares that is given to *n* participants. These *n* participants are called the qualified shares. VC works on binary image only. Images are not only monochrome format but in grayscale and color. For converting a grayscale [3] and a color image to binary image, halftoning techniques are applied. Commonly used halftone techniques for color image encryption are Error diffusion and Direct Binary Search (DBS) which is implemented in this paper.

To explain the basic principle of VC, consider a (k, n) VC scheme which encrypts a secret image into *n* shares to be distributed among *n* participants. Each share shows a random noise pattern of black and white and doesn't disclose any information on the secret image by itself. In a (k, n) VCS, *k* is the minimum qualifying participants required to decode the secret image. Fewer participants that is *k-1* will be forbidden which will not decode the secret image even if infinite computational power is available. Qualifying share will be stacking/superimposed to decrypt the secret image. Researches have developed several methods for VC in literature. An optimal contrast *k, n* VCS was proposed to analyze the contrast of the reconstructed image for a (k, n)-threshold VCS [4]. Blundo [5] developed VCS with general structure for grayscale images. To generate a halftone share, Hou [6] transformed a gray level image into halftone images and then applied to VC. Extended visual cryptography (EVC) was developed by Ateniese [7] in which shares carry not only secret image information but meaningful images also. Meaningful images have a higher security rather than random noise shares. Hypergraphy color is used in constructing meaningful binary shares. Image quality was improved by Nakajima [8] by extended EVC with natural grayscale images. Halftone methods are used to generate good quality halftone shares in VC [9]. Meaningful Halftone image using threshold array was proposed in [10]. Meaningful images using error diffusion [11] was developed for producing halftone shares. Color Extended Visual Cryptography using error diffusion was developed by Inkoo [12] and Halftone visual cryptography using Direct Binary Search (DBS) [13].

In the above mentioned methods, the shares that are produced have low visibilities. The different types of halftoning methods are point process, neighborhood process and iterative process. Neighborhood processing (Error Diffusion) and iterative process (DBS) of halftoning are implemented and compared. Halftone is applied on both the secret images and cover images.

2   Methodolgy

Encryption In this paper, encryption for a (2, 2) VC scheme is done using EVC using halftoning techniques for color images. A secret image of size $m \times m$ is taken and halftone is applied. The methods implemented for halftoning are Error diffusion or DBS. In Error diffusion halftoning, the quantization error is distributed to the nearby pixels which are unprocessed. Also the Visual information pixels position is retained. Whereas, in DBS which is a iterative search, a binary image is taken and a template is saved. It is then processed depending on the given iterative value. Each time when

the process gets completed, error is calculated and the least error found is selected as a DBS halftoned share. Share images taken for producing meaningful share of size $n \times n$ has to be double in size in comparison with the secret image. Here also halftone techniques are applied in the same manner as explained above to get two meaningful halftone shares. Encrypted share 1 and share 2 is now generated which carries both secret information and meaningful images. Now the share is ready to be given to the as qualified shares to the participant.

Decryption The qualified participant on stacking/superimposing will recover the original secret image. The stacking/superimposing is executed using the $\otimes$ the 'OR' boolean function.

DBS uses the minimum perceived error obtained by searching for the best possible binary value in the halftone image iterations. This gives DBS much better halftone image quality than error diffusion. This is further verified using various parameters. The parameter metrics used for analyzing the encrypted shares with the original halftoned share are PSNR, Correlation UQI and SSIM. PSNR is a measure to find of quality of recovered images and actual image. Correlation extracts the information of a image, then the encrypted share is compared with the halftoned image. UQI [14] is the ability to measure the information loss occurred during the image degradation process and SSIM [15] measures the similarity between reconstructed images and original image. By considering more parametric measures, a better understanding of the quality of the desired image can be achieved.

3   Result and Discussion

In this section, a 2-out of-2 Halftone VC is constructed using error diffusion and DBS. The secret image to be encoded is *Lena*. Two color images *Earth* and *Baboon* are taken as meaningful images. The size of the share is 256×256 and the size of the secret image is 128×128.

In Fig. 1, Fig. 1a is the original secret image which has to be encoded. Figure 1c and d are original cover images. Figure 1b, d, f are halftoned images using error diffusion. Encrypted shares generated are shown in Fig. 1g and h. Figure 1i shows the reconstructed image when encrypted shares 1 and 2 are stacked together using OR operation.

In Fig. 2, Fig. 2a is the original secret image which has to be encoded. Figure 2c and d are original cover images. Figure 2b, d, f are halftoned image using DBS. Encrypted shares generated are shown in Fig. 2g and h. Figure 2i shows the reconstructed image when encrypted shares 1 and 2 are stacked.
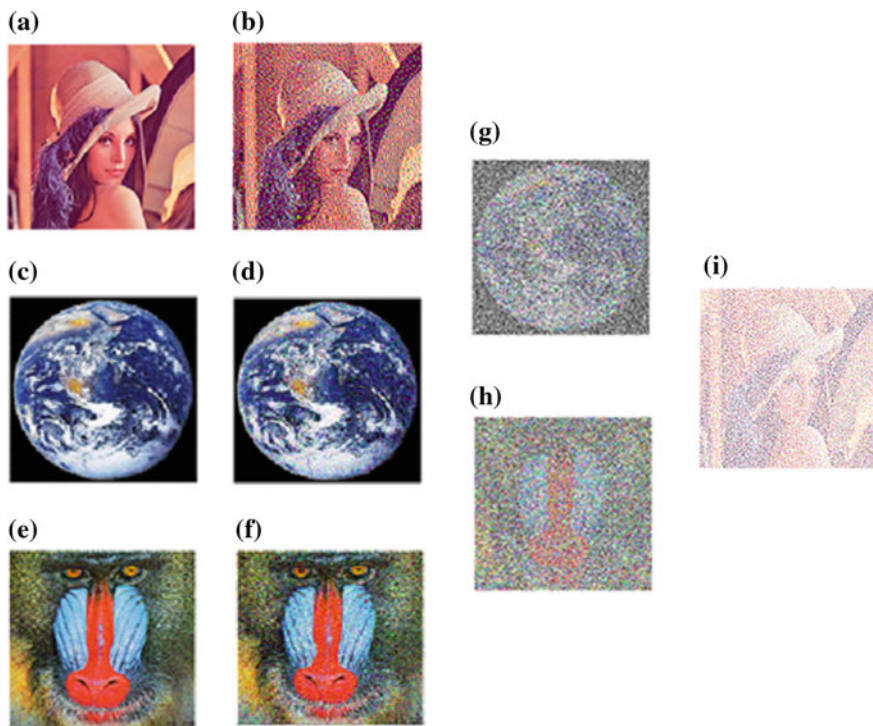
Fig. 1 Illustrative results of visual cryptography using Error Diffusion. **a** Original secret image lena, **b** halfone lena **c** and **e** original cover share image respectively, **d** halftoned earth, **f** halftoned baboon, **g** encrypted share 1, **h** encrypted share 2, **i** decrypted image

Table 1 shows PSNR, Correlation, UQI and SSIM of Encrypted Share 1 for 10 color secret images. The average value using Error Diffusion of PSNR is 51.41, Correlation is 0.3105, UQI is 0.1315 and SSIM is 0.0408. Using DBS, the average value of PSNR is 51.646, Correlation is 0.3027, UQI is 0.1331 and SSIM is 0.0843.

Table 2 shows PSNR, Correlation, UQI and SSIM of Encrypted Share 2 for 10 color secret images. The average value using Error Diffusion of PSNR is 51.291, Correlation is 0.2609, UQI is 0.0693 and SSIM is 0.0398. Using DBS, the average value of PSNR is 51.482, Correlation is 0.2788, UQI is 0.1066 and SSIM is 0.0647.

4 Conclusion

Visual Cryptography provides one of the secure ways to transfer images on the Internet. Images in color have been encoded and decoded using both Error diffusion and Direct Binary Search. Various parameters have been taken like PSNR, Correlation, UQI and SSIM. The proposed UQI model performs well without any Human Visual
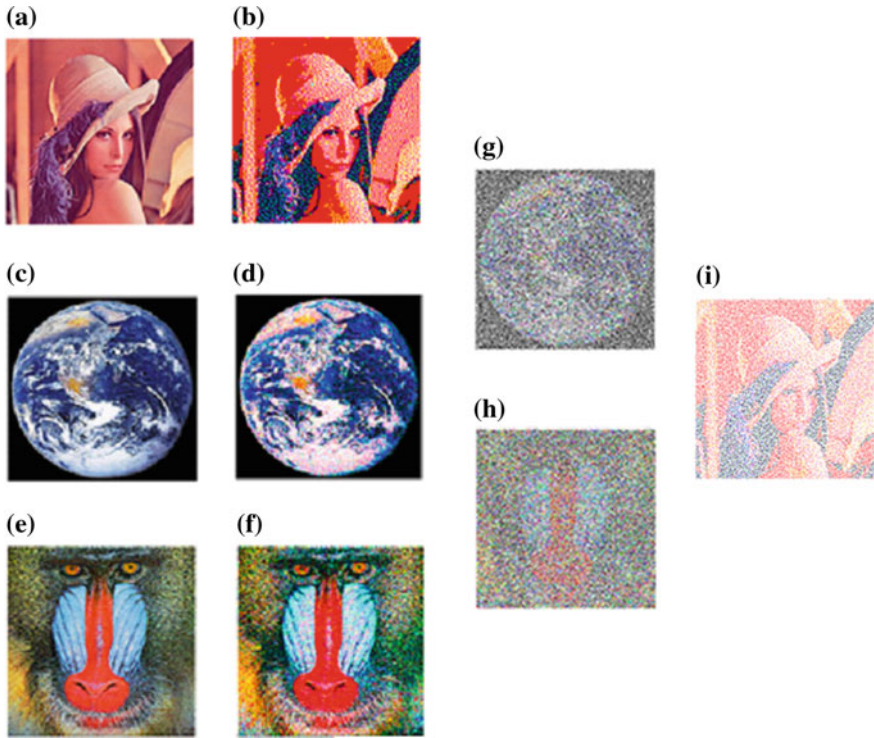
Fig. 2 Illustrative results of visual cryptography using direct binary search. **a** Original secret image lena, **b** halfoned lena **c** and **e** original cover share image respectively, **d** halftoned earth, **f** halftoned baboon, **g** encrypted share 1, **h** encrypted share 2, **i** decrypted image

Table 1 Encrypted share 1

Secret	Error diffusion				Direct binary search			
Image	PSNR	Correlation	UQI	SSIM	PSNR	Correlation	UQI	SSIM
Image text	51.411	0.3187	0.0678	0.0426	51.651	0.3066	0.1326	0.0889
Baboon	51.412	0.3188	0.6799	0.0436	51.662	0.3074	0.1350	0.0900
Barbara	51.405	0.3184	0.0665	0.0407	51.655	0.3069	0.1335	0.0883
Fruit	51.391	0.3177	0.0635	0.0382	51.653	0.3071	0.1329	0.0893
Peppers	51.417	0.3191	0.0691	0.0444	51.646	0.3062	0.1317	0.0872
Earth	51.405	0.3185	0.0665	0.0411	51.652	0.3069	0.1327	0.0880
Lena	51.368	0.2367	0.0957	0.0275	51.569	0.2642	0.1318	0.0455
Tulips	51.411	0.3188	0.0678	0.0420	51.663	0.3072	0.1350	0.0903
Vegetables	51.416	0.3190	0.0690	0.0439	51.655	0.3069	0.1334	0.0880
Space	51.416	0.3190	0.0689	0.0439	51.651	0.3070	0.1326	0.0870
Average	51.405	0.3105	0.1315	0.0408	51.646	0.3027	0.1331	0.0843

Table 2 Encrypted Share 2

Secret	Error diffusion				Direct binary search			
Image	PSNR	Correlation	UQI	SSIM	PSNR	Correlation	UQI	SSIM
Image text	51.266	0.2666	0.0615	0.0428	51.46	0.2826	0.1003	0.0696
Baboon	51.383	0.2377	0.0989	0.0264	51.586	0.2654	0.1353	0.0483
Barbara	51.393	0.2382	0.1010	0.0294	51.582	0.2652	0.1344	0.0478
Fruits	51.283	0.2676	0.0652	0.0464	51.45	0.2813	0.0983	0.0684
Peppers	51.236	0.2649	0.0551	0.0358	51.451	0.2820	0.0987	0.0678
Earth	51.286	0.2677	0.0659	0.0474	51.458	0.2824	0.0998	0.0690
Lena	51.271	0.2669	0.0627	0.0439	51.452	0.28204	0.0986	0.0677
Tulips	51.276	0.2672	0.0636	0.0444	51.467	0.2828	0.1019	0.0707
Vegetables	51.257	0.2661	0.0596	0.0412	51.437	0.2813	0.0956	0.0646
Space	51.259	0.2662	0.0599	0.0404	51.474	0.2832	0.1034	0.0730
Average	51.291	0.2609	0.0693	0.0398	51.482	0.2788	0.1066	0.06468

System model. Also algorithm supports not only monochrome images but grayscale and color images, even pixel expansion have been minimized. Correlation value is decreased in Encrypted share 1 but in the case of share 2, all the parameter measured value of DBS is better than Error Diffusion. The percentage of variation in PSNR, Correlation and UQI among these two methods is very small whereas improvement in SSIM is 50 percent in case of DBS. Visually also direct binary search gives us better results than Error Diffusion.

References

1. Naor M, Shamir A (1994) Visual cryptography. In: Proceedings of the EUROCRYPT, pp 1–12
2. Sandhya T, Saylee G (2017) Review on various cryptography schemes. In: International conference on current trends in computer, electrical, electronics and communication (ICCTCEEC), pp 360–363
3. Sandhya T, Saylee G (2018) Halftone visual cryptography for grayscale images using error diffusion and direct binary search. In: Proceedings of the 2nd international conference on trends in electronics and informatics (ICOEI) IEEE conference, pp 1091–1096
4. Blundo C, DArco P, De Santis A, Stinson DR (2003) Contrast optimal threshold visual cryptography schemes. SIAM J Discret Math 16, 224–261
5. Blundo C, Santis AD, Naor M (2000) Visual cryptography for grey level images. Inf Process Lett 75:255–259
6. Hou YC (2003) Visual cryptography for color images. Pattern Recognit 36:1619–1629
7. Ateniese G, Blundo C, Santis A, Stinson DR (2001) Extended capabilities for visual cryptography. ACM Theor Comput Sci 250:143–161
8. Nakajima M, Yamaguchi Y (2002) Extended visual cryptography for natural images. J WSCG 10
9. Zhou Z, Arce GR, Crescenzo GD (2006) Halftone visual cryptography. IEEE Trans Image Process 18:2441–2453

10. Myodo E, Sakazawa S, Takishima Y (2006) Visual cryptography based on void-and-cluster halftoning technique. In: IEEE international conference on image processing, pp 97–100
11. Wang ZM, Arce GR, Di Crescenzo G (2009) Halftone visual cryptography via error diffusion. IEEE Trans Inf Forensics Secur 4:383–396
12. Kang I, Arce GR, Lee HK (2011) Color extended visual cryptography using error diffusion. IEEE Trans Image Process 20
13. Wang ZM, Arce GR, Di Crescenzo G (2006) Halftone visual cryptography via direct binary search. In: EUSIPCO
14. Wang Z, Bovik AC (2002) A universal image quality index. IEEE Signal Process Lett 9
15. Wang Z, Bovik AC, Sheikh HR, Simoncelli EP (2004) Image quality assessment: from error visibility to structural similarity. IEEE Trans Image Process 13

Designing of p-Cycle Based Survivable Multicast RSA in Elastic Optical Networks

Susmita Das, Joy Halder and Uma Bhattacharya

Abstract Nowadays, Elastic Optical Network (EON) has attracted a lot of attention due to its efficient spectrum allocation. The popularity of different multicast applications is on the rise and survivability against single link failure has become a crucial issue. Our proposed scheme has considered pre-configured cycles or p-cycles for the protection of multicast sessions. Simulation shows quite good results in terms of blocking probability while ensuring survivability.

Keywords Elastic optical network (EON) · Orthogonal frequency division multiplexing (OFDM) · Dynamic · Multicasting · Distance adaptivity

1 Introduction

In present day, the demand of large data transmission is on the rise which has led to intensive research in the area of optical networks. In order to overcome the drawbacks of the under-utilization of a wavelength in Wavelength Division Multiplexing (WDM), Orthogonal Frequency Division Multiplexing (OFDM) technology was introduced in optical networks. This OFDM-based Elastic Optical Networks (EONs) have brought high scalability and efficiency to the utilization of spectrum [1]. Protection of EONs is very significant, as any failure in the network may cause severe disruption in data transmission. An efficient Routing and Spectrum Allocation (RSA) has been designed for optimization of network resources [2]. For dynamic environment, the requests are handled as they arrive. Distance adaptive spectrum resource alloca-

S. Das (✉) · J. Halder · U. Bhattacharya
Department of Computer Science and Technology, Indian Institute
of Engineering Science and Technology, Shibpur, India
e-mail: susmitad900@gmail.com

J. Halder
e-mail: mailmejoy1991@gmail.com

U. Bhattacharya
e-mail: ub@cs.iiests.ac.in

Table 1 Modulation formats ith FS capacity and transparent reach

Modulation format	FS capacity (Gb/s)	Transparent reach (km)
BPSK	25	4000
QPSK	50	2000
8-QAM	75	1000

tion is an efficient attribute of EON that can lower the spectrum utilization, based on the distance between the source-destination node pair [3] (Table 1). Recently, the applications of multicasting such as medical imaging and teleconferencing are being widely used and have eventually garnered some attention [4, 5]. For multicast session protection in EONs, different protection schemes such as Dedicated Path Protection (DPP) scheme and Shared Backup Path Protection (SBPP) scheme have been proposed [6, 7]. Pre-configured cycles (p-cycles) scheme is an approach which can be implemented to protect failure of links in EONs [8, 9]. The p-cycles provide a short recovery time along with spectrum efficiency compared to other protection schemes. Path-length-limited p-cycle design has been considered for this approach [10]. For the placement of subcarriers, the first fit and the exact fit policies have been considered [11]. In this paper, we have proposed **Online p-cycle based First fit Multicast Routing and Spectrum Allocation (O-PFM-RSA)** heuristic and **Online p-cycle based Exact fit Multicast Routing and Spectrum Allocation (O-PEM-RSA)**.

The problem definition has been illustrated in Sect. 2 with proposed work and complexity analysis. In Sect. 3, the simulation results have been explained. The conclusion has been drawn in Sect. 4 along with references.

2 Problem Definition

A directed graph $G = (V, E)$ is considered as the EON network in this paper, where V is the set of nodes present in the network and E is the directed fiber links set. We denote a multicast request as $r(s, D, B)$, where s is the source node, D is the destination nodes set for the multicast request and B is the total traffic demand to be transmitted. Our main objective is minimization of the blocking probability and protection of the network against single link failure using p-cycle in dynamic environment.

A. Proposed Work

In this paper, we have proposed two similar schemes; O-PFM-RSA which is based on the first fit policy and O-PEM-RSA which is based on the exact fit policy. In first fit policy, a request is placed on the first available free block of subcarriers, which can accommodate it. While in case of exact fit, find a free block which is exactly the size of the required number of subcarriers. In case of not finding such a block, use

the first free block available which can satisfy the request.
The scheme is described in the following steps:

1. All the cycles in the graph are enumerated.
2. For each set of node pairs, we calculate the first k shortest paths from the source node to the destination node.
3. All the blocks which are available are calculated for each fiber link.
4. A primary light tree is formed for a multicast request $r(s, D, B)$ by combining the available shortest path for each sub-request of the multicast request.
5. Check whether the new primary light tree is link disjoint with all the links which are already in use.

    5a. If the primary light tree is link disjoint with all the links which are being used, then check whether an already existing cycle in the network can be extended to protect this new multicast request.

    5b. If the primary light tree is not link disjoint with the links already occupied, then obtain a completely new cycle which can protect this new multicast request.
6. Obtain the modulation format for the multicast request depending upon the distances of the paths chosen. Calculate the number of subcarriers required to fulfill the traffic demand of the multicast request.
7. Search the available free blocks on the chosen paths for the primary light tree and the p-cycle protecting the request.

    7a. In case of O-PFM-RSA, place the required subcarriers on the first free block encountered.

    7b. In case of O-PEM-RSA, obtain the block whose size is same as the required subcarriers. If such a block is found, place the subcarriers. If no such free block is present, place subcarriers in the large enough block encountered first.
8. If the subcarriers cannot be accommodated in the links, then the request is blocked.

    The maximum number of subcarriers present in each fiber link in the network has been considered as 258. There has been no use of spectrum converters for this approach. Hence, the non-overlapping constraint, spectrum continuity and spectrum contiguity constraints have been maintained.

    Let us consider the network shown in Fig. 1a and there are already some multicast requests present with subcarriers $(1 - 6)$ and a p-cycle is already protect-

(a) The network considered   (b) Requests already placed in the network from earlier
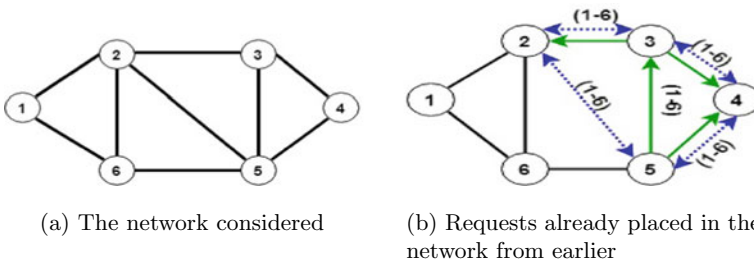
Fig. 1 Initial network condition

(a) One new request placed in the network

(b) Another new request placed in the network
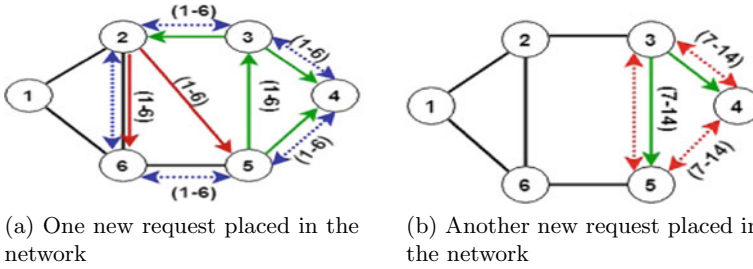
Fig. 2 Placement of requests in the network as they arrive

ing them as illustrated in Fig. 1b. One new multicast request $(2, \{6, 5\}, 124)$ needs to be placed on the network. The primary light tree for this multicast request has been chosen as $2 \rightarrow 6$ and $2 \rightarrow 5$. It is observed that the already existing p-cycle $2 \leftrightarrow 3 \leftrightarrow 4 \leftrightarrow 5 \leftrightarrow 2$ can be extended to protect the new multicast request. The new p-cycle after including the new multicast request is $2 \leftrightarrow 3 \leftrightarrow 4 \leftrightarrow 5 \leftrightarrow 6 \leftrightarrow 2$ as shown in Fig. 2a. The highest number of subcarriers required is calculated taking the appropriate modulation format and placed in each link of the new p-cycle. Let us consider a new request $(3, \{4, 5\}, 129)$. The primary light tree for this multicast request has been chosen as $3 \rightarrow 4$ and $3 \rightarrow 5$. The new primary light tree is not link disjoint with the previous primary light trees and also the p-cycle which can protect them cannot be extended. Hence, a new p-cycle $3 \leftrightarrow 4 \leftrightarrow 5 \leftrightarrow 3$ is used to protect the new multicast request as shown in Fig. 2b. Now, for provisioning the previous multicast request, assume that $(1 - 6)$ subcarriers has already been reserved. So, for this multicast request, the next index will be considered.

B. Complexity Analysis

For cycle enumeration in the graph, time complexity is $O(V + E)$. The k shortest paths for each multicast sub-request has time complexity of $O(kV(E + V \log V))$, where E is the amount of edges which are present in the graph, V is the number of nodes in the graph and k is the number of paths to be computed. For finding the free blocks in each link, the time complexity is $O(S|E|)$, where S is the number of subcarrier in each fiber link. The time complexity for formation of a primary light tree and placement of subcarriers is $O(n|E|)$. The run time complexity is $O(kV(E + V \log V) + (V + E) + n|E| + S|E|)$ which is polynomial time.

3 Performance Evaluation

In this section, the performance of O-PFM-RSA and O-PEM-RSA has been evaluated with the simulations being performed on COST239 network. We have varied the size of the destination node set for each multicast request as 2, 4, 6, 8 and 10. For each

Table 2 Simulation setup for heuristic algorithm

Parameters	Values
Link-disjoint paths computed(k)	5
Guard bands considered	1, 2, 3
Request demand range	100–200 GB
Number of destinations	2, 4, 6, 8, 10
Total requests for each number of destination	50
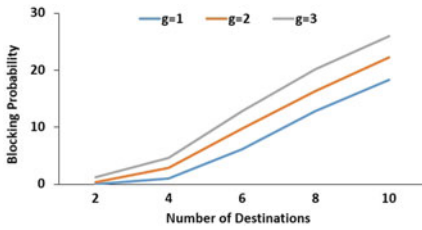
(a) Performance for varying guard band size in O-PEM-RSA
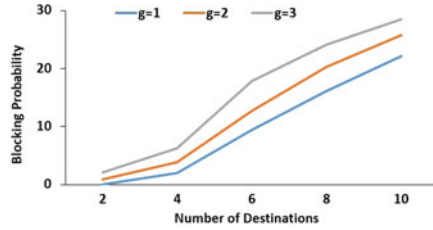
(b) Performance for varying guard band size in O-PFM-RSA

Fig. 3 Performance on COST239 network for different guard band sizes
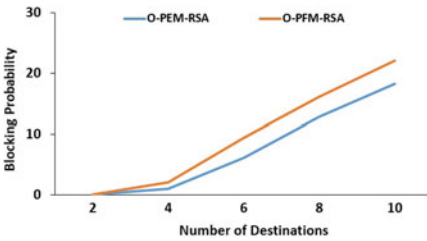
(a) Performance comparison for 50 requests
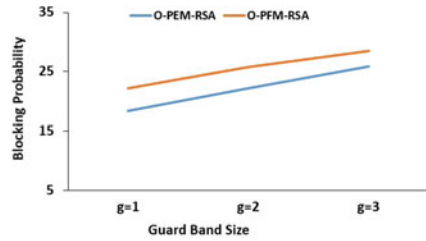
(b) Performance comparison for different guard band size

Fig. 4 Performance comparison of O-PEM-RSA and O-PFM-RSA on COST239 network

size of destination node set, we have considered 10 different iterations of each set of 50 requests. The number of guard bands is also varied as 1, 2 and 3 (Table 2).

The graphical results for O-PEM-RSA when the size of the guardband is varied are illustrated in Fig. 3a and that for O-PFM-RSA is shown in Fig. 3b. It is observed that with the increase in size of guardband, the blocking probability increases. This is because more number of subcarriers are being used as guard in between two multicast requests, due to which some of the requests cannot be accommodated in any free block. The results of the performance comparison of the O-PFM-RSA and O-PEM-RSA for 50 requests and different guard band sizes have been illustrated

in Fig. 4c and b, respectively. As per the calculated results, it is observed that the blocking probability for O-PEM-RSA approach is less compared to that of O-PFM-RSA. This is due to the fact that, with the selection of perfect sized free blocks, the number of free blocks which can satisfy a request is more compared to the case in O-PFM-RSA. As p-cycle is used as the protection scheme in both the proposed methods, the recovery time is short in case of any single link failure.

4   Conclusion

We have proposed a novel scheme O-PEM-RSA, where we have addressed the problem of ensuring survivability of EON against single link failure using p-cycles in a dynamic environment. It is an NP-Hard problem and the solution becomes intractable in case of larger sized networks. The heuristic O-PEM-RSA runs in polynomial time. In the design process of O-PEM-RSA, another scheme O-PFM-RSA has been considered. Performance evaluation of the two schemes has been carried out on COST239 network for 50 multicast requests. The comparison shows that O-PEM-RSA gives better results in terms of blocking probability. This scheme being based on p-cycles also gives better recovery time.

References

1. Gerstel O, Jinno M, Lord A, Yoo SB (2012) Elastic optical networking: a new dawn for the optical layer? IEEE Commun Mag 50(2)
2. Christodoulopoulos K, Tomkos I, Varvarigos EA (2010) Routing and spectrum allocation in ofdm-based optical networks with elastic bandwidth allocation. In: Global telecommunications conference (GLOBECOM 2010). IEEE, pp 1–6
3. Jinno M, Kozicki B, Takara H, Watanabe A, Sone Y, Tanaka T, Hirano A (2010) Distance-adaptive spectrum resource allocation in spectrum-sliced elastic optical path network [topics in optical communications]. IEEE Commun Mag 48(8)
4. Wang Q, Chen LK (2012) Performance analysis of multicast traffic over spectrum elastic optical networks. In: Optical Fiber Communication Conference. Optical Society of America, pp OTh3B.7
5. Walkowiak Krzysztof, Goścień Róża, Klinkowski Mirosław, Woźniak Michał (2014) Optimization of multicast traffic in elastic optical networks with distance-adaptive transmission. IEEE Commun Lett 18(12):2117–2120
6. Din DR, Lai IR (2015) Multicast protection problem on elastic optical networks using segment-base protection. In: 2015 International conference on informatics, electronics and vision (ICIEV). IEEE, pp 1–6
7. Cai Anliang, Guo Jun, Lin Rongping, Shen Gangxiang, Zukerman Moshe (2016) Multicast routing and distance-adaptive spectrum allocation in elastic optical networks with shared protection. J Light Technol 34(17):4076–4088

8. Ji F, Chen X, Lu W, Rodrigues JJ, Zhu Z (2014) Dynamic p-cycle protection in spectrum-sliced elastic optical networks. J Light Technol 32(6):1190–1199
9. Kiaei MS, Assi C, Jaumard B (2009) A survey on the p-cycle protection method. IEEE Commun Surv Tutor 11(3)
10. Kodian A, Sack A, Grover WD (2005) The threshold hop-limit effect in p-cycles: Comparing hop-and circumference-limited design. Opt Switch Netw 2(2):72–85
11. Rosa A, Cavdar C, Carvalho S, Costa J, Wosinska L (2012) Spectrum allocation policy modeling for elastic optical networks. In: 2012 9th international conference on high capacity optical networks and enabling technologies (HONET). IEEE, pp 242–246

Design and Development of Metamaterial Based High Performance Microstrip Antenna

N. Subramanyam Mahesh and D. Varun

Abstract   The primary objective of this paper is to design a high performance metamaterial antenna and benchmark the performance with a microstrip antenna. A circular microstrip patch antenna is considered for demonstrating the performance of the antenna with and without the metamaterial structures. This paper clearly brings out the advantages of the metamaterial circular patch antenna as compared to the standard circular microstrip antenna. Simulations and measurements are carried out for comparison purpose. The developed metamaterial based patch antenna shows a significant reduction in size by 25% when compared to a circular patch antenna. It has been found that reduction of size in developed metamaterial based antenna does not degrade the directivity performance which is found to be 6.5 dB. Further, the bandwidth of the metamaterial based antenna is found to be same as that of microstrip antenna. RCS simulation has shown reduction in RCS by 9 dBsm.

Keywords Metamaterial · Microstrip patch antenna · Radar cross section · Return loss

1   Introduction

Recent trend towards miniaturization and devices with RF technologies, antenna size reduction, efficiency play a very vital role. Size, weight, ease of installation, cost and performance are critical parameters. Microstrip antennas meet the said requirements. The microstrip patch antenna is also well suited for MMIC designs. Depending on the shape of the patch structure and mode selected, patch antennas are very versatile in terms of resonance, polarization, pattern and impedance. There have been several attempts to reduce the size of the microstrip patch antenna by using aperture stacked sheets and other variations. It has been found that the use of metamaterials results in size reduction in antenna. A comparative study in [1, 2] depicts the advantages of circular patch antenna when compared to rectangular patch. It is found the circular

N. Subramanyam Mahesh · D. Varun (✉)
Department of ECE, M. S. Ramaiah University of Applied Sciences, Bengaluru, India
e-mail: varun.ec.et@msruas.ac.in

patch antenna uses a lesser surface as compared to a rectangular microstrip antenna. There are a significant number of papers that elaborate on metamaterial based rectangular patch antenna. However, there are not many papers in the open source that have included circular patch antenna in the studies. The paper by [3–5] delve into the metamaterial based circular patch antenna but does not deliberate at size reduction. The paper [4] highlights the different methods to incorporate metamaterial structures in the antenna design such as the superstrate based antenna design or the CSRR perforated ground plane based design. The literature [6–9] shows that there is a size reduction in the patch array with the use of CSRR in the ground plane. However, the study in [5] has not simulated the performance of the antenna with the CSRR loaded and the antenna tuned to the original frequency for which it was designed. It is found that the intended frequency of antenna design increases and the dimensions of the resonator structures decrease. The interaction between the resonators also play a very critical role and this is dictated by the distance between the resonators which is again a function of the frequency [4]. As a result of the dimension restrictions, the fabrication of these materials requires a complex photo lithography mechanism. From the above observations based on the literature survey, it can be inferred that the circular patch antenna offers some inherent advantages. It is also seen that there are not many literature that have carried out a detailed analysis of the circular patch antenna with metamaterial structures. Hence there is a motivation to look into the behaviour of a circular microstrip antenna with metamaterial structures in the ground plane and compare its performance with a circular microstrip antenna. In this paper, an attempt has been made to develop a metamaterial specifically aimed at an X band circular path antenna and reduce the size of the said patch. It is also to be noted that the gain of the antenna is not reduced.

2   Antenna Modelling, Simulation and Optimization

The antenna has been developed by selecting X band frequency. X band is the chosen frequency due to the antenna aperture size restrictions for RADAR applications. The modelled antenna has been further optimized for its performance. The design goals for the high performance metamaterial antenna are as follows:

- Frequency Range: X—Band
- Resonant frequency: ~10 GHz
- Directivity(Goal): >4 dBi
- Input return loss < -14 dB

2.1 Design of the Circular Patch Antenna

An appropriate substrate suitable for 10 GHz has been selected with negligible (tan δ) losses. Based on a survey, it has been identified that the substrate material RT5880 from Rogers or the Arlon Diclad880 is suitable for X-band low loss applications. Arlon Diclad880 substrate has been selected for all simulation and fabrication purposes. Based on the antenna specifications and the substrate chosen, the following data is necessary for antenna development.

- $F_0 = 10$ GHz
- Substrate permittivity, $\varepsilon_r = 2.17$
- Loss tangent(D) $= 0.0009$

The Shen formula for computing the radius of the microstrip patch antenna is given by Eqs. (1) and (2).

$$a = \frac{F}{\sqrt{\left\{1 + \frac{2h}{\pi \varepsilon F}\lceil \ln(\pi F|2h) + 1.7726\rceil\right\}}} \tag{1}$$

$$F = \frac{8.791 * 10^9}{f_0\sqrt{\varepsilon}} \tag{2}$$

a = radius of the circular patch
μ = permittivity of the substrate
ε = permittivity of the substrate
h = thickness of the substrate in cm
f_0 = Resonant frequency of antenna

On substituting the values for the resonant frequency and the permittivity, the radius of the circular patch was found to be 5.9 mm. The antenna has been modelled and simulated with a radius of 6 mm for the said frequency.

2.2 Design of the Metamaterial Square Split Ring Resonator

A rectangular split ring resonator has been designed using empirical equations in [10]. One of the important assumptions is that the resonator must be lesser than $\frac{\lambda}{10}$. The split ring resonator resonates at a frequency determined by the total distributed inductance and capacitance provided by the inner and outer rings. The split ring resonator has a stop band around the desired resonant frequency of the antenna with split ring resonator in the ground plane.

The average loop length is computed as given in the Eq. 3.

$$L = 4X - S - 4W \tag{3}$$

where X is the length of the ring, S is the spacing and W is the width.

Fig. 1 Tuned circular patch
with CSRR structures
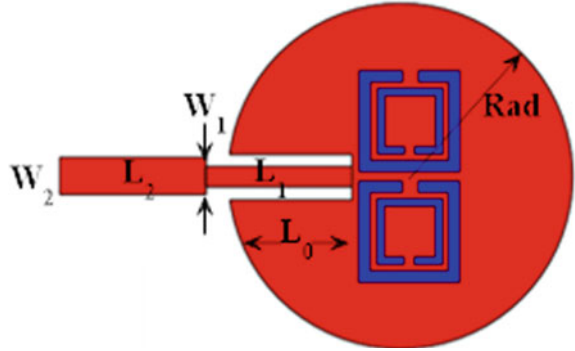
Table 1 Tuned patch dimensions with CSRR loaded

Parameter	Dimension (mm)	Parameter	Dimension (mm)
Radius of the patch	6	Length of outer ring (X_1)	3.0
Inset length (L_o)	3.936	Width of outer ring (W_1)	0.33
Length of microstrip feed line (L_2)	5.47	Spacer (S_1)	0.57
Length of microstrip feed line (L_1)	5.47	Length of inner ring (X_2)	1.95
Width of microstrip (W_1)	1.1	Width of outer ring (W_2)	0.31
Width of microstrip (W_2)	1.67	Spacer (S_2)	0.21

2.3 Design of Circular Patch Antenna with Square CSRR

Once the metamaterial structure is loaded in the ground plane, the resonant frequency of the patch antenna shifts to a lower frequency. This indicates a reduction in the size of the antenna. So to tune the antenna back to 10 GHz resonance, the antenna needs to be designed for a higher frequency than 10 GHz which is the design goal. The antenna simulation has to be performed and an iterative optimization has to be done. Figure 1 depicts the circular patch antenna loaded with square metamaterial structure. Table 1 shows the dimensions of the antenna.

3 Results and Analysis

Antenna with and without the CSRR structures has been fabricated to compare the results of the simulation. The antenna return loss has been measured using a network analyser and results are validated. The simulation results in Fig. 2a depicts the return loss for the circular patch antenna with PEC ground. The simulation results depict the resonance at 10 GHz with a return loss of—15 dB. Similarly Fig. 2b depicts the simulated return loss for the optimized antenna with CSRR in the ground plane.
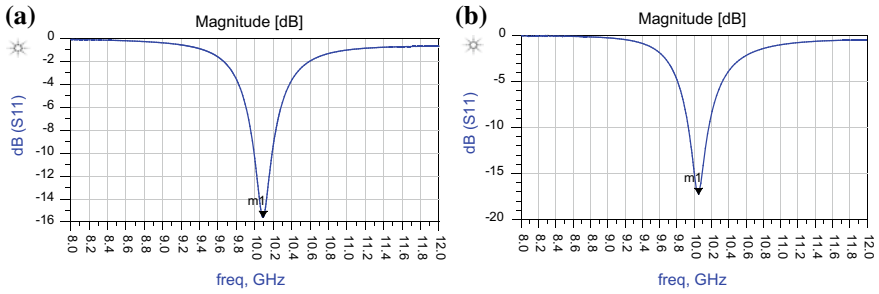
Fig. 2 Simulated return loss results for circular patch antenna **a** without CSRR **b** CSRR loaded

Comparison of simulated results depicts similar return loss results between PEC loaded and CSRR loaded antenna. It is pertinent to note the CSRR loading results in a 25% reduction in size. The CSRR loaded antenna fabricated is shown in Fig. 3. The return loss is measured to be at—12.33 dB from Fig. 4a in case of PEC ground
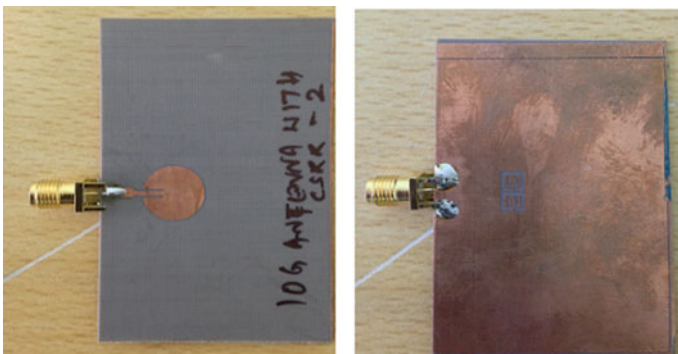
Fig. 3 Fabricated circular patch antenna (CSRR loaded)
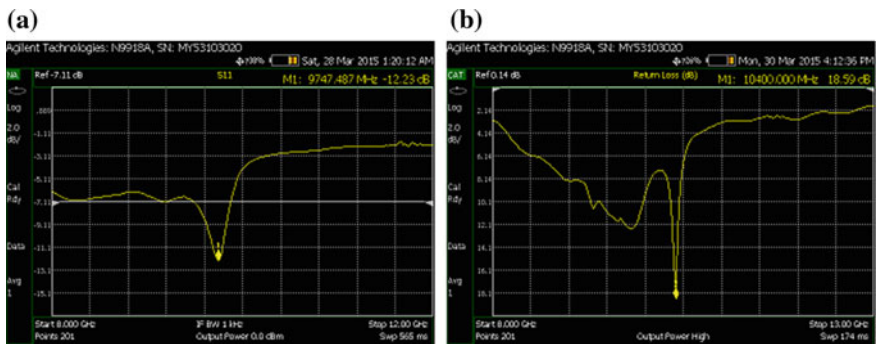
Fig. 4 Measured return loss for circular patch antenna **a** PEC Ground **b** CSRR Loaded

plane. Figure 4b shows the measured return loss of—18.5 dB for antenna loaded with CSRR. The error between the simulated and the fabricated antenna is less than 5%. The error can be attributed to the fabrications techniques that were used and also SMA connectors that were used at the feed point has not been modelled in the simulation. The antenna with the square CSRRs loaded in the ground plane was simulated for its directivity performance. The directivity is 6.26 dBi and is 1 dB lower than the circular patch antenna with PEC ground. The reduction in directivity is attributed due to reduction in the aperture size after CSRR loading.

4   Computation of Radar Cross Section (RCS) of the Antenna

The developed antenna with PEC ground and antenna with CSRR structures have been further simulated for its RCS performance. The layout of the antenna is developed, modelled and simulated using Method of Moments. The antenna under test is excited by a point source that produces a planar wave front to excite the antenna. The simulation setup has been configured for a monostatic radar configuration at $\theta = 0°$ and $\phi = 0°$. The reflections from the antenna under test have been captured by the sensor and the RCS plots are plot. The analysis has been carried at 10 GHz excitation frequency. Figure 5a shows the RCS for the patch antenna with PEC ground. The maximum RCS is at 0° theta and is—23 dBsm at 10 GHz. Figure 5b shows the RCS performance with CSRRs loaded on to the patch antenna. The RCS at 10 GHz is found to be—32 dBsm with the CSRRs.

The results in Fig. 5 shows a reduction in RCS as compared to the patch antenna with PEC ground. There is a reduction of 9 dBsm in the RCS. This clearly shows that using metamaterial structures, there is a reduction in the RCS and also a considerable reduction in the size of the metamaterial antenna.
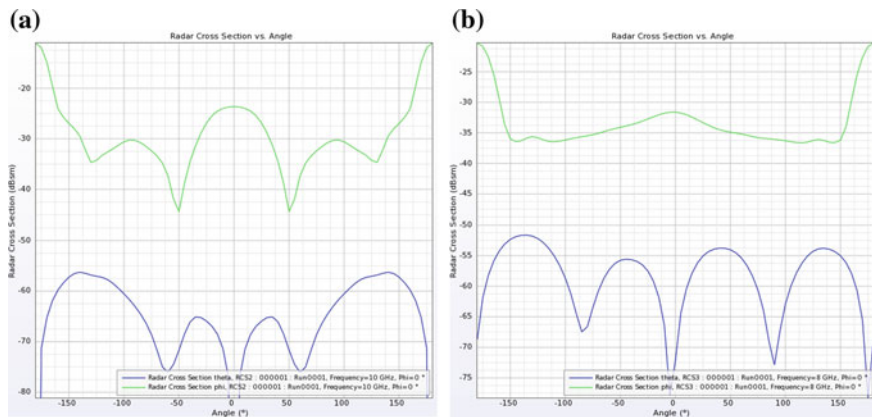
Fig. 5 Simulated RCS results—circular patch antenna (10 GHz) **a** PEC ground **b** CSRR loaded

5 Conclusion

This work attempts to highlight the advantages of two split ring resonators (CSRR) in an antenna. The CSRR results in size reduction, improved gain and decreased RCS based on simulation and measured results. A circular patch antenna with and without metamaterial structures has been simulated using EM solvers. It has been found the antenna size has been reduced by 25%. The Directivity and gain performance of the antennas are also validated. The circular patch antenna with CSRR structures is simulated and fabricated for the given design criteria. Developed metamaterial loaded antenna has a gain of 6.4 dBi and directivity of ~6.4 dBi. The RCS computation has also been carried out by simulating the antenna in the far field using a point source in an EM solver. RCS simulation shows a considerable reduction in RCS (~9 dBsm) for developed antenna with metamaterial structure. RCS reduction is due to the application of metamaterial structure in the ground plane of the antenna. The importance of using metamaterial structures in the design of microstrip circular patch antenna with a reduced size and RCS without altering the gain and directivity has been exemplified.

References

1. Burokur SN, Latrach M, Toutain S (2005) Study of the effect of dielectric split-ring resonators on microstrip-line transmission. Microw Opt Technol Lett 44(5):445–448
2. Dalli A, Zenkouar L, Bri S (2012) Comparison of circular sector and rectangular patch antenna arrays in c-band. J Electromagn Anal Applications 4(11):457
3. Garcia-Garcia J, Aznar F, Gil M, Bonache J, Martin F (2007) Size reduction of SRRs for metamaterial and left handed media design. PIERS Online 3(3):266–269
4. Gay-Balmaz P, Martin OJ (2002) Electromagnetic resonances in individual and coupled split-ring resonators. J Appl Phys 92(5):2929–2936
5. Luna DR, Neto VP, Vasconcelos CF, D'Assunção AG (2013) Microstrip patch antennas with metamaterial inspired substrates and superstrates. In: 2013 SBMO/IEEE MTT-S international microwave and optoelectronics conference (IMOC), 4 Aug 2014, pp 1–4. IEEE
6. Jang HA, Kim DO, Kim CY (2012) Size reduction of patch antenna array using CSRRs loaded ground plane. In: Progress in electromagnetics research symposium proceedings, KL, Malaysia, 27 Mar 2012, p 1487
7. Limaye AU, Venkataraman J (2007) Size reduction in microstrip antennas using left-handed materials realized by complementary split-ring resonators in ground plane. In: Antennas and propagation society international symposium, 9 Jun 2007, pp 1869–1872, IEEE
8. Majid HA, Abd Rahim MK, Masri T (2009) Microstrip antenna's gain enhancement using left-handed metamaterial structure. Prog Electromagn Research 8:235–247
9. Saha C, Siddiqui JY (2011) A comparative analyis for split ring resonators of different geometrical shapes. In: Applied electromagnetics conference (AEMC), 18 Dec 2011, pp 1–4, IEEE
10. Engheta N (2002) An idea for thin subwavelength cavity resonators using metamaterials with negative permittivity and permeability. IEEE Antennas Wirel Propag Lett 1(1):10–13

IoT-Based Walking Stick

S. Nagarajan and **Sanket Dessai**

Abstract People with limited mobility like elderly, physically challenged, vision impaired and orthopedic patients need support to move around. They depend on walking sticks or other such devices. Even if they fall accidently, it is difficult for them to seek for help. Automatically assessing such a situation and alerting their near and dear ones will be an ideal solution to this problem. In case of emergency, it is preferred that they stay connected to their family members and friends. To address this issue, we can add intelligence in the walking stick and walking stick will act as an IoT device. This paper aims to develop basic infrastructure for IoT-based walking stick, on which further sensors and analytics can be extended seamlessly.

Keywords IoT · Walking stick · IoT platform · RTOS

1 Introduction

This document describes design and development of IoT-based walking stick. Assisted walking needs can be addressed with advancement in sensor technologies, low cost, light weight, low power, networking capable chipsets and cloud infrastructure [1]. An effective solution can be worked out that can fit within the size of the walking stick.

"Walking stick" application as-a-service can be rolled out with IoT device and IoT platform combination. Figure 1 provides the pictorial representation of IoT-based walking stick.

S. Nagarajan (✉) · S. Dessai
M. S. Ramaiah University of Applied Sciences, Bengaluru, India
e-mail: nags2004@hotmail.com
URL: http://www.msruas.ac.in

Fig. 1 Introduction to cloud-based walking stick

2 Design of IoT-Based Walking Stick

The entire walking stick solution has been partitioned into two layers:

1. Walking stick (IoT device end application)
2. IoT platform application.

Three axes angle sensors are connected to IoT device. The data from sensors are acquired at regular required intervals. This data is posted to IoT platform for further analysis and action. The architecture of the system is shown in Fig. 2.

2.1 *Design of an IoT Device for Walking Stick*

As an IoT controller, "ESP8266" low-cost SoC having Wi-Fi module is selected. This SoC is having, Wi-Fi station, Wi-Fi access point capability and digital IOs, I2C interfaces and low-power 32-bit MCU [2].

An angle sensor is interfaced to IoT controller, to derive the position of angle of the walking stick. Walking stick uses MQTT protocol to communicate to IoT platform (IBM Watson). IoT platform is being hosted in cloud, and services like MQTT broker are used to retrieve and store the data from IoT devices.

For panic button input from the user, digital input should be connected to a button switch.

"NodeMCU" development boards based on ESP8266 are chosen, as it provides inbuilt power modules, serial interface and other general-purpose IOs.

The IoT device (walking stick, Fig. 3) should periodically publish the angle data to the IoT platform. It should acquire data from the sensors. It should use the industry
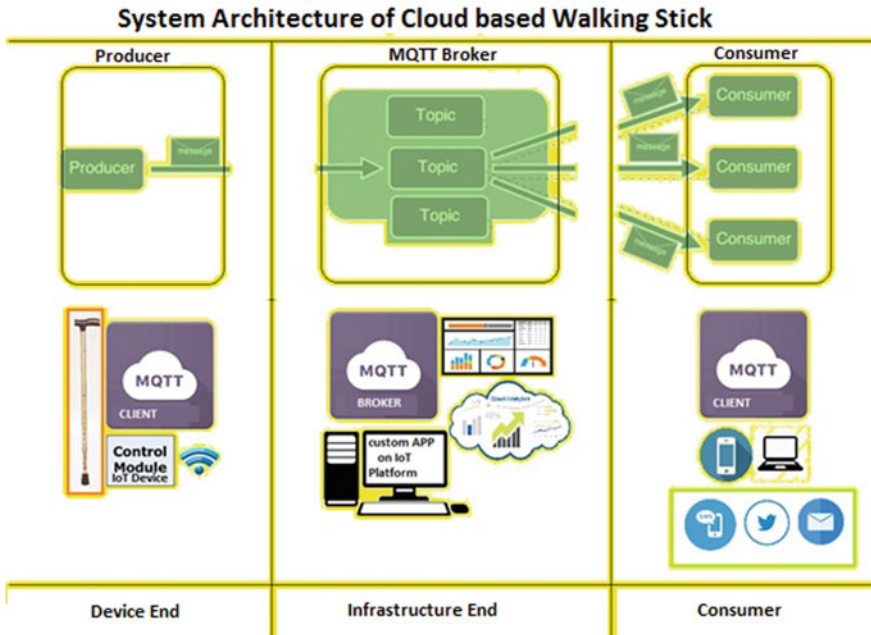
Fig. 2 System architecture of cloud-based walking stick

standard protocols to exchange information to IoT platform such as MQTT. The application should be flashed in the device. Any further firmware uploads should be possible.

2.2 Design of IoT Platform End Application

IoT platform should provide device management capabilities such as creating/deleting an IoT device for subscription management. Additionally, platform should support authenticating a device to the service deployed in the IoT platform. It should be possible to simulate devices and to verify the platform, even if the actual device is not available.

Data visualization should be possible for the sensor data. It should be able to plot the data in multiple formats like XY graphs, bar charts. All alarms should be captured and it should be possible to view in table formats.

For the demonstration of this solution, IBM's IoT platform has been selected [3]. In IoT platform the MQTT broker services are enabled. MQTT works in publish-subscribe model. It simplifies the connectivity between devices. MQTT is a lightweight protocol designed for connecting over low-bandwidth networks. It becomes more preferred protocol for IoT communications.

IoT Device - Block Diagram

Pin-Out	GPIO #	Function	Interface to
D1	GPIO5	SCL (I2C)	MPU-6050, SCL
D2	GPIO4	SDA (I2C)	MPU-6050, SDA
D5	GPIO14	Digital Input	Button (Switch) Input
RX	GPIO3	RxD0	Com port Tx
TX	GPIO1	TxD0	Com port Rx

Interface Details

NodeMCU ESP-12 development kit V1.0
PIN DEFINITION

Firmware

Access Point Module

ESP8266 Wifi STA

Control Module

COM port

I2C I/F

Angle data, Every 30 seconds

MPU6050 - 3 axis - gyro sensor

Digital Input

Read Switch Position

Fig. 3 Block diagram of IoT device for walking stick hardware

In the IoT platform, IoT device has been provisioned, so that it can perform specific device operations. Device operations like remote reset can be performed from IoT platform. The device statistics can be monitored and any number of devices can be added, without much programming effort.

3 Construction of IoT-Based Walking Stick Solution

Construction of IoT-based walking stick solution involves: (a) To design an IoT device to periodically publish the angle information to IoT platform; (b) To host application in IoT cloud, to retrieve data from IoT device and to manipulate; and (c) To integrate the system and to test against the requirements mentioned.

3.1 IoT Device Implementation

Angle sensor interface: For measuring angle information of walking stick in all three axis, the "x", "y" and "z" position of MPU-6050 sensor is used. The InvenSense MPU-6050 sensor contains an MEMS accelerometer and an MEMS gyro in a single chip. It is very accurate, as it contains 16 bits analog to digital conversion hardware for each channel. It captures the x, y and z channel at the same time. The sensor uses the I2C-bus to interface with the controllers. GY-521 is the sensor board, which has MPU6050 and has a voltage regulator (refer Fig. 4).

Fig. 4 Fabrication of the IoT-based walking stick

ESP8266 has inbuilt I2C controllers, which connects to MPU6050 to get data from the sensor. MPU6050 has the address of 0×68. The device register $0 \times 3B$ to 0×40 contains the X, Y and Z angle data (each 2 register location).

Configuring Wi-Fi Module: In this application Wi-Fi module is configured both as Wi-Fi access point and Wi-Fi station.

a. *Wi-Fi Access Point*

Providing Wi-Fi-AP support on the walking stick allows other Wi-Fi devices to connect to the stick. With the webserver running on the stick, mobile devices can access the webpage to collect the data from the walking stick. Typical data will be from the angle sensor.

Typical Wi-Fi stations may be smartphones. Smartphones can be connected through Wi-Fi interface to the stick. Browsers in the smartphones can be invoked to read the data from the walking stick.

b. *Wi-Fi Station*

The Wi-Fi module in the walking stick can also be configured as a wireless station. It can connect to the Wi-Fi access point and to the local network (or) to the internet. It fetches contents from the internet. Wi-Fi modules are assigned to an IP by external access point.

Webserver Implementation: ESP8266 SDKs are used to handle http request and response. The sensor data is read and formatted with http response, so that it can be accessed through any browser from laptop/smartphones. The Wi-Fi devices that are part of the network created by the device (walking stick) can access these webpages.

Requests are coming as part of the web address, "192.168.1.4/read". This address is parsed to know the kind of request. Based on the request, webpages are formed to provide the response. Angle sensor data is read from sensor and sent in the http response.

Also the number of times the switch pressed input is also sent.

X:<value>, Y:<value>, Z:<value>.

Panic Button Implementation: To help in emergencies panic button is interfaced. It is connected to GPIO as an input. Interrupt service routine is registered to take an action instead of button is pressed. Firmware maintains the counter for number of times switch pressed. Also, the firmware maintains the flag "switch_pressed"; this flag is cleared only when user reads via http request.

3.2 *IoT Platform End Application*

For demonstration of the solution, IBM's IoT platform has been selected. In the IoT platform the MQTT broker services are enabled. MQTT works in publish-subscribe

model. It simplifies the connectivity between devices. MQTT is a lightweight protocol designed for connecting over low-bandwidth networks. It becomes more preferred protocol for IoT communications.

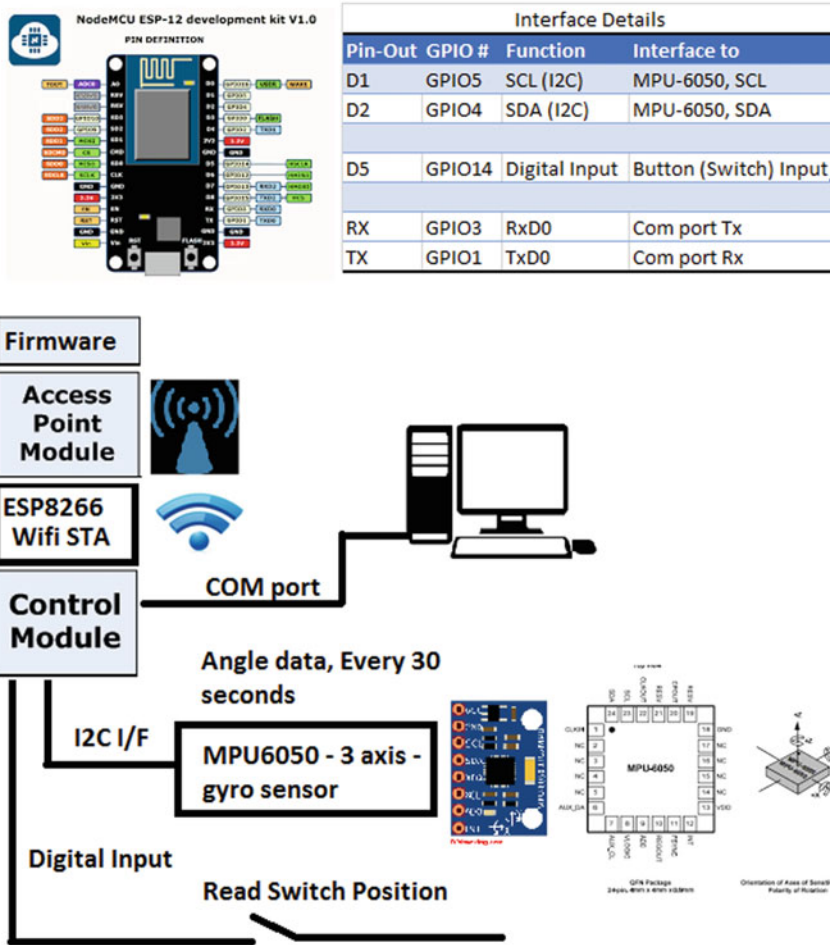In IoT platform, IoT devices have been provisioned, so that it can perform specific device operations. Device operations like remote reset can be performed from the IoT platform. The device statistics can be monitored and any number of devices can be added, without much programming effort.

Device Management: In the IoT platform, new devices types are created (type as "WalkingStick'), and then device instances (device serial numbers) are added to represent the real hardware. Each device has authentication token to communicate with IoT platform. If numbers of devices are more, the devices can be added with the APIs.

It is also possible to simulate the IoT device from the provisions provided in IoT platform. From the simulated IoT device, it is possible to send sensor data for integrating IoT device and IoT platform.

MQTT broker is hosted in IoT platform. Publish/subscribe topics are created to publish (to push the data to platform) and manage (to manage the device, like rebooting the device).

Visualize Data from Devices: Boards are configured to visualize the required data in the desired format (refer Fig. 5). We can configure multiple boards based on the requirement. In each board the desired data can be plotted as tables and charts. Boards are also configured to have the statistics of data usage by each device.
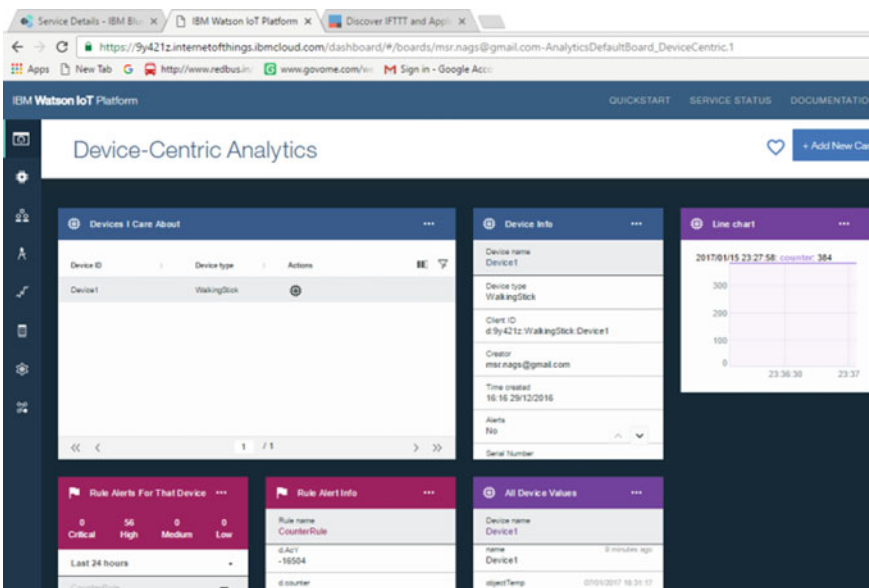
Fig. 5 Visualising device data on the IoT platform
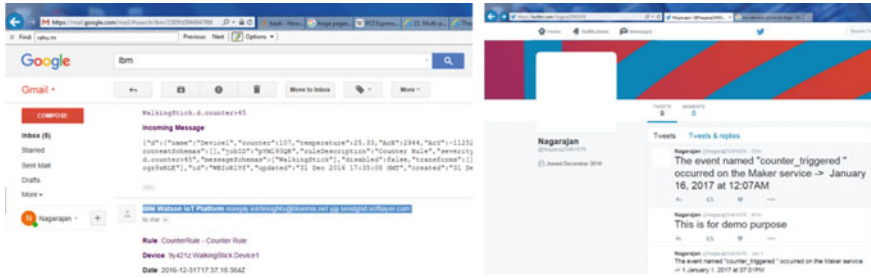
Fig. 6 E-mail and Twitter updates from IoT platform

Rebooting Walking Stick from IoT Platform: Reboot of the device is possible from IoT platform. The desired device needs to be selected from the IBM-Watson GUI, to reboot. The messages will be published in reboot topic.

The devices are subscribed to reboot topic, and on receiving the reboot message, the device invokes restarts. Debug console outputs print the boot up messages.

Alerts through SMS, E-mail and Twitter: When the threshold limit exceeds the configured parameters, alerts are triggered. These alerts are in the form of updates via SMS, E-mail and Twitter (social media). These alerts are also archived in the IoT platform for any further debugging. Fig. 6 shows the updates made to Twitter (social network), Gmail from the IOT platform.

3.3 Major Constraints, Future Directions

For the sensitive applications, data acquisition from the sensors at a guaranteed interval is must. Assuming for the given walking stick application, to effectively calculate the number of steps, minimum of three gyro/accelerometer readings are required per second. These requirements should be enforced only with the use of RTOS [4].

Linux also is not a suitable OS, compared to RTOS [5]. Though Linux can be customized, memory footprint still will be an issue, for micro-controller series. Even if ported, Linux itself will occupy large portion of memory, when compared to the actual application. Also RAM requirement for running Linux cannot be met with simpler embedded system. The IoT controllers may have few hundred kilobytes of on-board memory. Therefore, Linux won't be a choice.

Future enhancement may include:

(a) Voice Input: Interfacing voice codec hardware to the system will enable the natural language processing in the cloud platform.
(b) Feedback/Alert: Interfacing vibration and audible sensors serves as a feedback mechanism to the user. This will be useful in alerting the user in case of abnormality.

(c) Geo-Location Features: Implementation of features like route map, broadcasting our location to other users [6, 7].

(d) Obstacle Detection: Interfacing additional proximity sensors will enable obstacle detection. This will help in finding immediate obstacle (like walls and lampposts).

(e) RTOS-based software implementation.

(f) Connectivity: Interfacing GSM module ensures that there is 2G data connectivity regardless of internet availability. Since GSM coverage is widely available, SMS alerts can be sent on any panic situation.

4 Conclusion

The hardware module in walking stick acts as an IoT device and it is interfaced to IoT platform, to help people with mobility needs. IoT device has been interfaced with required sensors. Data from sensors are pushed to IoT cloud platform for analysis. The application hosted in the IoT platform performs actions like alerting the stakeholders in case of abnormalities via messaging (SMS, mail, social media, etc.).

Being a low-cost solution, the cost/benefit ratio provided by the system is very high. As entire solution can be fitted in the existing walking stick, with little engineering effort, its benefits can be immediately derived. The solution can be more reliable/robust for the people with the limited mobility.

The technologies used in the system are highly proven, open source and confirms to standards. This ensures robustness and reliability of the product and will not obsolete in near feature.

References

1. Vermesan O, Friess P (2014) Internet of things: from research and innovation to market deployment. River Publishers
2. Espressif Systems IOT Team (2015) ESP8266EX datasheet, Version 4.3, Retrieved September 3, 2016, from http://bbs.espressif.com/
3. IBM (2012) Building smarter planet solutions with MQTT and IBM WebSphere MQ telemetry, September 2012. www.ibm.com/redbooks
4. Lamie WE (2016) Using RTOS in embedded devices. Retrieved August 2016
5. http://electronicdesign.com/embedded/11-myths-about-using-rtos-iot-devices
6. Brickous R (2015) GPS guided walking cane. Patent: US 8812231 B1, Aug 2014
7. Jinuo L (2014) Street guiding device for the disabled. Patent: CN 104042431, date 17 Sep 2014

Design and Implementation of Universal Digital Demodulator Using Neural Network Approaches

J. Hariprasad , **Ugra Mohan Roy** , **and Hariharan Ramasangu**

Abstract Universal digital demodulator (UDD) is capable of demodulating more than one type of digital modulated signal. The existing universal demodulators/modulators demodulate the signal based on the input given to the select lines of the demodulator by the user. There is no inherent ability to detect the demodulation scheme. In this paper, a neural network-based universal demodulator for detection as well as demodulation of the received signal is proposed. The use of neural network enables the automatic identification of the demodulation scheme and minimizes the hardware redundancy. This paper presents the implementation of the probabilistic neural network-based universal demodulator for the demodulation of binary phase shift keying (BPSK), frequency shift keying (FSK) and amplitude shift keying (ASK) modulated signals. The functionality of the algorithm is validated by implementing it in MATLAB software. The designed algorithm is ported to Raspberry Pi hardware and it is found that the receiver works up to a signal-to-noise ratio (SNR) of 15 dB. Time taken to process a pair of bits is found to be $0.162\ \mu s$. Overall power consumption including the RF section of the design is found to be 2.5 W.

Keywords Universal demodulator · Probabilistic neural network · Artificial intelligence

1 Introduction to Universal Demodulator

The modern communication system demands for minimal radio frequency (RF) hardware, zero intermediate frequency (ZIF) signal processing and programmable architecture. The universal demodulator is a kind of demodulator which is capable of demodulating frequency shift keying (FSK), phase shift keying (PSK) and amplitude shift keying (ASK) signals.

In the universal demodulator, the RF signal from the antenna is fed to the mixer circuit. The RF frequency is converted to IF frequency using the mixer. The phase

J. Hariprasad · U. M. Roy (✉) · H. Ramasangu
Ramaiah University of Applied Sciences, Bengaluru, India
e-mail: ugraugra1976g@gmail.com

locked loop (PLL) helps to generate the local carrier for down conversion. The down-converted signal is digitized by using the analog to digital converter (ADC). The digital signal is processed either using a processor, field programmable gate arrays (FPGA) or application-specific integrated circuits (ASIC).

The sampled data from the ADC is given to the Costas-based detector for PSK demodulation, voltage-controlled oscillator (VCO) for FSK demodulation and square law detector for ASK demodulation. The demodulated data from each path is given to a 3:1 multiplexer. The output of the Mux depends on the user selection input. In order to get the correct data at the output, the user must have prior knowledge about the modulation scheme which is applied to the received signal.

In case the user does not know the modulation scheme which is used to modulate the signal, then the user cannot decide the selection of Mux [1]. Hence, there is a need to design a universal demodulator architecture which is capable of identifying the modulation scheme and demodulate the data according to the identified scheme. A neural network is capable of identifying the demodulation scheme based on the priory training and demodulates the signal according to the identified class of demodulation. The processing speed of probabilistic neural network provides an advantage over other neural networks, since there is no back propagation in the network.

In the universal demodulator, for each demodulation scheme, there is a separate hardware path to demodulate the signal. Due to the redundant hardware, there is loss of power in the receiver. If the architecture is implemented on the processor, because of the redundant processing, there is a possibility of delay in the processed bit [2]. By implementing the architecture using neural network, the receiver is provided with the ability to identify the modulation scheme, reduce the power by eliminating redundant hardware and also reduce latency of bit calculations.

2 Design of Universal Demodulator Using Probabilistic Neural Network

2.1 Proposed Architecture of the Universal Demodulator

In the proposed architecture of the universal demodulator, the incoming analog radio frequency signal is down converted and sampled using the ADC. The ADC samples are converted to frames of size 200k samples each, using FIFO, and fed to the probabilistic neural network, where it identifies the modulation scheme. Based on the class of the sample modulation scheme, a pair of data bits is identified [3]. These data bits are serially sent out of the hardware. The specifications of the universal demodulator are shown in Table 1.

The performance of the designed algorithm is evaluated by implementing it on Raspberry Pi hardware. Based on the hardware implementation, power, time taken for the computation and area of the hardware are analyzed. The top-level block diagram of the universal demodulator using probabilistic neural network is as shown in Fig. 1.

Table 1 Universal demodulator specifications	Modulation scheme	Data rate (kbps)	Carrier frequency
	BPSK	38	50 kHz
	FSK	38	F1 = 45 kHz, F2 = 48 kHz
	ASK	38	50 kHz
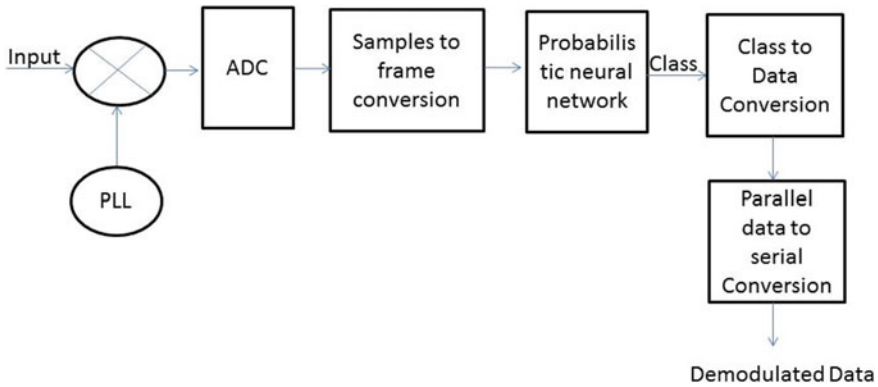
Fig. 1 Universal demodulator using probabilistic neural network

2.2 Probabilistic Neural Network Design

2.2.1 Training Vector Generation

The training set must represent the actual data set corresponding to the classification. Adding a training set is equivalent to adding a neuron to the pattern layer. As the training set increases, the estimated probability density function (PDF) reaches to the actual value. In the universal demodulator design, the training sets are the data bits, modulated with different modulation schemes [4].

Identification of the data bits embedded inside the incoming signal is possible only when there is a transition in the carrier wave. By using only one bit for the pattern layer, it is difficult to classify the data bits. Hence, in the proposed design, two data bits are used for the classification. Two data bits and three modulation schemes form 12 combinations. Hence, there are 12 classes for the classification with vector size of 200 samples for pair of bits.

To generate the training sets with the above parameters, transmitters are designed to modulate the data using the carrier of the required frequency and the generated signal is then stored as the training set. The required transmitter architecture for the training vector generation is designed using MATLAB software and samples are stored to train the neural network.

2.2.2   Designing the PNN Architecture

The probabilistic neural network has four layers: input layer, pattern layer, summation layer and output layer. The input layer consists of an array of 200k samples of the incoming signal to the demodulator. This input has to be passed to all the neurons of the pattern layer. The pattern layer consists of PDF estimator with respect to each class and various signal-to-noise ratio (SNR). The training vectors are generated corresponding to three different SNRs, which enable the classifier to handle the worst noise scenario [5].

The equation to estimate the PDF is given by Eq. 1.

$$y_{ik} = e^{-\frac{\|x - x_k^2\|}{\sigma^2}} \tag{1}$$

where σ is the smoothing parameter, y_{ik} is the output of the ith class—kth training set [each class has three different training sets], x_k is the kth training set and x is the input vector.

In the summation layer of the neural network, all the samples corresponding to the same class are averaged to get the precise value corresponding to that sample. General equation for the summation layer is given by Eq. 2

$$f_i(x) = \frac{1}{n\sigma} \sum_{k=1}^{n} y_{ik} \tag{2}$$

where $f_i(x)$ is the probability density function, n is the number of training vectors corresponding to same class; here $n = 3$.

In the output layer, the output corresponding to each class from the pattern layer is compared. The highest value among the pattern layer is declared as the class of the input vector [5].

The general architecture of the probabilistic neural network is as shown in Fig. 2.

2.2.3   Hardware Implementation of the Universal Demodulator

In order to validate the hardware performance of the designed universal demodulator, the algorithm implemented in MATLAB software is converted into equivalent python code for Raspberry Pi hardware. The hardware architecture of the universal demodulator on Raspberry Pi platform is as shown in Fig. 3.

3   Results

The BPSK, ASK and FSK modulated test signals, each containing 100 bits are generated using MATLAB software. The test sample is combined with Gaussian noise at various SNR levels and fed to the designed universal demodulator architecture.

Fig. 2 Deep neural network architecture for the universal demodulator
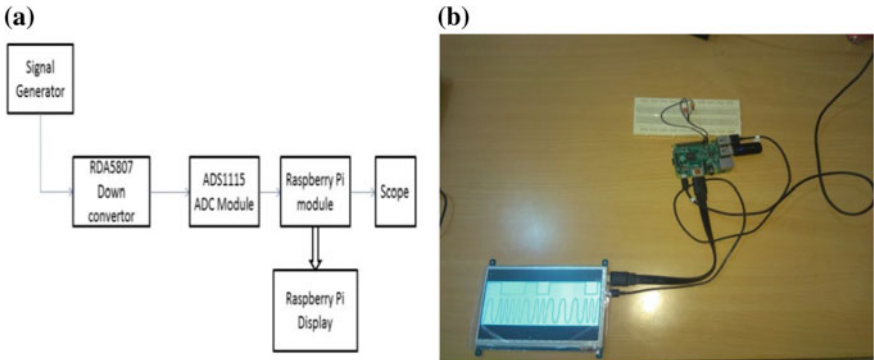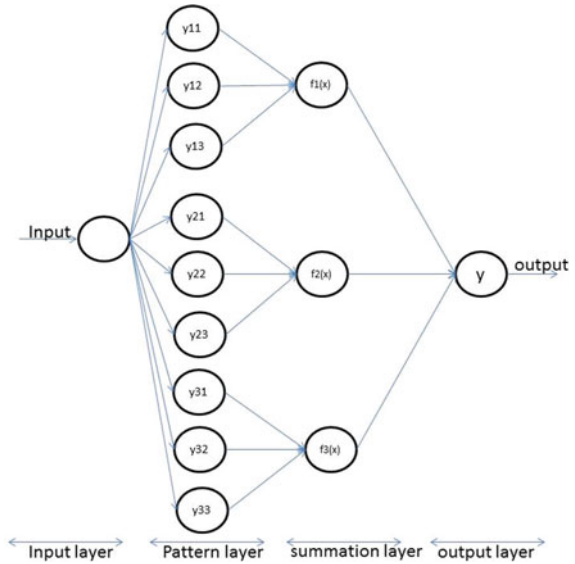
Fig. 3 **a** Top-level block diagram and **b** hardware setup for testing of the UDD

The demodulated data is compared with the original data to estimate the bit error rate (BER). It is found that the universal demodulator is able to demodulate the data without any error up to 15 dB SNR. The test result for the ASK, BPSK and FSK signals at various SNR levels is as shown in Figs. 4, 5 and 6. From the MATLAB results, it is found that the estimated time to compute 1 bit is 0.162 μs. The developed algorithm is implemented on the Raspberry Pi platform, the power consumption of the overall architecture, including ADC and down converter, is found to be 2.5 W and time taken to process a pair of bit is found to be 0.162 μs. Performance comparison of proposed architecture with respect to existing architectures is shown in Table 2.
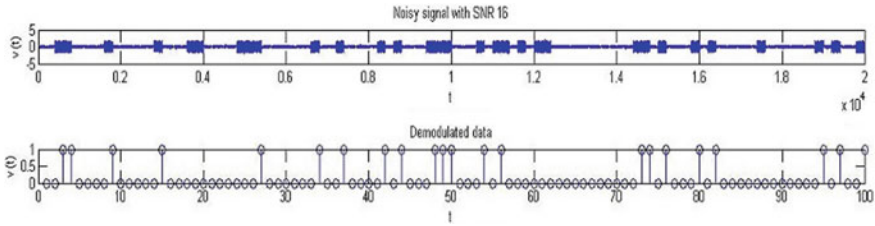
Fig. 4 ASK simulation result for demodulated data bits using UDD
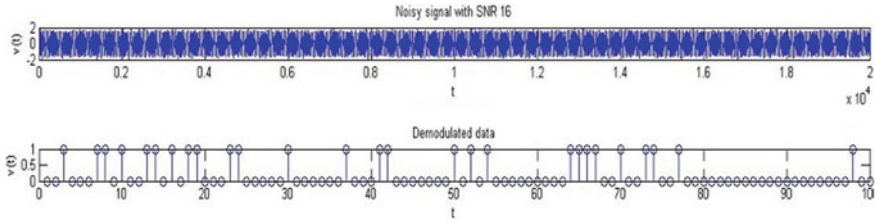
Fig. 5 PSK simulation result for demodulated data bits using UDD
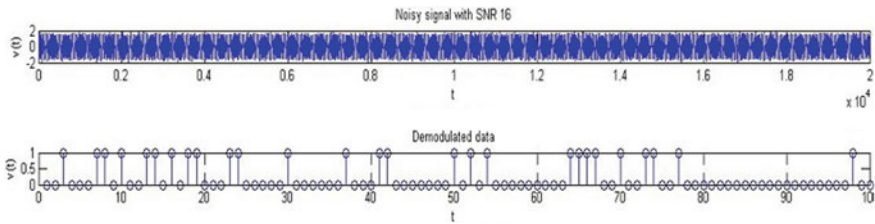
Fig. 6 FSK simulation result for demodulated data bits using UDD

Table 2 Performance comparison of various architectures

Bit calculation time	$0.162\,\mu s$ (UDD)	<1 s [6]
SNR	15 dB (UDD)	20 dB [6]
Power consumption	2.5 W (UDD)	25 W [7]

4 Conclusion

We have proposed a neural network-based universal demodulator for the detection as well as demodulation of the transmitted data. The use of neural network enables the automatic identification of the demodulation scheme and minimizes hardware redundancy. The simulation of the neural network-based universal demodulator for the demodulation of BPSK, BFSK and BASK has been carried out. It is concluded that the proposed neural network-based architecture is able to demodulate the data

without error, up to a SNR of 15 dB for ASK, PSK and FSK. From the hardware implementation, it is found that power consumption for the universal demodulator is 2.5 W and the time required to calculate the pair of bits is 0.162 µs.

References

1. Zhang M, Kim S, Universal soft decision demodulator for M-array adaptive modulation system. IEEE, pp 572–572
2. Zheng B, Wang X, Wen M, Chen F (2017) Soft demodulation algorithms for generalized spatial modulation using deterministic sequential monte carlo. IEEE Trans Wirel Commun
3. Amini M, Balarastaghi E (2011) Universal neural network demodulator for software defined radio. Int J Mach Learn Comput 305–310
4. Tang Y, Xiao-lan LV (2011) Research on the modulation and demodulation of BPSK and BDPSK simulator based on the MATLAB. IEEE, pp 1239–1241
5. Specht DF (1990) Neural network, vol 3. Pergamon Press
6. Mohamed MT (2012) Digital modulation classification through time and frequency domain features using neural networks. In: International symposium on telecommunication. IEEE
7. CISCO Homepage. https://www.cisco.com/c/dam/en/us/. Last accessed 14 Apr 2018

Design Approach Toward the Development of Three Logical Input Optical Look-up Table (OLUT) and Optical Memory

Durgaprasad Bhat [ID] **, Ugra Mohan Roy** [ID] **, and Abdul Imran Rasheed** [ID]

Abstract Look-up table (LUT) (Jiangt et al. in system on programmable chip research department, IEEE [1]) is the basic element used in field programmable gate arrays (FPGAs). These LUTs are implemented in optical domain called OLUT. Conventional three-input LUT has eight 1-bit SRAMs and seven 2:1 multiplexers connected in three layers. This design has an approach toward the development of OLUT with all the components as purely optical, including SRAM. Ring resonator is the basic component used in the development of 2:1 multiplexer and 1-bit SRAM has been developed by using Mach-Zehnder interferometer. 1-bit SRAM has been simulated separately, but during the integration of optical 2:1 MUX into OLUT, optical switches replace the actual 1-bit SRAM.

Keywords Optical look-up table (OLUT) · Wavelength division multiplexing (WDM) · Static random access memory (SRAM) · Ring resonator

1 Introduction

In twenty-first century, technology is rapidly growing in all domains. High-speed communication and data transfers are playing a key role in growing technologies, such as medical, aerospace and defense. Very large-scale integration (VLSI) plays a major role in terms of manufacturing high-speed low-power processors, system-on-chips (SOCs) and programmable integrated circuits (ICs). Existing CMOS transistor technology has upgraded till 7 nm to reduce the power and increase the speed and performance. Even though the emerging technologies such as Fin-FET and CNT-FET can still improve, the speed and performances are limited due to speed and power boundaries. Photonics is the state-of-the-art technology to satisfy the above-stated constraint of the existing technology. Integrated photonics technique has been used to develop an optical look-up table (OLUT), inherited from the Xilinx FPGA

D. Bhat (✉) · U. M. Roy · A. I. Rasheed
Ramaiah University of Applied Sciences, Bengaluru, India
e-mail: dprasad019@gmail.com

architecture [1, 2]. LUT is part of Slice, which is an intern part of configurable logic blocks (CLBs).

The three-input OLUT has three levels of 2:1 multiplexer (MUX), which is built into an 8:1 MUX with eight single-bit SRAMs to store the input weights at input. The same LUT architecture [1] is inherited into OLUT in a different manner using optical ring resonators. Symmetry and change in refractive index property of the micro-ring resonator (MRR) to build multiplexers is used to develop an OLUT [3].

2 Background and Related Works

2.1 Electro-optic Effect

Electro-optic is a phenomenon in which application of electric field changes the frequency response due to the property change in the optical material, also causing the change in refractive index. There are few theories and model with respect to electro-optic effect, like free carrier effect, and Soreff and Bennett model [4].

According to the Soreff and Bennett model [4] and Kerr's effect, the change in the electric field causes the change in refractive index, and depends on the Kerr's constant. Eq. 1 is given as:

$$\Delta n_{\text{eff}} = \lambda K E^2 \tag{1}$$

where λ is the wavelength, E is the electric field, Δn_{eff} is change in the effective refractive index and K is the Kerr's constant (2.7×10^{-9} m V^{-2}).

2.2 Micro-Ring Resonator and Silicon Photonics

Micro-ring resonator (MRR) works on the basic two concepts: (i) constructive interference and (ii) total internal reflection. MRR has four ports: input, through, add and drop ports, as shown in Fig. 1. Add-drop filtering, symmetry of ring resonators will be an advantage during the integration of optical devices.

In silicon photonics, a concept called silicon-on-insulator (SOI) is used, in which silicon is placed on the top of silica layer. Placing the optical components over the SOI has advantage that it will be less sensitive to noise. This arrangement can be easily fabricated by available semiconductor fabrication method [5].

Fig. 1 Micro-ring resonator (MRR)
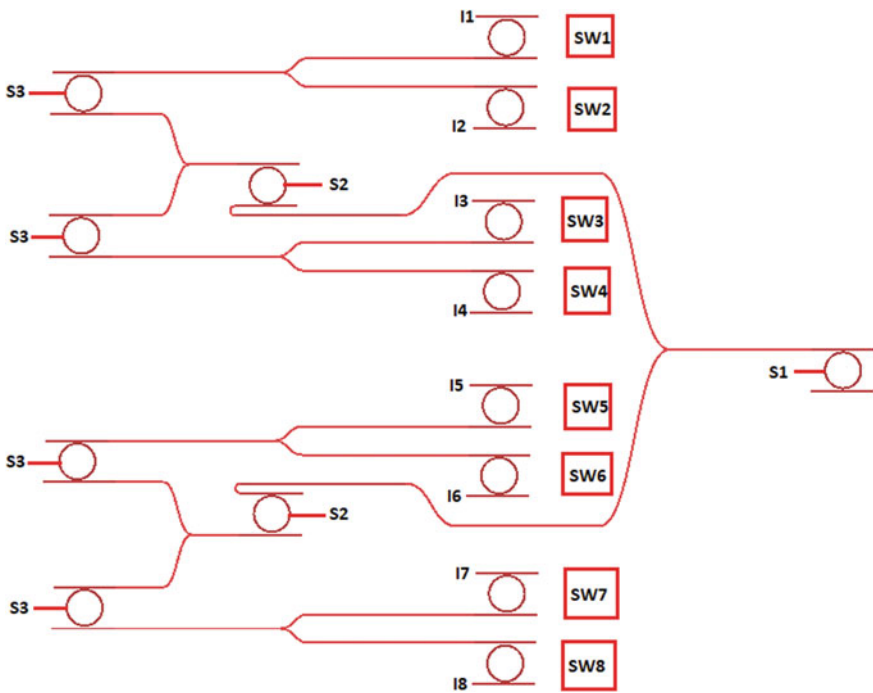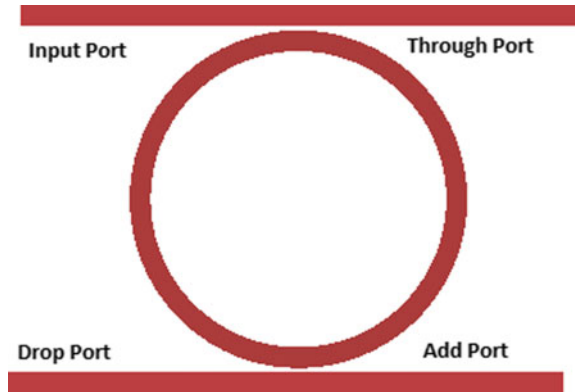
Fig. 2 8:1 Optical multiplexer forms three-input OLUT

3 Design and Implementation of OLUT and Optical Memory

Optical memory has been developed for replacing the SRAM part of conventional LUT during the development of OLUT. Existing OLUT has been designed using

2:1 optical multiplexer and opto-electric switch. Opto-electric switch replaces the SRAM part, since optical memories integration with developed 2:1 multiplexer has a challenge in simulation.

3.1   Ring Resonator Design

Designing of the optical components is very challenging, since small modification effects cause larger change in terms of output behavior. Relation between the ring radius, wavelength and n_{eff} is given by the formula:

$$m\lambda = 2\pi n_{eff} R \tag{2}$$

where m is the mode number, λ represents the wavelength to be used for the design (1.55 µm), n_{eff} is the effective refractive index depending on the material and dimensions (measured index is approx. 2.65) and R is the radius of the ring. Micro-ring resonator is designed using lumerical finite-difference time domain (FDTD). In FDTD wavelength can be found using frequency monitor. The laser input to the ring is ranging from 1.45 to 1.65 µm.

3.2   Design of PN Micro-Ring Resonator

According to the opto-electric effect when the voltage is applied there is a change in refractive index which in turn causes the shift in wavelength. As shown in Fig. 3, PN junction [6] is developed around the ring with p substrate (cathode) and n substrate (anode). The p and n substrates use the Al (aluminum) as the material. A voltage of 0.5 V causes the change in refractive index.

$$n_{eff} = F(V) \tag{3}$$

Equation (3) can be written as:
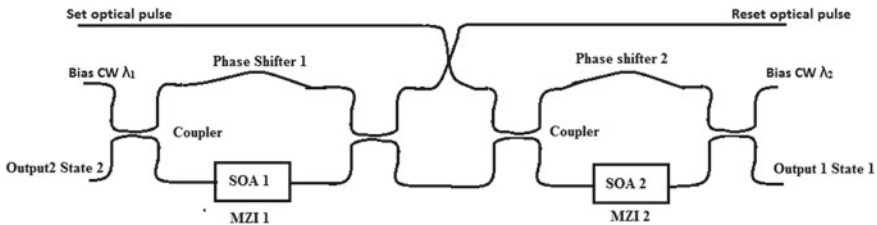
Fig. 3   MZI-based flip-flop [7]
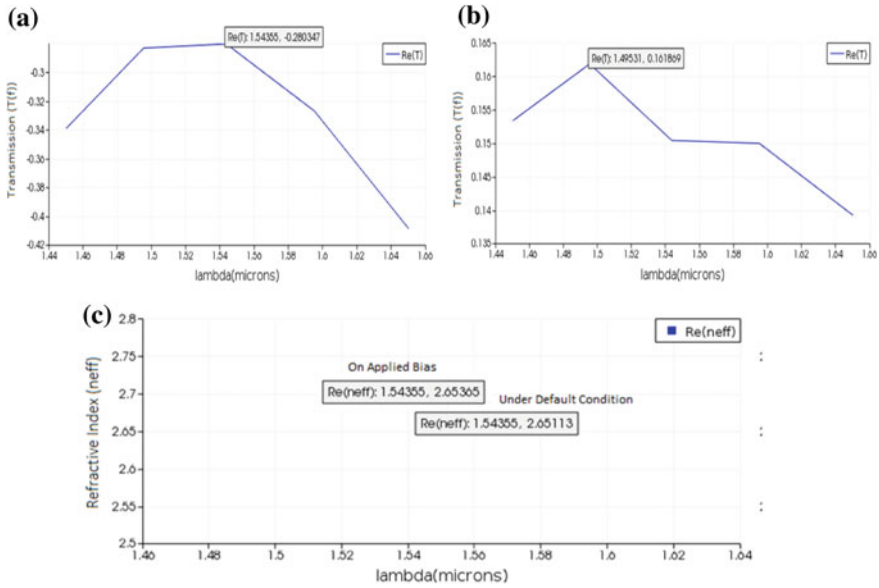
Fig. 4 **a** Default wavelength measured. **b** Shifted wavelength due to change in refractive index. **c** Change in refractive index measured

$$\Delta n_{\text{eff}} = \lambda K E^2 \tag{4}$$

In Eq. (3) n_{eff} is a function of applied bias, which can be represented in terms of electric field (E) as in Eq. (4). In Eq. (3), K is the Kerr constant (2.7×10^{-9} m V^{-2}) [4], λ is the wavelength and Δn_{eff} is the change in refractive index. PN junction [6] MRR is placed on silicon, and the SiO$_2$ layer is placed above the Si, and this forms SOI. These substrates are used with thickness of around 8–10 μm.

3.3 Development of 2:1 Multiplexer and 8:1 Multiplexer to Form Three-Input OLUT

Digital equivalent of multiplexer has one select line and two inputs. When select line is at logic state '0', then first input is selected; when select line is at logic state '1', then second input is selected. In case of optical 2:1 MUX select line is considered as external voltage input and different wavelength is considered as logic state '1' and '0', as shown in Table 1 (Fig. 3).

Refractive index measured before applying the bias is 2.65113, and change in refractive index of 2.65365 is measured after applying the bias voltage.

Developing 8:1 MUX involves integrating the developed 2:1 MUX according to the proposed architecture. Different waveguide structures are used to reduce the

Table 1 Interpretation of wavelength into logic states

Wavelength	Voltage input	Logic states
λ1 (1.54355 μm)	Without bias voltage (0 V)	'0'
λ2 (1.49531 μm)	Voltage (V1)	'1'

transmission loss. The three main waveguide structures used are: (i) bent waveguide; (ii) S waveguide and (iii) Y Combiner. Figure 2 shows the integrated 8:1 multiplexer into OLUT. The S1, S2 and S3 are three select lines that chose the one input out of eight inputs. These select lines are the voltage inputs indicating the logic states as per Table 1.

3.4 Design of Optical Memories (Flip-Flops)

Flip-flop is the basic element of the memory. It is used to store single-bit data. The digital flip-flop should be realized in optical domain to develop OLUT using all optical components. Optical flip-flop development can be explored in two ways, either by using Mach-Zehnder interferometer (MZI) or micro-ring resonator (MRR).

In this paper flip-flop using MZI has been simulated. MZI is developed using optical components such as semiconductor optical amplifier (SOA) couplers [7].

This MZI-based optical flip-flop is developed and simulated in Opti-system and the results are observed and shown in Fig. 5.
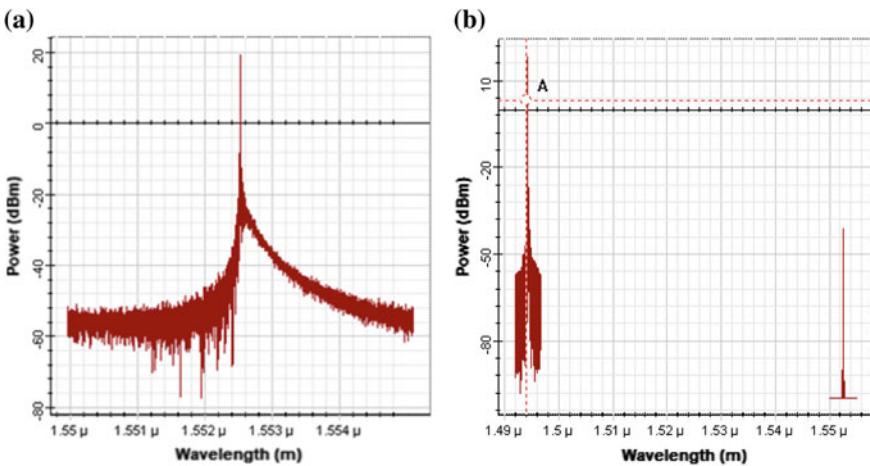
Fig. 5 **a** Under reset with default wavelength (1.5525 μm). **b** Under set condition with shifted wavelength (1.4947 μm)

Table 2 Comparison between existing OLUT and developed OLUT architecture

Properties	Existing OLUT [3]	Developed OLUT
Material used	Silicon (Si)	Silicon (Si)
Basic component	Micro-ring resonator	Micro-ring resonator
Power	10 mW [3]	5.3×10^{-10} W
Speed	Can able to achieve till 100 GHz with few limitations due to electrical components [3]	Can achieve speed up to 500 GHz, since it has optical waveguides
Wavelength	As the number of input to the LUT increases wavelength will increase accordingly	Only two wavelengths are used to interpret the logic states even when the number of input to the LUT increases

3.5 Comparison of Existing OLUT and Developed OLUT

See Table 2.

4 Results and Discussions

Ring resonator is designed for wavelength of 1.55 µm with input ranging from 1.45 to 1.65 µm. As shown in Fig. 4a, the default wavelength measured is 1.54355 µm with the refractive index as 2.65113, which is considered to be in logic state '0' when bias voltage of 0.5 V (logic '1') is applied, which produces the change in refractive index of 2.65365; hence wavelength gets shifted to 1.49531 µm is considered to be in logic state '1', as shown in Fig. 4b. Figure 4c shows measured refractive index for default condition and change due to the applied bias.

MZI-based optical memory has been simulated, and change in the state with respect to reset and set inputs is as shown in Fig. 5a and b, respectively. Under the reset condition output wavelength is found to be 1.5525 µm with logic state '0'; when the set input is given to the design, output wavelength is found to be 1.4947 µm with logic state as '1'.

5 Conclusions

In this paper, we proposed an OLUT architecture and memory design, which can be fabricated with existing semiconductor foundry. The designed OLUT consumes very less space (approx. 20,000 µm^2) and less power (around 5.3×10^{-10} W). MZI-based optical memory has been simulated, and set and reset conditions have been observed. Future development involves integrating optical memory into OLUT. Opto-electric

switch can be replaced with optical memory to have better performance, and optical pump beam-based flip-flop can be developed using micro-ring resonators.

References

1. Jiangt Z, Lint CY, Yangt L, Wangt F, Yan H (2014) Exploring architecture parameters for dual-output LUT based FPGAs. In: System on programmable chip research department. IEEE
2. Rose J, Francis RJ, Lewis D, Chow P (1990) Architecture of programmable gate arrays: the effect of logic block functionality on area efficiency. IEEE, pp 1217–1225
3. Li Z, Le Beux S, Monat C, Letartre X, O'Connor I (2013) Optical look up table. Lyon Institute of Nanotechnology, Ecole Centrale de Lyon, Ecully
4. Soref RA, Bennett BR (1987) Electrooptical effects in silicon. IEEE J Quantum Electron QE 23(1)
5. Vandana B (2013) A theoretical study of low power soi technology. IOSR J VLSI Signal Process (IOSR-JVSP) 2(5):30–37
6. Peter E, Thomas A, Dhawan A, Sarangi SR (2016) Active microring based tunable optical power splitters 2–3. Computer Science and Engineering, IIT Delhi
7. Bogoni A, Berrettini G, Ghelfi P, Malacarne A, Meloni G, Potì L, Wang J (2010) All-optical flip-flops based on semiconductor technologies. Intech

Automotive Crash Detection Using Multi-sensor Data Fusion

M. S. Supriya and N. D. Gangadhar

Abstract The focus of this paper is the early detection of the frontal crash in automobiles, for the purpose of effective Airbag deployment decision, using information from multiple sensors deployed on-board, specifically accelerometer sensors located on the vehicle engine and on the driver's seat-belt. Measured acceleration signal data streams from the sensors are fused, based on principles of Multi-Sensor Data Fusion (MSDF), for faster detection of a crash. Adaptive Kalman filtering is employed for simultaneous estimation of individual sensor data and their signal level fusion. The proposed crash detection system is simulated in MATLAB and validated using US-NHSTA (National Highway Safety Traffic Administration) automotive crash datasets. For comparative evaluation, crash detection algorithms for individual sensor data are also simulated and tested on the same datasets. The MSDF based system resulted in faster crash detection when compared to single sensor systems.

Keywords Crash detection · Airbag deployment · Sensor fusion · MSDF · Accelerometer · Automobile · Kalman filter · Adaptive Kalman filter · Change detection

1 Introduction

Automobile accidents are an important socio-economic problem, they cost human lives [1]. Hence, the Vehicle Safety System (VSS) is subject to increased attention and has become prominent research area [6]. One of the challenges of VSS is the quick

M. S. Supriya · N. D. Gangadhar (✉)
Computer Science and Engineering, Faculty of Engineering and Technology,
M. S. Ramaiah University of Applied Sciences, Bengaluru, India
e-mail: gangadhar.cs.et@msruas.ac.in

M. S. Supriya
e-mail: supriya.cs.et@msruas.ac.in

deployment of the airbag by detecting the crash early and accurately considering the crash severity [2, 6, 10]. In airbag deployment systems, sensors play a vital role in the evaluation of the crash severity for the arriving at the decision when and whether to deploy the airbag [10]. The associated control system should recognise crash severity and deploy the airbags during emergency within time [2, 10].

In recent past, Multi-Sensor Data Fusion (MSDF), wherein data from more than one sensor is employed, has seen tremendous progress and application to a wide variety of fields as it leads to improved measurement accuracy even in the presence of severe interference noise [11]. MSDF can be developed at signal or decision levels. In signal level fusion, the sensor data is fused using the signals before being used for control or decision making, whereas in decision fusion, independent control decisions arrived using individual sensor data are combined. In the automotive domain, MSDF based multiple object tracking and detection has been proposed for collision or *crash avoidance* [8]. MSDF for *crash detection* (or *crash sensing*) has hardly been investigated; to the best of our knowledge [6, 16], are the only works which employed MSDF for decision level data fusion. Majority of crash detection/sensing algorithms employ single sensor, mostly an accelerometer. When single sensor is located on vehicle to detect the crash, there are chances of sensor sensing resulting in wrong crash detection or failure to detect the crash. In order to predict or detect crash more effectively, more than one sensor may ben employed. Hence, MSDF has the potential to increase the efficiency of the crash detection by using more than one sensor. The sensor measurements can be fused to detect the crash early and accurately to deploy the airbag in time.

Research on Crash Sensing/Detection [2, 9], Collision Sensors [4, 13], Airbag Deployment [2, 7, 10], Adaptive Kalman Filtering for MSDF [5, 15] and Multi-Sensor Data Fusion [4, 8, 15] laid the foundation for this work. References [2, 3] discuss different automotive crash sensing techniques and airbag deployment. In [5], an Adaptive Fuzzy Logic System is developed to tackle the divergence of a Kalman filter under coloured noise used for robot navigation. Kalman gain fusion using Adaptive Kalman Filter is shown to be efficient compared to data fusion under data loss by [15]. Reference [8] demonstrates that signal level fusion of the sensor data resulted in improving the overall tracking accuracy by decreasing the false positives. In [6], decision level fusion for frontal crash detection for airbag deployment decision is proposed. Sangorrin [14] presents an automatic emergency braking system used during frontal collision avoidance and shows that high robustness in object detection can be achieved using MSDF. This work shows the potential of MSDF for situational awareness and decision fusion. MSDF using the Magneto-Resistive and Sonar sensors for imminent collision detection in cars to measure velocity, position and orientation in [17] shows that MSDF can be employed for reliable proximity estimation. Time-to-collision estimation prediction is carried out by using different out-of sequence algorithms in [18], wherein crash prediction is carried out using MSDF.

It can be concluded that most of the implemented crash sensing systems use single sensor (accelerometer), MSDF has potential to improve the accuracy and efficiency of automotive control system. With almost all of the papers employing MSDF focus

on crash prediction or collision avoidance, estimating the time to collision, there is a need for investigating its use in improving crash/collision detection performance. In the present work, signal level MSDF is developed for efficiently detecting the crash in automobiles for early airbag deployment in the event of a crash. It deals with frontal crash detection to help in the rescue of the driver by faster airbag deployment during crash.

The rest of the paper is organised as follows: Sect. 2 presents the development of the crash sensing system. Results from the validation of the system are presented in Sect. 3. Finally, the Conclusions section draws pertinent conclusions based on the work and discusses potential future directions.

2 MSDF Based Crash Detection System Development

The block diagram of the proposed crash detection system is shown in Fig. 1.

Sensors The electronic sensors used to develop the system are

1. Accelerometer on vehicle measuring vehicle acceleration or deceleration
2. Accelerometer on seat-belt, measuring acceleration or deceleration of human (driver).

System Dynamics The evolution of the position, velocity and acceleration of the automobile is given by (with the time step being normalised to unity)

$$p_{k+1} = p_k + v_k + 0.5a_k, \quad v_{k+1} = v_k + a_k, \quad a_{k+1} = 1.5a_k \tag{1}$$

where the last equation is empirically derived based on the deceleration dynamics from crash test data. With the state defined as $x_k = (p_k, v_k, a_k)^T$, the linear dynamic model of the system is given by $x_{k+1} = A x_k$, with A being the State Transition Matrix. Since the accelerometer sensors measures only the acceleration part of the state, the output/measurement equation is $y_k = C x_k$, $C = (0, 0, 1)^T$. The system evolutionary process noise and measurement noise are assumed to be zero mean additive white Gaussian whose variances are, respectively, Q and R.

Kalman Filter Design and its Tuning Owing to the linearity and additive white Gaussian noises, Kalman Filter is the optimal filter to estimate the system state. The Kalman Filter is tuned by choosing the process and measurement noise co-variances
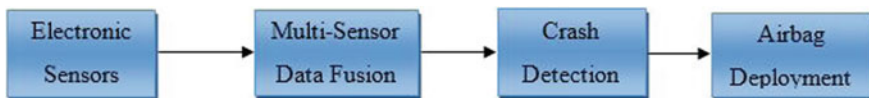
Fig. 1 Block diagram of sensor data fusion system

using test data. Due to the high uncertain dynamics during crash, the process noise co-variance Q is to be set a high value (equal to 6.5) and measurement noise co-variance R is relatively set a low value (equal to 1).

Crash Detection Algorithm using Sensors Individually The measured crash test data of the sensor will be passed to the Kalman Filter tuned for that sensor. The output of the Kalman Filter is the estimated values of position, velocity and acceleration of the vehicle. The estimated acceleration is then passed to change detection algorithm.

Crash Detection Algorithm using Signal Level Multi-Sensor Data Fusion The crash detection algorithm using signal level fusion of accelerometer measurements using MSDF. The measured crash test data of accelerometer sensors on the vehicle and the seat-belt of the driver are passed to individual Kalman Filters to filter the noise and estimate the state of the vehicle. A Kalman filter based MSDF [15] is employed for signal level fusion of the accelerometer measurements to obtain a single acceleration sequence data. This is achieved by subtracting the estimated vehicle acceleration from the estimated acceleration of the driver seat-belt. This difference gives the error which is then used to correct the measured crash test data of the vehicle acceleration by a multiplication factor based on the prediction of co-variances of both the sensors. The corresponding Kalman update equation, adapted from [15], is

$$X_{\text{fused}} = (P_1(P_1 + P_2)^{-1})(X_{1,\text{estimated}} - X_{2,\text{estimated}}) \tag{2}$$

The resultant fused acceleration is then passed to the change detection algorithm setup to detect the crash based on the threshold fixed.

Change Detection Algorithm CUMSUM (Cumulative Sum) algorithm is used as the change detection algorithm to detect the change in the estimated state of the system. The output of the Kalman Filter estimation of the signal is passed to the CUMSUM with an appropriately chosen threshold to detect the crash. The CUMSUM repeatedly checks if the signal crosses the threshold set, given the time at which the crash is detected. The airbag control unit must be triggered or signalled to be deployed to protect the driver during crash. The time at which the signal changes is the time the crash is detected. If crash is detected, airbag control unit can be triggered to deploy the airbag immediately. As long as the crash is not detected, airbag is not deployed.

Crash Detection Thresholds The deceleration ranges employed in some real-life vehicle models for crash detection [10] are used to determine the thresholds for the crash detection algorithms. The thresholds fixed are tabulated in Table 1.

Implementation All the algorithms and data processing functionality is implemented and simulated in MATLAB.

Table 1 Crash detection thresholds

Sensor	Threshold g units (m/s^2)
Accelerometer on vehicle	$-7.85g$ (-76.93)
Accelerometer on seat-belt (Driver)	$-1g$ (-9.8)
Fused sensor acceleration	$-2.85g$ (-27.93)

3   Results and Discussion

The validation is carried out for two measured frontal impact collision crash test datasets from National Highway Traffic Safety Administration (NHTSA), the government agency of U.S. [12]. The results of MSDF obtained from one of the datasets are shown in Figs. 2 and 3. The plots contain measured and estimated data from vehicle accelerometer, driver seat-belt accelerometer and the acceleration estimated using MSDF, CUMSUM of the fused acceleration for crash detection and airbag deployment decision.

The time taken for crash detection using the measurements of accelerometer on the vehicle, accelerometer on the driver seat-belt and fused acceleration are tabulated in Table 2. The table also gives the relative gain in efficiency (in %) of the MSDF algorithm with respect to the fastest single sensor based crash detection time. It can be observed that the MSDF based crash sensing algorithm provides faster detection of the crash when compared to vehicle accelerometer based on its performance on the crash datasets tested. From the plots, it is clear that the CUMSUM based change detection helps in more reliable detection in the presence of high noise clutter accompanying the accelerometer measurements during the crash.
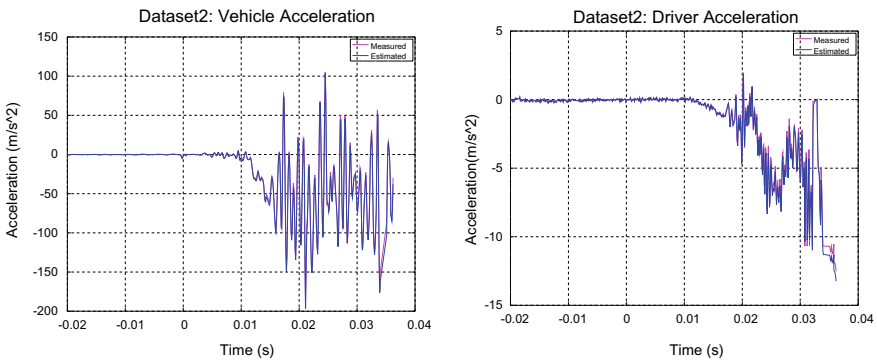
Fig. 2   MSDF based crash detection: individual sensor estimation
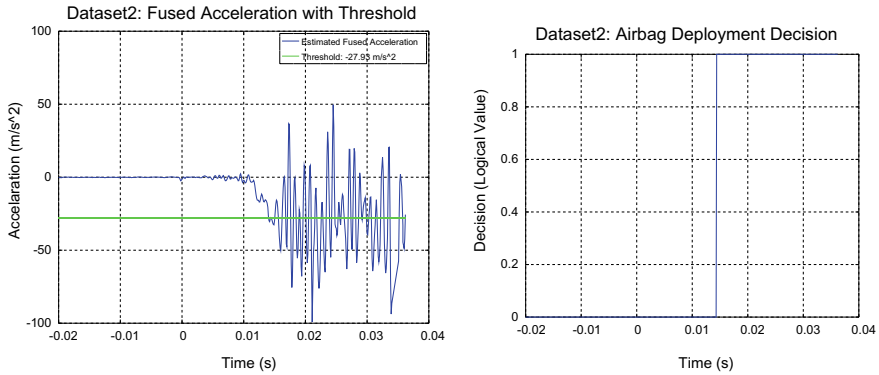
Fig. 3 MSDF based crash detection: fused signal based detection

Table 2 Crash detection performance

Measurement	Detection time (s)	
	Dataset2	Dataset1
Accelerometer on vehicle	0.0345	0.0235
Accelerometer on seat-belt	0.0310	0.0320
Fused sensor acceleration	0.0140	0.0222
Relative gain	59.42%	5.53%

4 Conclusion

An automobile crash detection algorithm using Multi-Sensor Data Fusion is developed which combines data from accelerometers on the vehicle and driver's seat-belt. Kalman filters are employed for estimation of the measurement values from noisy data as well as for signal level fusion. CUMSUM based change detection is employed for reliable change detection. MSDF based crash sensing using signal level fusion of two accelerometers reduces the crash sensing time when compared to the sensing using only one accelerometer. The work can be used as a basis for the development of a new class of crash detection systems for automobiles and other vehicles based on Multi-Sensor Data Fusion which has the potential for efficient and reliable detection of a crash.

The work can be extended in several directions: The fusion algorithm can be used to develop an embedded system incorporating actual sensors and actuators. The trade-off between the crash efficiency and reliability needs to be investigated. The paper deals with the frontal crash which can be extended to determine the side impact by using suitable sensors. To increase the system accuracy in detecting automobile crash, more than two sensors can be fused.

References

1. Blincoe LJ, Miller TR, Zaloshnja E, Lawrence BA (2015) The economic and societal impact of motor vehicle crashes, 2010 (Revised). DOT HS 812 013. (US) National Highway Traffic Safety Administration, Washington, DC
2. Chan CY (2002) A treatise on crash sensing for automotive air bag systems. IEEE/ASME Trans Mechatron 7(2):220–234
3. Chan CY (2002) On the detection of vehicular crashes-system characteristics and architecture. IEEE Trans Veh Technol 51(1):180–193
4. García Fernández F (2012) Data fusion architecture for intelligent vehicles
5. Green D, Sasiadek J (1998) Path tracking, obstacle avoidance and dead reckoning by an autonomous planetary rover. Int J Heavy Veh Syst 5(1):1–24
6. Hannan M, Hussain A, Mohamed A, Samad SA (2008) Development of an embedded vehicle safety system for frontal crash detection. Int J Crashworthiness 13(5):579–587
7. Hannan M, Hussain A, Samad SA (2011) Sensing systems and algorithms for airbag deployment decision. IEEE Sens J 11(4):888–890
8. Herpel T, Lauer C, German R, Salzberger J (2008) Multi-sensor data fusion in automotive applications. In: 2008 3rd international conference on sensing technology. IEEE, pp 206–211
9. Kamiński T, Niezgoda M, Kruszewski M, Grzeszczyk R, Drop T, Filipek P (2012) Collision detection algorithms in the ecall system. J KONES 19:267–274
10. Kendall J, Solomon KA (2014) Air bag deployment criteria. Forensic Exam
11. Liggins M, Hall D, Llinas J (eds) (2008) Handbook of multisensor data fusion: theory and practice. CRC Press
12. NHTSA: National highway traffic safety administration (US). www.nhtsa.gov
13. Robert Bosch (2017) Method and control unit for detecting an impact of a collision object on a vehicle. US Patent 9,586,548 B2
14. Sangorrin JS, Sparbert J, Ahlrichs U, Branz W, Schwindt O (2010) Sensor data fusion for active safety systems. SAE Int J Passeng Cars-Electron Electr Syst 3(2010-01-2332):154–161
15. Shanthakumar N, Girija G, Raol J (2001) Performance of kalman and gain fusion algorithms for sensor data fusion with measurement loss. In: International radar symposium India (IRSI)
16. Supriya MS, Gangadhar ND, Manjunath AG (2017) Reliable automotive crash detection using multi sensor decision fusion. SasTech J 16(2):46–49
17. Taghvaeeyan S, Rajamani R (2014) Two-dimensional sensor system for automotive crash prediction. IEEE Trans Intell Transp Syst 15(1):178–190
18. Westenberger A, Muntzinger M, Gabb M, Fritzsche M, Dietmayer K (2013) Time-to-collision estimation in automotive multi-sensor fusion with delayed measurements. In: Advanced microsystems for automotive applications 2013. Springer, Berlin, pp 13–20

Optical Micro-ring Resonator for Detection of Carbon Dioxide Gas

Karanam Pallavi Koushik and **Sathish Malathi**

Abstract A simulation model of a polymer clad micro-ring resonator gas sensor is proposed. The designed sensor detects carbon dioxide gas. Ring resonator of 11 µm radius is designed with strip waveguide on SOI substrate. Sensitivity of the sensor is calculated and ppm levels are validated with an existing fabricated sensor. The resonant wavelength shift is observed as 0.96 pm with the designed specifications wherein the range of ppm levels is 200–500. Based on the wavelength shifts, the ppm levels are validated with the existing fabricated sensor.

Keywords Micro-ring resonator · Resonant wavelength shift · Silicon on insulator (SOI) · Sensor

1 Introduction

In recent years, integrated optical sensors emerged with an immense usage due to various reasons such as their immunity to electromagnetic interference, high sensitivity, compactness, and compatibility for fiber networks [1]. Detection of gases using a sensor is a challenging task. The basic gas-detecting methods include Metal Oxide Semiconductor (MOS), carbon nanotubes, conducting polymers, moisture-absorbing materials, optical methods, calorimetric, etc. [2]. Conventional MOS sensors require pre-heating to sense gas molecules. Hence a conducting polymer-based gas has been chosen for the simulation of the proposed work. Similarly, the sensing methods used in optical sensors are classified as refractive index sensing, absorption sensing, and fluorescence sensing, and out of these the most commonly used method is refractive index sensing [3]. In this paper, we propose a compact Silicon-On-Insulator (SOI) micro-ring resonator-based gas sensor. The sensor is designed to detect the carbon dioxide gas with the chosen conducting polymers.

K. P. Koushik (✉) · S. Malathi
Ramaiah University of Applied Sciences, Bengaluru, India
e-mail: pallavikoushik@gmail.com

2 Theory

2.1 Micro-ring Resonator

Micro-ring resonators are optical structures having numerous applications such as add-drop filters, optical switches, WDM multiplexers and also have attractive features toward sensing applications. A basic micro-ring resonator consists of a ring waveguide as the resonant cavity which is closely coupled with one or two straight bus waveguides which are serving as input and output [4]. Integral multiple of input optical signal referred to as the resonant wavelength (λ_r), that satisfies the condition given in (1), gets coupled into the ring through evanescent coupling phenomenon. Optical signal undergoes light enhancement due to constructive interferences appearing only at these wavelengths [5].

$$m\lambda_r = 2\pi \eta_{\mathrm{eff}} R \tag{1}$$

where m = order of resonance, λ_r = resonant wavelength, η_{eff} = effective refractive index of the mode, and R = radius of the ring.

The simulated model of the sensor ring-resonator consists of polymer-sensing layers to sense chemical compounds in a gaseous environment.

2.2 Choice of Material

The principle involved in sensing the gas is when the gas is passed then there will be a change in the refractive index of the coated polymer which results in shift in the resonant wavelength. A change in the refractive index of the medium of the waveguide is a must when it interacts with the analyte, which can be achieved by the suitable selection of functional material which hence exhibits the property of change in refractive index upon interaction with physical or chemical properties. The functional material also imparts selectivity to the sensor if it reacts only to the target analyte [6]. Suitable polymer which is compatible is chosen for the gas and is coated upon the ring resonator with few nm thickness.

Conducting polymers such as Poly Aniline (PAni), polypyrrole, Poly Methyl MethAcrylate (PMMA), Poly Hexa Methylene Biguanide (PHMB), and polythiophene have been extensively studied and used for fabrication of chemical sensors as well as detection of toxic gases. The polymer selected for detection of CO_2 gas is PHMB [6].

3 Design

The waveguide selected for designing both bus/straight and ring waveguides is strip waveguide.

3.1 Strip Waveguide Design

The strip waveguide has a dimension of (W × H) 500 nm × 220 nm that supports single mode at a wavelength of 1550 nm. The silicon and silicon dioxide form the core and cladding whose refractive indices are 3.467 and 1.44, respectively. The single-mode condition of strip waveguide is given by (2)

$$W \times H < 0.13\,\mu m^2 \tag{2}$$

3.2 Ring Resonator Design

The ring resonator designed has a radius of 11 μm. The ring resonator is coated with polymer of 240 nm thickness and the gap between ring and bus waveguide is maintained as 50 nm. The schematic of an optical micro-ring resonator is as shown in Fig. 1.

The simulations are carried out in Lumerical^{TM} FDE solver. Evanescent field of an integrated optic bent waveguide is essential for sensing application [7]. The simulation model of a ring resonator has been shown in Fig. 2a. The output is measured at the port. The resonant wavelength shift without and with polymer coating is observed and tabulated, and the shift is shown in Fig. 2b.

Fig. 1 Schematic of optical micro ring resonator
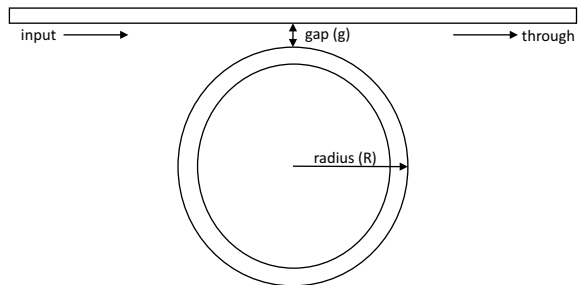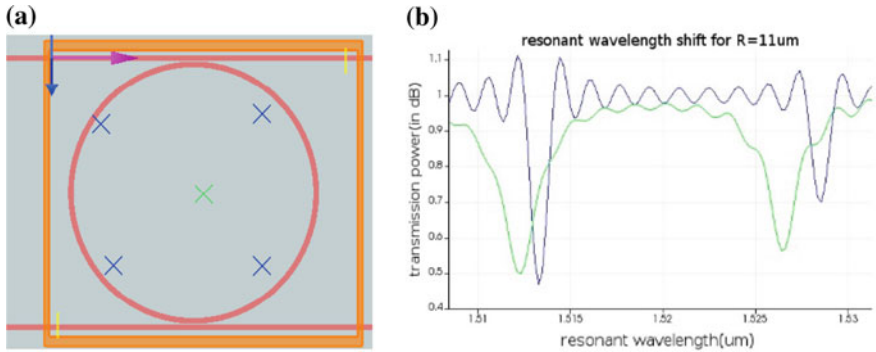
Fig. 2 **a** Simulation model of an IOMRR. **b** The resonant wavelength shift with/without polymer coating

4 Results and Discussion

The values are tabulated for wavelength shifts, and the ppm levels are validated with the reference paper [6]. Based on the resonant wavelength shift, the ppm levels are calculated by varying the refractive index of the coated polymer (Tables 1 and 2).

The developed simulation model serves as a reference for MRR-based gas sensor with a polymer coating. By extrapolating the results, one can determine the change in the refractive index of the polymer which reacts with gas molecules. Comparison

Table 1 The resonant wavelengths and shift in the ring resonator

Radius (μm)	Resonant wavelength (nm)		Resonant wavelength (Λ_{res}) shift in (pm)
	Without polymer coating	With polymer coating	
11	1.51327	1.51321	0.96

Table 2 Resonant wavelength shift with respect to refractive index change of the material and gas concentration

S. No.	Refractive index (η)	Resonant wavelength shift ($\Delta\Lambda_{res}$) in pm	CO_2 concentration levels (ppm)
1.	1.48	1.91	524
2.	1.49	1.72	434
3.	1.50	1.53	366
4.	1.51	1.53	366
5.	1.52	1.34	328
6.	1.53	1.15	262
7.	1.54	0.96	215
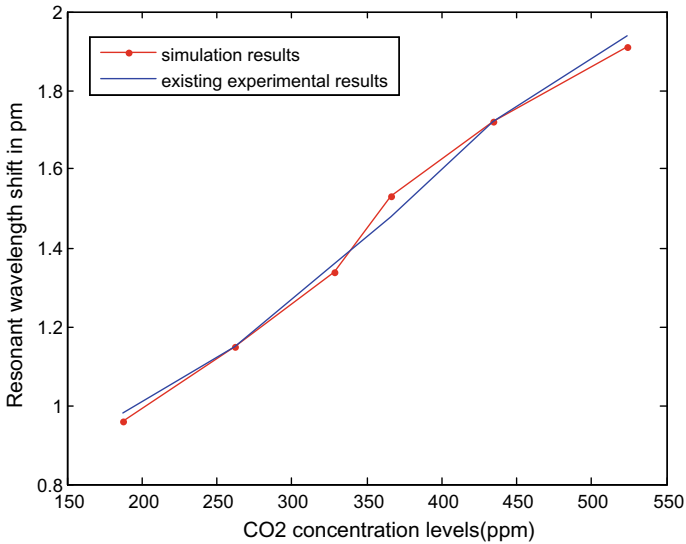
Fig. 3 Plot of calculated resonance wavelength shift versus CO_2 gas concentration. Blue line represents experimental results where red line represents simulation results

between the developed sensor's response and a published experimental work is shown in Fig. 3.

References

1. Passaro V, Dell'Olio F, De Leonardis F (2007) Ammonia optical sensing by microring resonators. Sensors 7(11):2741–2749
2. Liu X, Cheng S, Liu H, Sha H, Zhang D, Ning H (2012) A survey on gas sensing technology. Sensors 12(7):9635–9665
3. Sathish M, Raghunath U, Srinivas T (2010) Ultra-compact SOI micro rings for sensing applications. In: 2010 photonics global conference
4. Chao C-Y, Jay Guo L (2006) Design and optimization of microring resonators in biochemical sensing applications. J Light Technol 24(3):1395–1402
5. Meziane F, Raimbault V, Hallil H, Joly S, Conédéra V, Lachaud J-L, Béchou L, Rebière D, Dejous C (2015) Study of a polymer optical microring resonator for hexavalent chromium sensing. Sens Actuators B Chem 209:1049–1056
6. Mi G, Horvath C, Aktary M, Van V (2016) Silicon microring refractometric sensor for atmospheric CO 2 gas monitoring. Opt Express 24(2):1773–1780
7. Aditya V (2007) Analysis of integrated optic micro ring resonators and arrays

Design and Development of Fuel Efficiency Monitoring System

S. Raval Parth and D. Sagar

Abstract Automotive Research Association of India (ARAI) is one of the pioneer testing bodies administered by Indian government to evaluate the emissions and fuel efficiency using empirical formulas through Indian Driving Cycle (IDC) test. But based on real-time environment testing, the values rarely match; in this work, fuel efficiency monitoring system is being developed to calculate: fuel efficiency based on load applied on vehicle, speed of the vehicle, tire pressure, road type, road traffic conditions, power management system, and possible distance coverable, based on the fuel level. Developed system is the result of fusing software simulation and hardware components in LabVIEW graphical coding language where Arduino UNO is embedded into the system as hardware data acquisition component. The function of fuel efficiency-monitoring system is to monitor the fuel present in fuel tank and based on the input from load sensor, type of road conditions, traffic conditions, power management, calculate the efficiency of the fuel, and mileage of the vehicle at given instance of time. Based on the results obtained, calculated value from simulation setup deviates by 5.49% by set standard values. And comparative analysis of derived value from simulation and real-time tested values acquired from the Honda Jazz vx (diesel) gives the results with an accuracy of 94.51%.

Keywords Fuel efficiency · LabVIEW simulation · Real-time environment

1 Introduction

More demand for the vehicles with new features as well as good fuel efficiency also affects the market value of the vehicles. By introducing new techniques for improvement to existing systems, it includes more parameters to get reviewed. Calculating exact fuel efficiency and improved mileage is not easy to define. Without testing new methods in simulation, it is not a realistic approach to implement directly in real time. From the problems and challenges introduced in previous works and existed systems,

S. R. Parth · D. Sagar (✉)
M. S. Ramaiah University of Applied Sciences, Bengaluru, India
e-mail: sagar.cs.et@msruas.ac.in

it is necessary to come up with new methods which can focus on fuel efficiency from the parameters which mainly affect the performance of vehicle like total load, speed of the vehicle, tire pressure conditions, road conditions, etc. Instead of focusing on the hardware changes by analysis of existed system performance, it is possible to improve the fuel efficiency and can predict the mileage of the vehicle at that instance of time. Analysis can be done by measuring all parameters and readings of some test results.

2   Background

Fuel efficiency of vehicle needs to be improved for today's era due to less amount of fuel available compared to the number of vehicles in the world [3, 5]. Some of the researchers also did some study on different factors which affect fuel efficiency at some significant level. As given in [1], author studied existed methods to measure wheel slip for off-road vehicles only. In that author used hall sensor and magnetic rings to improve efficiency and achieved 32% of improvement in fuel efficiency.

Relationship between speed of vehicle and fuel consumption will be directly proportional [2]. If speed is S, fuel consumption is Fc, and fuel efficiency is Fe, then it will give

$$S \propto Fc \propto 1/Fe$$

Load on the vehicle plays an important role in varying the fuel efficiency. As more amount of load is applied on the vehicle, the fuel consumption increases [4]. Therefore the relation between load on the vehicle (L) and fuel consumption can be defined as follows:

$$Fc \propto L$$

Driving strategy also affects the efficiency to some extent [6]. As driver should maintain his behavior during driving the vehicle, it is more important to switch between gears and apply brakes or clutch at correct time of action.

Efficiency of fuel is not easy to define. The traditional approach to calculate fuel efficiency is just based on the distance traveled by the vehicle in the unit amount of fuel that can be either gallon or liter. It can be defined as follows:

$$\text{Fuel efficiency} = \text{Distance (kms or miles)}/\text{(liter or gallon)}$$
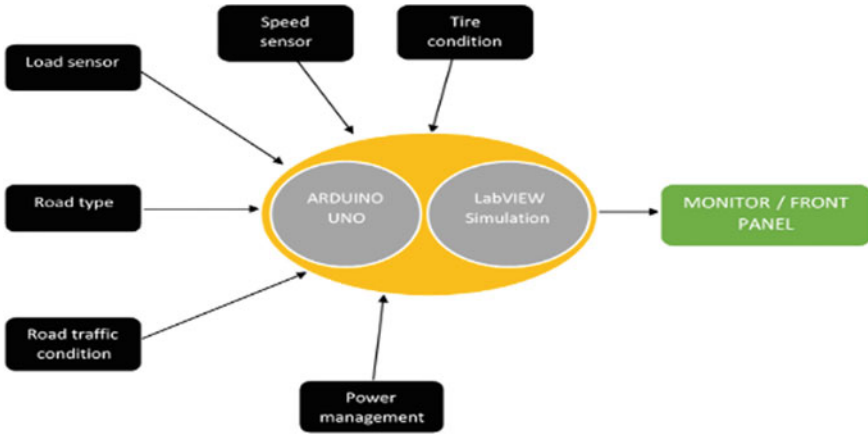
Fig. 1 Low level block diagram of the system

3 Design of the System

To design the system proposed based on defined specifications, it is required to design block diagrams, system flow charts, and schematic diagrams for hardware connections.

Fuel efficiency-monitoring system block diagram shows basic idea about how subsystems are connected with each other. Fig. 1 shows block diagram with subsystems. All concerned parameters taken for the calculations of fuel efficiency of the vehicle are displayed in the diagram.

Based on designed block diagram as shown in Fig. 1, hardware components are selected and schematic is drawn as shown in Fig. 2.

4 System Implementation

After designing the system, it is implemented with designed setup of hardware and selected software tool. In this section, hardware setup and software scripting with required GUI is implemented.

4.1 Hardware and Software Implementation Setup

Fig. 3a shows the hardware setup for the proposed system, based on the proposed design, giving a clear idea about how system hardware is connected with different
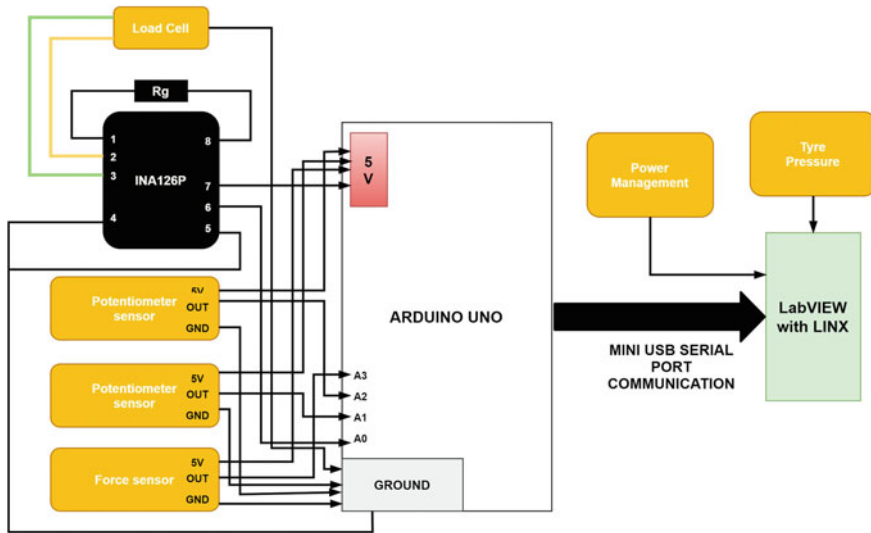
Fig. 2 Schematic diagram of the system
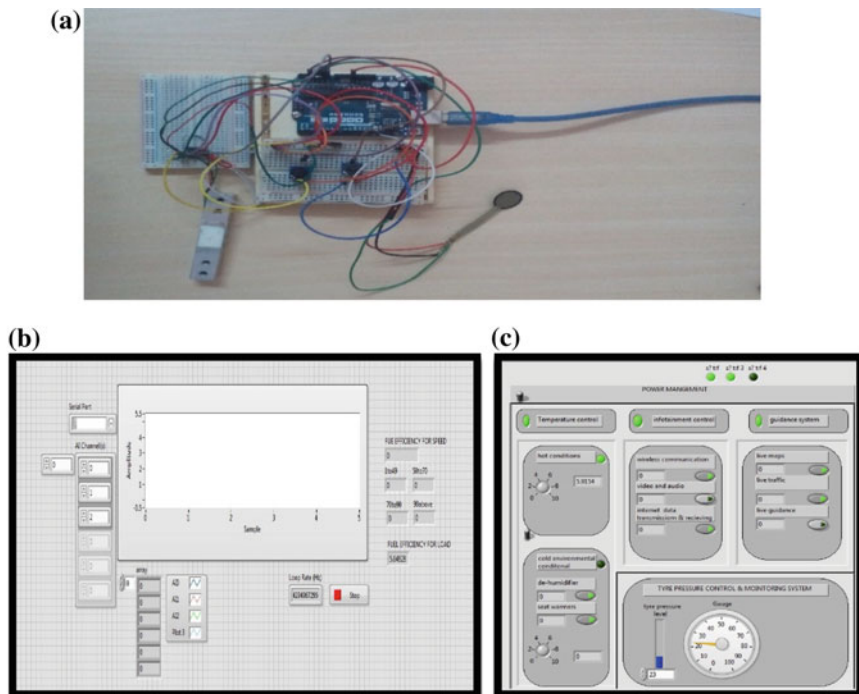
Fig. 3 **a** Hardware setup of fuel efficiency monitoring system. **b** GUI for Load and Speed sensor results. **c** GUI for PMS sensor results

sensors. In this system, to get analog inputs continuously, potentiometers and load sensors are connected with Arduino UNO.

Based on the designed system and hardware schematics, GUI is developed to represent the sensor data flow, and subsequently results are generated based on the individual input.

GUI is designed on the LabVIEW platform. Fig. 3b represents the subsystem that can acquire the data from two sensors mentioned in the model developed, and Fig. 3c represents the subsystem which can simulate and monitor Power Management System (PMS).

4.2 System Logic Implementation

Based on the literature survey and background study, the logic of the system is being developed. Fig. 4a represents the logic schematic that handles ports and opens the channel for interaction between the software and hardware, in addition, initiates hardware to connect and transfers collected data from serial port to LabVIEW.

Figure 4b shows the logic for power management and tire pressure influence on fuel efficiency of the vehicle. And Fig. 4c shows the logic to calculate the efficiency of the vehicle based on load of the vehicle with an appropriate scale down ratio.
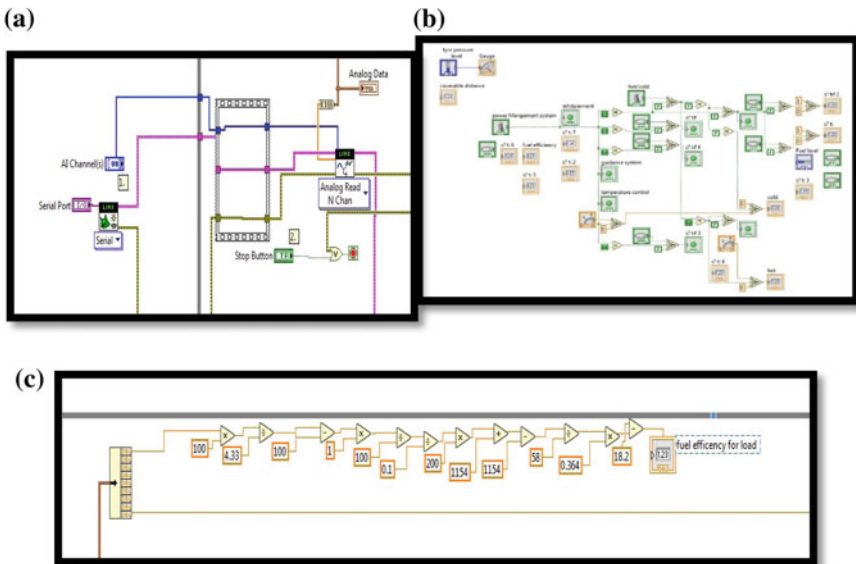
Fig. 4 **a** Logic for data collection using LINX. **b** Power management and Tire pressure. **c** Fuel efficiency for Load applied on the vehicle
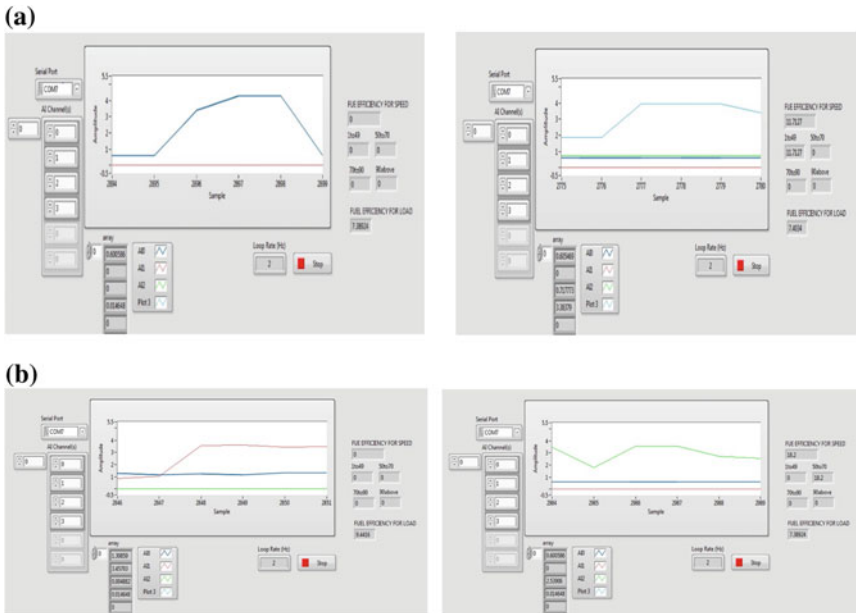
Fig. 5 **a** and **b** Load and tire/power management based fuel efficiency output graph. **c** and **d** Force resistive load and speed based fuel efficiency output graph

Fig. 6 Comparative analysis of standard and actual mileage graph
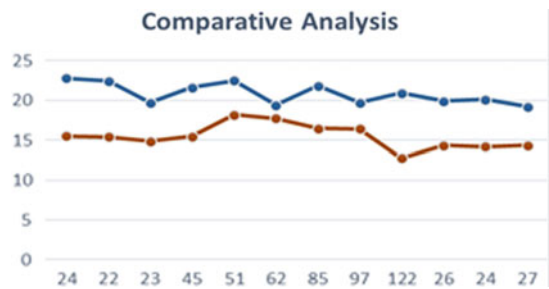
4.3   Real-Time Date Log

Snippet 1 shows the data collection from the real-time testing in different scenarios. Nine hundred and seventy-two different test cases were conducted to get the closest real-time fuel efficiency of the mentioned model.

Test case No	Tire pressure	Load	Road-type	Road-environment	Road angle	Speed	Power management	Standard mileage	Actual mileage	Efficiency
	Minimum limit	Car load + user	On-road	Normal traffic	Linear plain	Minimum	Minimum			
	Normal limit	100 kg	Off-road	Dense traffic	Inclined angle	Economical	Normal			
	Max limit	200 kg			slope angle	High speed	Luxury			
Test case No	Tire pressure	Load	Road-type	Road-environment	Road angle	Speed	Power management	Standard mileage	Actual mileage	Efficiency
Tc_1	Minimum limit	Car load + user	On-road	Normal traffic	Linear plain	Minimum	Minimum			
Tc_2	Minimum limit	Car load + user	On-road				Normal			
Tc_3	Minimum limit	Car load + user	On-road				luxury			
Tc_4	Minimum limit	Car load + user	On-road			economical	Minimum			
Tc_5	Minimum limit	Car load + user	On-road				Normal			
Tc_6	Minimum limit	Car load + user	On-road				luxury			
Tc_7	Minimum limit	Car load + user	On-road			High speed	Minimum			
Tc_8	Minimum limit	Car load + user	On-road				Normal			
Tc_9	Minimum limit	Car load + user	On-road				luxury			
Tc_10	Minimum limit	Car load + user	On-road		inclined angle	Minimum	Minimum			
Tc_11	Minimum limit	Car load + user	On-road				Normal			

Snippet 1 Data log for real time fuel efficiency of a vehicle

5 Results and Discussion

To calculate theoretically the readings for comparative analysis consider load sensor fuel efficiency and speed sensor efficiency obtained from the system simulated in LabVIEW. Final fuel efficiency for the maximum speed and load can be given as follows:

$$\text{Fuel efficiency} = ((18.2 + 12.74))/2 = 15.47 \text{ km/ltr.}$$

Fig. 5a–d shows the fuel efficiency of the vehicle based on the given parameters and how this parameter influences the efficiency of the fuel for a given model.

6 Conclusion and Future Work

The fuel efficiency got reduced and actual fuel efficiency is less than standard defined fuel efficiency. The comparison graph is shown in Fig. 6 for the real-time acquired data and standard mileage data defined by companies. It shows the deviation of the obtained result from the standard values by 5.49%. So the accuracy matches the standard calculation by 94.51%.

It is an important aspect to consider the future expansion of any developed work and to concentrate on future scope of the implemented work. Some future extensions can be considered for the developed fuel efficiency system as follows:

- More parameters can be considered to improve the accuracy of the system.
- In real time, data like angle of road can be considered by using more appropriate sensors to make system prototype more real time.
- As no data were fetched from the engine, which can be acquired from On-Board Diagnostics (OBD), integrating these data with the developed system will result in better results for fuel efficiency monitoring.
- In this paper, the scope was restricted to the monitoring of fuel efficiency which can be further extended for actuation process for improving the fuel efficiency.

References

1. Ashok Kumar A, Tewari V, Gupta C, Pareek C (2016) A device to measure wheel slip to improve the fuel efficiency of off road vehicles. J Terrramech 70:1–11
2. Brabec CJ, Dyakonov V, Parisi J, Sariciftci NS (eds) (2013) Organic photovoltaics: concepts and realization, vol 60. Springer Science & Business Media
3. Chaim MB, Shmerling E, Kuperman A (2010) Vehicle fuel consumption at urban operating conditions. Recent researches in energy, environment and sustainable development, pp 79–81
4. Fässler M (2010) Force sensing technologies. Report, Swiss Federal Institute of Technology Zurich
5. Ke B, Lin C, Cao F, Wang C (2014) Optimisation of fuel efficiency for freeway vehicles. IET Intel Transport Syst 8(5):490–498
6. Li C, Li J, Shen J (2009) Simulation of non-Gaussian fluctuating wind pressure through spectral representation method. In: WCSE'09. WRI World Congress on Software Engineering, 2009, vol 4, May. IEEE, pp 497–501

Design and Development of Prognosis Based Body Monitoring and Reporting System Using Time Series Analysis

Pari Patel, D. Sagar , and Nithin Rao

Abstract In today's increasingly busy world, people hardly have any time to look after their health conditions which leads to ignoring routine checkups which help in diagnosing the health conditions and keeping updates on current condition of the body. Day by day, death ratio is at a high pace because of delay in treatment due to lack of infra-structure in science and technology to identify and take corrective action for any disease, one of the paradigms that can use the IoT to improve the human lifestyle. This proposed work presents that IoT-based system is able to collect the sensors data of user's heart rate and from that it will help in predicting the value for prognosis using ARMA model time series analysis. Based on prognosis, condition, abnormality and criticality rates are calculated and notified through E-mail to personnel health consultant.

Keywords Body monitoring and reporting system · IoT · Time series analysis · Prediction · Embedded system · Cloud

1 Introduction

Health monitoring plays an important role in e-health care system [1]. Body monitoring system deals with the body parameter and vital signs of patients with the help of biomedical sensor. Sensor-based embedded system measures different body parameters like heart rate (HR), blood glucose, blood pressure (BP), temperature, etc. Body diagnosis is the method of understanding diseases, disorders, or problems by detailed analysis of the background history with the currently achieved results [2]. Prognosis in the system comprises the situation where the patient's vital signs are monitored and based on the reading acquired, predictions are done on whether the patients is going to continue to be in healthy condition or detroit to critical condition within the predicted duration of time. The data collected through the experiment can

P. Patel · D. Sagar (✉) · N. Rao
M. S. Ramaiah University of Applied Sciences, Bengaluru, India
e-mail: sagar.cs.et@msruas.ac.in

be used for better analytical accuracy, prior notification or detection, and reducing cost in overall health care.

2 Background Theory

2.1 Internet of Thing (IoT)

Internet of Things is a concept in which various devices are connected with each other by different available resources and techniques to exchange the real-time data [3]. Internet of things integrates hardware and software platforms to allow full communication between M2M (machine to machine) and M2C (Machine to Cloud) for transferring the data which improves health care for patients. Health monitoring system based on IoT enhances the performance of biomedical instrument by allowing real-time sensor data which leads the system to reduce the error in the process of diagnosis and prognosis treatment of a patient.

2.2 Cloud Storage

Cloud storage service is mainly used to effectively manage huge real-time data and decide upon the ownership of data, real-time response, stored large amount of structured and unstructured physiological medical history data of the patient with a precise database concerning each patient [4]. Data storage and analysis will be a challenge when the whole world will be connected with Internet of Things technology [5].

2.3 Embedded System

System integrated with software to control the hardware to perform specific objectives is term as embedded system. In healthcare center, embedded system helps in accurate diagnosis of disease symptoms. Smart, trivial, and powerful monitoring devices ambitious by embedded technology and connected with the help of IoT are helping these people monitor and treat their health conditions. Embedded systems have managed to revolutionize the healthcare industry.

2.4   Time Series Analysis

Time series analysis is collection of huge number of data within a uniform time interval and analyses of the same to predict the change that will happen in future condition. It is used in copious field such as economics, pattern recognition, biometrics, etc. This process is applied in a wide range of spheres where the predicted value is helpful in many ways to take future decision.

In this proposed developed prognosis based body monitoring and reporting system, choose Autoregressive–moving-average (ARMA) model for analysis and prediction to get accurate predicted data [6].

The data series of patient's concentration over a time is considered as a random time series.

$$X_t = \sum_{j=1}^{p} a_j X_{t-j} + \sum_{j=1}^{q} b_j \epsilon_{t-j} + \epsilon_t$$

Current and future reading of pulse rate can be expressed as a previous pulse rate data with ARMA model [1].

X_t indicates the pulse rate at current time instant t, X_{t-k} is the previous reading of k time-units before current time t, $a_{1,}$ $a_{2,}$ $a_3,\ldots,$ a_p are the p order of autoregressive coefficient and b_1, b_2, $b_3,\ldots,$ b_q are the q order of moving average coefficient, and ε_t is the white noise.

3   System Design and Architecture

Figure. 1a, b represents the system level block diagram and flow chart of the system which measure the data from user's body with different biomedical sensors attached as an input stage. Furthermore, the data will get fetched and sent over cloud to create a history of data. If the user is encompassed in Wi-Fi range of raspberry pi connectivity, it will transmit the data directly to Raspberry Pi board through NodeMCU v0.9. In the next stage, ECU as a Raspberry Pi board is configured using LINX toolkit with IP address with LabVIEW. Control unit of the system fetches data and feeds it to LabVIEW for further analysis and predicts the future condition of users. All history of the patient data will be stored over a cloud. From the predicted value and prognosis condition of the patient, we can identify the abnormality of the disease and calculate the criticality data rate and notify the user and their relatives and also alert the medical health care consultant for the criticality issue through E-mail.

Important tools required for Software Simulation Setup are as follows:-

- Python Language
- Embedded C with Arduino IDE
- LabVIEW (Laboratory Virtual Instrument Engineering Workbench).

(a) (b)
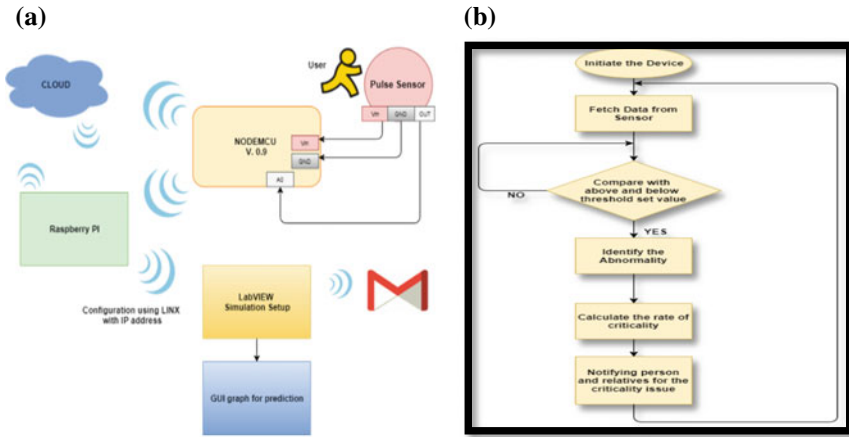
Fig. 1 **a** System block diagram. **b** Flowchart of system design

4 System Implementation

4.1 Hardware and Software Implementation Setup

Figure 2a, b shows the overall physical model of the system that the user will be working within this experiment.
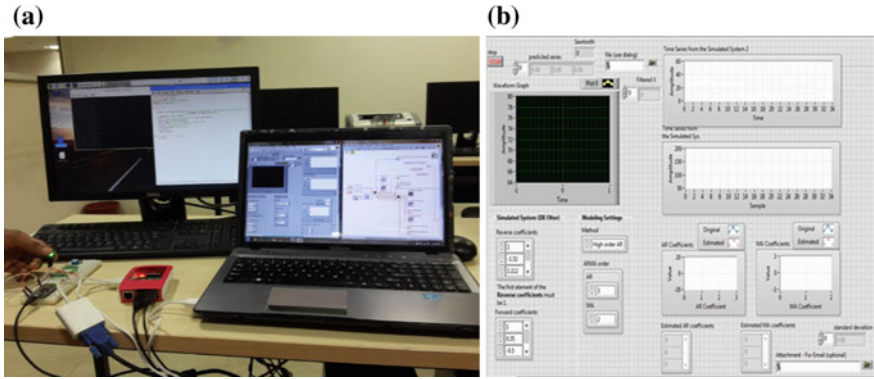
Fig. 2 **a** Hardware setup. **b** Software setup of system developed
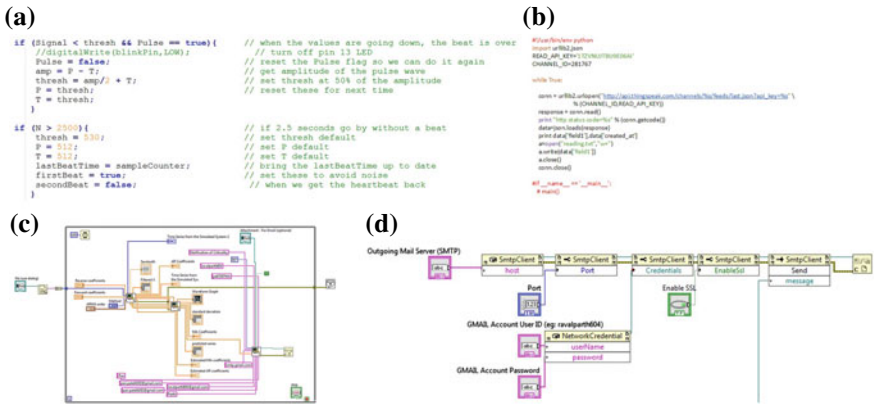
Fig. 3 **a**–**d** System implementation code

4.2 *System Logic Implementation*

Figure. 3a–d shows the logic design of the system designed in LabVIEW, GUI designed for ARMA modeling, and prediction for heart rate analysis. Reverse and forward coefficient used for the IIR filter will be set according to our real-time data series for filter design. Filter X shows the array of filtered samples as output. High-order AR method is used in ARMA modeling and prediction analysis because it gives high accuracy than Yule–Walker and polynomial methods for univariate time series data. ARMA order is a combination of AR and MA coefficients and it can be set according to our application requirement of prediction series. AR and MA coefficient values should be greater than or equal to zero and AR coefficient order is greater than MA coefficient order. Estimated AR and MA coefficients are used for predicting future value of prognosis condition. Standard deviation gives the error between original data and each predicted value.

5 Results and Discussion

Figure. 4a, b shows the results obtained from analog signal collected from pulse sensor. Real-time data feed to LabVIEW for analysis through NodeMCU module.
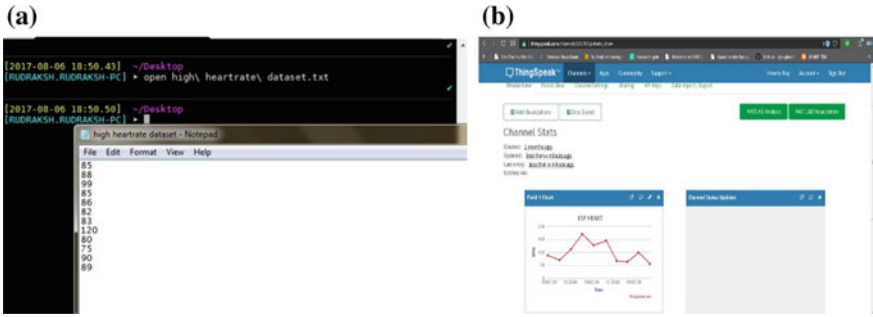
Fig. 4 **a** Pulse sensor values. **b** Prediction series result

6 Conclusion and Future Work

The system is able to identify the disease issue by analyzing collected real-time data from sensors using ARMA model and detect the critical condition of a particular disease and notify patients and registered medical experts as shown in Fig. 5.

It is an important aspect to consider the future expansion of any developed work and to concentrate on future scope of the implemented work. Some future extensions can be considered for the developed prognosis and diagnosis based body monitoring and reporting system as follows:

- System can import more than one vital sign parameter included in the developed system.
- In future work, system can provide solution for the avoidance of the critical state.
- Scalability and accuracy can be improved by implementing new algorithm for gateway medium.
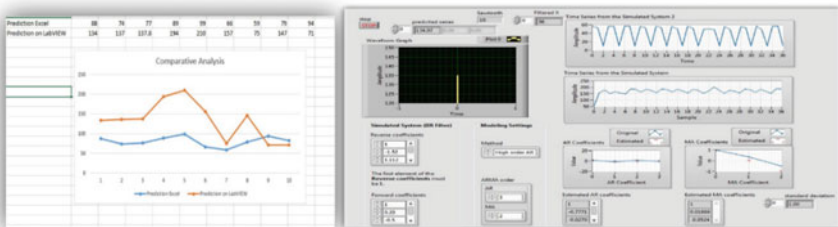
Fig. 5 Comparative analysis between ARMA model and real-time data log

References

1. Ying Z, Rui K, Shihong X (2014) Research on glucose concentration predicting based on ARMA model. In: 2014 prognostics and system health management conference (PHM-2014 Hunan)
2. Mohanraj T, Keshore R (2017) Patient monitoring system using LabVIEW. In: Int J Emerg Technol Comput Sci Electron (IJETCSE) 24(4). ISSN: 0976-1353
3. Singh D, Tripathi G, Jara A (2014) A survey of internet-of-things: future vision, architecture, challenges and services. In: 2014 IEEE world forum on internet of things (WF-IoT)
4. Mukherjee S, Dolui K, Datta S (2014) Patient health management system using e-health monitoring architecture. In: 2014 IEEE international advance computing conference (IACC)
5. Zhou B, Ma Q, Song Y, Bian C (2016) Cloud-based dynamic electrocardiogram monitoring and analysis system. In: 2016 9th international congress on image and signal processing, biomedical engineering and informatics (CISP-BMEI)
6. Mahalakshmi G, Sridevi S, Rajaram S (2016) A survey on forecasting of time series data. In: 2016 international conference on computing technologies and intelligent data engineering (ICCTIDE '16)

Analysis of Routing Protocol Performance for V2X Communication

R. Priya, R. Nithin Rao , **and K. R. Narasimha Murthy**

Abstract   Exchange of data from a vehicle to another object/person which affects the vehicle is known as vehicle-to-everything (V2X) communication. One of the major decisions that has to be taken during the design of new routing protocols for V2X is whether the route discovery will be done reactively or proactively. We envisage that specialized routing protocols will be able to use the special features of V2X more effectively. This paper compares the proactive and reactive approaches to route discovery in V2X communication. We have performed this comparison using two well-known protocols used extensively for mobile ad hoc networks (MANETs): Ad hoc on-demand distance vector (AODV) protocol, which is a reactive protocol and direct sequence distance vector (DSDV) protocol, which is a proactive protocol. Both of these compute routes based on distance vector principles. Based on the results of the simulation presented previously, it is evident that DSDV is a better choice than AODV for V2X communication. While it may not be feasible to use DSDV directly, it may serve as a good starting point for developing routing protocols exclusively for V2X communication.

Keywords   Routing in V2X · Vehicular ad hoc networks · Proactive and reactive route discovery

1   Introduction

Vehicular ad hoc networks (VANETs) are ad hoc networks where the communicating nodes are vehicles. This application has been made possible by the tremendous development in the electronics of a typical automobile, right from multiple sensors to powerful processors. This development has enabled a plethora of applications such as safety, traffic efficiency, driver assistance, infotainment, and urban sensing [1]. However, it is worth noting that in most cases VANETs are restricted to vehicle-to-vehicle (V2V) and vehicle-to-infrastructure (V2I) communication. Because of

R. Priya · R. N. Rao (✉) · K. R. Narasimha Murthy
M. S. Ramaiah University of Applied Sciences, Bengaluru, India
e-mail: nithin.cs.et@msruas.ac.in

this, generic ad hoc routing protocols such as those presented in [2, 3] can be a good starting point for development.

Exchange of data from a vehicle to another object/person which affects the vehicle is known as vehicle-to-everything (V2X) communication. It can be further distributed into explicit types centered on the requirements such as vehicle-to-infrastructure (V2I), vehicle-to-vehicle (V2V), vehicle–to-pedestrian (V2P), vehicle-to-device (V2D), and vehicle-to-grid (V2G) communication [4]. V2X plays a vital role in autonomous driving; earlier it was implemented using wireless access in vehicular environments (WAVE) later on IEEE 802.11p was set for the local wireless communication.

1.1 Routing in V2X Communication

For a typical V2X system, the routing protocol is of tremendous significance because of the inherent heterogeneity involved. Typically for ad hoc networks, routing can be broadly classified as proactive or reactive, based on the time at which routes are discovered. There are other classifications too, but we choose to ignore them to restrict the scope of our work.

The remainder of this paper is organized as follows. The next section presents the related work done in this domain while the subsequent section details the formation of a V2I network using network simulator-2 (ns2) and introduces the different types of communication links it has. Section 4 details the results of the simulation analysis and Sect. 5 concludes our paper, making recommendations and suggestions for enhancement.

2 Related Work

This section presents an overview of the quantum of work done with respect to routing in VANETs. Most V2X communication uses the same protocols; this is because VANETs can be envisaged as a subset of V2X communication.

One of the important areas of research in routing protocols for VANETs has been the performance analysis of ad hoc routing protocols for VANETs. Some of the literature such as [5–7] talk about the comparison of AODV with other routing protocols and also enhance the AODV protocol to increase its efficiency in VANET scenarios.

One of the major distinguishing characters of VANETs is the somewhat predictable nature of the road and the availability of geographic information. From this starting point, many geo-location-based and road information-based protocols were proposed for VANETs. Some examples of such protocols are presented in [8–10].

2.1 Trends in V2X Communication and Theme of Paper

An overview of the research in V2X communication throws up an interesting aspect. Most of the work done in V2X is focused on the applications of it, such as congestion avoidance, intersection safety, and reduced traveling time. This is shown in Refs. [11–13].

Even though, as stated previously, VANETs are considered a subset of V2X, it is our opinion that there can be specialized routing protocols for V2X. One of the major decisions that has to be taken during the design of new routing protocols is whether the route discovery will be done reactively or proactively. We envisage that specialized routing protocols will be able to use the special features of V2X more effectively, such as V2P, V2D, and V2G. As it stands, such efforts are few and far in between, as shown by the work done in [14–16].

This paper compares the proactive and reactive approaches to route discovery in V2X communication. We have performed this comparison using two well-known protocols used extensively for mobile ad hoc networks (MANETs): Ad hoc on-demand distance vector (AODV) protocol, which is a reactive protocol, and direct sequence distance vector (DSDV) protocol, which is a proactive protocol. Both of these compute routes based on distance vector principles.

3 Design of the V2X System

This section presents the design of the V2X system created using ns-2 [17]. We have also indicated the types of applications the V2X system can be used for and the simulation parameters.

3.1 Design of the V2X System

Figure 1 demonstrates the network setup for the V2X communication in network simulator. In this scenario, a route is assumed which has several different vehicles moving to the desired destination. These vehicles will be equipped with an on board unit (OBU) which helps in communicating with the corresponding vehicle, road side unit (RSU), devices, or pedestrians.

Fig. 1 The V2X system

A normal traffic condition is assumed in the scenario where the vehicles deliver their information to the nearby RSU which will have all the details regarding the vehicle.

3.2 Flowchart

Figure 2 shows the flowchart that represents the different types of messages that the V2X system can handle. Table 1 presents the various simulation parameters.

4 Simulation Results

This section presents the results of the simulation. We have evaluated the performance of the protocols based on packet delivery ratio (PDR) and the number of packet drops.

Figure 3 presents the performance of the protocols as mobility increases. We can see here that DSDV outperforms AODV by delivering more packets. DSDV suffers from more packet drops.

Figure 4 presents the performance of the protocols as the size of the packets transmitted increases. Here too, DSDV is more efficient than AODV, delivering a comparatively higher PDR.
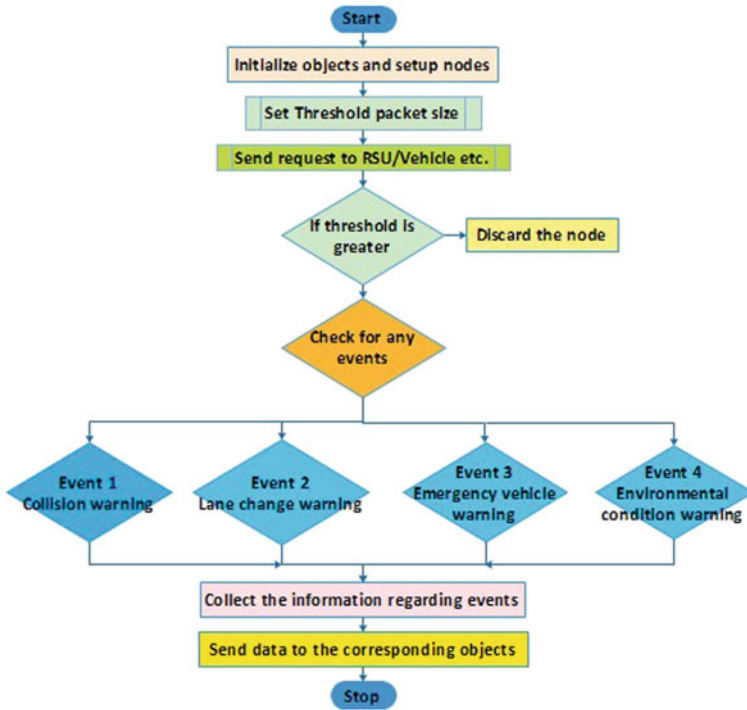
Fig. 2 Flowchart showing the different messages

Table 1 Simulation parameters

Routing protocol	AODV, DSDV
Number of nodes	19
Simulation time	20 min
Packet size	250–1024 bps
Mobility	0–20 Kmph
Traffic	CBR
MAC layer	IEEE 802.11p

5 Conclusion and Future Work

Based on the results of the simulation presented previously, it is evident that DSDV is a better choice than AODV for V2X communication. While it may not be feasible to use DSDV directly, it may serve as a good starting point for developing routing protocols exclusively for V2X communication.

As a continuation of this research, we propose to test the performance similarly for more varied types of messages. Also, the latency of message communication merits further investigation.
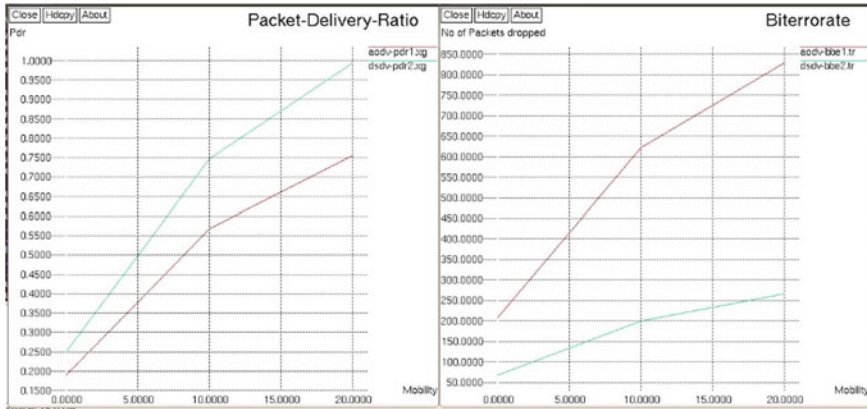
Fig. 3 Performance of AODV and DSDV with varying mobility
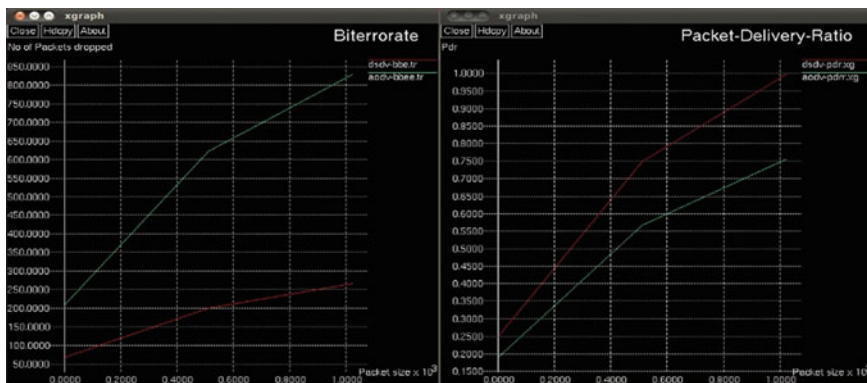
Fig. 4 Performance of AODV and DSDV with varying packet size

References

1. Cunha F, Villas L, Boukerche A, Maia G, Viana A, Mini RA, Loureiro AA (2016) Data communication in VANETs: protocols, applications and challenges. Ad Hoc Netw 44(1):90–103
2. Chakeres ID, Belding-Royer EM (2004) AODV routing protocol implementation design. In: Proceedings of 24th international conference on distributed computing systems workshops. IEEE, Tokyo, pp 698–703
3. Perkins CE, Bhagwat P (1994) Highly dynamic destination-sequenced distance-vector routing (DSDV) for mobile computers. ACM SIGCOMM Comput Commun Rev 24(4):234–244
4. Bian K, Zhang G, Song L (2017) Security in use cases of vehicle-to-everything communications. In: Proceedings of IEEE 86th vehicular technology conference (VTC-Fall). IEEE, Toronto, pp 1–5
5. Haerri J, Filali F, Bonnet C (2006) Performance comparison of AODV and OLSR in VANETs urban environments under realistic mobility patterns. In: Proceedings of the 5th IFIP mediterranean ad-hoc networking workshop. IEEE, Italy, pp 14–17

6. Abedi O, Fathy M, Taghiloo J (2008) Enhancing AODV routing protocol using mobility parameters in VANET. In: Proceedings of the IEEE/ACS international conference on computer systems and applications. IEEE, Qatar, pp 229–235
7. Ding B, Chen Z, Wang Y, Yu H (2008) An improved AODV routing protocol for VANETs. In: Proceedings of the 2011 international conference on wireless communications and signal processing. IEEE, China, pp 1–5
8. Saleet H, Langar R, Naik K, Boutaba R, Nayak A, Goel N (2011) Intersection-based geographical routing protocol for VANETs: a proposal and analysis. IEEE Trans Veh Technol 60(9):4560–4574
9. Fonseca A, Vazão T (2013) Applicability of position-based routing for VANET in highways and urban environment. J Netw Comput Appl 36(3):961–973
10. Granelli F, Boato G, Kliazovich D (2006) MORA: a movement-based routing algorithm for vehicle ad hoc networks. In: Proceedings of the 2006 IEEE global communication conference. IEEE, California
11. Wedel JW, Schünemann B, Radusch I (2009) V2X-based traffic congestion recognition and avoidance. In: Proceedings of the 10th international symposium on pervasive systems, algorithms and networks. IEEE, Taiwan, pp 637–641
12. Le L, Festag A, Baldessari R, Zhang W (2009) V2X communication and intersection safety. In: Meyer G, Valldorf J, Gessner W (eds) Advanced microsystems for automotive applications. Springer, Berlin, Heidelberg
13. Noori H, Valkama M (2013) Impact of VANET-based V2X communication using IEEE 802.11 p on reducing vehicles traveling time in realistic large scale urban area. In: Proceedings of the 2013 international conference on connected vehicles and expo. IEEE, Las Vegas, pp 654–661
14. Yao L, Wang J, Wang X, Chen A, Wang Y (2018) V2X routing in a VANET based on the hidden Markov model. IEEE Trans Intell Transp Syst 19(3):889–899
15. Krajzewicz D, Bieker L, Härri J, Blokpoel R (2012) Simulation of V2X applications with the iTETRIS system. Procedia-Soc Behav Sci 48(1):1482–1492
16. Er NI, Singh KD, Bonnin JM (2017) On the performance of VDTN routing protocols with V2X communications for data delivery in smart cities. In: Proceedings of the second international workshop on smart sensing systems. HAL, Finland, pp 6–7
17. Issariyakul T, Hossain E (2012) Introduction to network simulator NS2. Springer Science & Business Media, New York

Assessment of Remineralisation Potential of Cranberry Extract and Grape Seed Extract Dentifrice on Primary Teeth Using Laser Fluorescence Device

C. Pushpalatha, N. Sneha, R. Deveswaran, and Latha Anandakrishna

Abstract Early detection of dental caries with optical instruments and promoting remineralisation is one of the measures in the prevention of early carious lesion. The present study was conducted to assess and compare the remineralisation potential of cranberry extract and grape seed extract dentifrice on primary teeth using DIAGNOdent pen. 20 over retained non-carious primary teeth with intact crown were extracted and sectioned into coronal and root part at cementoenamel junction. They were placed in demineralising solution for 96 h. The demineralized teeth were randomly divided into the following four groups. Group 1 was control group, Group 2 was Cranberry extract dentifrice, Group 3 was Grape seed extract dentifrice and Group 4 was Fluoridated dentifrice. Demineralised enamel blocks were then brushed with their respective dentifrice twice daily at an interval of 12 h for 2 min using soft bristle toothbrush over the demineralised area for 7 days. Remineralisation was assessed using DIAGNOdent pen after 7 days and subjected to statistical analysis using one-way ANOVA test and Tukey's HSD Post Hoc analysis. Results revealed that cranberry extract dentifrice (4.2 ± 0.4) had maximum remineralisation of demineralised primary enamel followed by grape seed extract dentifrice (4.8 ± 0.8) and then fluoridated dentifrice (5.0 ± 1.2). Hence cranberry and grape seed extract dentifrice are promising novel natural non-fluoridated remineralizing dentifrice for primary teeth.

Keywords DIAGNOdent · Cranberry extract · Grape seed extract

C. Pushpalatha (✉) · N. Sneha · L. Anandakrishna
Faculty of Dental Sciences, M.S. Ramaiah University of Applied Sciences, Bengaluru, India
e-mail: drpushpalatha29@gmail.com

R. Deveswaran
Faculty of Pharmacy, M.S. Ramaiah University of Applied Sciences, Bengaluru, India

1   Introduction

Fluoride in the form of dentifrice, rinses and varnish has declined dental caries by promoting remineralisation of tooth structures by utilizing calcium and phosphate ions present in the saliva. Fluoride in the early stages of caries development reduces demineralization and enhances remineralisation by crystal growth and formed crystal is more resistant to acid attack. However, the ingestion of fluoride in preschool children and in children with special health care needs is used in caution due to inability to expectorate as a result of poor development of oral musculature, this leads to excessive fluoride in the blood plasma resulting in dental and skeletal fluorosis where the outer portion (enamel) of the teeth and bones in the body becomes brittle and weak if consumed over a long period of time [1–3]. Therefore, several new non-fluoridated remineralising agents have been studied since last decade [4]. Literature supports that herbal extracts rich in proanthocyanidins are gaining a lot of attention in the prevention of dental caries especially grape seed extract and cranberry extract. These proanthocyanidins rich extract are reported to possess antibacterial, antioxidant, anti-adhesion and anti-inflammatory activities. Grape seed extract has remineralisation properties on both enamel and dentine in primary and permanent teeth [4–7]. Whereas remineralisation potential of cranberry extract is still not explored either in primary or permanent teeth. There are no study reports of grape seed extract and cranberry extract in dental formulation like dentifrice. Hence the present study was designed to assess and compare the remineralisation potential of cranberry extract and grape seed extract dentifrice on primary teeth using DIAGNOdent pen (KaVo Germany).

2   Materials and Methodology

2.1   Materials

Cranberry extract powder and Grape seed extract powder were procured from HerboNutra, Delhi. Carbopol 140 and Xanthan gum were purchased from Micromaster Pvt Ltd., Mumbai. Ethanol was purchased from Rankem, Mumbai. All other reagents used were of analytical grade.

2.2   Preparation of Enamel Blocks

The current in vitro study was approved by institutional ethics committee. The teeth samples of 20 over retained non-carious primary teeth with intact crown which were extracted after informed consent from patient for therapeutic purpose were collected. Teeth with any dental anomalies and cracks were excluded from the study. Teeth were sectioned into coronal and apical halves. The coronal part of the tooth was used for the study. The teeth were cleaned and polished with pumice using prophylactic brush.

The teeth were then randomly divided into 4 experimental groups of 5 teeth in each group. The groups were Group 1 (Control), Group 2 (Cranberry extract dentifrice), Group 3 (Grape seed extract dentifrice) and Group 4 (Fluoridated dentifrice). The samples were covered with two coats of acid resistant nail varnish except for a window of 3×3 mm on the buccal surface [8, 9].

2.3 Preparation of Demineralization Solution

The demineralizing solution of pH 4.5 was prepared by dissolving one pH buffer capsule of pH 4.0 in 100 ml of deionized water by stirring until the capsule got completely dissolved. Digital pH meter was used to check the pH value.

2.4 Demineralization of the Samples

Baseline values of all the samples were assessed with DIAGNOdent pen. Samples were then immersed individually into four separate 500 ml circular polyvinyl containers each containing 100 ml demineralizing solution for a period of 96 h at 37 °C.

2.5 Preparation of Cranberry Extract and Grape Seed Extract Dentifrice

Required quantity of xanthan gum was mixed with glycerine and water, stirred for 5 min and set aside for 30 min. Grape seed extract powder and cranberry extract powder were taken separately in a pestle and mortar. Calcium carbonate and Dicalcium phosphate was added to this and triturated till fine powder was obtained. To this fine powder, glycerine mixture was added and blended evenly to form a paste. Methylparaben and flavouring agent were added to the paste and mixed thoroughly. Required quantity of glycerine was added to obtain desired consistency. A total of 6 formulations were prepared for both cranberry and grape seed extract and the one that had better consistency was chosen for further studies.

2.6 Remineralisation of Teeth

The demineralized samples were mounted on the acrylic resin blocks. The readings of demineralised blocks were examined using DIAGNOdent pen. Enamel blocks were brushed with their respective toothpaste twice daily for 2 min at an interval of 12 h using soft bristle toothbrush in a circular motion over the demineralised area. Dentifrice was washed from the sample thoroughly with water. The samples were dried. This procedure was carried out for 7 days. At the end of the 7th day, remineralisation was checked using DIAGNOdent pen for all the groups.

3   Statistical Analysis

Statistical analysis was done using Statistical Package for the Social Sciences (SPSS) of Windows Version 22.0. One-way ANOVA test followed by Tukey's HSD post hoc analysis was used to compare the mean moment values between the study groups. The level of significance was set at $P < 0.05$. Bonferroni's Post hoc Analysis was used to compare the mean moment values between different time intervals in each study group.

4   Results and Discussion

See Tables 1, 2 and 3.

Formulation F3 of Cranberry and F6 of grape seed extract were chosen for the study as they had better consistency in comparison to other formulations. To detect and quantify the carious lesions on occlusal and smooth surface, the in vitro studies have shown that original laser device (DIAGNOdent 2095) has good performance and reproducibility [10]. The literature review on Laser fluorescence device suggests that sensitivity values for detection of caries ranged from 0.19 to 1.0 which is high. Whereas, the sensitivity values ranged from 0.52 to 1.0 have shown that laser fluorescence device exhibited almost high sensitivity and almost low specificity in comparison to visual assessment method. The latest version of laser fluorescence pen (DIAGNOdent pen) showed sensitivity value of 0.67 and specificity was 0.79 for enamel and dentinal caries at cut-off value of 25 which was a threshold value.

Table 1 Composition of formulations

Ingredients	Grape seed extract dentifrice			Cranberry extract dentifrice		
	Qty in g			Qty in g		
	F1	F2	F3	F4	F5	F6
Grape seed extract powder	10.0	10.0	10.0	–	–	–
Cranberry seed extract powder	–	–	–	10.0	10.0	10.0
Xanthan gum	1.0	1.25	1.5	1.0	1.25	1.5
Calcium carbonate	5.0	5.0	5.0	5.0	5.0	5.0
Glycerine (ml)	5	5	5	5	5	5
Flavour	0.5	0.5	0.5	0.5	0.5	0.5
Methyl paraben	0.5	0.5	0.5	0.5	0.5	0.5
Dicalcium phosphate	q.s to 50 g	q.s to 50 g	q.s to 50 g	q.s to 50 g	q.s to 50 g	q.s to 50 g

Table 2 Mean DIAGNOdent pen moment values for different study groups at different treatment procedures

Time	Groups	N	Mean ± SD	P-value
Baseline	Group 1	5	6.6 ± 1.7	0.689
	Group 2 (F3)	5	6.2 ± 1.6	
	Group 3 (F6)	5	7.0 ± 2.1	
	Group 4	5	5.8 ± 0.8	
After demineralisation	Group 1	5	12.2 ± 2.6	
	Group 2 (F3)	5	10.4 ± 1.3	0.529
	Group 3 (F6)	5	11.4 ± 2.3	
	Group 4	5	10.8 ± 1.5	
After remineralisation	Group 1	5	10.2 ± 0.4	<0.001*
	Group 2 (F3)	5	4.2 ± 0.4	
	Group 3 (F6)	5	4.8 ± 0.8	
	Group 4	5	5.0 ± 1.2	

*Statistically significant

Table 3 Comparison of DIAGNOdent pen moment values for all the three groups at baseline, after demineralization and after remineralisation

Group	Time	N	Mean ± SD	P-value[a]	Sig. diff	P-value[b]
Group 1	BL	5	6.6 ± 1.7	0.03*	BL versus AD	0.11
	AD	5	12.2 ± 2.6		BL versus AR	0.04*
	AR	5	10.2 ± 0.4		AD versus AR	0.39
Group 2 (F3)	BL	5	6.2 ± 1.6		BL versus AD	0.001*
	AD	5	10.4 ± 1.3	<0.001*	BL versus AR	0.14
	AR	5	4.2 ± 0.4		AD versus AR	0.001*
Group 3 (F6)	BL	5	7.0 ± 2.1		BL versus AD	0.003*
	AD	5	11.4 ± 2.3	<0.001*	BL versus AR	0.12
	AR	5	4.8 ± 0.8		AD versus AR	0.003*
Group 4	BL	5	5.8 ± 0.8		BL versus AD	0.006*
	AD	5	10.8 ± 1.5	0.001*	BL versus AR	1.00
	AR	5	5.0 ± 1.2		AD versus AR	0.01*

BL: Baseline, *AD*: After Demineralisation, *AR*: After Remineralisation
*Statistically significant

These laser devices are used to supervise the carious lesion and to check the effect of preventive interventions [11]. Hence for the present study, the latest version of laser fluorescence device, i.e. DIAGNOdent pen was used to assess the outcome of the remineralisation potential of novel dentifrices on initial caries lesion. In the present era of minimal intervention of dentistry, a variety of natural compounds have been

refined to develop remineralizing agents in prevention of caries. Proanthocyanidins is a natural plant metabolite present in fruits, vegetables, nuts, seeds, flowers and barks. Proanthocyanidins have been certified to be safe as a dietary supplement and in different clinical applications. Proanthocyanidins from cranberry extract and grape seed extract have shown to have antibacterial, anti-inflammatory and antioxidant properties [5]. Grape seed extract also exhibits remineralizing action on the superficial layer of the lesion through mineral deposition by combining with the calcium at pH of 7.4 leading to the formation of insoluble complex [7]. Since there were no studies on remineralisation of potential of cranberry extract. Hence in the previous study, the concentration of cranberry extract and grape seed extract in intracanal medicament was determined and assessed for antibacterial and surface microhardness. The results showed 95% bacterial reduction in cranberry and grape seed extract groups where chlorhexidine group (control) showed 99% bacterial reduction. There was an increase in microhardness in both cranberry extract and grape seed extract intracanal medicament groups in comparison to chlorhexidine group showing no change [12]. In the present study, the same concentration of cranberry extract and grape seed extract was used to formulate novel dentifrices. In the present experimental study, DIAGN-Odent measurement was obtained at three different time intervals before demineralisation, after demineralisation and after remineralisation. The baseline data using DIAGNOdent pen the mean moment value for Group 1 was 6.6 ± 1.7, Group 2 was 6.2 ± 1.and Group 3 was 5.8 ± 0.8 showing statistically no significant difference ($P < 0.05$). Whereas in Group 1, there was no statistical significance difference ($P < 0.05$). The results of the present study suggest that after 7 days of application of cranberry extract dentifrice, Grape seed extract dentifrice and fluoridated dentifrice onto the tooth surface, there was a noticeable remineralisation of initial carious lesion. This suggests that cranberry extract dentifrice and Grape seed extract dentifrice helps in mineral deposition on the superficial layer of the lesion. The present study correlates with our previous study in which there was a 95% increase in microhardness in both intracanal medicaments containing cranberry extract and Grape seed extract [12]. The results of the present study indicate that both cranberry extract and grape seed extract dentifrices can be used for enamel remineralisation in the case of initial caries lesion. However, these novel dentifrices should be used with caution clinically since in vitro remineralisation is different when compared with dynamic complex biological system.

5   Conclusion

In conclusion, this work assessed and compared the remineralisation potential of cranberry extract and grape seed extract dentifrice on primary teeth using DIAGN-Odent pen. Both cranberry extract dentifrice and grape seed extract dentifrice are promising alternatives to enhance the remineralisation of artificially induced enamel caries lesion in primary teeth. These novel dentifrices might be an effective natural dentifrice for non-invasive therapy for the reduction of initial enamel caries.

References

1. Schäfer F (1989) Evaluation of the anticaries benefit of fluoride toothpastes using an enamel insert model. Caries Res 23(2):81–6. Wefel JS, Jensen ME, Triolo PT, Faller RV, Hogan MM, Bowman WD, De/remineralization from sodium fluoride dentifrices. Am J Dent 8(4):217–220
2. Wefel JS, Jensen ME, Triolo PT, Faller RV, Hogan MM, Bowman WD (1995) De/remineralization from sodium fluoride dentifrices. Am J Dent 8(4):217–220
3. Pendrys DG, Stamm JW (1990) Relationship of total fluoride intake to beneficial effects and enamel fluorosis. J Dent Res 69(2_suppl):529–38
4. Mandel ID (1989) Impact of saliva on dental caries. Compendium (Newtown, Pa.). Supplement (13):S476–81
5. Andrian S, Stoleriu S, Tărăboanţă I, Gamen AC, Dîmbu E, Negraia D (2018) Remineralization of incipient enamel lesions using non-fluoride agents. A review. Int J Med Dent 8(1):41–9
6. Feghali K, Feldman M, La VD, Santos J, Grenier D (2011) Cranberry proanthocyanidins: natural weapons against periodontal diseases. J Agric Food Chem 60(23):5728–5735
7. Silva AP, Gonçalves RS, Borges AF, Bedran-Russo AK, Shinohara MS (2015) Effectiveness of plant-derived proanthocyanidins on demineralization on enamel and dentin under artificial cariogenic challenge. J Appl Oral Sci 23(3):302–309
8. Xie Q, Bedran-Russo AK, Wu CD (2008) In vitro remineralization effects of grape seed extract on artificial root caries. J Dent 36(11):900–906
9. Creanor SL, Awawdeh LA, Saunders WP, Foye RH, Gilmour WH (1998) The effect of a resin-modified glass ionomer restorative material on artificially demineralised dentine caries in vitro. J Dent 26(5–6):527–531
10. Khalife MA, Boynton JR, Dennison JB, Yaman P, Hamilton JC (2009) In vivo evaluation of DIAGNOdent for the quantification of occlusal dental caries. Oper Dent 34(2):136–141
11. Huth KC, Neuhaus KW, Gygax M, Bücher K, Crispin A, Paschos E, Hickel R, Lussi A (2008) Clinical performance of a new laser fluorescence device for detection of occlusal caries lesions in permanent molars. J Dent 36(12):1033–1040
12. Sneha N, Pushpalatha C (2017) In vitro evaluation of antibacterial activity and surface micro-hardness of cranberry extract, grape seed extract and chlorhexidine as an intra-canal medicament. J Indian Soc Pedod Prev Dent 35(supplement issue):90

Assessment of Remineralization Potential of Novel Varnish on Early Enamel Lesions Using Different Optical Methods

C. Pushpalatha, Swaroop Hegde, R. Deveswaran, and Latha Anandakrishna

Abstract The aim of the present study was to assess the remineralization potential of novel varnish on early enamel lesions created artificially using laser induced DIAGNOdent pen and optical based Vickers microhardness. 45 extracted, sound, caries free premolars were selected. The initial baseline data and after demineralizing the selected tooth, the readings were recorded. The demineralized teeth were treated with three different remineralization groups. The three remineralizing groups were Group 1 (Commercial 5% NaF varnish), Group 2 (Novel varnish) and Group 3 (Placebo varnish). After 28 days of pH cycling regimen daily, the readings were recorded for mineral content and microhardness of the tooth using the DIAGNOdent and Vickers hardness test. Statistical analysis revealed that using the DIAGNOdent pen, Group 1 (6.00 ± 0.00) and Group 2 (5.27 ± 0.46) had high amount of remineralization than Group 3 (8.3 ± 0.35). In both Group 1 and Group 2, there was a decrease in mean moment value after remineralization suggesting there is a mineral gain in both groups. Vickers microhardness test indicated significant ($P < 0.001$) remineralization in both Group 1 and Group 2, whereas Group 3 had no significant difference. The results confirmed that novel varnish containing cocoa compounds has almost similar remineralizing effect in comparison to commercially available fluoride varnish.

Keywords Cocoa · Theobromine · Fluoride varnish

1 Introduction

Dental caries in early stages can be reversed through the process of remineralization using fluoride agents delivered in the form of dentifrice, mouth rinses and varnishes [1]. Of these, varnish is effective in reducing early enamel lesions due to better

---

C. Pushpalatha (✉) · S. Hegde · L. Anandakrishna
Faculty of Dental Sciences, M.S. Ramaiah University of Applied Sciences, Bengaluru, India
e-mail: drpushpalatha29@gmail.com

R. Deveswaran
Faculty of Pharmacy, M.S. Ramaiah University of Applied Sciences, Bengaluru, India

adhesion, longer retention time and availability of drug for a long duration for its action. The major drawback associated with the use of fluoride is dental fluorosis [2]. Hence there is a paradigm shift towards the use of natural products with remineralization potential. Among the natural products, extensive study was carried out on the effect of cocoa on mineralization of the teeth. The results of the previous study demonstrate that cocoa containing theobromine enhanced the remineralization of the teeth in comparison to that of fluoride [3]. Studies also reported that polyphenols present in cocoa are effective in antibacterial activities [4, 5]. To reduce the risks associated with synthetic fluoride, a natural novel varnish was formulated containing cocoa compounds like theobromine, catechin and epicatechin along with other natural ingredients like agarose and benzoin. The developed varnish was assessed for remineralization potential using optical device considering the mineral loss during early enamel lesion.

2 Materials and Methods

2.1 Materials

Cocoa seeds were procured from Puttur, Mangalore and subjected to isolation using Reverse HPLC to obtain phytochemicals such as theobromine, catechin and epicatechin. Agarose, benzoin powder and ethanol were purchased from HiMedia Pvt Ltd., India.

2.2 Preparation of Varnish

The 25 ml of novel varnish was prepared by adding 1.8% theobromine, 0.005% catechin, 0.005% epicatechin, 0.3% agarose, 2% benzoin powder and 2% ethanol. The 25 ml placebo varnish was prepared by adding 0.3% agarose, 2% benzoin powder and 2% ethanol without theobromine, catechin and epicatechin.

2.3 Preparation of Demineralization Solution

100 ml of demineralized solution was prepared by adding 32 mg of $CaCl_2 \cdot 2H_2O$, 303 mg of KH_2PO_4 and 450 mg of lactic acid in 100 ml of deionized water. The pH of the demineralized solution prepared was adjusted with 1M sodium hydroxide to a pH of 4.5.

2.4 Preparation of Artificial Saliva

1L of artificial saliva was prepared by adding methyl-p-hydroxybenzoate (2.00 g/l), sodium carboxy methyl cellulose (10.0 g/l), $Mgcl_2 \cdot 6 \cdot H_2O$ (0.29 mM), $Cacl_2 \cdot 2H_2O$ (1.13 mM), potassium dihydrogen phosphate (2.40 mM) and Potassium chloride (8.38 mM) in 1000 ml of distilled water. The pH of the solution was adjusted to 6.75 by adding 1 M potassium hydroxide.

2.5 Sample Selection

The present study was approved by the institutional ethics committee. After informed consent from the patient, 45 freshly extracted human first premolar teeth for orthodontic purpose were collected from the Department of maxillofacial and oral surgery, FDS, M.S.R.U.A.S. Teeth with caries, cracks and enamel deformations were excluded from the experimental study. The tooth was thoroughly cleaned for debris or stains with a ultrasonic device. The tooth with a moment value of 2 or 3 on the digital display of the DIAGNOdent was used for the study. The randomly selected teeth were sectioned into two halves mesio-distally using water cooled saw, each group containing 15 tooth blocks. The three groups were Group 1 (5% NaF, Voco-Profluor), Group 2 (Novel varnish) and Group 3(Placebo varnish). The sectioned enamel samples were cut into 4 mm in lengthX2 mm in widthX1.5 mm in thickness using low speed saw with a diamond disc. The enamel samples were made flat using water cooled silicon carbides discs of varying sizes of 320 grade paper followed with 600 and 1200 grade paper. Enamel samples were cleaned with deionized water for 5 min and completely air dried. The enamel blocks were then coated with acid resistant nail polish except the buccal surface. The baseline data was obtained using the DIAGNOdent pen and Vickers hardness test.

2.6 Preparation of Artificial Enamel Lesions

Each tooth of all three groups was immersed in a beaker containing 4 ml of demineralizing solution for 96 h at 37 °C. After 96 h, the reading of demineralized tooth was observed using the DIAGNOdent pen and Vickers microhardness indenter. These demineralized enamel samples were mounted on acrylic blocks which were later subjected to remineralization process.

2.7 Treatment Procedure

The mounted acrylic enamel blocks were subjected to remineralization process using 28 days pH cycling model that simulates the oral environment. The treatment procedure involves 3 steps for three times per day. On the first day, all the groups were stored in artificial saliva. From 2nd day to 28th day, the regimen is shown in Table 1.

After the treatment of enamel blocks of all the groups, the readings were recorded using the DIAGNOdent pen and Vickers microhardness indenter.

Table 1 Daily regimen of pH cycling from 2nd day to 28th day

Time	Treatment procedure
At 8.00 a.m.	• Acid challenge for 1 h—all groups
	• Storage in artificial saliva for 1 h—all the groups
	• Rubbing with varnish for 2 min
	Group1: Rubbed with Placebo varnish
	Group 2: Rubbed with Novel Varnish
	Group 3: Rubbed with commercial Varnish
At 11.00 a.m.	• Acid challenge for 1 h—all groups
	• Storage in artificial saliva for 1 h—all the groups
	• Rubbing with varnish for 2 min
	Group1: Rubbed with Placebo varnish
	Group 2: Rubbed with Novel Varnish
	Group 3: Rubbed with commercial Varnish
At 2.00 p.m.	• Acid challenge for 1 h—all groups
	• Storage in artificial saliva for 1 h—all the groups
	• Rubbing with varnish for 2 min
	Group1: Rubbed with Placebo varnish
	Group 2: Rubbed with Novel Varnish
	Group 3: Rubbed with commercial Varnish
Till 8.00 a.m. next day	Stored in artificial saliva

3   Statistical Analysis

SPSS statistical software version 22 was used at 0.05 level significance and 95% confidence interval. ANOVA followed by post hoc multistep comparisons (Tukey HSD) was used to compare between and within the groups.

4   Results and Discussion

The results of the DIAGNOdent pen and Vickers microhardness test revealed no statistical significance from baseline to after demineralization data in all the three groups ($P > 0.005$). But there was a noticeable change in mean values from baseline data to after demineralization between all the groups suggesting that there was a subsurface lesion formation (demineralization) on the enamel block. The mean value change after remineralization process evaluated using DIAGNOdent pen in Group 1 was 6.00 ± 0.00, in Group 2 it was 5.27 ± 0.46 and in Group 3 it was 8.3 ± 0.35 and it was statistically significant ($P < 0.001$). The Vickers microhardness test data also revealed a significant increase in microhardness after remineralization in Group 1 (280.48 ± 3.91) and Group 2 (284.3 ± 7.47) compared to Group 3 (261.02 ± 8.05). On comparison of Group 1 and Group 2 with DIAGNOdent pen moment values after remineralization, the statistical analysis showed significant difference($P < 0.001$), whereas Vicker's microhardness test values showed no statistical difference ($P > 0.005$). The values of Group 2 suggested that it is slightly better than Group 1 whereas it is not statistically significant. Thus statistical analysis showed that Group 1 and Group 2 had maximum remineralization potential compared to Group 3. The data revealed that Group 3 had no significant change in values after remineralization with both DIAGNOdent pen and Vicker's microhardness test thereby confirming the absence of remineralization. The results demonstrated that Group 2 containing theobromine, catechin and epicatechin was effective in depositing the mineral thus increasing the enamel hardness. Thus developed varnish was equally effective in remineralizing the enamel surface compared to commercially available varnish. The present observation can be correlated with previous studies in both in-vitro and in-vivo animal models, where the addition of theobromine led to increased crystallite size and increased surface recrystallization suggesting increased mineral deposition [6]. A study regarding remineralization by theobromine suggested that regular exposure of demineralized enamel surface increases the surface microhardness and induces recrystallization of enamel in comparison with sodium fluoride. The surface microhardness of enamel treated with theobromine is much harder and resistant to dissolution when compared to fluoride [7]. The enhanced hardness of enamel surface was noticed with a concentration of 200 mg/L of theobromine which is much lesser than fluoride [8]. In the present study also, Group 2 containing 1.8% theobromine showed increased microhardness values compared to Group 1 with 5% Sodium fluoride. The theobromine promotes remineralization by bringing mineral changes in

Table 2 Comparison of DIAGNOdent moment values at different experimental phases between the groups at baseline, after demineralization and after remineralization

	One way ANOVA test			Significance value	Tukey's HSD post hoc test		
Experimental phases	Group 1	Group 2	Group 3		G1 versus G2	G1 versus G2	G2 versus G3
	Mean ± SD	Mean ± SD	Mean ± SD	*P* value	*P* value	*P* value	*P* value
Baseline	2.54 ± 0.52	2.53 ± 0.52	2.60 ± 0.51	0.92	1.00	0.93	0.93
After demineralization	8.53 ± 0.52	8.40 ± 0.51	8.40 ± 0.51	0.71	0.76	0.76	1.00
After remineralization	6.00 ± 0.00	5.27 ± 0.46	8.3 ± 0.35	<0.001*	<0.001*	<0.001*	<0.001*

*Statistically significant
G1—Group 1, G2—Group 2, G3—Group 3

the superficial enamel layer which increases the surface microhardness, crystal formation and crystal size. Theobromine also inhibits the dissolution of enamel thus increasing remineralization. The increase in mineral gain and surface microhardness of enamel using novel varnish in this work could be due to the promotion of calcium deposition leading to increased crystal formation and crystal size. Thus the results of the present study suggest that novel varnish is superior to fluoride in the prevention of early enamel lesions (Tables 2 and 3).

5   Conclusion

The novel varnish developed in this study demonstrated enhanced mineral gain and surface microhardness of demineralized enamel suggesting satisfactory remineralization potential of early enamel lesions. The findings of the study show that developed novel varnish is a promising alternative for remineralization of early enamel lesions. Furthermore, assessment of antibacterial activity of the novel varnish is desirable and a further clinical trial on remineralization of enamel lesions using novel varnish is necessary.

Table 3 Comparison of Vicker's hardness values at different experimental phases between the groups at baseline, after demineralization and after remineralization

Experimental phases	One way ANOVA test			Significance value	Tukey's HSD post hoc test		
	Group 1	Group 2	Group 3		G1 versus G2	G1 versus G3	G2 versus G3
	Mean ± SD	Mean ± SD	Mean ± SD	P value	P value	P value	P value
Baseline	323.76 ± 2.60	325.14 ± 3.76	324.98 ± 3.27	0.45	0.48	0.56	0.99
After demineralization	260.92 ± 6.02	260.69 ± 7.65	260.69 ± 8.00	1.00	1.00	1.00	1.00
After remineralization	280.48 ± 3.91	284.37 ± 7.47	261.02 ± 8.05	<0.001*	0.26	<0.001*	<0.001*

*Statistically significant
G1—Group 1, G2—Group 2, G3—Group 3

References

1. Featherstone JD (2008) Dental caries: a dynamic disease process. Aust Dent J 53(3):286–291
2. Pendrys DG, Stamm JW (1990) Relationship of total fluoride intake to beneficial effects and enamel fluorosis. J Dent Res 69(2_suppl):529–38
3. Amaechi BT, Porteous N, Ramalingam K, Mensinkai PK, Vasquez RC, Sadeghpour A, Nakamoto T (2013) Remineralization of artificial enamel lesions by theobromine. Caries Res 47(5):399–405
4. Ooshima T, Osaka Y, Sasaki H, Osawa K, Yasuda H, Matsumura M, Sobue S, Matsumoto M (2000) Caries inhibitory activity of cacao bean husk extract in in-vitro and animal experiments. Arch Oral Biol 45(8):639–645
5. Andújar I, Recio MC, Giner RM, Ríos JL (2012) Cocoa polyphenols and their potential benefits for human health. Oxidative Med Cell Longev 24:2012
6. Nakamoto T, Simmons WB Jr, Falster AU, inventors; Biomedical Development Corp, assignee. Products of apatite-forming-systems. United States patent US 5,919,426. 1999 Jul 6
7. Besic FC, Bayard M, Weimann MR Jr, Burrell KH (1975) Comparison and structure of dental enamel: elemental composition and crystalline structure of dental enamel as they relate to its solubility. J Am Dent Assoc 91:594–601
8. Kargul B, Ozcan M, Peker S, Nakamoto T, Simmons WB, Falster AU (2012) Evaluation of human enamel surfaces treated with theobromine: a pilot study. Oral Health Prev Dent. 10:275–282

Development and Validation of an Innovative Hand-Held Device for Early Detection of Oral Cancer and Oral Potentially Malignant Disorders

Shwetha Venkataramana and Preetham Shankapal

Abstract Delay in diagnosis of oral precancers and oral cancers is increasing the burden of this disease in India. There is a need for early chairside detection of these precancerous lesions. This paper presents an innovative hand-held mobile phone device exploiting the properties of tissue autofluorescence for the early detection of these lesions.

Keywords Oral cancer · Precancer · Autofluorescence

1 Introduction

Oral cancer is the sixth most common cancer reported globally with an annual incidence of over 300,000 cases, of which 62% arise in developing countries. There is a significant difference in the incidence of oral cancer in different regions of the world, with the age-adjusted rates varying from over 20 per 100,000 populations in India to 10 per 100,000 in the U.S.A, and less than 2 per 100,000 in the Middle East. Age-adjusted rates of oral cancer in India are high and account for over 30% of all cancers in the country [1]. Use of tobacco in the form of cigarettes, smokeless tobacco, betel nut chewing, alcoholism, and Human Papilloma Virus (HPV) are the most common risk factors for oral cancer [2, 3].

Oral cancer affects people from the lower socioeconomic status of society and people in rural areas due to a higher exposure to risk factors such as the use of tobacco, poor diet, and poor oral hygiene [3]. In rural areas, patients have inadequate access to trained healthcare providers with very limited health care services, leading to delayed presentation at advanced stages of oral cancer. Hence early detection of

S. Venkataramana (✉)
Faculty of Dental Sciences, Ramaiah University of Applied Sciences, Bengaluru, India
e-mail: shwetha.vg@gmail.com

P. Shankapal
Faculty of Engineering and Technology, Ramaiah University of Applied Sciences, Bengaluru, India

oral cancer offers the best chance for long-term survival and has the potential to improve treatment outcomes and make healthcare affordable.

Oral squamous cell carcinoma or oral cancer usually originates from oral potentially malignant lesions like—hyperplasia, increasing the degree of dysplasia (mild, moderate, and severe) into Carcinoma In Situ (CIS), and finally to invasive squamous cell carcinoma. Oral potentially malignant lesions are present in sites that are easily accessible for visual inspection. However, the diagnosis of these lesions is challenging even for experienced oncologists [4].

A Conventional Oral Examination (COE), using normal (incandescent) light, has been the standard method for oral cancer screening for many decades but has limitations on detecting early premalignant lesions. Its utility for detecting early precancerous lesions is controversial, as it does not accurately detect the small proportion of biologically relevant lesions that are likely to progress to cancer [5].

Autofluorescence is an established method proposed for early detection. There are many devices like the VELscope, Vizilite, and others which use autofluorescence technique which costs around $1500–3000 and turns out to be expensive with respect to population-based oral cancer screening in India as seen in Fig. 1. Also, these devices may indicate the presence of cancer but not really validate the malignancy by means of automated analysis of the images obtained on initial screening [6].

The proposed paper aims to develop a very cost-effective hand-held camera like device with blue light source and filters to detect early onset oral cancer using tissue fluorescence techniques. The blue light filters will clearly identify the presence of malignancy based on images obtained from the camera. When viewed through the device, malignant and potentially malignant tissues will appear as dark spots indicating the absence of autofluorescence. While normal oral mucosa will appear green and inflammations and plaque are always observed as red fluorescence.

On being positively classified as malignant through tissue fluorescence technique, patient would undergo an incisional biopsy with appropriate protocols at

Fig. 1 VELscope device

the screening site and the tissue will be subjected to histopathology for validation purposes.

2 Device Development

2.1 Device

An innovative hand-held mobile device was designed using the principle of wideband imaging and autofluorescence. Wideband here means viewing the image at all the wavelengths of visible light except blue, i.e., imaging will be performed at 500–700 nm filtering out 400–500 nm of the visible range [7].

This hand-held camera like device as seen in Fig. 2 with blue light source and filters is being used to detect early onset oral cancer using tissue fluorescence techniques [7]. The blue light filters will clearly identify the presence of malignancy based on images obtained from the camera. When viewed through the device, malignant and potentially malignant tissues will appear as dark spots indicating the absence of autofluorescence as seen in Fig. 3.

The lesion, when viewed under normal visible light, appeared innocuous as a cheek bite but when viewed through the device, however, revealed dark areas which indicate the invasive fronts of the lesion as well as the site to be chosen for biopsy, since loss of fluorescence is an indicator for malignancy as seen in Fig. 4. While normal oral mucosa will appear green and inflammations and plaque are always observed as red fluorescence.

Since this device can be easily fitted over to any mobile phone camera, data storage and communication are very easy. This feature helps health care workers situated at remote health care centers to communicate with specialists at urban health care setups via mobile applications easily avoiding unnecessary delay in diagnosis.

Autofluorescence uses naturally occurring fluorochromes that are located in the epithelium and submucosa and which are irradiated with different excitation wavelengths [8]. A portion of photons is absorbed by fluorophores present in oral mucosal
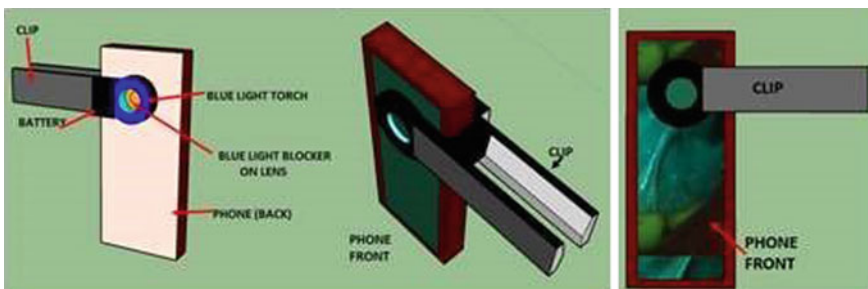

Fig. 2　The hand-held device which can be fitted onto any mobile phone camera

Fig. 3 The innovative device at use
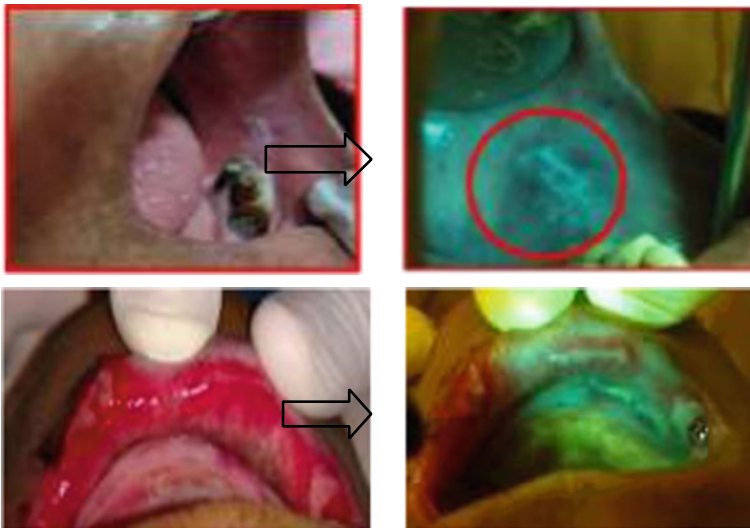
Fig. 4 Images of oral potentially malignant disorders using the device

molecules when the mucosa is illuminated at blue and UV visible wavelengths (375–400 nm). The fluorophores emit photons with lower energy, and subsequently, the photons can be viewed as fluorescence from the oral mucosal surface in the green spectral range [8, 9].

Abnormal mucosa appears dark due to the reduction or change in the quantity and quality of the fluorophores in the mucosa [10]. The reduced fluorophores include nicotinamide adenine dinucleotide and flavin adenine dinucleotide in the epithelium, and collagen and elastin crosslinks in the stroma have been associated with the development and progression of oral neoplasia [9].

3 Materials and Methods

Sixty patients were with potentially malignant disorders (16 with oral leukoplakia, 24 with oral lichen planus and 20 with oral submucous fibrosis). Of the 60 patients, 40 were male and remaining 20 were females. Patients in the age range between 30 and 70 years of age were included in the study. An informed consent was obtained from all participants of the study. Patients unwilling for biopsy were excluded from the study. The study was approved by the institutional ethics committee and review board. The oral cavity was examined under conventional visible light (white light/yellow incandescent light of the dental chair) initially and then a blue light from a LED light source was used to illuminate the oral cavity. All clinical examinations were performed by one clinician. First, all patients underwent a visible/white light examination and based on the clinical evaluation the findings were classified as (a) grade 1: clinically normal mucosa; (b) grade 2: abnormal but innocuous lesions like inflammation, cheek bite; and (c) grade three: possibly premalignant or malignant.

Following the visible light examination, the oral cavity was irradiated with the blue light source and viewed through the blue light blocker device fitted on to the mobile phone camera. The images were viewed and imaged simultaneously with the click of a camera. When illuminated through the blue light and viewed through the blue light blocker/filter, because of the property of tissue autofluorescence the normal oral mucosa emits various shades of pale green autofluorescence. The autofluorescence images were classified as (a) Normal-green areas exhibiting no loss of autofluorescence, (b) Inflammatory-areas appearing pink/red, and (c) Dysplastic-Dark Gray or black areas showing loss of fluorescence. One control biopsy per patient was obtained from a distant site, preferably on the contralateral or on the same side away from the lesion proper.

Since histopathology is considered the gold standard for confirming any malignancy, the areas appearing dark due to loss of tissue autofluorescence were involved in the incisional biopsy for histopathological evaluation. All biopsied specimens were fixed in 10% buffered formaldehyde, paraffin embedded, cut as 4 µm sections, and stained with Hematoxylin and Eosin. The pathologist was blinded to the clinical impression, patient history, visible light, and autofluorescence image findings. Histopathological evaluation was performed and a histological diagnosis was assigned for each lesion as seen in Fig. 5.
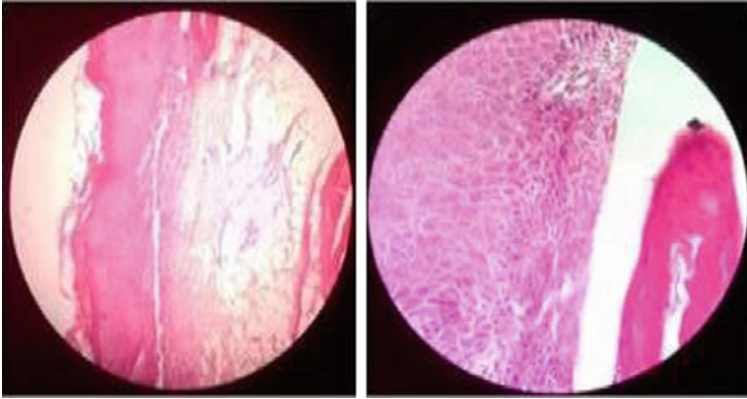
Fig. 5 Histopathologic images of the dysplastic areas detected by the device confirming the diagnosis

4 Results

Of the samples chosen, a total of 80 lesions were biopsied including the normal controls. The biopsies were obtained from various sites like buccal mucosa, gingiva, vestibule dorsolateral tongue, etc. Two-thirds of the patients enrolled were males and the overall mean age was 60 years.

Of the 80 biopsy samples, 35 samples showed loss of autofluorescence, while 45 samples showed retention of pale green autofluorescence. Of the 45 samples which showed pale green autofluorescence, 40 were from normal tissue samples and 5 tissue samples were from the oral submucous fibrosis patients.

Using histology as the gold standard, the device achieved a sensitivity of 100% and specificity of 100% in detection of oral leukoplakia. The device achieved a sensitivity of 50% and specificity of 100% in the detection of oral submucous fibrosis. Sensitivity of 100% and specificity of 50% were achieved in detection of oral lichen planus. In case of normal controls, both sensitivity and specificity were found to be 100%.

5 Discussion

These results suggest the potential of this simple low-cost innovative device for the early detection of oral potentially malignant disorders. This device works on the principle of tissue autofluorescence and can be snuggly fitted over to any mobile phone camera for easy operation. The proposed device has inbuilt filters and is easily operable and does not require a skilled professional for identification of the lesions; whereas the VELscope system requires the expertise of a skilled professional who will require an external filter to view the existing lesions. Also, the VELscope

systems are more expensive than this device, and they have no scope for any image data storage or communication unlike this device.

Oral cancer is one of the most common malignancies worldwide, and carries one of the lowest overall survival rates. Despite the easy accessibility of the oral cavity to examination, most patients present to the clinician at advanced stages, when treatment is associated with higher morbidity, is more expensive, and less successful than earlier interventions [4]. Early detection of oral cancer can greatly improve treatment outcomes. Unfortunately, there has been no method till date to adequately screen and diagnose early oral cancers and precancers because detection still relies on the clinicians' ability to visually identify subtle neoplastic changes, and to distinguish these changes from more common inflammatory conditions.

Also considering the painful and invasive nature of the biopsy procedures, patients may be reluctant to undergo a biopsy for the diagnosis of lesions. In such circumstances, noninvasive diagnostic methods like autofluorescence imaging provide promising results, especially in mass screening or population-based screening programmes [4, 11].

A single-blind evaluation study conducted by Henning et al. in Germany to assess the suitability of autofluorescence as an adjunct in screening for oral cancer and oral potentially malignant disorders concluded its sensitivity to be 97% against 75% and specificity to be 41.4% against 33.3% for the autofluorescence and white light group, respectively. They concluded autofluorescence to be a simple noninvasive test which could be used by a trained personnel to find oral precursor malignant lesions and also serve as a guide to locate the area to obtain biopsy tissue. However, the authors' opined human bias to be a limitation as the analysis solely depended on physician's experience [8].

A study was carried out to examine the autofluorescence status of lesions suspected to be Oral Squamous Cell carcinoma (OSCC) under ultraviolet light and to correlate it with the clinical diagnosis made visually on standard white light inspection and histopathological diagnosis by Kriti et al. In addition, the fluorescence status was correlated with the rate of cell proliferation using Argyrophilic Nucleolar Organizer Region (AgNORs) analysis. The importance of autofluorescence as a screening tool was further supported by a statistically significant correlation between autofluorescence status and cell proliferative rate. The study proposed that autofluorescence may be used as a guideline while taking an incisional biopsy, to avoid underdiagnoses of lesions [12].

The proposed device could easily be used by any health care worker at rural outreach center for mass screening purposes. Routinely after screening at rural outreach centers, patients are referred to urban health care setups for further investigations and follow-ups. Thus patients are lost to follow up resulting in patients reporting only at advanced stages of the disease. The images obtained by this device could be easily shared via mobile applications to oncologists who could opine and advise biopsy looking at the images obtained; thus addressing the diagnostic delay associated with this disease. We at our institution have implemented the same in the rural outreach centers of Kaiwara where the device has been brought to use, thus benefitting the rural population.

Moreover, the cost of this device is very less (~Rs 1000/per piece) when compared to the VELscope device in market which costs ~Rs 1,50,000–Rs, 3,00,000. Thus this device can be easily distributed at various rural health care setups connecting the health care workers and oncologists and improve the awareness, pick-up rates, and thus long-term survival of patients.

Autofluorescence imaging has been used successfully to rapidly and noninvasively distinguish malignant oral lesions from surrounding tissue in several pilot studies. The proposed device could thus bring a paradigm shift in early diagnosis of oral cancer and oral potentially malignant disorders, thereby improving the survival rates and quality of life of the people.

References

1. Coelho KR (2012) Challenges of the oral cancer burden in India. J Cancer Epidemiol 1–17. Article ID 701932
2. Sujha S, Rengaswamy S, Bela B, Thara S, Gigi T, Babu M, Jissa V, Kunnambath R (2009) Cost-effectiveness of oral cancer screening: results from a cluster randomized controlled trial in India. Bull World Health Organ 87:200–206
3. Kumar M, Ronak N, Tapan GM, Chintan D (2016) Oral cancer: etiologic and risk factors. A review. J Cancer Res Ther 12(2):458–63
4. Lane PM, Whitehead TGP, Zeng H, Catherine FP, Williams M, Zhang L, Rosin MP, MacAulay CE (2006) Simple device for the direct visualisation of oral cavity tissue fluorescence. J Biomed Opt 11(2):024006
5. Lingen MW, Kalmar JR, Karrison T, Speight PM (2008) Critical evaluation of diagnostic aids for the detection of oral cancer. Oral Oncol 44(1):10–22
6. Rahman et al (2010) Evaluation of a low cost portable imaging system for early detection of oral cancer. Head Neck Oncol 2(10):1–8
7. Shin D, Vigneswaran N, Gillenwater A, Richards-Kortum R (2010) Advances in fluorescence imaging techniques to detect oral cancer and its precursors. Future Oncol 6(7):1143–1154
8. Hanken H, Kraatz J, Smeets R, Heiland M, Blessmann M, Eichhorn W, Clauditz TS, Grobe A, Kolk A, Rana M (2013) The detection of oral pre-malignant lesions with an autofluorescence based imaging system (VELscopeTM)—a single blinded clinical evaluation. Head Face Med 9(23):1–7
9. Yan Y-J, Huang T-W, Cheng N-L, Hsieh Y-F, Tsai MH, Chiou J-C, Duann J-R, Lin Y-J, Yang C-S, Ou-Yang M (2017) Portable LED-induced autofluorescence spectroscopy for oral cancer diagnosis. J Biomed Opt 22(4):045007
10. Balasubramaniam AM, Sriraman R, Sindhuja P, Mohideen K, Parameshwar RA, Harris KTM (2015) Autofluorescence based diagnostic techniques for oral cancer. J Pharm Bioallied Sci 7(2):S374–S377
11. Huang TT, Huang J-S, Wang Y-Y, Chen K-C, Wong T-Y, Chen Y-C, Wu C-W, Chan L-P, Lin Y-C, Kao Y-H, Nioka S, Yuan S-SF, Chung P-C (2017) Novel quantitative analysis of autofluorescence images for oral cancer screening. Oral Oncol 68:20–26
12. Bagri Manjrekar K, Chaudhary M, Sridharan G, Tekade SR, Gadbail R, Khot K (2017) In vivo autofluorescence of oral squamous cell carcinoma correlated to cell proliferation rate. J Cancer Res Ther

Singer Identification Using Time-Series Auto-Regressive Moving Average

Check for updates

Ananya Bonjyotsna and Manabendra Bhuyan

Abstract Singer Identification (SID) is one of the major interests in the field of Music Information Retrieval (MIR). The researches in SID in the last decade have been primarily focused in improving the identification accuracy by using better features in addition to Mel-frequency Cepstral Coefficients (MFCC). This work primarily attempts to explore a time-domain feature from the model parameters of the time-series Auto-regressive-Moving Average (ARMA) model to be used as one of the features for SID. The ARMA features are also combined along with MFCC to compare the results and observe its performance in SID. The MFCC and ARMA features are trained and classified using the Gaussian Mixture Model (GMM). Most of the literature deals in the spectral domain for feature extraction. Therefore, this paper mainly seeks to find the scope of using time-domain model parameters as one of the features in decision-making problems in the field of MIR.

Keywords Singer identification · MFCC · ARMA · GMM · MIR

1 Introduction

Singer Identification (SID) is the process of retrieving the identification of the singer in a song through extraction of the most efficient and robust features from the singers voice and their processing. This interest in identifying the singer is motivated by the growing amount of music exchange using the internet and the need to categorize the songs based on the singer. One of the method of characterization of most audio systems, music servers and online music stores is by the name of the singers. For content based MIR, it is necessary to represent the singing voice by its characteristics. Generally the process of SID can be divided into three steps—(i) Locating vocal/non-vocal

A. Bonjyotsna (✉) · M. Bhuyan
Tezpur University, Tezpur, India
e-mail: ananyab@tezu.ernet.in

M. Bhuyan
e-mail: manab@tezu.ernet.in

segments in the song and extracting the vocal segments, (ii) Feature extraction of the vocal segments and (iii) Statistical Classification. If the data used are monophonic, the first step may not be taken into consideration. Some of the commonly used features in SID are Mel-frequency Cepstral Coefficients (MFCC), Linear Predictive Coefficients (LPCs), Perceptual Linear Prediction Coefficients (PLPs) and the Harmonic Coefficients. Similarly, most common classifiers that are seen to be used in SID are Gaussian Mixture Models (GMM), Hidden Markov Model (HMM), Support Vector Machines (SVMs) and Multilayer Perceptrons (MLPs). Kim and Whitman [6] used traditional LPC features for speech coding to extract singing voice features. They used two different classifiers GMM and SVM to model their feature vectors using established pattern recognition algorithms. Zhang [10] computed the LPCC to extract the audio features of each audio frame which form the feature vectors of the audio frame and used a GMM classifier classify singers. Tsai and Wang [9] and Nwe and Li [7] have also employed MFCC and another feature called Octave Frequency Cepstral Coefficient (OFCC), respectively. Bartsch and Wakefield [1] proposed an algorithm for identifying the singing voice in a song with no accompaniment using the spectral envelope of the signal to build a composite transfer function as the feature and have used a standard quadratic classifier for classification. Cai et al. [2] proposed a new auditory feature called Gammatone Cepstral Coefficient combined with MFCC and LPCC to represent different singing voice features. Patil et al. [8] used Cepstral Mean Subtraction (CMS) based MFCC (CMSMFCC) feature vectors for SID and compared the result with MFCC using second-order polynomial classifier. Johnson et al. in [5] analysed the Long-term Average spectrum as an objective measurement for singing voice classification. Deshmukh et al. [3] worked only on timbre features in SID applied to North Indian classical singers. Devaney in [4] has also used similar features like pitch, timing, dynamics and timbre descriptors and implemented them on western classical trained singers for intra and inter-singer similarity.

The existing research works mentioned above have mostly considered the frequency-domain auditory features for characterizing the singing voice signal. And also it is seen that time-domain stochastic methods were only used in speech signals and not in singing voice yet. In this work, time-domain approach is directly applied to singing voice and explored to find a new feature of the singing voice signal. The model builds a transfer function model of the framed input signal and the coefficients of the polynomial transfer function are used to form the feature vector of the signal. This work finally compares the performance of SID using MFCC and ARMA model coefficients as the primary features.

2 Methodology

The SID technique is performed using the conventional system as in [9]. The singing voices of the singers are the signals that are fed to the system. There are two phases in the system, i.e. Training phase and Testing phase. In the training phase, the Feature Vectors (FV) formed from the feature extraction are fed to the training block to

Fig. 1 Feature extraction for SID
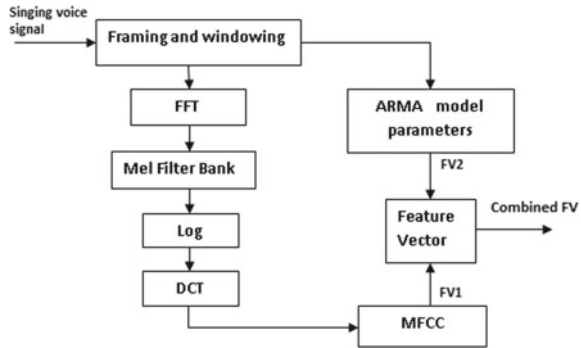
build GMM model for each singer. In the testing phase, the FVs extracted from the unknown sample are then subjected to the classifier block to classify the given test signal to one of the trained singer models.

2.1 Feature Extraction

Prior to training the singer models, the singing voice waveforms are converted to MFCC frame by frame and ARMA model functions are computed frame by frame. The computation of ARMA model functions is described in Sect. 2.2. The block diagram for the feature extraction process is shown in Fig. 1. Let $FV1 = \{X_1, X_2, \ldots, X_L\}^T$ and $FV2 = \{Y_1, Y_2, \ldots, Y_L\}^T$ be the M-dimensional MFCCs and N-dimensional ARMA coefficients computed, respectively, for each signal where 'L' is the total number of frames. The combined FV is then given as $FV = \{FV1, FV2\}$. The experiment is conducted at first by taking MFCC features only, then the combined FV and lastly by taking ARMA features alone. And the results are compared thereafter.

2.2 Time-Series ARMA Modeling

Generally in ARMAX (Auto-regressive-Moving Average with eXogenous input), the present output has a relationship with the previous values of the inputs and outputs. Moving average denotes the noise model used in the system. The system also depends not only on the present inputs but also the previous inputs, i.e. the exogenous inputs. Considering a linear time-invariant system with an input signal u(n), output y(n) and disturbance e(n), first we define the univariate time-series 'y' into delay coordinates Y(n) = y(n−1), y(n−2), …, y(n−na); 'u' into U(n) = u(n−1), u(n−2), …, u(n−na)

and 'e' into E(n) = e(n−1), e(n−2), …, e(n−nc) which is given by a difference equation,

$$y(n) + a_1 y(n-1) + a_2 y(n-2) + \cdots + a_{na} y(n-n_a) = b_1 u(n-1) + \cdots$$
$$+ b_{nb} u(n-n_b) + e(n) + c_1 e(n-1) + \cdots + c_{nc} e(n-n_c) \tag{1}$$

Equation 1 can be written as

$$y(n) + \sum_{k=1}^{na} a_{na} y(n-k) = \sum_{k=1}^{nb} b_{nb} u(n-k) + e(n) + \sum_{k=1}^{nc} c_k e(n-k) \tag{2}$$

Expressing Eq. 2 in discrete domain, we get

$$y(n) \left[1 + \sum_{k=1}^{na} a_k q^{-k} \right] = u(n) \sum_{k=1}^{nb} b_k q^{-k} + e(n) \left[1 + \sum_{k=1}^{nc} c_k q^{-k} \right] \tag{3}$$

where 'n_a' is the order of the polynomial A(q), 'n_b' is the order of the polynomial B(q) and 'n_c' is the order of the polynomial C(q).

Now, the singing voice as a time-series model without any input to the system is expressed as

$$y(n) \left[1 + \sum_{k=1}^{n_a} a_k q^{-k} \right] = e(n) \left[1 + \sum_{k=1}^{n_c} c_k q^{-k} \right] \tag{4}$$

3 Experiments and Results

The SID accuracy is evaluated first by using MFCC alone, then by using both MFCC and ARMA features and lastly by using only ARMA features. The method is implemented in MATLAB platform. 10 monophonic songs of duration 30–50 s were considered for each of the 7 singers. The recording is done in the recording setup by using condenser microphone under a noise-proof environment. The sampling frequency of all the audio segments is 44.1 KHz of 16-bit mono tracks. A total of 35 songs with 5 songs from each singer were used for training and the rest 35 songs are used for testing. The extracted features from the audio segments are subjected to the training phase to build GMM model for the singers. 12 MFCC coefficients are considered for the experiment and the FV1 is a 12-dimensional matrix $L \times 12$ where 'L' is the total number of frames computed from the segment. The frame size in samples is considered to be 1024 and the moving window size is taken to be half of the frame size, i.e 512 samples. In order to find the ARMA model parameters, the AIC values were calculated for different orders and the minimum AIC value was found for the order(4, 2). So the fourth-order transfer function was computed for each frame of
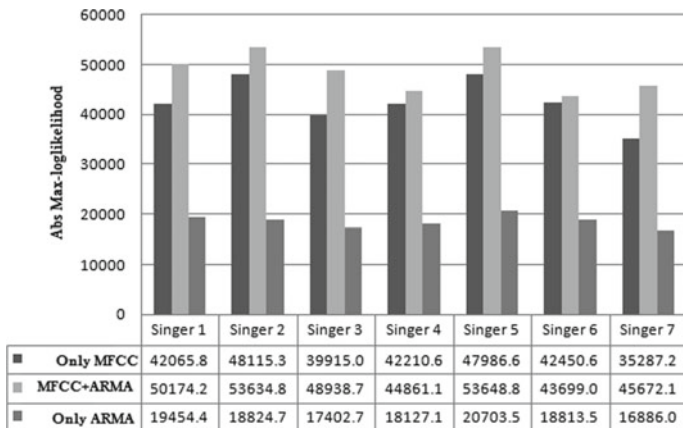
		Singer 1	Singer 2	Singer 3	Singer 4	Singer 5	Singer 6	Singer 7
■	Only MFCC	42065.8	48115.3	39915.0	42210.6	47986.6	42450.6	35287.2
▥	MFCC+ARMA	50174.2	53634.8	48938.7	44861.1	53648.8	43699.0	45672.1
■	Only ARMA	19454.4	18824.7	17402.7	18127.1	20703.5	18813.5	16886.0

Fig. 2 Scores of absolute Max log-likelihood of the three cases

the audio segment. For each frame, the fourth-order polynomial transfer function is expressed as

$$G(q) = \frac{1 + c_1 q^{-1} + c_2 q^{-2}}{1 + a_1 q^{-1} + a_2 q^{-2} + a_3 q^{-3} + a_4 q^{-4}} \qquad (5)$$

The coefficients of the polynomial transfer function a_1, a_2, a_3, a_4, c_1 and c_2 are used to form the feature vector. The 12 MFCC coefficients and 6 coefficients of the ARMA model are combined to form an 18-dimensional Feature Vector FV for modeling the GMM. For each class, 8 mixture Gaussian model is built. The feature vectors of the testing class is then matched to the already built GMM singer model.

Considering only MFCC and both MFCC and ARMA, the testing accuracy came out to be 100% for both the cases which means that all the audio segments were correctly identified to the respective singers. In case of only ARMA, FV2 is trained instead of FV. It has been observed that testing resulted is 94.28% accuracy, i.e. 33 audio segments out of 35 have been identified correctly. According to the results, the percentage accuracy of ARMA is less than MFCC. Now, in order to compare which method performs better, the maximum log-likelihood score is used as the metric. The higher the value of this metric, the closer the test signal is to the target singer. In Fig. 2, the absolute values are taken which means the smaller values denote the higher probabilities of matching. It could be seen that the combined Features showed increase in the absolute maximum log-likelihood score compared to only MFCC. This shows that adding the ARMA parameters as the feature decreases the performance of SID compared to only MFCC. However, another observation that is worth analysing is that the maximum log-likelihood scores in case of ARMA shows much smaller values than the other methods. It has been observed that in case of ARMA, the values are considerably less than the other two cases.

4 Conclusion

The objective of this work was to explore the possibility of using time-domain ARMA model parameters as a characteristic feature for classification of singers in the application of SID. The research works of the existing literature mentioned in Sect. 1 have been trying to improve the percentage accuracy of SID by adding new features in addition to MFCC. However, it is seen that no work has been done to inspect the applicability of time-domain features in SID. From this experiment, it is found that ARMA alone or when combined with MFCC could not perform better than MFCC in SID accuracy. But we cannot nullify the time-domain approach right away based on the accuracy results alone. The scores of the max log-likelihood of the ARMA case contradicts the accuracy performance. The reason for this should be because of considering the time-domain signal directly and applying to modeling without any transformation. Since we know that voice signals are quasi-stationary in nature, therefore such short-time modeling may further be investigated to improve the accuracy of SID. Therefore, the work in this paper could lead the research toward analysing the applicability of ARMA model coefficients as a feature in applications of SID or other identification applications of MIR.

References

1. Bartsch MA, Wakefield GH (2004) Singing voice identification using spectral envelope estimation. IEEE Trans Speech Audio Process 12(2):100–109. https://doi.org/10.1109/TSA.2003.822637
2. Cai W, Li Q, Guan X (2011) Automatic singer identification based on auditory features. In: 2011 seventh international conference on natural computation, vol 3, pp 1624–1628. https://doi.org/10.1109/ICNC.2011.6022500
3. Deshmukh S (2014) North indian classical musics singer identification by timbre recognition using mir toolbox. Int J Comput Appl 91(4):1–4
4. Devaney J (2016) Inter-versus intra-singer similarity and variation in vocal performances. Int J Comput Appl 45(3):252–264. https://doi.org/10.1080/09298215.2016.1205631
5. Johnson AM, Kempster GB (2011) Classification of the classical male singing voice using long-term average spectrum. J Voice 25(5):538–543. https://doi.org/10.1016/j.jvoice.2010.05.009, http://www.sciencedirect.com/science/article/pii/S089219971000130X
6. Kim YE, Whitman, B (2002) Singer identification in popular music recordings using voice coding features. In: Proceedings of the 3rd international conference on music information retrieval, pp 164–169
7. Nwe TL, Li H (2007) Exploring vibrato-motivated acoustic features for singer identification. IEEE Trans Audio Speech Lang Process 15(2):519–530. https://doi.org/10.1109/TASL.2006.876756
8. Patil HA, Radadia PG, Basu TK (2012) Combining evidences from Mel cepstral features and cepstral mean subtracted features for singer identification. In: 2012 international conference on Asian language processing, pp 145–148. https://doi.org/10.1109/IALP.2012.33

9. Tsai WH, Wang HM (2006) Automatic singer recognition of popular music recordings via estimation and modeling of solo vocal signals. IEEE Trans Audio Speech Lang Process 14(1):330–341. https://doi.org/10.1109/TSA.2005.854091
10. Zhang T (2003) Automatic singer identification. In: Proceedings of the 2003 international conference on multimedia and expo, ICME '03, vol 2, pp 33–36. IEEE Computer Society, Washington, DC. http://dl.acm.org/citation.cfm?id=1170745.1171614

Design and Development of Photon Counter for Silicon Carbide Ultraviolet Photometer Used in Space Instruments

Praveen Kumar Mogre, S. P. Karanth, M. A. Sumesh, Vijay, Dilip Yadav, and K. Sreelakshmi

Abstract Photon counting is one of the advanced methods of measurement, and this type of measurement is required when the measuring signal is very small and accuracy requirement is large. Photon counting methods are most commonly used in medical UV imaging, missile seeker system, ozone emission study, and dosimeter applications. Photon counting methods can be carried over a complete spectrum of light, but mostly done on a selective band of light like UV, IR, X-rays, or visible light, to analyze the intensity variation of light. UV photon counting is analyzed using silicon carbide (SiC) detector which was developed at LEOS and was designed to operate at a wavelength of 200–300 nm (solar blind). Design and implementation of a UV photon counting electronics is developed for the solar-blind on-board UV intensity measurement. This work deals with the design of essential readout electronics required to support the measurement of signals detected by SiC detectors developed by scientists at LEOS. LEOS detector and SGLUX detector (imported) are compared and performance analysis is carried out. The responsivity of both detectors is measured with the change in wavelength and also the quantum efficiency of the detector is measured over a solar-blind UV-C band. The number of photons present in the detected signal has been calculated and also the obtained results are matched with the solar photon count per second in space.

Keywords Solar blind · Silicon carbide (SiC) · Readout electronics · Solar irradiance

P. K. Mogre (✉) · K. Sreelakshmi
Department of Telecommunication Engineering, R.V. College of Engineering, Bengaluru 560059, India
e-mail: praveenmogre@gmail.com

K. Sreelakshmi
e-mail: sreelakshmik@rvce.edu.in

S. P. Karanth · M. A. Sumesh · Vijay · D. Yadav
Detector Section, Laboratory for Electro-Optics Systems, Indian Space Research Organization, Bengaluru 560058, India
e-mail: dspkaranth@gmail.com

219

1   Introduction

Sun is the source of electromagnetic radiations; of which UV electromagnetic radiations are of great interest to develop UV instruments, for space, military, and domestic applications. UV radiations are produced from various man-made sources like the missile launch site, missile plume, and welding flames. The UV signals produced from the above-mentioned sources are measured with instruments like UV radiometer or UV meter which are equipped with UV detector and electronic readout circuits for measuring the signal. Ultraviolet light comprises high photon energy as approximately 9 % of emitted energy by the sun lies in UV range, which covers the wide wavelength range of 400 nm down to 10 nm [1].

UV detectors are used in a wide range of applications like UV dosimetry and imaging, including solar UV measurements, astronomical studies, spacial optical communications (intra and inter-satellite secured communication), and military applications like missile warning, missile plume sensing, etc. [2].

The ultraviolet (UV) region is commonly divided into the following subdivisions and is commonly named according to the wavelength regions as mentioned in Table 1.

Silicon carbide (SiC) is one of the most promising candidates for the next-generation semiconductor material. The major advantages include a wide bandgap, high critical breakdown voltage, high saturation drift velocity, and high thermal conductivity [3]. Photon counting/detection involves the detection of photoelectrons released by light over a photosensitive surface of a photomultiplier tube, avalanche photodiode, and semiconductor photodiode.

Photon counting technique is employed to count a number of photons present in weak light signals generated from a distant light source. The number of photons generated from the light source depends on the wavelength of the light source, as it was observed that photon generation rate follows Planck's curve.

2   Theoretical Solar Photon Count Analysis

Planck's blackbody radiation distribution, S_λ, is given by Eq. (1)

Table 1 Classification of UV band

Name of Ultraviolet subband	Band abbreviation	Wavelength range (nm)
Ultraviolet A	UVA	400–320
Ultraviolet B	UVB	320–280
Ultraviolet C	UVC	280–220

$$s_\lambda = \frac{2\mathbf{h}c^2}{\lambda^5 \left(e^{\frac{hc}{(\lambda kT)}} - 1 \right)} \text{ w/m}^2/\text{sr}^{-1}/\text{nm}, \tag{1}$$

where h is Planck's constant (6.626×10^{-34} J/s), T is the temperature of the blackbody in Kelvin (K), k is the Boltzmann constant (1.381×10^{-23} J/K), C is the speed of light (3×10^8 m/s), and λ is the wavelength.

Spectral intensity of radiation from blackbody can be calculated using Eq. (2)

$$I = s_\lambda \times \text{ Area of Blackbody w/sr/nm}, \tag{2}$$

where area of blackbody is given by Eq. (3)

$$A = \pi \times R^2, \tag{3}$$

where R is the radius of the blackbody, i.e., sun ($R = 6.98 \times 10^8$ m).

Power of blackbody radiation in space per unit area is given by Eq. (4)

$$P = \frac{I}{r^2}\text{W /mm}^2, \tag{4}$$

where r is the distance between blackbody (sun) and the earth, also known as astronomical unit ($r = 1.5 \times 10^{11}$ m).

The power of the incident radiation falling on the area equivalent to detector area in space is calculated by Eq. (5)

$$P_0 = P \times \text{ Detector area }, \tag{5}$$

where the area of the detector is 4×4 mm (LEOS Detector).

The number of photons generated per second from blackbody can be calculated by using calculated detector power Po as shown in Eq. (6).

$$\text{Number of photons per second (N)} = \frac{P_0}{E}, \tag{6}$$

where E is the energy of photon at particular wavelength. Energy can be calculated by using the Planck Einstein relation given by Eq. (7)

$$E = \frac{hc}{\lambda}. \tag{7}$$

The number of photons is calculated for a wavelength band of 200–600 nm and the response is plotted, as shown in Fig. 1.

Fig. 1 Photons emitted per second from a blackbody at 5782 K
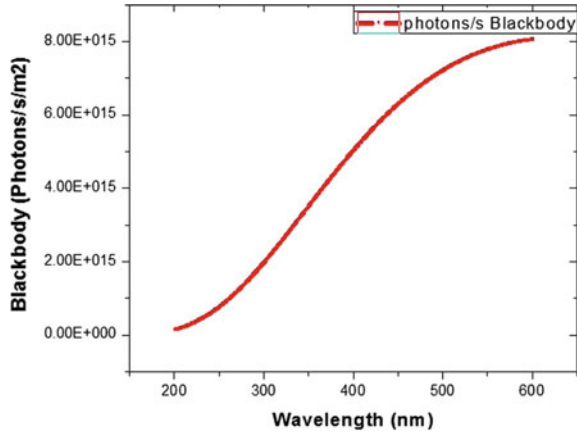
3 Design and Analysis

Signal readout electronics play a major role in any of the UV detection applications. Information is extracted from UV signal and projected on to the interfacing device with the help of processing electronics, as it acts as a central processing unit of the system. The basic requirements of the electronics are it should be a standalone, compact, fast, user-friendly, and simple system. The main intention while designing processing electronics was to have a basic functional design, and then peripherals are added to it, so as to make it more user-friendly and customized system.

In this paper, the photon counting module is equipped with silicon carbide detector which is designed and fabricated at LEOS (ISRO). The output from the detector is current with very low amplitude; the current has to be converted to voltage so it requires an I-V converter (trans-impedance amplifier) and there should be an ADC to convert the analog voltage into digital. The digital values are further processed using a controller, and the required data are to be displayed to 16 × 2 LCD display and PC simultaneously. Figure 2 shows the schematic diagram of proposed photon counter system. The controller used here is a 8-bit ATMEL microcontroller. In an
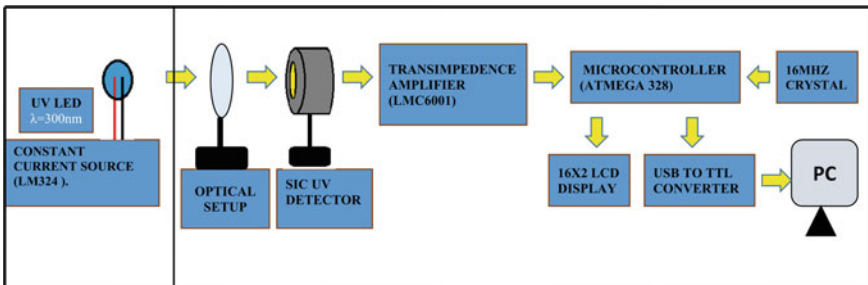
Fig. 2 Schematic diagram of Photon counting system

attempt to make the interpretation of data user-friendly, a graphical user interface (GUI) application is developed using Python-Tkinter software, and a live graph of the real-time photon values is plotted and data log is created to trace the received data over a period of time. The data log is stored on the computer.

4 Results and Discussions

The results of photon counting module obtained are discussed in this section. Spectral responsivity and the quantum efficiency of LEOS UV detector and standard SGLUX detector are being measured and compared. The number of photons that are falling on the detector is measured and compared with the standard photon number emitted from the surface of the sun.

4.1 Detector Performance Analysis

LEOS and SGLUX detector performance is analyzed and it is observed that the LEOS detector has a maximum spectral response and quantum efficiency at 260 nm as shown in Fig. 3 and SGLUX detector has maximum spectral responsivity, and quantum efficiency at 280 nm as shown in Fig. 4. From the comparative analysis, it was concluded that SGLUX was designed for a UV-C spectral band and LEOS detector was designed for a single wavelength monitoring applications.

Active area of LEOS detector is 4×4 mm, dark current is 1 pA, and breakdown voltage ≤ 100 V. Active area of SGLUX detector is 7.6 mm^2, darkcurrent is 25.6 fA, and breakdown voltage is 20 V.

A number of photons falling on the single detector for different intensity of UV LED light of 260 nm wavelength was measured over a period of 5 min, and graph

Fig. 3 Responsivity comparison of LEOS and SGLUX detectors
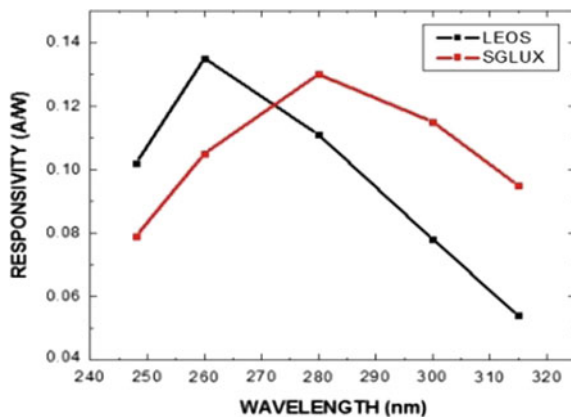
Fig. 4 QE comparison of
LEOS and SGLUX detectors
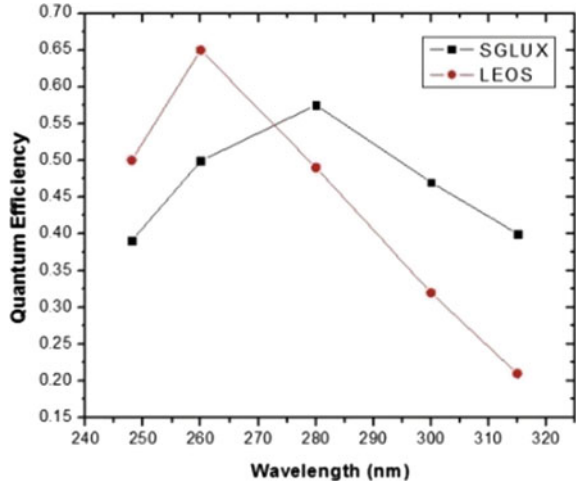
was plotted from collected data. A number of photons calculated from LED was compared with the theoretical calculation of photons generated from the sun over solar spectrum.
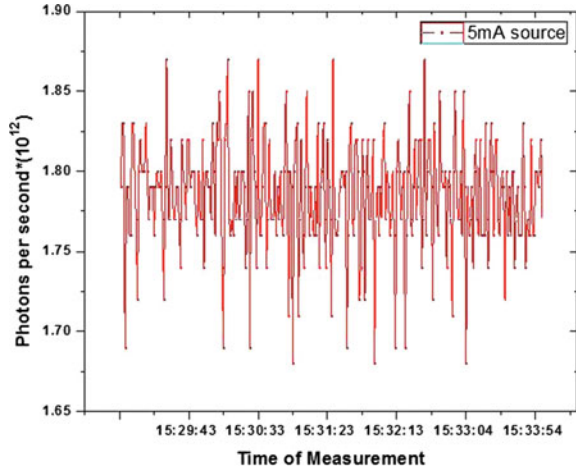
Figures 5, 6, 7, and 8 show the fluctuation in photons detected for different intensity of UV LED light like 20 mA, 10 mA, 5 mA, and 1 mA, respectively. The time of measurement is 5 min of duration and X-axis shows the actual time at measurement.

Fig. 5 Photon count at
1 mA current drive to LED
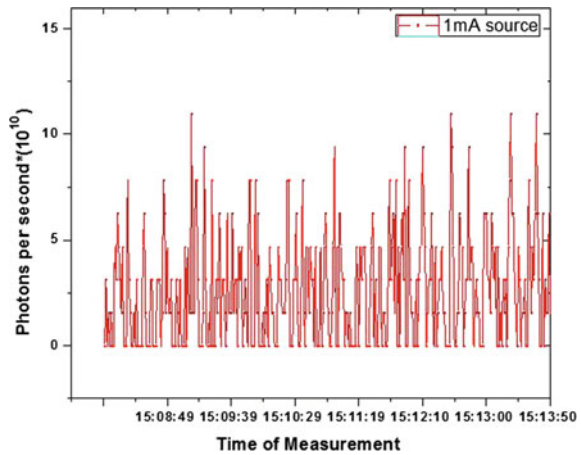
Fig. 6 Photon count at
5 mA current drive to LED

Fig. 7 Photon count at
10 mA current drive to LED
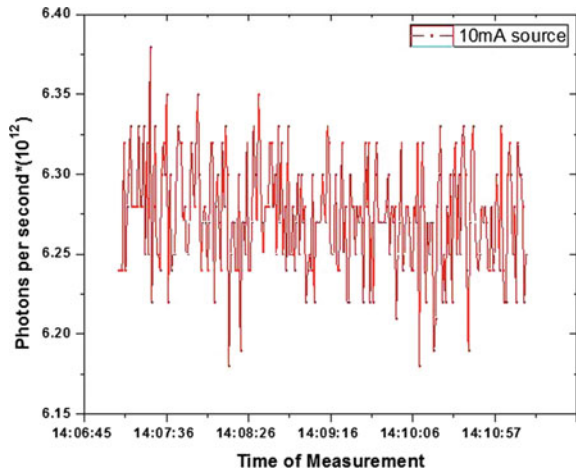
5   Conclusion

The photon-counting system has been proposed for SiC UV detector. A comparative study of LEOS detector and SGLUX detector performance has been carried out, and it is observed that LEOS detector has maximum responsivity at 260 nm and the quantum efficiency of both the detectors is measured and compared. The number of photons generated from the UV source for different intensity of light is characterized and analyzed. We observed a two-order increase in photon count as we increase the intensity of UV source.

Fig. 8 Photon count at
20 mA current drive to LED
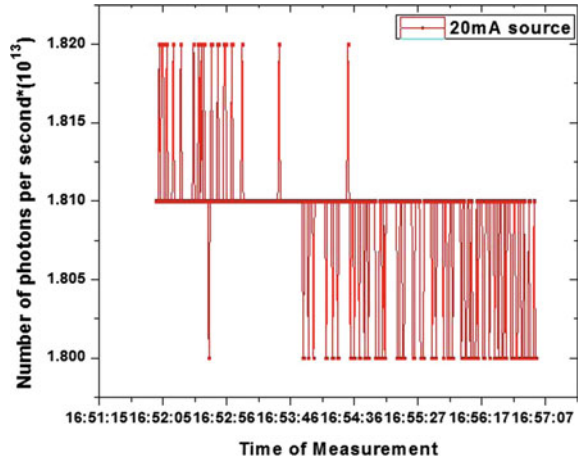
A graphical user interface has been developed using python script. This GUI makes characterization and analysis of different detectors more effective and convenient, as we have made a provision for logging the detector data over a period of time into the computer.

References

1. Razeghi M, Rogalski A (1996) Semiconductor ultraviolet detectors. J Appl Phys 79(10):7433–7473
2. Chen X, Zhu H, Cai J, Wu Z (2007) High-performance 4H-SiC-based ultraviolet p-i-n photodetector. J Appl Phys 102(2):024505
3. Moscatelli F (2007) Silicon carbide for UV, alpha, beta and X-ray detectors: results and perspectives. Nucl Instrum Methods Phys Res A 583:157–161

Design of an Optical Orbital Angular Momentum Sorter

E. S. Shivaleela, Shreya Jaiswal, and Shweta Katti

Abstract Optical orbital angular momentum has caught the attention of researchers from various fields due to its wide range of applications. For use in quantum communications, a photon has to be prepared in a state of orbital angular momentum (OAM). As photons in a light beam with distinct angular momentum are orthogonal to each other, we can use them to represent different data symbols. Thus it is possible to carry a large number of bits on a single photon. In this paper, we report the design of a sorter for 16 OAM helices, which involves simple signal processing techniques.

Keywords Quantum communications · Optical orbital angular momentum · OAM sorter

1 Introduction to Optical Orbital Angular Momentum

Light wave has associated with it various parameters like polarization, frequency/wavelength, and amplitude. When it is required to use light wave as a carrier for communication applications, we can use any one or combination of the above parameters for modulation purpose in accordance with the variation of the message signal. As there is ever increasing demand to carry data at higher speeds, in addition to wavelength-time division multiplexing, space division multiplexing using fibers with multi-core and multi-modes has been explored in the past. OAM is exploited as another dimension, along with other dimensions to enhance the data carrying capacity of fibers, for short reach and high data density applications like data centers [1, 2, 3].
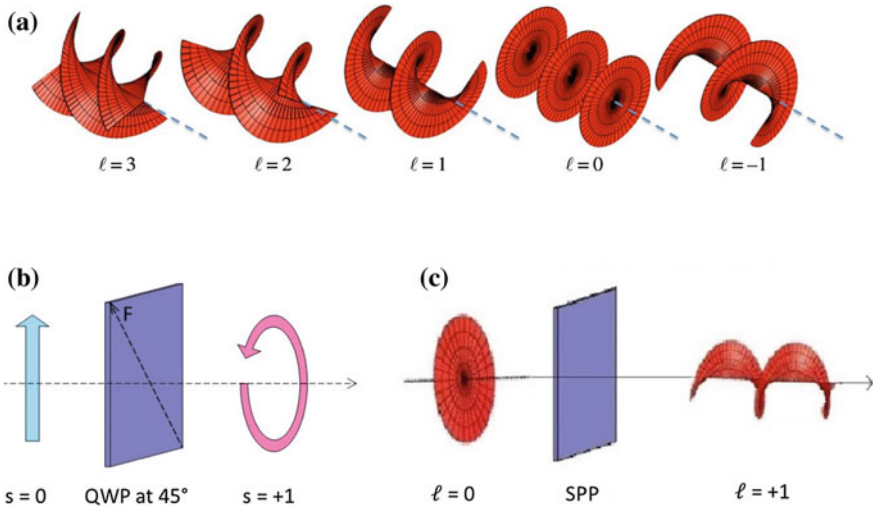
In 1992, Les Allen observed that photon has OAM [1]. Earlier to this, the photon was known to have Spin Angular Momentum (SAM), s = ±1 which describes the right or left circular polarization, respectively. If the E-field vector of the light beam

E. S. Shivaleela (✉)
Indian Institute of Science, Bengaluru, India
e-mail: lila@iisc.ac.in

S. Jaiswal · S. Katti
PES University, Bengaluru, India

Fig. 1 **a** OAM modes $\ell = -1$, 0, 1, 2, and 3 **b** spin conversion **c** OAM conversion

is in a constant plane as it propagates, then the phase plane is stationary, it is linearly polarized and when the E-vector rotates around the propagation axis, it is circularly polarized, and the Poynting vector is parallel to the axis. A photon can have OAM of $\ell = 0, \pm 1, \pm 2 \ldots$, ($\ell$, an integer) denotes the number of inter-wined helices, with each of them orthogonal to the other. The OAM beam has the phase term $\exp(i\,\ell\,\varphi)$, where φ is the azimuthal co-ordinate. The OAM carried by a photon is equal to $\ell\hbar$. The total angular momentum of a photon is the sum of spin and orbital momentum, $(s + \ell)\,\hbar$.

Figure 1 shows OAM beams for $\ell = -1$, 0, 1, 2, and 3; the spin conversion of a linearly polarized light to circularly polarized light using quarter wave plate (QWP) placed at 45° with respect to the incident wave polarization; and OAM conversion achieved using spiral phase plate (SPP) from a circularly polarized light [1]. The total phase change for an OAM beam with ℓ is equal to $\ell\varphi$. A circularly polarized light has no OAM, i.e., $\ell = 0$. An OAM with $\ell > 0$ has a helical phase front. Under the paraxial limit, both SAM and OAM are attributed as independent properties of light. An OAM beam for ℓ may be expanded into a group of Laguerre–Gaussian (LG) beam (each with the same ℓ but with a different p index, for radial distribution) [1].

Along with LG beams, other beams that carry orbital angular momentum are Bessel beams, Mathieu beams, and Ince–Gaussian beams [4]. A mode converter such as a pair of cylindrical lenses can be used for the production of higher order LG modes. The same is being achieved using holograms much more easily.
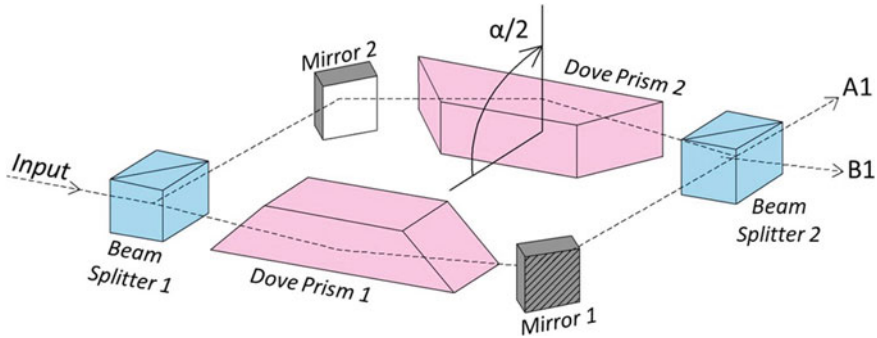
**Fig. 2** Mach–Zehnder interferometer sorts odd and even OAM modes to different ports

2   Generation and Detection of OAM

OAM beams can be obtained from different methods, (1) directly from a laser cavity (2) by converting fundamental Gaussian beam into an OAM beam outside a cavity. In the latter case, the converter could be a SPP, diffractive phase hologram also known as forked hologram, cylindrical lens pairs, etc. OAM can be detected by using a converter that creates a conjugate helical phase or a plasmonic detector.

2.1   *Mach–Zehnder Interferometer for Sorting OAM of Odd and Even Modes*

We describe a method of sorting of OAM using Mach–Zehnder (M-Z) interferometer, with Dove prism in the second arm rotated by $\alpha/2$ with respect to the Dove prism in the first (reference) arm [5], as shown in the Fig. 2. When passed through the rotated Dove prism, the phase of the beam undergoes a phase change α equal to twice the rotation angle of the prism (w.r.t. to the prism in the first arm). In [6], a detailed analysis of dove prism is given. OAM modes with even values of ℓ are sorted to port A1 and those with odd values of ℓ to port B1.

The beam after passing through the rotated Dove prism in the second arm has phase $\exp(i\,\ell\,(\varphi + \alpha))$, which corresponds to a phase shift of $\ell\alpha$ w.r.t. the original beam. By choosing particular combinations of the values of ℓ and $-\alpha$, we can get the rotated beam to be in phase or out of phase w.r.t. to the original beam (or the beam in the first arm if the path length is the same). By adjusting the path lengths in the two arms of the M-Z interferometer, photons with even ℓ, at port A1 and with odd ℓ, at port B1 can be ensured [5]. We propose to extend this principle to sort 16 OAM states, when the input beam consists of mixed odd and even ℓ OAM, ranging from 0 to 15, by cascading four stages of M-Z interferometers. The sorter consists of four stages of Mach–Zehnder interferometer as shown in Fig. 3. The I stage of the sorter
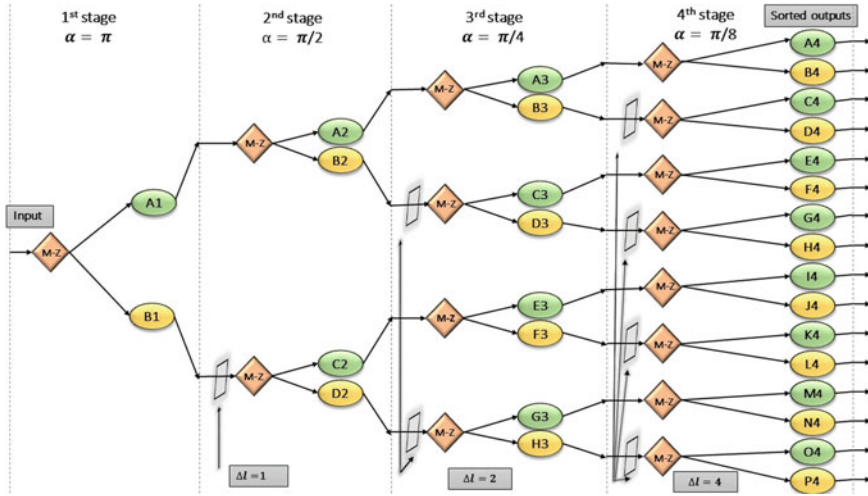
Fig. 3 A cascaded four-stage M-Z interferometer sorts mixed OAM modes. $\ell = 0$–15 to different output ports

is as described earlier (Fig. 2) with all even ℓ OAMs appearing at the port A1, and odd values of ℓ at the port B1. The rotation of the phase of the beams in the upper arm of each of the M-Z interferometer in I, II, III, and IV stages are π, $\pi/2$, $\pi/,4$ and $\pi/8$, and the corresponding prism rotations angles are $\pi/2$, $\pi/4$, $\pi/8$, and $\pi/16$, respectively. Since there is no scheme to separate the OAMS for odd ℓ value OAMs in the same fashion, odd ℓ values are incremented by 1, 2, and 4 in the II, III, and IV stages, respectively, as shown in the Fig. 3, so that they are converted to even values and sorted as described earlier. Table 1 shows the flow of signals through the four stages of M-Z interferometer for 16 OAM modes.

In the stage I of the sorter, all the even ℓ OAMs are sorted to the port A1 and the odd ℓ OAMs to the port B1. Port A1 outputs further get sorted in the second stage as follows, with $\ell = 4n$ to port A2 and $\ell = 4n + 2$ to port B2. However, since there is no method which sorts the odd ℓ value OAMs in the same fashion, outputs corresponding to B1 are incremented by 1, $\Delta = 1$, and then sorted to the ports C2 and D2 in the lower branch of the second stage. A2, B2, C2, and D2 correspond to

Table 1 Signal flow through four stages of M-Z interferometers

the outputs of stage II. Similarly, port A2 outputs further get sorted in the third stage as follows, with $\ell = 8n$ to port A3 and $\ell = 8n + 4$ to port B3 and in the fourth stage with $\ell = 16n$ to port A4 and $\ell = 16n + 8$ to port B4. The sorting process continues with $\Delta\ell = 2$ and 4 in the lower branches of stage III and stage IV, respectively. The mixed 16 OAM modes are thus sorted as shown in Table 1 and appear at distinct ports of the fourth stage M-Z interferometer.

3 Conclusions

OAM has a wide spectrum of applications such as wired communication, free space communication, quantum communication, RF communication, imaging, non-invasive detection, and many more. The photons prepared in distinct OAMs can be used as different states in quantum communication or in space division multiplexing to multiply the data carrying capacity for short range-high data density applications such as data centers. We have designed a sorter for mixed 16 OAM modes, by cascading four stages of M-Z interferometer. Unlike multi-input-multi-output (MIMO), a space division multiplexing scheme, this method does not involve complicated digital signal processing.

References

1. Willner AE et al (2015) Optical Communications using orbital angular momentum beams. Adv Opt Photonics 7(5):66–97
2. Barnett SM et al (2017) Optical orbital angular momentum. Phylosophical Trans A
3. Yao AM, Padgett M (2012). http://eprints.gla.ac.uk/67185
4. Allen L, Padgett M (2011) The orbital angular momentum of light: an introduction. In: Twisted photons: application of light and orbital angular momentum. Wiley, Hoboken
5. Leach J, Padgett MJ et al (2002) Measuring the orbital angular momentum of a single photon. Phys Rev Lett 88(25):257901–257904
6. Moreno I, Paez G, Strojnik M (2003) Polariz Transform Prop Dove Prism 220:257–268

Design and Implementation of IoT Based Rodent Monitoring and Avoidance System in Agricultural Storage Bins

Rohini M. Kariduraganavar and S. G. Shivaprasad Yadav

Abstract India is one of the largest producers of agricultural products having diverse agro-climate zones across the country with a vast range of agricultural products This paper is oriented to accentuate the methods to solve the problems of monitoring the rodents and to take the suitable actions to avoid the rodent's movement. The real-time implementation was based on the image segmentation using an Embedded DSP processor. Several algorithms were reviewed for identifying the rodents using the vision-based techniques and optimized the solutions. The proposed system is used to monitor the attack of rodents and avoid large-scale grain storages such as in warehouses, go-downs, and agricultural grain stores without any human intervention. The implementation was made based on IoT approach for communicating the data onto the server and maintained the database.

Keywords Embedded DSP processor · IoT · Rodent

1 Introduction

Agricultural sector being the backbone of the Indian economy is one of the key areas in the development of the country. India is one of the largest producers of agricultural products having diverse agro-climate zones across the country with a vast range of agricultural products. The storage is an important marketing function, which involves holding and preserving goods from the time they are produced until they are needed for consumption. The reprehensible storage results in high losses in grains as per 20% agriculture, 30% of fruits and vegetables grown [1]. Thus, there are several challenges to be addressed in these storages. Some of the challenges are attacks of rodents or insects, worms, and so on, which may result in heavy losses. The safety of grain storage is a significant thing that concerns people's living quality

R. M. Kariduraganavar · S. G. Shivaprasad Yadav (✉)
Department of Electronics & Telecommunication Engineering, RIT, Bengaluru, India
e-mail: shivaspy@gmail.com

R. M. Kariduraganavar
e-mail: rohinimk1993@gmail.com

Fig. 1 Agricultural grain stores

and national economic development. It is exceedingly important to monitor the grain storage condition periodically. Improving the automation level of monitor system is the key to assure the safety of grain storage.

Rodents are the best and inexhaustible mammalian gathering on earth to offer human natural surroundings and nourishment. A colossal measure of grain and nourishment is lost to the pests, especially rats and environment is tainted because of utilizing the pesticides. Rodents including mice, rats, moles, rabbits, raccoons, squirrels, and voles are the most various and boundless of all warm-blooded animals. Figure 1 shows the agricultural grain store.

Creation of monitoring and avoidance systems on embedded platforms includes selection of appropriate platform, and the corresponding tracking algorithm able to provide acceptable reliability and speed.

For our study, we used a digital signal processor (DSP) oriented to video image processing. Particularly, we considered the DSP, type TMS320DM6437, and used as a basis for the debugging means called Spectrum Digital DM6437 EVM—in accordance with the task to be solved.

2 Proposed System

The developed algorithm in this paper is to monitor and avoid the rodent in large-scale storage of grains without human intervention. The algorithm is used in MATLAB R2013b and used to interface with DSP processor kit, i.e., TMS320DM6437 EVM.

Using MATLAB, we proposed two algorithms; One is Background Subtraction Method and the other one is Feature Extraction method. In Background Subtraction Method, we detected the motion of the rodent [2]. We captured the image of rodent and subtracted with current image and if it is similar to rodent, then rodent has

Fig. 2 Basic block diagram
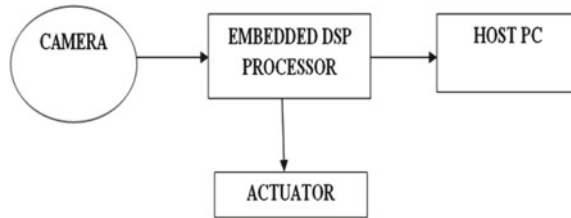
been detected or else rodent has not been found. In Feature Extraction Method, we took predefined image of rodent and compared with the current image of any moment captured in the camera may be it is rodent or human [2]. We compared with 13 features namely Contrast, Correlation, Energy, Homogeneity, Mean, Standard Deviation, Entropy, RMS, Variance, Smoothness, Kurtosis, Skewness, and IDM [9].

After debugging the algorithm, it was ported to DSP TMS320DM6437 EVM kit. To implement this, we used the Code Composer Studio v4 IDE.

We employed two methods in our algorithm for rodent detection and avoidance in large-scale storage of grains like in warehouses or in go-downs. They are sensor-based algorithm and vision-based algorithm. For sensor-based algorithm, we used PIR SENSORS/IR SENSORS to capture the image as input. PIR sensors were used to classify the moving object with high precision and localize the moving object [3]. For vision-based algorithm, the image and video processing were employed. To implement the data from PIR sensors which are used to capture the image from those inputs, we can detect the rodents [4].

As we have used both the techniques in our work to implement the IoT based Rodent Monitoring and Avoidance for Large-Scale Storage of grains in warehouses as well as in go-downs, we can detect rodent and avoid using repeller.

The basic block diagram for implementation of IoT based rodent monitoring and avoidance in large-scale storage of grains is illustrated in Fig. 2.

3 Design and Development of the System

The design and development of the proposed system is implemented using software and hardware.

3.1 Software Implementation

The implementation of software was done using two techniques. They are Background Subtraction Method and Feature Extraction Method [8]. The operation of the proposed system in the software part is shown in Fig. 3.
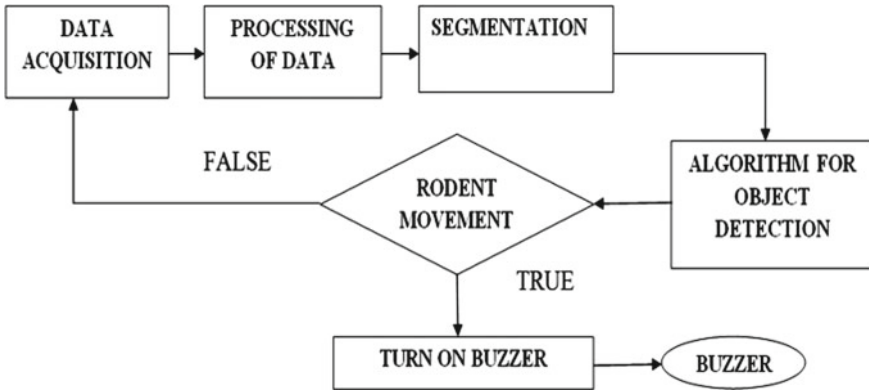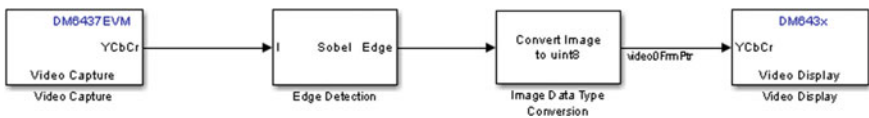
Fig. 3 Operation of the proposed system

Fig. 4 Block diagram using edge detection

The rodent monitoring and avoidance is implemented by capturing the data from the camera and processed using segmentation method. We can detect rodent and avoid turning on the buzzer.

Using Edge Detection method, we can detect the rodent by its edges. By its shape, we can determine the rodent and if it is, we can turn on the buzzer to avoid it. Figure 4 shows the block diagram of rodent monitoring and avoidance using Edge Detection method which is implemented in MATLAB R2013b [5]. The same software is converted to Code Composer Studio to integrate with DSP processor, i.e., TMS320DM6437 EVM.

3.2 Hardware Implementation

The software was integrated to hardware using two different IDE. We used two hardware for our proposed work, i.e., DSP processor and Raspberry Pi 3.

Using Edge Detection method, we integrated to DSP Processor TMS320DM6437 EVM. The hardware implementation is displayed in Fig. 5.

Using Python language, we implemented on Raspberry Pi 3 module. Here the movement of Rodent was sensed by IR or PIR sensor. If the movement is detected by IR sensor, the Raspberry Pi 3 senses send the message to the client using GSM module [6]. The client can monitor the live video anywhere sitting in anyplace using IP camera

Fig. 5 Implementation of TMS320DM6437

placed in warehouses or in go-downs. The client if observed the rodent movement can turn on the buzzer [7]. Figure 6 shows the implementation of Raspberry Pi 3.

4 Results and Discussion

The hardware used to interface with CCv4/CCv5 is DSP Processor which is audio/video processing, i.e., TMS320DM6437 EVM module. Here the rodent movement is determined by Edge Detection Technique. If any movement of the rodent is found by its edge, we can determine whether it is Rodent or not. We can determine the edge of human being or any animal which is moving in the storages or go-downs or warehouses.

The rodent movement using Edge Detection is displayed using Projector. The snapshot of the output is given in Figs. 7a–e. The rodent movement is captured by the camera and displayed using projector. Here the edge detection of the movement can be seen whether if it is Rodent or not [10]. So the rodent has been captured and by its edge, we can determine that is Rodent which is illustrated in Fig. 7c, d.
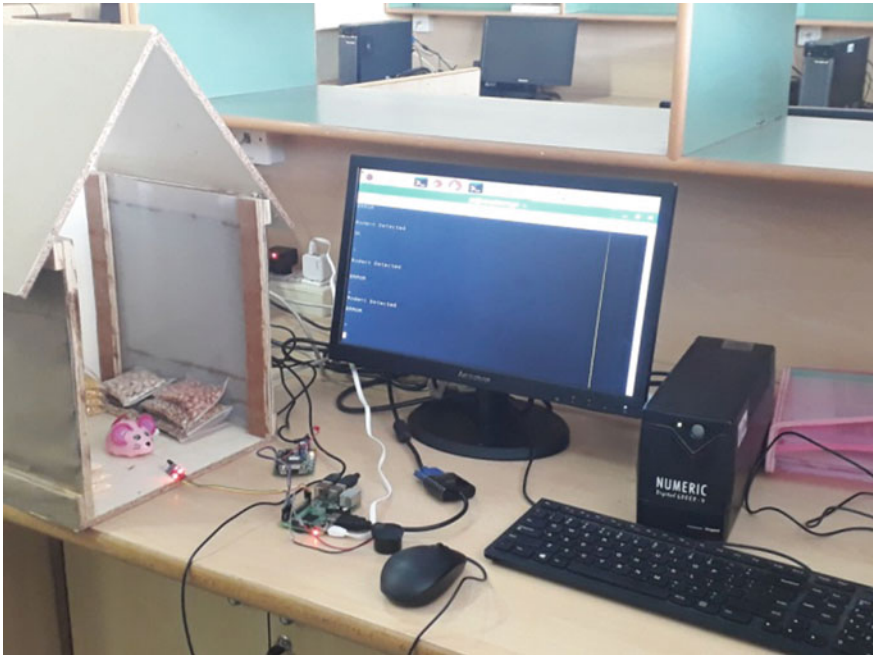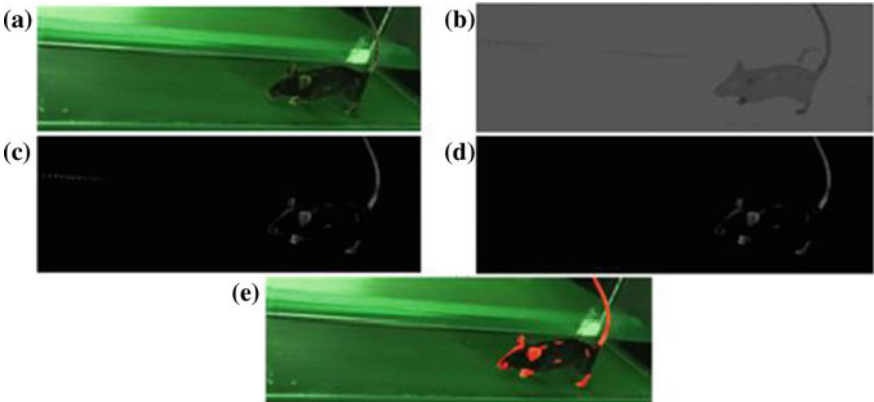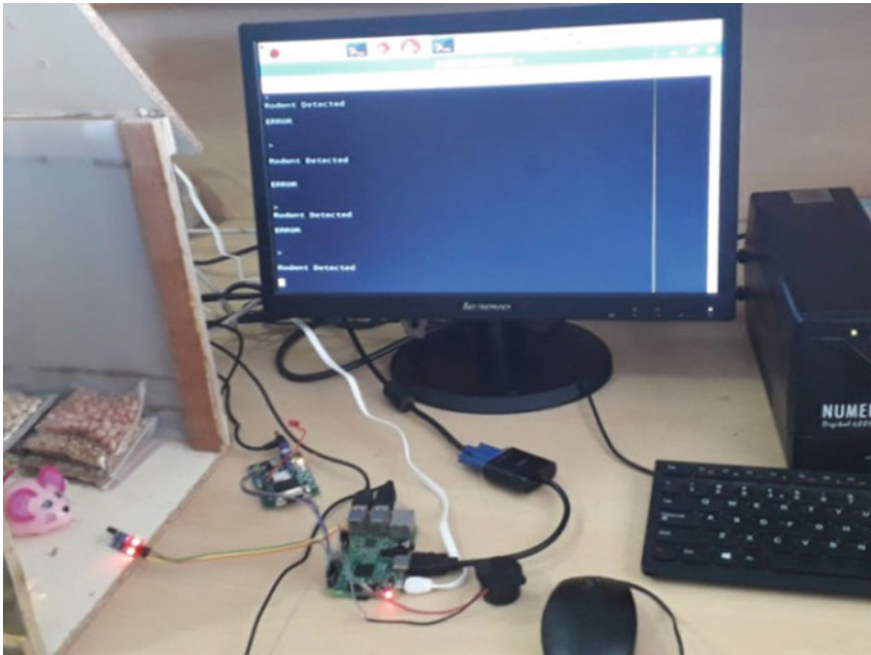
Fig. 6 Implementation on Raspberry Pi 3

Fig. 7 Output displayed from projector using TMS320DM6437

The hardware which is used to detect the rodent and send a SMS to client via Python language is Raspberry Pi 3. Here if the rodent movement is observed, then the IR sensor detects and sends a message to GSM module. The GSM module sends

Fig. 8 Output displaying on terminal of Python language using Raspberry Pi 3

the SMS to client that Rodent is detected and the client observes it from IP camera. He turns on the buzzer or repeller to avoid the Rodent. The snapshot of the output displaying Rodent Detected is shown in Fig. 8. The terminal window displaying Rodent has been detected when it observes the rodent movement in storages which is illustrated in Fig. 7.

The SMS that is generated by GSM module is displayed in Fig. 9. Here if the movement is observed by the IR sensor, it enables the GSM module and sends an SMS to clients mobile saying that Rodent has been detected. This has been illustrated in Fig. 9. If the client sees the message displayed in his android mobile, then he can turn on the buzzer to avoid it.

Fig. 9 SMS generated by GSM module using Raspberry Pi
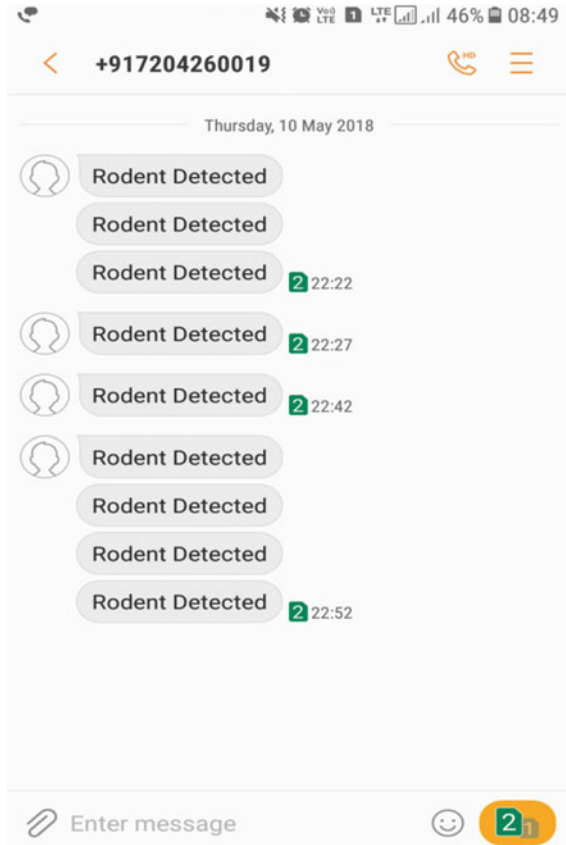
References

1. Anton V, Oleksandr A, Oleksandr L (2017) CAMSHIFT object tracking algorithm implementation DM6437EVM. In: Proceedings of the 4th European DSP in education and research conference, ISBN 978-0-9552047-5-3
2. Venkatesh D, Tatti M, Hardikar PG, Ahmed SS, Sharavana K (2017) Cold storage management system for farmers based on IOT. Int J Recent Trends Eng Res. ISSN: 2455-1457
3. Kavya P, Pallavi KN, Shwetha MN, Swetha K, Jayasri BS (2017) Use of smart sensor and IOT to monitor the preservation of food grains at warehouse. Int J Res Trends Innov 2(6). ISSN: 2456-3315
4. Cruvinel PE, Koenigkan LV, Pereira MFL (2016) Visualizing thermal information and knowledge creation in grain storage bin based on three-dimensional (3D) interface model and computer graphic techniques. In: IEEE tenth international conference on semantic computing. 978-1-5090-0662-5/16
5. Rezaei B, Lowe J, Yee JR, Porges S, Ostadabbas S (2016) Non-contact automatic respiration monitoring in residential rodents. IEEE 978-1-4577-0220-4/16
6. Baranwal T, Nitika, Pateriya PK (2016) Development of IOT based smart security and monitoring devices for agriculture. IEEE 978-1-4673-8203-8/16

7. Badr BM, Somogyi-Gsizmazai R, Delaney KR, Dechev N (2015) Wireless power transfer for telemetric devices with variable orientation for small rodent behavior monitoring. IEEE Sens J 15(4)
8. Dewi RK, Hari Ginardi RV (2014) Feature extraction for identification of sugarcane rust disease. In: International conference on information, communication technology and system, IEEE 978-1-14799-6858-9/14
9. Mohanaiah P, Sathya Narayana P, Guru Kumar L (2013) Image texture feature extraction using GLCM approach. Int J Sci Res Publ 3(5). ISSN 2250-3153
10. Bradski GR (2012) Computer vision face tracking for use in perceptual user interface. Intel Technol J Q2

Implementation of Security System and Its Interconnection with Lighting

K. M. Akshay, Rahul Hebbar, R. Harshavardan, Roshan, and P. S. Manjunath

Abstract Nowadays like home security, building security is also becoming prominent since the possibilities of intrusion and other kinds of security threats are growing day by day. For an organization, safeguarding their assets is of utmost importance. Thus, with the help of latest technology, our project aims to design and implement the highest level of security that an organization can have in order to protect and control the assets of the organization. The work focuses on constructing a state-of-the-art security for buildings which includes integrating four different types of securities which are access control, surveillance, geofencing, intrusion detection and asset management. This system can alert the authorized persons by sending SMS/email to their mobile phones. An alarm is also raised if required. The advantage of using this system over the existing ones is that the current security systems are all stand-alone systems. The surveillance, intrusion detection, access control, and asset management are not integrated into the existing system. Our work focuses on integrating these into a single microcontroller. First stage of the work consists of building a prototype by using different sensors such as ultrasonic sensor, IR sensor, radio frequency identification card reader, GSM module, etc. The main controller used for the prototype is ATmega 2560. Second stage consists of implementing it in real time. According to the company's requirement different brands such as DSC, Bluvision, and Zavio were used. These stand-alone systems were integrated into Vantage lighting system, which is the main controller used for real-time implementation. Both in prototype and real-time implementation of the work, the security system is completely automatic and it will enable the authorized persons to remotely control and monitor the areas of the building from any place. The result of the project shows that whether there is an intrusion and security breach from one's own employees of an organization, they are all monitored and controlled automatically through different systems which in turn are integrated into a single system so that immediate action can be taken to prevent such breaches.

Keywords Automatic security · Integration · Lighting · Foolproof system

K. M. Akshay · R. Hebbar · R. Harshavardan · Roshan · P. S. Manjunath (✉)
Department of Telecommunication Engineering, B.M.S College of Engineering, Bengaluru, India
e-mail: manjunathps.tce@bmsce.ac.in

1 Introduction

In this twenty-first century, the crime rates are ever increasing; everybody wants to safeguard one's own assets. Thus, the security system plays an important role. Suppose a CEO of an organization is away from the building and he/she needs to ensure that the building is secured. The CEO can use anyone of the stand-alone security systems in the market. But in today's world everything is becoming automatic. Hence, it is important to have an automatic security system which inculcates various categories of security like intrusion, access control, asset management, surveillance, etc. All these types of security need to be integrated into one stand-alone system from which it can be monitored and controlled. An automated security system which integrates different types of security into a single system provides an additional layer of security. The security might comprise of user verification to prevent break-ins at entry points and also to track unwanted activities or illegal intrusions within the locality of the building.

The stand-alone system that is used in the real-time implementation of the project includes DSC, Bluvison, and Zavio. These systems are integrated into a microcontroller, which is the lighting system of the building. The provision to send alert message to security guard during security breaches is also built into this system. Also if the employees of the organization are deceptive in nature, they can be monitored and controlled through this system. Thus, the building security system proposed in the project provides the state of security for the CEO and the employees of an organization. The rest of the paper is organized as follows. The literature survey of this paper is described in Sect. 2. Section 3 lists the architecture design for security. Sections 4 and 5 describe prototype and real-time implementation of the work, respectively. The conclusion and future work of this project is described in Sects. 6 and 7, respectively.

2 Related Work

Office or building security is one of the important issues where crime rates are increasing day by day and due to this the organization faces a huge loss. In order to have a sustainable growth in the organization, proper security measures have to be incorporated. The security system should be able to identify the intruder and not an employee of an organization. And if there is attempt for breaking in, the owner or the required person should be alerted so that he/she can take immediate action. Also, there should be a device for recording in order to trace what is happening, and this can be used as an evidence to help the police to identify the intruder and to be able to search the misplaced or stolen object [1].

Earlier research about building security was conducted by Aditya Shankar where the security system included fingerprint activation for access control and a camera for surveillance [2]. Another study that was conducted about building security systems included using LabVIEW for face detection. Their technology uses histogram as a

feature for face detection [3]. One more study by Alvin Kabir, where he designed a system which could send the alerts to a cellular device like a portable mobile phone of the required person. GSM technology was used in this system so that an SMS was used to alert the individual. This setup used three components: a GSM module, PIC microcontroller, and one or more sensors to detect the intrusion [4]. This method which uses portable mobile handsets to receive warning or alert messages is very helpful since the user need not hold any additional piece of equipment to receive the warning messages, because most of the people already have a handset that supports GSM technology. But this system does not include surveillance and measures to monitor the assets. The prototype of the automatic security system was designed and developed using Arduino mega [5]. This included using different sensors for motion, intrusion detection, etc. A motor was used to integrate the camera into the existing system. Alert messages are sent to the owner via SMS using GSM technology. The main idea of using wireless technology was to send alerts and to make sure that the owner is alerted even if he is away from the office. There were different types of wireless technologies such as Bluetooth, CDMA, etc. but we choose GSM since we compared it with other techniques and found out that it is more efficient and cheaper and also we were more familiar with it than other technologies [6].

The microcontroller that we use to build the prototype was ATmega 2560 [7]. We used this since it simplifies the amount of software and hardware development needed to get the system working and also in the hardware platform reset and power circuit setup are readily available. It also supports circuits through which we can directly program and communicate with the microcontroller using USB. On the software end, Arduino Mega 2560 provides a number of different libraries so that the microcontroller can be programmed effortlessly [8]. The prototype design of the security system consisted of using Radio Frequency Identification (RFID) cards and reader for access control. It is basically a wireless technology which works on radio waves. The tags and the RFID reader will be emitting these waves and are picked up by the reader when these cards come near it. The tags/cards consist of microchip ID data, which stores the UID of different employees of the organization [9]. The electronic circuits of RFID Tags have memory and because of this they can store data. This memory is divided into different cells. Some cells can store only read-only data, such as UID number, rest can store UID, major and minor together [10]. These IDs are generated at the time when the tag is produced.

3 Architecture Design

Security is a strategy by which something is secured through an arrangement of inter-working components and gadgets. All security systems deal with a similar essential guideline of securing entry points, like the main building door and windows, and in addition inside space of an office/building containing assets. The building/office security system consists of networks of integrated devices which are all working together with a central controller in order to protect against intruders and burglars
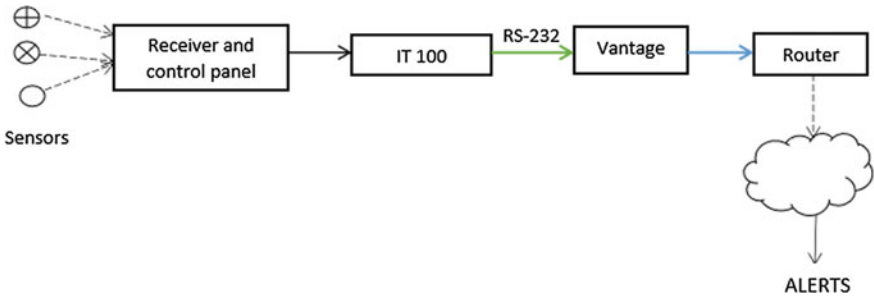
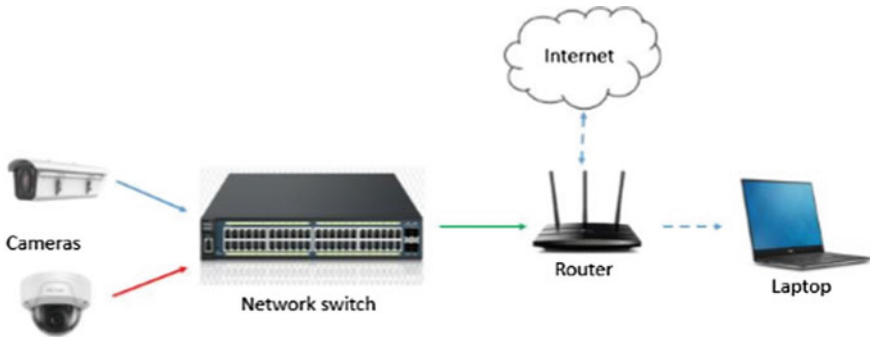**Fig. 1** Architecture of intrusion detection

Fig. 2 Architecture of surveillance

and other potential threats. Mainly a security system has four domains: surveillance, intrusion detection, access control and geofencing and asset management.

A simple architecture was designed for each part of the security system as shown in Figs. 1 and 2.

3.1 Intrusion Detection Surveillance

See Figs. 1 and 2.

4 Prototype Implementation

The block diagram of the prototype is shown in Fig. 3. The main controller used for the prototype is ATmega 2560. In this prototype, ultrasonic sensors are used to detect any motion or intrusion and RFID-based access control to provide access to
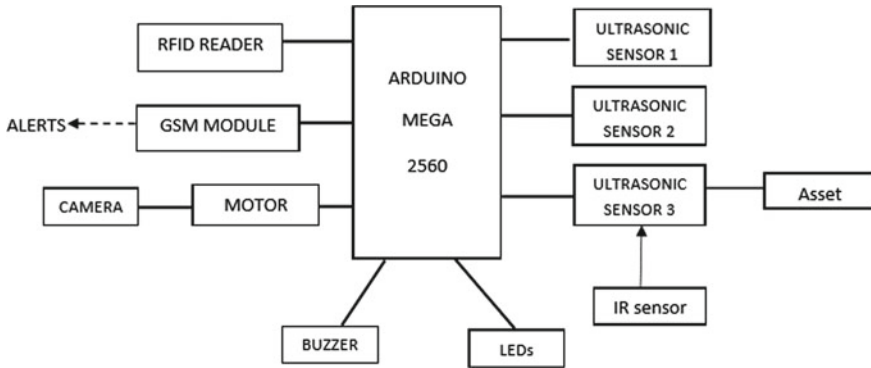
Fig. 3 General block diagram of prototype

authorized users. IR sensor is used to detect if the asset is moved or not. The control of camera is done through a motor. There is a main door through which a person can enter by scanning the RFID cards. Each room consists of LED's to which the security system is integrated.

The implemented circuit is shown in Fig. 4. The prototype requires a power supply of 12 V. There are two modes defined for the prototype, Intrusion ON mode and Intrusion OFF mode. When a supply of 12 V is given to the Arduino Mega controller, the prototype will start with Intrusion ON mode. This mode is to detect any unwanted or unauthorized entry. If any movement or presence is detected in this mode, alarm will go on and an alert text is sent to authorized mobile phones via a GSM module. Along with this, a camera model, which is controlled by a motor, tracks the intrusion. Also if an asset is moved which is kept in the asset room, alarm and text message are sent to the authorized person.

The Intrusion OFF mode is activated by scanning an authorized RFID card on the RFID reader near the door. Any unauthorized card is rejected by the controller and an authorized card is accepted and acknowledged with a short beep sound. As soon as an authorized card is accepted, the door automatically opens and closes with a slight

Fig. 4 Implementation setup
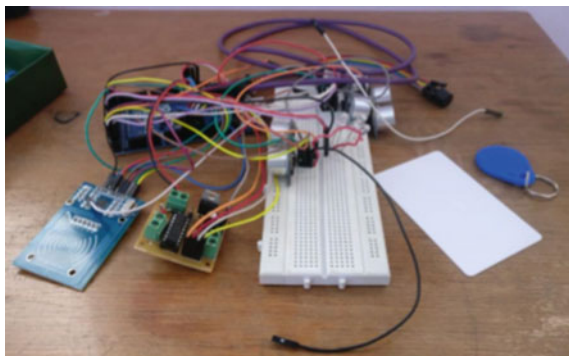
Fig. 5 Layout of prototype

delay to allow a person to enter. The opening and closing of a door are controlled by a motor. Once an authorized person enters any cabin, the LED in that cabin will turn on by detecting the presence of that person. Later, the LED automatically turns off when there is no one present in the cabin. When there is no movement or presence of anyone in any of the cabins, then the prototype switches to Intrusion ON mode. Then any movement before scanning an authorized card will be treated as an intrusion. The layout for the prototype is shown in Fig. 5 (Fig. 6).

The brand selected for intrusion detection system is DSC which is shown in Fig. 7. Different sensors that were used are motion sensor to detect motion, glass break sensor to detect breaking of a glass, contact sensor to detect opening and closing of a door or window, flood sensor to detect any water leakage, and smoke sensor to detect smoke caused by fire in the building. These sensors are wireless sensors and communicate with a DSC control panel, PC-1864, at 433 MHz; the DSC panel PC-1864 is a hybrid panel which supports both wired and wireless sensors. This stand-alone system is integrated into Vantage controller through an interface module, IT-100, via RS-232 cable. Interfacing module IT100 converts the signals of the DSC control panel to a format which is compatible with Vantage and vice versa. So one can arm or disarm the intrusion system through mobile phone.

5 Conclusion

The designed automatic building security system was tested a number of times and it can be certified as a completely foolproof system. The chief executive officer can remotely monitor how each employee is spending their time in office as well as control certain restricted areas to manage assets. The Vantage system to which we have integrated provides both security and building automation. Finally, the work was designed and implemented in such a manner so as to make it user-friendly and also
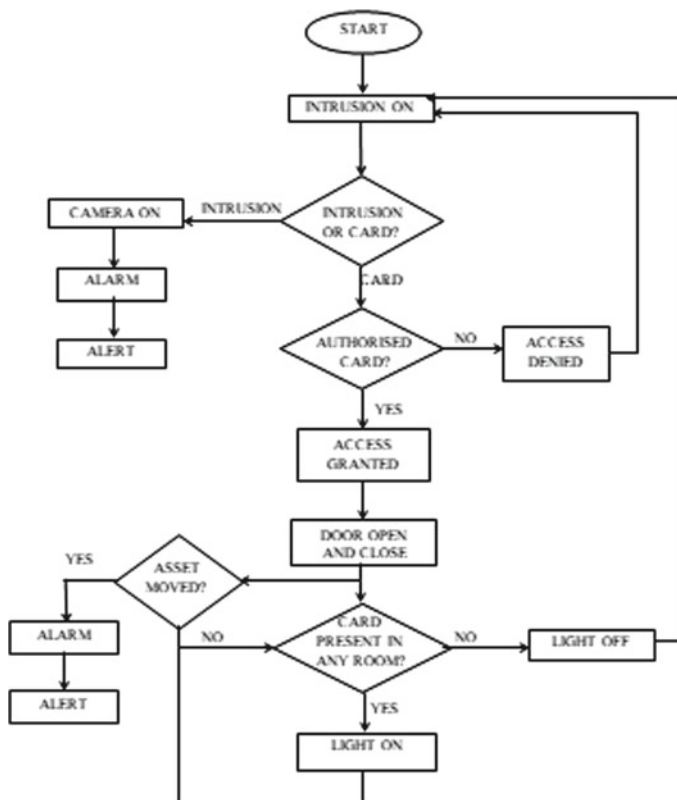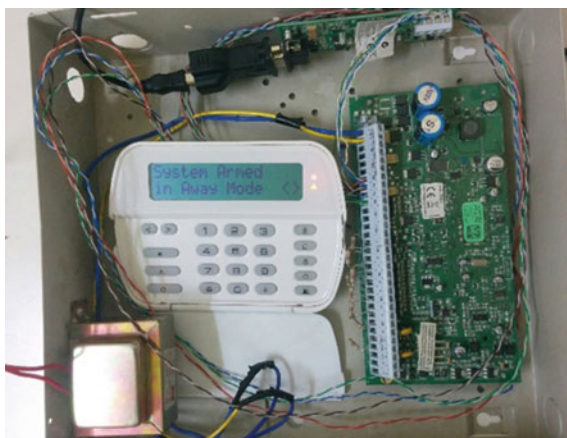
Fig. 6 Working flowchart

Fig. 7 DSC intrusion detection system

to set it up in different offices with ease and convince. Thus, the required objectives and goals of our work have been accomplished.

As of now, the system is dependent on the employees of the building. As soon as the employees leave the building the system will be in "armed" mode. If a guest wants to visit the building, it will lead to security breach. This can be improved by having a camera which can send pictures of the person who wish to enter the building to the CEO and he/she can remotely disable the security system to welcome the guest.

References

1. Fry E, Johnson S (2014) Embedded home security system. Computer Science, College of Natural Sciences Colorado State University Fort Collins, United States
2. AdityaShankar A, Sastry PRK, Vishnuram AL, Vamsidhar A (2015) Fingerprint based door locking system. Int J Eng Comput Sci
3. Yoo TW, Oh IS (2006) A fast algorithm for tracking human faces based on chromatic histograms. Pattern Recogn Lett 20(10):967–978
4. Khan SR, Al Mansur A, Kabir A, Jaman S (2012) Design and implementation of low cost home security system using GSM network. Int J Sci Eng Res 3(3):1
5. Nayyar S, Valarmathi B, Santhi K (2017) Home security and energy efficient home automation system using Arduino. In: International conference on communication and signal processing
6. Khan SR, Al Mansur A, Kabir A, Jaman S (2012) Design and implementation of low cost home security system using GSM network. Int J Sci Eng
7. Zhenghua X, Guolong C (2014) The smart home system based on Arduino mega 2560 And GSM. Int J Smart Sens Intell Syst
8. Gill K, Yang S, Yao F, Xin L (2013) A ZigBee-based home automation system using ATmega 2560 microcontroller. IEEE Trans Consum Electron
9. Rao KVS, Nikitin PV, Lam SF (2014) Antenna design for UHF RFID tags. IEEE Trans Antennas Propag 2014
10. Want R, Vetrivel PS (2011) An introduction to RFID technology. IEEE Pervasive Comput